Springer Proceedings in Physics 182

José-Enrique García-Ramos
Clara E. Alonso
María Victoria Andrés
Francisco Pérez-Bernal *Editors*

Basic Concepts in Nuclear Physics: Theory, Experiments and Applications

2015 La Rábida International Scientific Meeting on Nuclear Physics

Springer

Springer Proceedings in Physics

Volume 182

More information about this series at http://www.springer.com/series/361

José-Enrique García-Ramos · Clara E. Alonso
María Victoria Andrés · Francisco Pérez-Bernal
Editors

Basic Concepts in Nuclear Physics: Theory, Experiments and Applications

2015 La Rábida International Scientific Meeting on Nuclear Physics

Springer

Editors
José-Enrique García-Ramos
Faculty of Experimental Sciences
University of Huelva
Huelva
Spain

María Victoria Andrés
Faculty of Physics
University of Seville
Seville
Spain

Clara E. Alonso
Faculty of Physics
University of Seville
Seville
Spain

Francisco Pérez-Bernal
Faculty of Experimental Sciences
University of Huelva
Huelva
Spain

ISSN 0930-8989 ISSN 1867-4941 (electronic)
Springer Proceedings in Physics
ISBN 978-3-319-21190-9 ISBN 978-3-319-21191-6 (eBook)
DOI 10.1007/978-3-319-21191-6

Library of Congress Control Number: 2016936961

Printed on acid-free paper

This Springer imprint is published by Springer Nature
The registered company is Springer International Publishing AG Switzerland

Preface

The 2015 La Rábida International Scientific Meeting on Nuclear Physics was held from June 1 to 5, 2015 in the campus of the International University of Andalucía (UNIA) at La Rábida (Huelva, Spain).

The name of La Rábida has a special significance for the nuclear physics community. Since the beginning of the eighties, professors from the University of Seville have been organizing summer schools on nuclear physics, which were first named as "La Rábida Summer Schools" and later as "Hispalensis Summer Schools". The first edition took place in 1982, that is, 33 years ago. After eight editions and a gap of some years, in 2009 we revived this event by organizing a new edition, which was named *International Scientific Meeting on Nuclear Physics*. This present edition follows closely the two previous ones, with the same general title, i.e., "Basic concepts in Nuclear Physics: theory, experiments and applications". The opening ceremony was presided over by the Director of the International University of Andalucía (UNIA) at La Rábida, Prof. Yolanda Pelayo Díaz, with the presence of the Vice-rector of Research of the University of Huelva, Prof. Antonio Jesús Díaz Blanco, and the Director of the Meeting, Prof. José Enrique García Ramos.

The objective of the school has been to provide the attendance (students and young postdocs) a wide and solid education in the field of nuclear physics. The course was divided into three main topics: theory, experiments, and applications. Six experienced and well-known researchers have participated in the event, each giving four-hour lectures covering the topics of interest. In addition, young participants have also presented their own research works through seminars and posters. Most of the lectures and contributions have been published in this special number of Springer Proceedings in Physics.

The topics presented by the speakers in their lectures covered the whole field of nuclear physics, from applications with a great social impact as nuclear wastes and medicine, to fundamental topics in basic research, theory, and experiment. Here we list the speakers and topics:

- Prof. L.E. Herranz, CIEMAT (Spain). *Severe accidents in Nuclear Power Plants*.
- Prof. Iain Moore, University of Jyväskylä (Finland). *Laser spectroscopy*.
- Prof. Juan M. Nieves, IFIC-CSIC (Spain). *Neutrinos in Nuclear Physics*.
- Prof. Dieter Schardt, GSI (Germany). *Hadrontherapy*.
- Prof. José J. Valiente Dobón, INFN Laboratori Nazionali di Legnaro (Italy). *Gamma ray spectroscopy of exotic nuclei*.
- Prof. Dario Vretenar, University of Zagreb (Croatia). *Nuclear structure, relativistic mean field theory*.

The number of registered Ph.D. students and postdocs has been around 55 coming from different countries: Brazil, Bulgaria, China, Colombia, Cuba, India, Italy, Germany, Jordania, Libya, Morocco, Nigeria, Poland, Rumania, Russia, Spain, Turkey, UK, and Ukraine. In the particular case of Spain, participants came from 8 different universities and research centers, covering basically all institutions where active nuclear physics groups are working.

Grants covering partly lodging and boarding were supplied to 35 participants. This has been possible and thanks to the economical support received from CPAN (Center of high energy particles, astroparticles and nuclear physics) and Cátedra AIQBE (Asociación de Empresas Químicas, Básicas y Energéticas de Huelva, Universidad de Huelva).

Lectures given by the speakers and the contributions of the young participants have undoubtedly shown the interest and the impact of nuclear physics on many brilliant students working in fundamental research as well as in very diverse applications of nuclear physics.

We would like to conclude with a special gratitude to the students and the young postdocs who have helped us with the daily work. Organizing this event would have been impossible without their support.

Huelva — José-Enrique García-Ramos
Seville — Clara E. Alonso
Seville — María Victoria Andrés
Huelva — Francisco Pérez-Bernal

Logos of the Sponsors

Rábida 2015 Sponsoring Institutions

Rábida 2015 Organizing Institutions

Photographs

We are grateful to Jim Lei and the rest who made their photographs available to us.

Basic concepts in Nuclear Physics: theory, experiments and applications.
June 1st - 5th, 2015
La Rábida, Huelva (Spain)

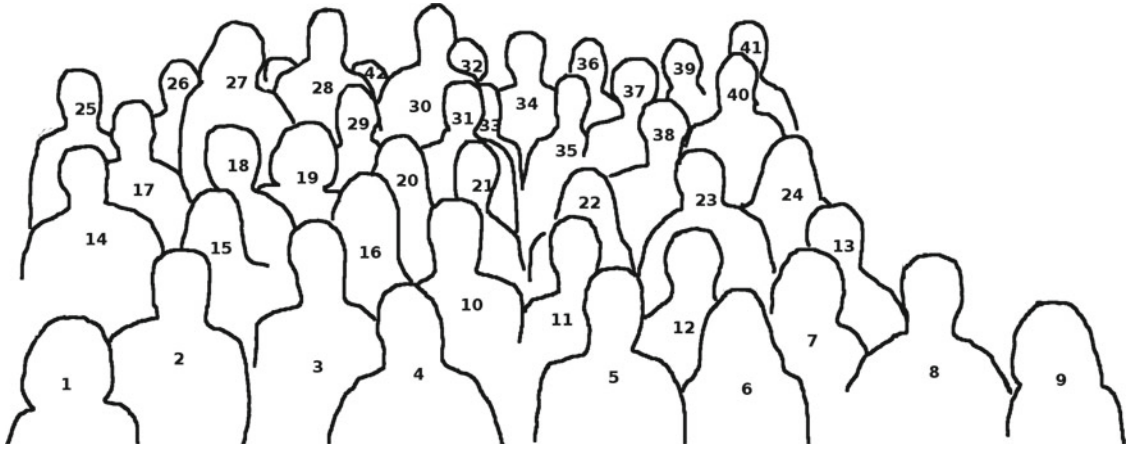

1 Clara E. Alonso
2 Juan Nieves
3 José Javier Valiente
4 José Enrique García-Ramos
5 Javier Balibrea
6 Maria Cristina Battaglia
7 Lorena Vázquez
8 Dieter Schardt
9 Mª Victoria Andrés
10 Francisco Pérez-Bernal
11 Jorge Lerendegui
12 Fitzgerald Ramírez Moreno
13 Francisco Manchado de Sola
14 Max Emde
15 Laura Moschini
16 Yisel Martinez
17 Julius Wilhelmy
18 Lei Jin
19 Jeannie Rangel
20 Aysegul Ertoprak
21 Jesús Casal
22 Elisa Rodríguez López
23 Terver Daniel
24 Marta Sabate-Gilarte
25 Guillermo D Megías Vázquez
26 Ivan Grachev
27 Mario Gómez Ramos
28 Baki Akkus
29 Yesim Oktem
30 Alexandru Dumitrescu
31 Rahal Saadi
32 Samuel Ayet San Andres
33 Andreea Budaca
34 Thomas Day Goodacre
35 Gloria Marquínez-Durán
36 Iain Moore
37 José L Guerrero Márquez
38 Miguel Macías Martínez
39 Dario Vretenar
40 Victor Guadilla
41 Andrii Torgovkin
42 Rashmi Ramesh

Not shown in the picture: Maryam Ahannach el M'Siri, Conrado Albertus Torres, Mohammad Alda'ajeh, Miguel Antonio Cortes-Giraldo, Alfonso Gijón Gijón, Laila Gurgi, Luis Enrique Herranz, Grzegorz Kaminski, Mohamed Said Krikiz, Tetiana Malykhina, Angie Orduz, Mª del Carmen Ovejero Mayoral, Mª del Canto Pedrosa García, Hanan Saleh, Lucía Sevilla Horrillo and Anna Zdeb


un
Universida


Rábida 15

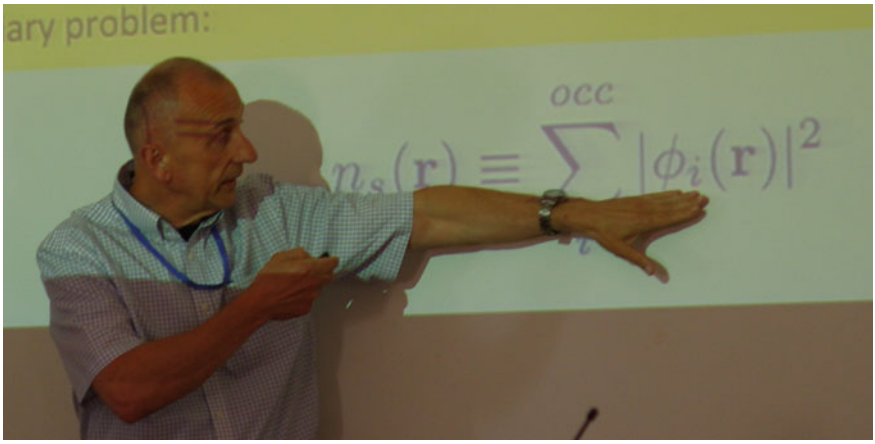
ary problem:
$n_s(\mathbf{r}) \equiv \sum_i^{occ} |\phi_i(\mathbf{r})|^2$

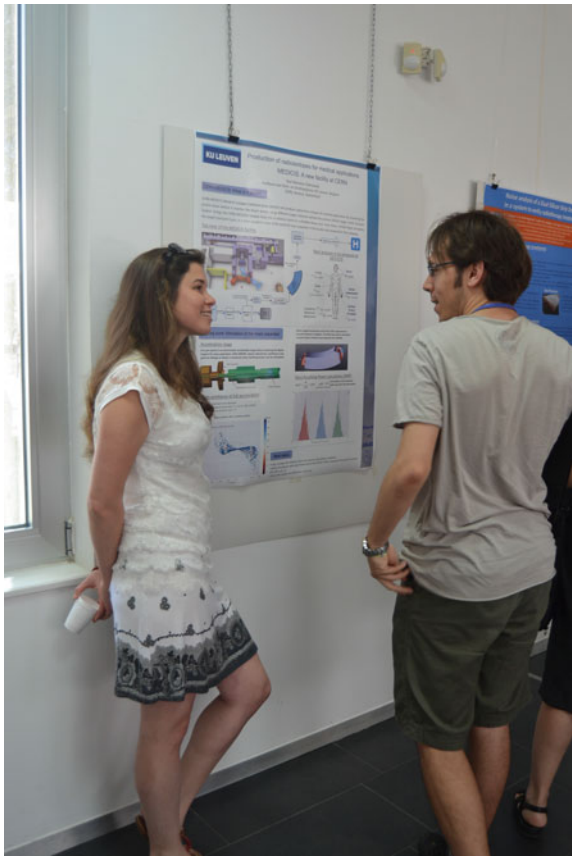
KU LEUVEN


International Scientific Meeting
on
Nuclear Physics
Basic concepts in Nuclear Physics:
theory, experiments and applications.
La Rábida (Spain)
1-5 June 2015

Contents

List of Participants

Maryam Ahannach El M'Siri
maryam.ahannach86@gmail.com
University AbdelMalek Essadi, Hay Foum Oulik Av. Elmourskieene Zkt.
Andalousienne N3 M'DIQ 93200, Morocco

Baki Akkus
akkus@istanbul.edu.tr
Istanbul University, Science Faculty, Physics Department,
34134 Vezneciler Istanbul, Turkey

Conrado Albertus Torres
conrado.albertus@dfa.uhu.es
Dep. de Física Aplicada, Universidad de Huelva, Avda de las Fuerzas
Armadas s/n, E-21071, Huelva, Spain

Mohammad Alda'ajeh
mohammadmajed57@gmail.com
Facultad de Física, University de Santiago de Compostela,
c/ Xosé María Suárez Núñez, s/n. Campus Vida E-15782, Santiago de Compostela,
Spain

Clara E. Alonso Alonso
calonso@us.es
Dep. de FAMN, Facultad de Física, Universidad de Sevilla,
Apartado 1065, E-41080 Sevilla, Spain

María Victoria Andrés Martín
m-v-andres@us.es
Dep. de FAMN, Facultad de Física. Universidad de Sevilla,
Apartado 1065, E-41080 Sevilla, Spain

Samuel Ayet San Andres
s.ayet@gsi.de
GSI Helmholtzzentrum für Schwerionenforschung
GmbH Planckstraße 1. D-64291 Darmstadt, Germany

Javier Balibrea
javier.balibrea@ciemat.es
Av. Complutense, 40, 28040 Madrid, Spain

Maria Cristina Battaglia
mbattaglia@us.es
CNA, c/ Thomas Alva Edison 7, 41092, Sevilla, Spain

Andreea Budaca
abudaca@theory.nipne.ro
Horia Hulubei National Institute for R&D in Physics and Nuclear
Engineering (IFIN-HH) Str. Reactorului no.30, P.O.BOX MG-6,
Bucharest, Magurele, Romania

Juan A. Caballero Carretero
jac@us.es
Dep. de FAMN, Facultad de Física. Universidad de Sevilla.
Apartado 1065, E-41080 Sevilla, Spain

Jesús Casal
jcasal@us.es
Dep. de FAMN, Facultad de Física, Universidad de Sevilla,
Apartado 1065, E-41080 Sevilla, Spain

Miguel A. Cortes-Giraldo
miancortes@us.es
Dep. de FAMN, Facultad de Física. Universidad de Sevilla.
Apartado 1065, E-41080 Sevilla, Spain

Terver Daniel
t.daniel@surrey.ac.uk
Department of Physics, University of Surrey, Guildford, Surrey,
UK GU2 7XH, UK

Carlos Dasso
dasso@us.es
Dep. de FAMN, Facultad de Física. Universidad de Sevilla.
Apartado 1065, E-41080 Sevilla, Spain

Thomas Day Goodacre
thomas.day.goodacre@cern.ch
CERN 176-2-005 CH-1211 Geneva-23, Switzerland

Alexandru Dumitrescu
alexandru.dumitrescu@theory.nipne.ro
Horia Hulubei, National Institute of R&D for Physics and Nuclear Engineering, Moldoveni street no. 16, bloc B19, apartment 20, sector 4, Postal code 040965, Bucharest, Romania

Max Emde
max.emde@physik.rwth-aachen.de
III. Physikalisches Institut B, RWTH Aachen University, hysikzentrum, Otto-Blumenthal-Str. 52074 Aachen, Germany

Aysegul Ertoprak
aysegulertoprak@gmail.com
Istanbul University, Science Faculty. Physics Department 34134 Vezneciler Istanbul, Turkey

José E. García Ramos
enrique.ramos@dfaie.uhu.es
Dep. de Física Aplicada, Universidad de Huelva, Avda de las Fuerzas Armadas s/n, E-21071, Huelva, Spain

Alfonso Gijón Gijón
agijon7@gmail.com
Universidad de Granada, Granada, Spain

Mario Gómez Ramos
mgomez40@us.es
Dep. de FAMN, Facultad de Física. Universidad de Sevilla. Apartado 1065, E-41080 Sevilla, Spain

Ivan Grachev
grachev@lpsc.in2p3.fr
LPSC, 51 rue de Martyrs, Grenoble, France

Victor Guadilla
guadilla@ific.uv.es
Instituto de Física Corpuscular, Apdo Correos 22085 E-46071 Valencia, Spain

José Luis Guerrero Márquez
jlgm91@gmail.com
Dep. de Física Aplicada, Universidad de Huelva, Avda de las Fuerzas Armadas s/n, E-21071, Huelva, Spain

Laila Gurgi
l.a.gurgi@surrey.ac.uk
Department of Physics, University of Surrey, Guildford, Surrey, UK GU2 7XH, UK

Luis Enrique Herranz Puebla
luisen.herranz@ciemat.es
CIEMAT, Departamento de Energía. Unidad de Seguridad Nuclear.
Av. Complutense, 40, 28040 Madrid, Spain

Lei Jin
jinlei@us.es
Dep. de FAMN, Facultad de Física. Universidad de Sevilla.
Apartado 1065, E-41080 Sevilla, Spain

Grzegorz Kaminski
Grzegorz.Kaminski@ifj.edu.pl
Join Institute for Nuclear Research, Joliot Curie 6, 141980 Dubna,
Moscow Region, Russia

Mohamed Said Krikiz
Mohamed.krikiz@gmail.com
University AbdelMalek Essadi, ue Alandaloss tariq Al ouatassiyin,
Chefchaouen, Morocco

Jorge Lerendegui
jlerendegui@us.es
Dep. de FAMN, Facultad de Física. Universidad de Sevilla.
Apartado 1065, E-41080 Sevilla, Spain

Miguel Macías Martínez
miguelmacias61@gmail.com
CNA, Parque Tecnológico Cartuja 93 Av. Thomas A. Edison,
7 E-41092 Sevilla, Spain

Tetiana Malykhina
malykhina@karazin.ua
V.N. Karazin Kharkiv National University, Kurchatov ave., 53,
Kharkiv, 61108, Ukraine

Francisco Manchado De Sola
franciscomanchadodesola@gmail.com
Juan Ramón Jiménez University Hospital, Av. de la Orden,
s/n E-21005, Huelva, Spain

Gloria Marquínez-Durán
gloria.marquinez@dfa.uhu.es
Dep. de Física Aplicada, Universidad de Huelva,
Avda de las Fuerzas Armadas s/n, E-21071, Huelva, Spain

Yisel Martínez
yisel.martinez@fys.kuleuven.be
Instituut voor Kern- en Stralingsfysica, University of Leuven,
Celestijnenlaan 200d—bus 2418, B-3001 Heverlee, Belgium

Guillermo D. Megías Vázquez
megias@us.es
Dep. de FAMN, Facultad de Física. Universidad de Sevilla.
Apartado 1065, E-41080 Sevilla, Spain

Iain Moore
iain.d.moore@jyu.fi
University of Jyväskylä, Department of Physics. PB 35 (YFL). FIN-40014,
Finland

Laura Moschini
laura.moschini@pd.infn.it
University of Padova—INFN Padova, Dip. di Fisica e Astronomia G. Galilei,
Via Marzolo, 8, I-35131 Padova, Italy

Juan M. Nieves Pamplona
Juan.M.Nieves@ific.uv.es
Instituto de Física Corpuscular (IFIC),Parque CientÍfico,
c/ Catedrático José Beltrán, 2. E-46980 Paterna,Spain

Yesim Oktem
sgyks@istanbul.edu.tr
Istanbul University. Science Faculty. Physics Department
34134 Vezneciler Istanbul, Turkey

Angie Orduz
angie.orduz@dfa.uhu.es
Dep. de Física Aplicada, Universidad de Huelva, Avda de las Fuerzas
Armadas s/n, E-21071, Huelva, Spain

Mª C. Ovejero Mayoral
movejero@us.es
Universidad de Sevilla, Sevilla, Spain

Mª C. Pedrosa García
canty@usal.es
University of Salamanca, edificio Multiusos I+D+i, c/Espejo s/n,
E-37008, Salamanca, Spain

Curro Pérez Bernal
francisco.perez@dfaie.uhu.es
Dep. de Física Aplicada, Universidad de Huelva, Avda de las Fuerzas
Armadas s/n, E-21071, Huelva, Spain

José M. Quesada Molina
quesada@us.es
Dep. de FAMN, Facultad de Física. Universidad de Sevilla. Apartado 1065,
E-41080 Sevilla, Spain

Rashmi Ramesh
johnsonrashmi@gmail.com
Ssn college of engineering, OMR Road,Chennai 603110, India

Fitzgerald Ramírez Moreno
framirezmo@unal.edu.co
Universidad Nacional de Colombia, ll. 8 No. 1B-18 sur,
Facatativá, Código postal: 253052524, Colombia

Jeannie Rangel
jeannie@if.uff.br
Instituto de Física, Universidade Federal Fluminense,
Av. Lintoranea S/n, Gragoatá, Niterói, RJ 24210340, Brazil

Elisa Rodríguez López
yle_gd_27@hotmail.com
Dep. de Física Aplicada, Universidad de Huelva,
Avda de las Fuerzas Armadas s/n, E-21071, Huelva, Spain

Rahal Saaidi
saaidirahal@gmail.com
Faculty of sciences Rabat, Mohamed 5 University Rabat,
ay El Firdaouss N335 Temara, Morocco

Marta Sabate-Gilarte
msabate@us.es
CERN/Universidad de Sevilla, Spain

Hanan Saleh
hanhas2002@gmail.com
Facultad de Física, University of Santiago de Compostela,
c/ Xosé María Suárez Núñez, s/n. Campus Vida E-15782,
Santiago de Compostela, Spain

Dieter Schardt
D.Schardt@gsi.de
Biophysics group. GSI Helmholtzzentrum für Schwerionenforschung GmbH
Planckstraße 1. D-64291 Darmstadt, Germany

Lucía Sevilla Horrillo
lucsevhor@alum.us.es
Universidad de Sevilla, Sevilla, Spain

Andrii Torgovkin
andrii.a.torgovkin@jyu.fi
Nanoscience Center, P.O.Box 35, FI-40014 University of Jyväskylä, Finland

J. Javier Valiente Dobón
javier.valiente@lnl.infn.it
INFN Laboratori Nazionali di Legnaro, viale dell'Universitá,
2 35020 Legnaro (Padua), Italy

Lorena Vázquez
lorena.vazquez@usal.es
Universidad de Salamanca, Salamanca, Spain

Dario Vretenar
vretenar@phy.hr
University of Zagreb, Physics Department. Faculty of Science,
University of Zagreb, Bijenicka c. 32, Zagreb, Croatia

Julius Wilhelmy
wilhelmy@ikp.uni-koeln.de
Institute for Nuclear Physics, University of Cologne,
D-50937 Köln, Germany

Part I
Keynote Speakers

Neutrinos in Nuclear Physics: RPA, MEC, 2p2h (Pionic Modes of Excitation in Nuclei)

J. Nieves

Abstract This chapter is devoted to the study of weak interactions on nucleons and nuclei. I pay a special attention to the study of neutrino and antineutrino quasi-elastic reactions in nuclei, which are of the greatest importance for neutrino oscillation experiments, and crucial to achieve the precision goals required to make new discoveries, like the CP violation in the leptonic sector, possible. In particular, I discuss RPA correlations and 2p2h (multi-nucleon) effects on charged-current neutrino-nucleus reactions, and the influence of these nuclear effects on the recently measured MiniBooNE flux folded differential cross sections, and on the so-called nucleon axial mass puzzle. The modification of the nucleon-nucleon interaction inside of a nuclear medium, specially in the spin-isospin channel, will be also studied, since it plays a central role in understanding these nuclear effects. Other physical processes involving electrons and muons which are sensitive to this part of the interaction are also discussed, underlying the importance of the medium corrections also in these systems.

1 Introduction

A correct understanding of neutrino-nucleus interactions is crucial to minimize systematic uncertainties in neutrino oscillation experiments [1]. Most of the new generation of neutrino experiments are exploring neutrino-nuclear scattering processes at intermediate energies ($\leq$1 GeV), for which quasi-elastic (QE) and pion production reactions become dominant. Experiments like SciBooNE [2] or MiniBooNE [3–6] have produced good quality data for QE scattering and pion production in this region of neutrino energies. These new data show interesting deviations from the predictions of present models that have raised doubts in the areas which seemed to be well understood [7–9]. The list of new puzzles is quite long and seems to be expanding. In

J. Nieves (✉)
Instituto de Física Corpuscular (IFIC), Institutos de Investigación de Paterna, Centro Mixto CSIC-Universidad de Valencia, Aptd. 22085, 46071 Valencia, Spain
e-mail: jmnieves@ific.uv.es

J.-E. García-Ramos et al. (eds.), *Basic Concepts in Nuclear Physics: Theory, Experiments and Applications*, Springer Proceedings in Physics 182,
DOI 10.1007/978-3-319-21191-6_1

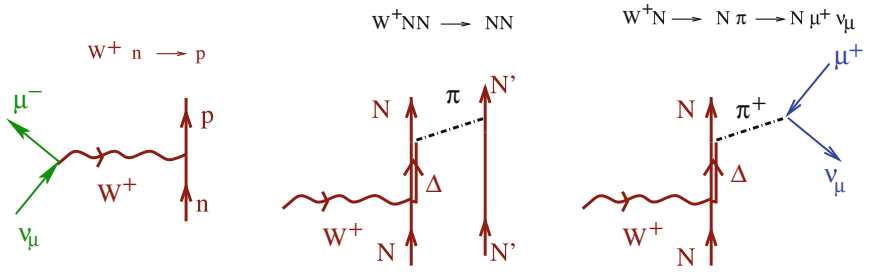

Fig. 1 Mechanisms for W absorption inside of a nucleus

this chapter, we will pay attention to the so called MiniBooNE charged-current (CC) QE puzzle. Its origin has been extensively debated (see for instance [7, 9]) since this collaboration presented in 2009 a new CCQE cross section measurement [3] using a high-statistics sample of ν_μ interactions on ^{12}C. The size of the cross section was found to be unexpectedly large, and within the relativistic global Fermi gas model employed in the MiniBooNE analysis, a difficult to accept[1] large nucleon axial mass of $M_A = 1.35 \pm 0.17$ GeV was needed to describe the data. Moreover, the results of [13], based on the impulse approximation scheme and a state-of-the-art model of the nuclear spectral functions, suggested that the electron cross section and the MiniBooNE flux averaged neutrino cross sections, corresponding to the same target and comparable kinematical conditions, could not be described within the same theoretical approach using the value of the nucleon axial mass obtained from deuterium measurements.

In most theoretical works QE is used for processes where the gauge boson W is absorbed by just one nucleon, which together with a lepton is emitted (see Fig. 1 left). The MiniBooNE data-set accounted for events with no pions in the final state (events in which only one muon is detected), but Monte Carlo correcting for those cases where CC pion production was followed by pion absorption. It was customary to take for granted that most of those events could be attributed to the QE scattering of the weak probe on a nucleon, and thus the initial neutrino energy could be approximately determined from the energy and angle of the final lepton assuming QE kinematics [14]. In what follows, we will refer as QE-like to this data sample. This choice discards pions coming off the nucleus, since they will give rise to additional leptons after their decay (see Fig. 1 right). Theoretical QE predictions greatly underestimate the measured MiniBooNE QE-like cross section [15], as mentioned above it occurred for the case of the model employed in [13].

[1] The value of M_A extracted from early CCQE measurements on deuterium and, to a lesser extent, hydrogen targets is $M_A = 1.016 \pm 0.026$ GeV [10], which is in excellent agreement with the pion electro-production result, $M_A = 1.014 \pm 0.016$ GeV, obtained from the nucleon axial radius [7, 11]. Furthermore, NOMAD also reported in 2008 a small value of $M_A = 1.05 \pm 0.02$ (stat) $\pm$ 0.06 (syst) GeV [12].

A natural solution to this puzzle came from the incorporation of RPA[2] corrections to the QE cross section [17, 18] and multi-nucleon mechanisms [18–21]. The MiniBooNE data-set includes events where the gauge boson is absorbed by two interacting nucleons (in the many body language, this amounts to the excitation of a 2p2h nuclear component). An example of this type of processes is depicted in the middle panel of Fig. 1. Up to re-scattering processes which could eventually produce secondary pions, 2p2h events will give rise to only one muon to be detected. Thus, they could be experimentally misidentified as QE events.

In these lectures, I present the needed ingredients to undertake a microscopic calculation of the CCQE-like double differential cross section measured by MiniBooNE. It is evaluated as the sum of the theoretical QE (Fig. 1 left) contribution and the cross section induced by multi-nucleon mechanisms (see for instance Fig. 1 middle panel), where the gauge boson is being absorbed by two or more nucleons without producing pions. The QE contribution was studied in [17] incorporating several nuclear effects. The main one is the medium polarization (RPA), including Δ-hole degrees of freedom and explicit π and ρ meson exchanges in the vector-isovector channel of the effective nucleon-nucleon interaction. The model for multi-nucleon mechanisms (not properly QE but included in the MiniBooNE data [3]) is fully discussed in [21]. The model includes one, two, and even three-nucleon mechanisms, as well as the excitation of Δ isobars. There are no free parameters in the description of nuclear effects, since they were fixed in previous successful studies of photon, electron, pion, kaon, Λ, $\Sigma-$hyperons etc. interactions with nuclei [22–38].

These lectures pretend also to be an exercise on many body quantum field theory by applying basic principles to a variety of physical processes which seem originally rather disconnected, but that, as we will see, share a common factor: the essential role play by the medium renormalization of the vacuum interactions in order to achieve a correct understanding of their dynamics inside of a nuclear environment.

In order to follow the lectures, some knowledge of many body theory has been assumed, although some of the concepts are introduced here. Excellent reviews on the topic can be found in [39, 40].

The lectures begin in Sect. 2 with an analogy by looking at the way the well known Coulomb interaction is screened in an electron gas. This analogy allows us to introduce concepts like the medium polarization, which will help us to study the way the NN interaction is modified inside of a nuclear medium, leading to the concept of induced interaction, which will play a central role in the rest of the lectures. We next review in Sect. 3 the theoretical situation of muon capture in nuclei, which clearly illustrates the importance of the nuclear medium modifications. In Sect. 4 we develop a nuclear many-body scheme to study the inclusive electron-nucleus scattering at intermediate energies, which will be extended to the study of

[2] Medium polarization or collective RPA correlations account for the change of the electroweak coupling strengths, from their free nucleon values, due to the presence of strongly interacting nucleons [16, 17].

neutrino induced reactions in Sect. 5. In this latter section, RPA and 2p2h effects on CC neutrino nucleus reactions are discussed, and their role in solving the so-called MiniBooNE M_A puzzle is highlighted.

2 Induced Spin-Isospin Nucleon-Nucleon Interaction in a Nuclear Medium

2.1 Screening of the Coulomb Interaction in an Electron Gas

Let us begin with a qualitative discussion, extracted from the excellent book of Fetter and Walecka [39], of the properties of the instantaneous Coulomb interaction in an electron gas (Fig. 2). The problem has an obvious resemblance with the modification of the strong interaction in a nuclear medium in which we will be interested in the next sections.

As a consequence of this polarization, the photon acquires an effective mass, which leads to the screening of the Coulomb interaction [39]. The original Coulomb interaction is changed to one of shorter range,

$$\frac{1}{4\pi}\frac{1}{r} \to \frac{1}{4\pi}\frac{e^{-\mu(\rho)r}}{r} \tag{1}$$

where ρ is the electron density of the gas and μ a certain function of it. Note that the effect of the polarization has been to convert the infinite range interaction into one of finite range. The positive charge around one electron, coming from the polarization of the medium, cancels the electron negative charge, and at large distances we see an effective charge zero. Equation (1) in momentum space is now

$$\frac{1}{\mathbf{q}^2} \to \frac{1}{\mathbf{q}^2 + \mu^2(\rho)} \tag{2}$$

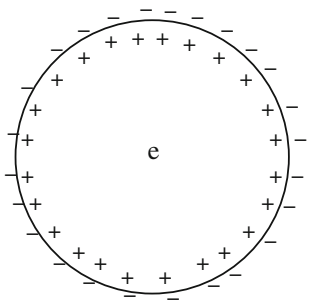

Fig. 2 Polarization of an electron gas due to the presence of an external charge

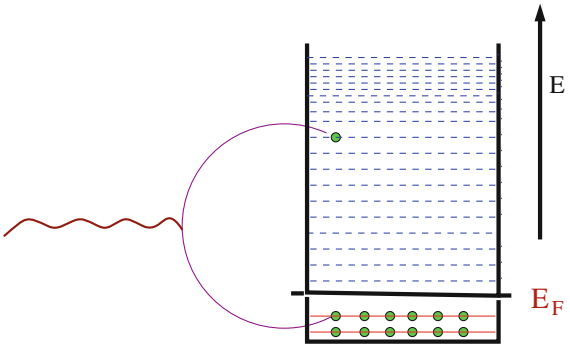

Fig. 3 The energy levels of the Fermi sea are occupied. The photon induces a transition of one electron from one occupied state of the Fermi sea to some unoccupied state

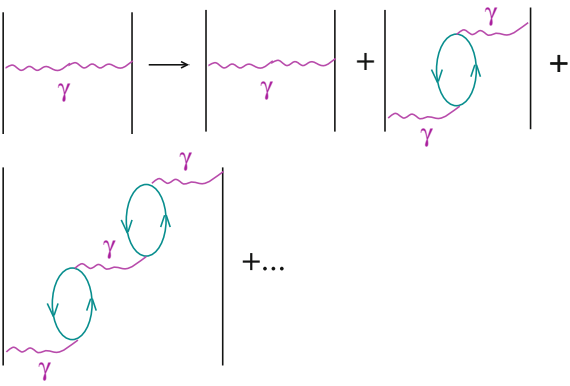

Fig. 4 Modification of the Coulomb interaction due to the polarization of the electron Fermi sea

which corresponds to the instantaneous ($q^0 = 0$) Coulomb term of the photon propagator and its modification in the electron medium. The physical mechanism for the polarization consists in a transfer of some electrons from occupied states of a Fermi sea to some unoccupied states (Fig. 3), or more technically in producing particle-hole (ph) excitations. In many body language we express diagrammatically the modification of the interaction as shown in Fig. 4.

The graphs in Fig. 4 are Feynman Many Body diagrams which allow to evaluate the modification of the photon propagator. Hence we can consider the term of the photon propagator associated to the instantaneous Coulomb part of the interaction (${}_C D_F^{\mu\nu}$) [41], which is now modified in the following way

$$
\begin{aligned}
{}_C D_F^{\mu\nu}(\mathbf{q}) &= g^{\mu 0} g^{\nu 0} D_0(\mathbf{q}) \\
D_0(\mathbf{q}) &= \frac{1}{\mathbf{q}^2}
\end{aligned}
$$

$$
\begin{aligned}
i D_0(\mathbf{q}) \rightarrow\ & i D_0(\mathbf{q}) + i D_0(\mathbf{q})(-i\Pi(q)) i D_0(\mathbf{q}) + \\
& + i D_0(\mathbf{q})(-i\Pi(q)) i D_0(\mathbf{q})(-i\Pi(q)) i D_0(\mathbf{q}) + \cdots = i D(q) \quad (3)
\end{aligned}
$$

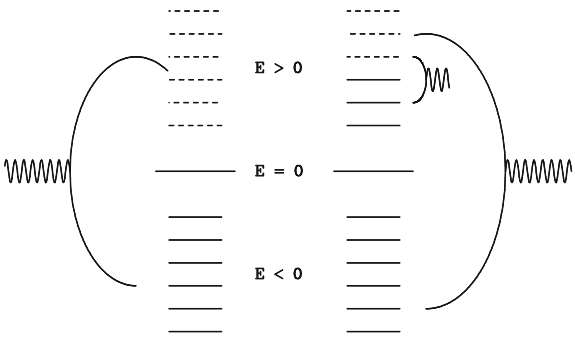

Fig. 5 *Left* Representation of the Dirac sea and of e^+e^- excitations. *Right* Representation of the ph excitations (transitions in the positive energy region of the spectrum)

Thus we have,

$$D(q) = \frac{D_0(\mathbf{q})}{1 - \Pi(q) D_0(\mathbf{q})} = \frac{1}{D_0^{-1}(\mathbf{q}) - \Pi(q)} = \frac{1}{\mathbf{q}^2 - \Pi(q^0, \mathbf{q})} \tag{4}$$

where $\Pi(q^0, \mathbf{q})$ is the component 00 of the photon self-energy due to a single ph excitation. It is a function of q^0, $\mathbf{q}$ and the electron density, and it determines the effective photon mass, $\mu(\rho)$, in the electron gas.

The loop in Fig. 4 stands for a ph excitation as depicted in Fig. 3. The photon would also be renormalized through e^+e^- excitations. One can realize of the analogies by recalling the picture of the Dirac sea. There, one assumes that all the states of negative energy are filled by electrons. Then a particle-antiparticle excitation is represented (see Fig. 5 left) by a transition of one electron from an occupied state of negative energy to an unoccupied state of positive energy. If now in addition we have some states of positive energy occupied (states of the Fermi sea), then we can also excite electrons from these occupied states to other unoccupied states of the Fermi sea. These transitions are additional to those from the negative energy states to the positive energy states. In this sense we can now think of the contribution of the ph excitation to the photon self-energy as an additional contribution to the free photon self-energy. This latter one will renormalize the electron mass and charge and the γee coupling parameters which determine the free electron-electron interaction. Thus the many body corrections renormalize the physical free space magnitudes of the theory under study, when the interaction takes place in a medium.

2.2 Particle and Particle-Hole Propagators in a Fermi Sea: Occupation Number and the Lindhard Function

2.2.1 Electron Gas

For the electromagnetic interaction, given by

$$H_{em}(x) = -e\bar{\psi}(x)\gamma^{\mu}\psi(x)A_{\mu}(x) \tag{5}$$

the Coulomb part of the interaction (zeroth component) in the non-relativistic limit has a trivial limit for the γee vertex, which is just the electron charge e. Thus the self-energy $\Pi(q^0, \mathbf{q})$ can be evaluated and one finds

$$-i\Pi(q^0, \mathbf{q}) = (-ie)(-ie)(-)2\int \frac{d^4k}{(2\pi)^4} iG_0(k)iG_0(k+q) \tag{6}$$

where $(-ie)$ is the coupling constant times the factor $-i$ from the perturbative expansion, the minus sign comes because of the fermionic loop, the factor 2 accounts for the two possible spin states of the electron and finally $G_0(k)$ is the electron propagator in a Fermi sea given by [39]

$$G_0(k) = \frac{1 - n(\mathbf{k})}{k^0 - \varepsilon(\mathbf{k}) + i\eta} + \frac{n(\mathbf{k})}{k^0 - \varepsilon(\mathbf{k}) - i\eta} \tag{7}$$

where $n(\mathbf{k})$ is the occupation number ($n(\mathbf{k}) = 0$ for $|\mathbf{k}| \geq k_F, n(\mathbf{k}) = 1$ for $|\mathbf{k}| \leq k_F$) and $\varepsilon(\mathbf{k})$ is the kinetic energy of the electrons. The k^0 integration in (6) can be performed in the complex plane and because of the nature of the poles only the first term of $G_0(k)$ times the second one of $G_0(k+q)$, or the second one of $G_0(k)$ times the first one of $G_0(k+q)$ contribute. Thus we get [39]

$$\Pi(q^0, \mathbf{q}) = e^2 U_e(q^0, \mathbf{q}) \tag{8}$$

where $U_e(q^0, \mathbf{q})$, called the Lindhard function is given by

$$U_e(q^0, \mathbf{q}) = 2\int \frac{d^3k}{(2\pi)^3} \left\{ \frac{n(\mathbf{k})(1 - n(\mathbf{k}+\mathbf{q}))}{q^0 - \varepsilon(\mathbf{k}+\mathbf{q}) + \varepsilon(\mathbf{k}) + i\eta} + \frac{n(\mathbf{k}+\mathbf{q})(1 - n(\mathbf{k}))}{-q^0 + \varepsilon(\mathbf{k}+\mathbf{q}) - \varepsilon(\mathbf{k}) + i\eta} \right\} \tag{9}$$

The two terms in (9) account for the direct and crossed terms of the *ph* excitation depicted in Fig. 6. Note that $U_e(q)$ can have both real and imaginary parts, which can be calculated by using

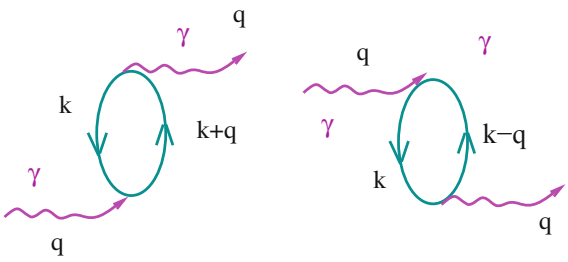

Fig. 6 Direct and crossed terms contributing to the Lindhard function or the photon self-energy

$$\frac{1}{k^0 - \varepsilon(\mathbf{k}) + i\eta} = P\left\{\frac{1}{k^0 - \varepsilon(\mathbf{k})}\right\} - i\pi\delta(k^0 - \varepsilon(\mathbf{k})) \tag{10}$$

being $P\{...\}$ the principal part, always understood under the integration symbol. Thus, assuming $q^0 > 0$, then only the first term of (9) gives rise to an imaginary part and we get

$$\mathrm{Im}U_e(q) = 2\int \frac{d^3k}{(2\pi)^3}(-)\pi\delta(q^0 - \varepsilon(\mathbf{k}+\mathbf{q}) + \varepsilon(\mathbf{k}))n(\mathbf{k})(1 - n(\mathbf{k}+\mathbf{q})) \tag{11}$$

The imaginary part of $U_e(q)$ comes from situations in the intermediate states integration, where the particles are placed on shell (momentum conservation in an infinite homogeneous medium is built from beginning and energy conservation is imposed by the δ function). This is a consequence of a more general theorem, contained in Cutkowski's rules [42], which expresses that if we draw a straight line which cuts several lines corresponding to intermediate states in a Feynman diagram, when these lines are placed on shell in the integrations one will get a contribution to the imaginary part of this diagram in the scattering matrix, self-energy, etc.

In the complex q^0 plane, $U_e(q^0, \mathbf{q})$ has a continuous set of poles in the fourth quadrant ($q^0 = \varepsilon_{par} - \varepsilon_{hole} - i\eta$, from the first term of (9)) or in the second quadrant ($q^0 = \varepsilon_{hole} - \varepsilon_{par} + i\eta$, from the second term of (9)). Hence, $U_e(q^0, \mathbf{q})$ has an analytical cut in the second and fourth quadrants as depicted in Fig. 7. The function $U_e(q)$ has an imaginary part for real values of q^0 situated in the analytical cuts.

The integrals in (9) can be done analytically and analytical expressions for both the real and imaginary parts will be given below.

It is interesting to note that if we open the hole line in Fig. 6 we find the two diagrams that contribute to the photon electron scattering, as shown in Fig. 8. Thus we can think of the self-energy (8) as an integral of the γe scattering matrix over the occupied states.

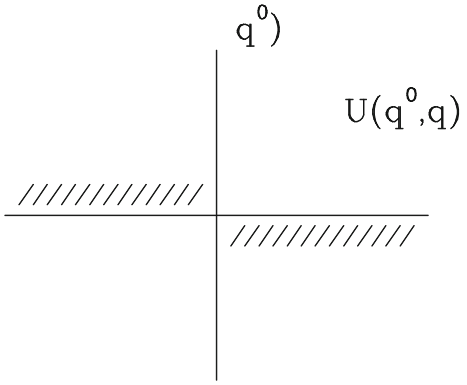

Fig. 7 Analytical structure of the Lindhard function. The *dashes* represent the analytical cuts. The function $U_e(q^0, \mathbf{q})$ is continuous up to the real axis in the first a third quadrant

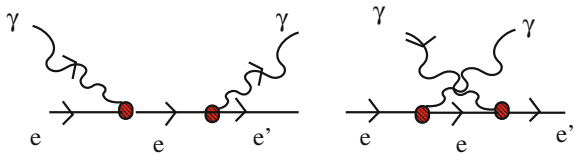

Fig. 8 Direct and crossed diagrams corresponding to the $\gamma - e$ scattering process

2.2.2 Nucleon Fermi Gas

The introduction in the last subsection of the propagation of photons through an electron medium simplifies now the discussion of the propagation of pions and other mesons through a nuclear medium. The electric charge of the electron is now substituted by the axial charge of the nucleon, which produces an axial polarization of the medium [43]. The pion and other mesons will play now the role of the photon as the carriers of the interaction. In this subsection we follow [38].

Diagrammatically the picture for the modification of the pion propagator is identical to the one of Fig. 4, by substituting the photons by pions. The πNN effective Hamiltonian, in its non-relativistic form, is given by ($\mu = m_\pi$)

$$\delta H_{\pi NN}(x) = \frac{f}{\mu}\psi^\dagger(x)\sigma_i\partial_i\phi^\lambda(x)\tau^\lambda\psi(x) \tag{12}$$

with ($f^2/4\pi = 0.08$). Besides, $\psi(x)$ is the nucleon field in the isospin space

$$\psi^\dagger(x) = \left(\psi_p^\dagger(x), \psi_n^\dagger(x)\right) \tag{13}$$

with $\psi_{p,n}(x)$ the proton and neutron fields and $\phi^\lambda(x)$ the pion field in Cartesian isospin basis [44]. In momentum space the πNN vertex for an incoming pion of momentum $\mathbf{q}$ and isospin λ is given by

$$-iV_{\pi NN} = \frac{f}{\mu}\boldsymbol{\sigma}\,\mathbf{q}\,\tau^\lambda \tag{14}$$

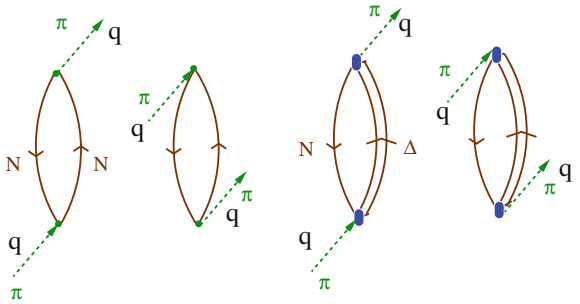

Fig. 9 Diagrams entering the calculation of the pion self-energy in a nuclear medium

The pion self-energy is now evaluated by summing over the spin and isospin of the particles and we find

$$\Pi(q^0, \mathbf{q}) = \frac{f^2}{\mu^2}\mathbf{q}^2 U_N(q^0, \mathbf{q}) \tag{15}$$

omitting the trivial $\delta_{\lambda\lambda'}$ dependence, where

$$U_N(q) = 2U_e(q); \;\; (m_e \to M_N) \tag{16}$$

Hence formally U_N is equal to U_e except that we must substitute the electron mass by the nucleon mass. The extra factor two appears since now we also sum over the isospin degrees of freedom of the nucleon. Hence the pion propagator is now modified from its free value:

$$D_0(q) = \frac{1}{q^{0\,2} - \mathbf{q}^2 - \mu^2 + i\eta} \to D(q) = \frac{1}{q^{0\,2} - \mathbf{q}^2 - \mu^2 - \Pi(q^0, \mathbf{q})} \tag{17}$$

In an analogous way to Fig. 6, we will now have for the pion self-energy a graphical expression shown in the first two diagrams depicted in Fig. 9. The expression in (15) for the pion self-energy is however only a first step. Indeed the pion cannot only excite nucleons above the Fermi sea, as implicitly assumed in (15), but it can also excite the internal degrees of freedom of the nucleon since it is a composite particle made out of quarks. Hence a nucleon can be converted into a Δ, N^*, $\Delta^* \cdots$ Out of these, the Δ plays an important role at intermediate energies because of its lower mass and strong coupling to the πN system. The $\pi N \Delta$ effective Hamiltonian is now given by ($f^{*2}/4\pi = 0.36$)

$$H_{\pi N\Delta} = \frac{f^*}{\mu}\psi_N^\dagger(x) S_i \partial_i \phi^\lambda(x) T^\lambda \psi_\Delta(x) + h.c. \tag{18}$$

where $\mathbf{S}$, $\mathbf{T}$ are the transition spin and isospin operators defined by means of the Wigner Eckart theorem as

$$\left\langle \frac{3}{2} M_s \left| S_\nu^\dagger \right| \frac{1}{2} m_s \right\rangle = \left(\frac{1}{2}, 1, \frac{3}{2} \middle| m_s, \nu, M_s \right) \left\langle \frac{3}{2} \middle\| S^\dagger \middle\| \frac{1}{2} \right\rangle \tag{19}$$

with ν the index of a rank one tensor in the spherical basis. The reduced matrix element in (19) is taken to be the unity, which serves to define the operator[3] S. A completely analogous expression holds for $T_\lambda^\dagger$.

The pion self-energy for Δh excitation, corresponding to the last two diagrams of Fig. 9, can be evaluated by using the same procedure used in the ph excitation, substituting the vertex $V_{\pi NN}$ by $V_{\pi N\Delta}$ (for the $\pi N \to \Delta$ transition)

$$-i V_{\pi N\Delta}(q) = \frac{f^*}{\mu} \mathbf{S}^\dagger \mathbf{q} \; T^\lambda \tag{21}$$

and the particle part of the propagator in the Lindhard function by a Δ propagator

$$G_\Delta(k) = \frac{1}{k^0 - w_R - T_\Delta + i\Gamma_\Delta/2} \tag{22}$$

with $w_R = M_\Delta - M_N$, T_Δ the Δ kinetic energy and Γ_Δ the Δ decay width,

$$\frac{\Gamma_\Delta}{2} = \frac{1}{3} \frac{1}{4\pi} \frac{f^{*2}}{\mu^2} \frac{M_N}{\sqrt{s}} q_N^3 \theta(\sqrt{s} - M_\Delta) \tag{23}$$

with q_N the πN CM momentum for the decay of a Δ of energy $\sqrt{s}$, CM energy of this system. Note that there is no a Fermi sea of Δ resonances and hence the Δ propagator does not have the hole part. With these ingredients, the pion self-energy now reads

$$\Pi(q^0, \mathbf{q}) = \frac{f^2}{\mu^2} \mathbf{q}^2 U(q^0, \mathbf{q}) \tag{24}$$

with

$$U(q) = U_N(q) + U_\Delta(q) \tag{25}$$

$$U_\Delta(q) = -i \left(\frac{4}{3} \right)^2 \left(\frac{f^*}{f} \right)^2 \int \frac{d^4k}{(2\pi)^4} \left\{ G^0(k) G_\Delta(k+q) + G^0(k) G_\Delta(k-q) \right\} \tag{26}$$

[3] A useful expression needed to evaluate the pion self-energy through Δh excitation is given by the closure property,

$$\sum_{M_s} S_i | \frac{3}{2} M_s \rangle \langle \frac{3}{2} M_s | S_j^\dagger = \delta_{ij} - \frac{1}{3} \sigma_i \sigma_j \tag{20}$$

in Cartesian basis.

Defining the dimensionless variables

$$\nu = q^0 m/k_F^2; \;\; \hat{q} = q/k_F \tag{27}$$

we have [38] ($m = M_N$)

$$U_N(\nu,\hat{q}) = \frac{mk_F}{\pi^2}\left\{-1 + \frac{1}{2\hat{q}}\left(1 - \left(\frac{\nu}{\hat{q}} - \frac{\hat{q}}{2}\right)^2\right)\ln\frac{\frac{\nu}{\hat{q}} - \frac{\hat{q}}{2} + 1}{\frac{\nu}{\hat{q}} - \frac{\hat{q}}{2} - 1}\right.$$
$$\left. - \frac{1}{2\hat{q}}\left(1 - \left(\frac{\nu}{\hat{q}} + \frac{\hat{q}}{2}\right)^2\right)\ln\frac{\frac{\nu}{\hat{q}} + \frac{\hat{q}}{2} + 1}{\frac{\nu}{\hat{q}} + \frac{\hat{q}}{2} - 1}\right\} \tag{28}$$

for complex values of q^0. For real values of q^0, (28) provides the real part of $U_N(q)$ by taking the absolute value of the arguments of the ln function. In this latter case we also have

$$\mathrm{Im}U_N(\nu,\hat{q}) = \frac{-2mk_F}{4\pi\hat{q}}\left(1 - \left(\frac{|\nu|}{\hat{q}} - \frac{\hat{q}}{2}\right)^2\right) \tag{29}$$

for $\hat{q} > 2$; $\frac{1}{2}\hat{q}^2 + \hat{q} \geq |\nu| \geq \frac{1}{2}\hat{q}^2 - \hat{q}$ or $\hat{q} < 2$; $\frac{1}{2}\hat{q}^2 + \hat{q} \geq |\nu| \geq \hat{q} - \frac{1}{2}\hat{q}^2$

$$\mathrm{Im}U_N(\nu,\hat{q}) = -\frac{mk_F}{\pi\hat{q}}|\nu| \tag{30}$$

for $\hat{q} < 2$; $0 \leq |\nu| \leq \hat{q} - \frac{1}{2}\hat{q}^2$ and $\mathrm{Im}U_N(\nu,\hat{q}) = 0$ otherwise.

On the other hand U_Δ is given by

$$U_\Delta(q^0,\mathbf{q}) = \left(\frac{4}{3}\frac{f^*}{f}\frac{k_F}{2\pi}\right)^2\left\{\frac{(a+a')}{b^2} + \frac{b^2-a^2}{2b^3}\ln\frac{a+b}{a-b}\right.$$
$$\left. + \frac{b^2-a'^2}{2b^3}\ln\frac{a'+b}{a'-b}\right\} \tag{31}$$

where $b = |\mathbf{q}\,|/M_\Delta$ and

$$a = \frac{1}{k_F}\left(q^0 - \hat{w}_R(q^0) - \frac{\mathbf{q}^{\,2}}{2M_\Delta}\right), \quad a' = \frac{1}{k_F}\left(-q^0 - \hat{w}_R(-q^0) - \frac{\mathbf{q}^{\,2}}{2M_\Delta}\right) \tag{32}$$

$$\hat{w}_R(q^0) = w_R = M_\Delta - M_N, \quad q^0 \in \mathbf{C}, \qquad \hat{w}_R(q^0) = w_R - i\frac{\Gamma_\Delta(q^0)}{2}, \quad q^0 \in \mathbf{R} \tag{33}$$

For real values of q^0 for which $\hat{w}_R(q^0)$ is complex, the arguments in the logarithms must be substituted by their absolute values.

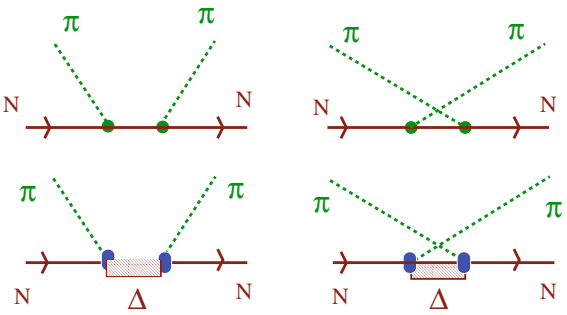

Fig. 10 Model for the πN scattering amplitude implicit in the diagrams of Fig. 9

2.3 *RPA Re-Summation in the Spin-Isospin Part of the Nucleon-Nucleon Interaction*

By analogy to Fig. 8, the model of Fig. 9 implies an assumption for the πN scattering matrix which is given in Fig. 10.

The model of Fig. 10, which contains the nucleon and Δ poles and their crossed terms, accounts for the p-wave of the πN scattering matrix. The s-wave part gives only a small correction for cases where the momentum is not too small, as for example the case of pionic atoms where it should be taken into account [34].

The series of (3) implicitly assumes that a photon (a pion here) propagates in between two particle-hole excitations. It is well known that one pion exchange only accounts for the long range part of the NN interaction, and that a short distances a repulsive force should also be included. The repulsive short range part of the interaction will modify the pion exchange by cutting its contribution to the interaction at short distances. In many problems, which are selective to the pionic part of the NN interaction one is only selecting the exchange of a $T = 1$ object, for what the ρ-meson will also play some role. On the other hand in the propagation of a pion, in those iterated diagrams where more than one ph excitation occur, the ρ exchange, modified by the effect of short range correlations, plays also some role. For this reason it is customary to talk about the spin-isospin part of the interaction [38, 45].

The ρ meson coupling to the nucleon $V_{\rho NN}$ is given in the non-relativistic limit, by

$$H_{\rho NN}(q) = i\frac{f_\rho}{m_\rho}(\boldsymbol{\sigma} \times \mathbf{q})\boldsymbol{\varepsilon}\,\tau^\lambda \tag{34}$$

where $\boldsymbol{\varepsilon}$ is the ρ meson polarization vector. Similarly the $\rho\Delta N$ coupling for the $\rho N \to \Delta$ transition is given by

$$H_{\rho N\Delta}(q) = i\frac{f^*_\rho}{m_\rho}(\mathbf{S}^\dagger \times \mathbf{q})\boldsymbol{\varepsilon}\,T^\lambda \tag{35}$$

with

$$C_\rho = \frac{f_\rho^2/m_\rho^2}{f^2/\mu^2} \approx 2, \qquad \frac{f_\rho^*}{f_\rho} = \frac{f^*}{f} \tag{36}$$

The short range repulsion, assumed independent of spin-isospin, is attributed to the exchange of the w-meson in the meson exchange language, although some pictures based in the bag model generate the repulsion from the antisymmetry of the quarks when the two bags overlap [46, 47].

With the couplings πNN and ρNN of (14) and (34), we can write the NN potential due to one pion or one ρ-meson exchange. Thus, we obtain

$$\begin{aligned} -iV_\pi(q) &= \frac{f}{\mu}\boldsymbol{\sigma}\mathbf{q}\tau^\lambda \frac{i}{q^{0\,2}-\mathbf{q}^{\,2}-\mu^2+i\varepsilon}\frac{f}{\mu}\boldsymbol{\sigma}(-\mathbf{q})\tau^\lambda \\ V_\pi(q) &= \frac{f^2}{\mu^2}\frac{\mathbf{q}^{\,2}}{q^{0\,2}-\mathbf{q}^{\,2}-\mu^2+i\varepsilon}\hat{q}_i\hat{q}_j\sigma_i^{(1)}\sigma_j^{(2)}\boldsymbol{\tau}^{(1)}\boldsymbol{\tau}^{(2)} \end{aligned} \tag{37}$$

where the short distance repulsion in coordinate space has still to be implemented and $\hat{q}_i = q_i/|\mathbf{q}\,|$. Analogously when summing over the intermediate ρ polarization

$$\begin{aligned} V_\rho(q) &= \frac{f_\rho^2}{m_\rho^2}\frac{(\boldsymbol{\sigma}\times\mathbf{q}\,)(\boldsymbol{\sigma}\times\mathbf{q}\,)}{q^{0\,2}-\mathbf{q}^{\,2}-m_\rho^2+i\varepsilon}\boldsymbol{\tau}\boldsymbol{\tau} \\ &= \frac{f_\rho^2}{m_\rho^2}\frac{\mathbf{q}^{\,2}}{q^{0\,2}-\mathbf{q}^{\,2}-m_\rho^2+i\varepsilon}(\delta_{ij}-\hat{q}_i\hat{q}_j)\sigma_i^{(1)}\sigma_j^{(2)}\boldsymbol{\tau}^{(1)}\boldsymbol{\tau}^{(2)} \end{aligned} \tag{38}$$

The potential $V_\pi(q)+V_\rho(q)$ provides the spin-isospin part of the NN interaction in the meson exchange model. We observe that $V_\pi(q)$ is of a longitudinal type, $\hat{q}_i\hat{q}_j$, while $V_\rho(q)$ is of a transverse type, $(\delta_{ij}-\hat{q}_i\hat{q}_j)$. These two operators are mutually orthogonal.

In addition we must include vertex form factors to account for the off shell mesons. We include a monopole form factor per vertex of the type

$$F_i(q^0,\mathbf{q}\,) = \frac{\Lambda_i^2-m_i^2}{\Lambda_i-q^2} \tag{39}$$

with $\Lambda_\pi = 1200$ MeV and $\Lambda_\rho = 2500$ MeV [48]. With all these ingredients, we are now in position to evaluate the G-matrix. We could think that the hard core is produced by a strong repulsive spin-isospin independent force and we can use the results of Brown and Jackson [49] to construct the G matrix. Thus, we find that if the potential is split into a "weak" spin-isospin dependent part, V_ω, and a "strong" spin-isospin independent part, V_s,

$$V = V_s + V_w \tag{40}$$

the G matrix is given by

$$G = G_s + \Omega_s^\dagger V_W \Omega_s + \cdots \tag{41}$$

where G_s is the G matrix for the spin-isospin independent part of the interaction constructed with V_s alone and $\Omega_s^\dagger$, Ω_s are wave operators which in the case of a short-range repulsive potential can be approximated by a local correlation function due to the short range repulsive part. Equation (41) then separates the G matrix into a spin-isospin independent part and one which is spin-isospin dependent. This last term will be found by multiplying the spin-isospin dependent potential by the correlation function. This is the procedure followed in [38], where an easy analytical correlation function in coordinate space (which vanishes as $r \to 0$ and goes to 1 as $r \to +\infty$) of the type $g(r) = 1 - j_0(q_c)$ with $q_c \approx m_w \approx 770$ MeV is assumed. One can then find the corresponding modification of the potential in the momentum space and thus the modified $\pi + \rho$ interaction reads now,

$$\begin{aligned}\hat{V}_{s-i}(q) &= (a\delta_{ij} + b\frac{q^i q^j}{\mathbf{q}^2})\sigma^i_{(1)}\sigma^j_{(2)}\boldsymbol{\tau}_{(1)}\boldsymbol{\tau}_{(2)} \\ &= \left\{V_t\left(\delta_{ij} - \frac{q^i q^j}{\mathbf{q}^2}\right) + V_l\frac{q^i q^j}{\mathbf{q}^2}\right\}\sigma^i_{(1)}\sigma^j_{(2)}\boldsymbol{\tau}_{(1)}\boldsymbol{\tau}_{(2)}\end{aligned} \tag{42}$$

with $V_t(q)$ and $V_l(q)$ given by

$$\begin{aligned}V_t(q) = \frac{f^2}{\mu^2}\{&\mathbf{q}^2 D_0^\rho(q)F_\rho^2(q)C_\rho - \frac{q_c^2}{3}\hat{D_0}^\pi(q)\hat{F_\pi}^2(q) \\ &-(\mathbf{q}^2 + \frac{2}{3}q_c^2)\hat{D_0}^\rho(q)\hat{F_\rho}^2(q)C_\rho\} \\ V_l(q) = \frac{f^2}{\mu^2}\{&\mathbf{q}^2 D_0^\pi(q)F_\pi^2(q) - (\mathbf{q}^2 + \frac{q_c^2}{3})\hat{D_0}^\pi(q)\hat{F_\pi}^2(q) \\ &-\frac{2q_c^2}{3}\hat{D_0}^\rho(q)\hat{F_\rho}^2(q)C_\rho\}\end{aligned} \tag{43}$$

$D_0^\pi(q)$, $D_0^\rho(q)$ are the pion or ρ-meson propagators and $\hat{D}_0$, $\hat{F}$ the propagators or form factors by substituting $\mathbf{q}^2$ by $\mathbf{q}^2 + q_c^2$. We call the interaction in (42) the nucleon effective interaction.

The second form in (42) is quite useful because it separates the interaction into a transverse piece, the V_t term, and a longitudinal piece, the V_l term.

Because we take $C_\rho = C_\rho^*$, $\Lambda_{\pi,\rho}^* = \Lambda_{\pi,\rho}$ the potential of (42) describes also the interactions $\Delta N \to NN$, $NN \to \Delta N$, $\Delta N \to \Delta N$ and $\Delta\Delta \to NN$ in the vacuum and inside of the nuclear medium respectively, by means of the following replacements:

$$\frac{f}{\mu}\sigma\tau \to \frac{f^*}{\mu}S^{(\dagger)}T^{(\dagger)} \tag{44}$$

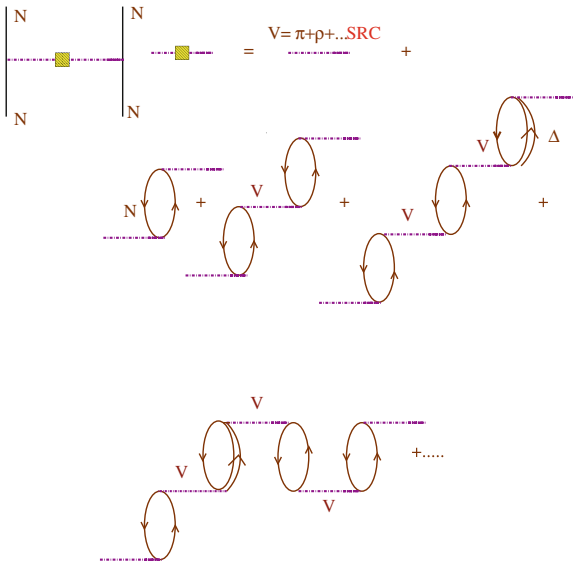

Fig. 11 Picture for the induced spin-isospin interaction in a nuclear medium. The *line* with the *square* stands now for the interaction of (45)

The interaction in (42) acts now between the ph or Δh excitations (the different coupling constant for the $\pi N\Delta$ is incorporated in the Lindhard function, U_Δ). Hence ultimately the picture for the spin-isospin dependent part of the interaction, by accounting also for the propagation of the mesons through the medium, will be, by analogy to Fig. 4, the one shown in Fig. 11. The series implicit in Fig. 11 can be easily summed up by using the orthogonality between the longitudinal and transverse modes of the interaction. Thus, one finds two (longitudinal and transverse) geometrical series, which do not interfere,

$$\left\{\hat{V}_{ij}(q)+\hat{V}_{ik}(q)U(q)\hat{V}_{kj}(q)+\hat{V}_{ik}(q)U(q)\hat{V}_{km}(q)U(q)\hat{V}_{mj}(q)+\cdots\right\}\sigma_i^{(1)}\sigma_j^{(2)}\boldsymbol{\tau}^{(1)}\boldsymbol{\tau}^{(2)}$$

$$=\left\{\frac{V_t(q)}{1-U(q)V_t(q)}(\delta_{ij}-\frac{q_iq_j}{\mathbf{q}^2})+\frac{V_l(q)}{1-U(q)V_l(q)}\frac{q_iq_j}{\mathbf{q}^2}\right\}\sigma_i^{(1)}\sigma_j^{(2)}\boldsymbol{\tau}^{(1)}\boldsymbol{\tau}^{(2)} \tag{45}$$

The interaction in (45) is called in the literature the induced interaction [50]. Very often in the literature one uses other expressions for V_l, V_t. The most widely used, in terms of the Landau-Migdal parameter g', can be obtained from (43) in the limit $|\mathbf{q}| << q_c$

$$\begin{aligned} V_l(q) &\approx \frac{f^2}{\mu^2}(\mathbf{q}^2 D_0^\pi(q)F_\pi^2(q)+g') \\ V_t(q) &\approx \frac{f^2}{\mu^2}(\mathbf{q}^2 D_0^\rho(q)F_\rho^2(q)C_\rho+g') \end{aligned} \tag{46}$$

with

$$g' = -\frac{q_c^2}{3}\hat{D_0}^{\pi}(q)\hat{F_\pi}^2(q) - \frac{2}{3}q_c^2\hat{D_0}^{\rho}(q)\hat{F_\rho}^2(q)C_\rho \tag{47}$$

This expression gives $g' \approx 0.6$. Accepted values of g' would range from $g' \approx 0.6 - 0.8$.

In the problems which we will study in the next sections $V_t(q) > 0, \mathrm{Re}U(q) < 0$, $V_l(q) < 0$. Thus one finds a decrease of the transverse mode (quenching) and an increase (enhancement) of the longitudinal one [38]. The net effect of considering the whole induced interaction instead of the bare one depends on the kinematical conditions (range of q) and the weight given to the transverse and longitudinal parts in (45).

3 Muon Capture in Nuclei

The problem of inclusive muon capture in nuclei is revised in this section from an unconventional point of view. The section is mainly based on the findings of [17, 51]. We study the μ-atom inclusive decay,

$$\left(A_Z - \mu^-\right)^{1s}_{\text{bound}} \rightarrow \nu_\mu(k) + X \tag{48}$$

depicted in the left panel of Fig. 12.

From the early days of Primakoff [52] the subject has attracted much interest [17, 51, 53–64], since this reaction has been used traditionally to extract information on the value of the pseudoscalar coupling constant [16]. The usual approach consists in performing the non-relativistic approximation in the transition operators, neglecting the nucleon-momentum, taking an average nuclear excitation energy (see for instance [52, 61]), and then doing a closure sum over the final nuclear states, in some cases improved by means of sum-rule approaches [63]. The final results are then obtained after the evaluation of non-trivial two-body matrix elements in the ground state of the nucleus.

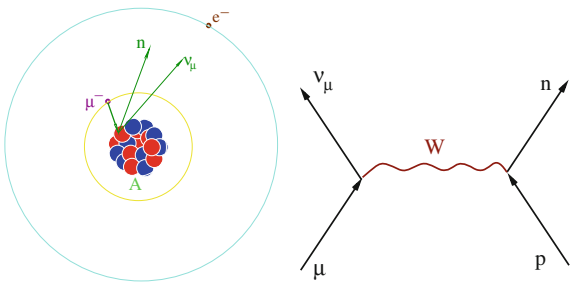

Fig. 12 Inclusive muon capture reaction in nuclei

Another approximation traditionally used, to take into account the fact that a muon penetrating into the nucleus does not experience the full charge Z but only the charge included within its orbit, is the use of the effective charge, $Z_{\rm eff}$, which introduces a non-negligible source of error in the calculation since the capture rate is proportional to $Z^4_{\rm eff}$ and certain approximations are involved in its evaluation. In addition there are strong nuclear renormalization effects which are very important and deserve special attention. Thus the traditional method is subject to different (and difficult to control) sources of theoretical uncertainties [51].

The approach of [17, 51] avoids all of these problems and provides an accurate method to evaluate the total capture rate in nuclei. The method consists in evaluating the capture rate of a muon in a Fermi sea of neutrons and protons (we will see that the only relevant nuclear information needed is the neutron and proton densities of the nuclear ground state, which will be taken from experiment to minimize errors). The calculation can be done exactly in a relativistic framework going beyond the closure sum or the sum rule approach. With the neutrino energy as a variable of integration, the pion pole structure of the pseudoscalar term is kept in the calculations making thus more reliable the information extracted, from this process, about the pseudoscalar coupling.

The step from infinite matter to finite nuclei is done by means of the local density approximation (LDA), which turns out to be highly accurate in this case, given the very weak q dependence of the matrix elements involved, which makes the transition of very short range [51]. The infinite matter calculation provides the muon width, $\hat{\Gamma}(\rho_p, \rho_n)$, as a function of $\rho_{p,n}$, the neutron and proton densities. The LDA to go to finite nuclei is obtained by replacing $\rho_p \to \rho_p(r)$, $\rho_n \to \rho_n(r)$ for the actual nuclei and then folding this functional with the muon density distribution, $|\Phi_{1s}(\mathbf{r})|^2$, in the $1s$ state of the muon atom, from which the capture takes place

$$\Gamma = \int d^3r |\Phi_{1s}(\mathbf{r})|^2 \hat{\Gamma}(\rho_p(r), \rho_n(r)) \tag{49}$$

This scheme does not use the concept of $Z_{\rm eff}$ and in addition, it also accounts for effects due to strong nuclear renormalization in the operators and due to binding energies. We will pay here a special attention to the effects due to the nuclear renormalization (main objective of these lectures) in medium and heavy nuclei, and we will see how this renormalization reduces the capture rates in about of a factor two from the results without renormalization.

3.1 Muon Capture Rate in Infinite Matter

We start from the basic Lagrangian for the $\mu^- p \to n\nu_\mu$ reaction depicted in the Feynman diagram of Fig. 12.

$$L(x) = \frac{G_F}{\sqrt{2}} J^\mu(x) L^\dagger_\mu(x) \tag{50}$$

with L^μ, J^μ the leptonic and hadronic currents respectively and G_F the Pauli constant ($G_F = 1.166 \times 10^{-5}\text{GeV}^{-2}$). The matrix elements of the leptonic and hadronic currents between spinors give:

$$L_\mu(x) \to \bar{u}_\nu(p_\nu)\gamma^\mu(1-\gamma_5)u_\mu(p_\mu)$$

$$J^\mu(x) \to \bar{u}_n(p_n)\left(g_v\gamma^\mu + i\frac{g_M}{2m_p}\sigma^{\mu\nu}q_\nu + g_A\gamma^\mu\gamma_5 + \frac{g_p}{m_\mu}q^\mu\gamma_5\right)u_p(p_p) \tag{51}$$

where we follow Itzykson and Zuber [42] convention for the γ matrices and spinors, with $p_{n,p,\nu,\mu}$ the neutron, proton, neutrino, muon four vectors, $q = p_n - p_p$ and g_V, g_M, g_A, g_p the vector, magnetic, axial-vector and pseudoscalar couplings constants respectively, including a form factor dependent on q^2. The values of the coupling constants and the expressions for the form factors can be seen in [51].

The width of a muon in the infinite Fermi sea of protons and neutrons with $N \neq Z$, due to a single ph excitation (first diagram of Fig. 13) is given by,[4]

$$\Gamma = -2\int \frac{d^3p_\nu}{(2\pi)^3}\frac{m_\mu}{E_\mu}\frac{m_p}{E_p}\frac{m_n}{E_n}\overline{\sum}\sum|T|^2\text{Im}\bar{U}(p_\nu - p_\mu) \tag{52}$$

where T denotes the T-matrix for the $\mu^- p \to n\nu_\mu$ process averaged over the Fermi sea (the full expression for $\overline{\sum}\sum|T|^2$ can be found in [51]) and $\bar{U}$ is the Lindhard function (see (16)) for the particle hole excitation of the first diagram of Fig. 13 in asymmetric nuclear matter and it is given by,

$$\bar{U}(p_\mu - p_\nu) = 2\int \frac{d^3p}{(2\pi)^3}\frac{n_1(\mathbf{p})(1-n_2(\mathbf{p}+\mathbf{p}_\mu-\mathbf{p}_\nu))}{E_\mu - E_\nu + E_p(\mathbf{p}) - E_n(\mathbf{p}+\mathbf{p}_\mu-\mathbf{p}_\nu) + i\varepsilon} \tag{53}$$

where $n_{1,2}(\mathbf{p})$ are the occupation numbers in the Fermi sea of protons and neutrons respectively.[5] Equation (52) provides the muon capture width as a function of $k_{F,p}$ and $k_{F,n}$, the proton and neutron Fermi momenta or equivalently ρ_p and ρ_n, the proton and neutron densities of the medium ($\rho_{p,n} = k^3_{F,p,n}/3/\pi^2$).

[4] Note that the lowest order contribution to Γ is essentially given by the imaginary part of the first μ-selfenergy diagram depicted in Fig. 13, when the ph excitation and the outgoing neutrino are put on shell. Up to some kinematical corrections, this imaginary part is given by the imaginary part of the Lindhard function $\bar{U}(p_\nu - p_\mu)$, which accounts for the ph excitation, and by $\overline{\sum}\sum|T|^2$ which accounts for transition squared operator [51].

[5] Note that in (53) the second term of (9) has not been included because it does not provide imaginary part for $q^0 = E_\mu - E_\nu > 0$.

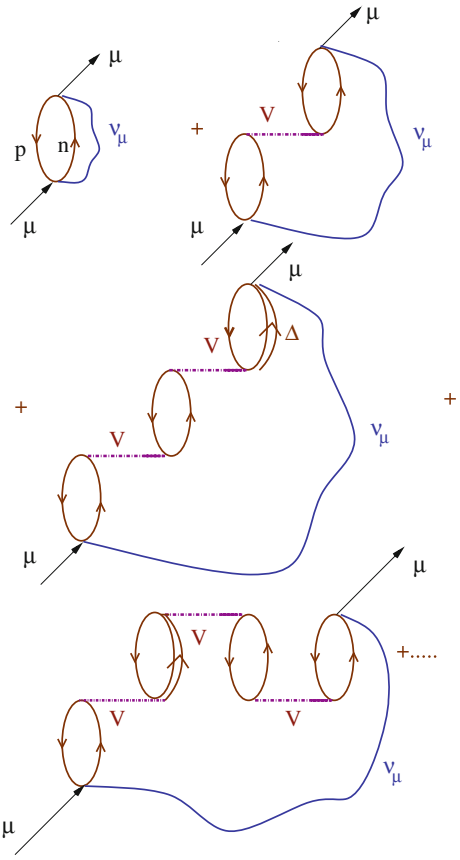

Fig. 13 Many-body Feynman diagrams for the muon self-energy related to the $\mu^- p \to n\nu_\mu$ process. The first diagram corresponds to a single ph excitation, while the rest of many-body Feynman diagrams account for the medium polarization in the spin-isospin channel driven by the $\mu^- p \to n\nu_\mu$ transition

3.2 *Strong Renormalization Effects*

The dominant contribution, ($\approx$80 %), to the process comes from the term proportional to g_A^2 in $\overline{\sum}\sum |T|^2$. The non-relativistic reduction of the axial-vector term in the nucleon current is of the type $g_A \sigma^i \tau^\lambda$. We know (see Sect. 2.3) that this external source has the virtue of polarizing the axial charge of the nuclear medium which can produce an important renormalization of the capture rate. Microscopically we can depict the situation by saying that the first Feynman diagram (a single ph excitation) of Fig. 13 is now modified to include the series of diagrams implicit in the rest of diagrams depicted in the same Fig. 13, where the intermediate lines stand for the spin-isospin ph or Δh interaction, $\hat{V}_{s-i}$ defined in (42) for the ph-ph interaction case, or a similar one for the case of ph-Δh or Δh-Δh interactions by means of the replacements in (44).

To carried out the sum implicit in Fig. 13 we follow here, the simplified treatment of [51]. The more exact calculation performed in [17] involves more complicated expressions and it might obscure a bit the discussion. However it leads to similar results in this case, where neglecting the bound muon three momentum and some terms of order p/M_N become an accurate approximation. The sum in Fig. 13 leads to two independent geometric series in the longitudinal and transverse channels (the term with g_A^2 involves the trace of $g_A^2\sigma_i\sigma_i\bar{U}$, which equivalently can be written as $g_A^2\sigma_i\sigma_j\bar{U}(\hat{q}_i\hat{q}_j + (\delta ij - \hat{q}_i\hat{q}_j))$, explicitly separated into a longitudinal and a transverse parts). After a little of algebra one finds that the renormalization can be taken into account by substituting

$$g_A^2 \mathrm{Im}\bar{U} \rightarrow g_A^2 \left(\frac{1}{3} \frac{\mathrm{Im}\bar{U}}{|1 - U V_l|^2} + \frac{2}{3} \frac{\mathrm{Im}\bar{U}}{|1 - U V_t|^2} \right) \tag{54}$$

where $U(= U_N + U_\Delta)$ is the Lindhard function defined in (25) and accounts for ph as well as Δh excitations in Fig. 13. In obtaining (54) above, the fact that U_Δ does not have an imaginary part, in the kinematical regime explored by the muon capture process, has been taken into account.

The pieces involving the pseudoscalar term, g_p, behave differently. Indeed the $g_P \boldsymbol{\sigma}\mathbf{q}$ coupling, in the non-relativistic limit, singles out the longitudinal part of the interaction and the renormalization is then

$$g_p^2 \mathrm{Im}\bar{U} \rightarrow g_p^2 \frac{\mathrm{Im}\bar{U}}{|1 - U V_l|^2} \tag{55}$$

Analogously, the terms involving g_M single out the transverse part of the interaction and we have

$$g_M^2 \mathrm{Im}\bar{U} \rightarrow g_M^2 \frac{\mathrm{Im}\bar{U}}{|1 - U V_t|^2} \tag{56}$$

The other terms, which are rather small, are not renormalized.

After performing the renormalization of (52), we obtain the new capture width $\hat{\Gamma}(\rho_p, \rho_n)$, and use the LDA to go to finite nuclei as discussed in (49). The LDA assumes implicitly a zero range of the interaction, or no dependence on $\mathbf{q}$ equivalently. The q-dependence of the form factors is extremely weak and thus the LDA prescription becomes highly accurate [51]. Note that the approach of [17, 51] and presented here differs substantially from standard ones, which require the evaluation of two-body matrix elements for the ground state of the nucleus. In this approach, one does not evaluate any nuclear matrix element and the only nuclear information needed is the proton and neutron densities. As pointed out in the introduction some approaches use a closure sum over the nuclear intermediate states [52, 54–62, 64]. Others, adopt a different strategy [63], and use a sum rule approach which still relies

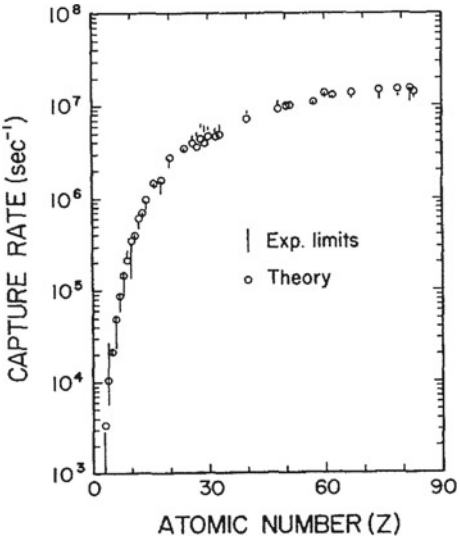

Fig. 14 Total rates for negative muons captured by the most stable isotopes from [51]. *Circles* are theoretical results. Experimental limits from different groups are also shown

upon an average excitation energy, although the dependence of Γ on this variable is rather smooth, unlike in the closure sum case. Here the Lindhard function has summed the contribution from intermediate nuclear states (the excited states of neutrons on top of the Fermi sea). On the other hand, the concept of Z_{eff} has not been needed. Equation (49) provides Γ directly from the muon wave function and the function $\hat{\Gamma}(\rho_p(r), \rho_n(r))$.

3.3 Results and Concluding Remarks

A rather exhaustive list of nuclei was studied in [51]. In this reference results for nuclei from ^6Li ($\Gamma \approx 0.3 \times 10^4 s^{-1}$) up to ^{209}Bi ($\Gamma \approx 0.15 \times 10^8 s^{-1}$) are presented. The overall agreement between the theoretical results and the experiment is spectacular considering the amount of nuclei studied and the large variation of the rates (four orders of magnitude) from light to heavy nuclei. In Fig. 14, a selection of the most stable isotopes as a function of Z are shown in order to give a visual idea of the quality of the agreement found in [51]. In [17, 51], the effects of the muon momentum and binding energy, Pauli blocking (which turns out to be very important, because the outgoing n in the $\mu^- p \to n\nu_\mu$ reaction can not go to any of the neutron occupied states[6]) on the rate are carefully examined. Here, we will concentrate on the effects of the renormalization discussed briefly in Sect. 3.2 and more carefully in [51]. These

[6]This is taken into account by means of the factor $1 - n_2(k)$ in the Lindhard function of (53).

Table 1 Experimental and theoretical [17] total muon capture widths for different nuclei

	Pauli ($10^4\,s^{-1}$)	RPA ($10^4\,s^{-1}$)	Exp ($10^4\,s^{-1}$)	$\left(\Gamma^{\rm Exp}-\Gamma^{\rm Th}\right)/\Gamma^{\rm Exp}$
^{12}C	5.42	3.21	3.78 ± 0.03	0.15
^{16}O	17.56	10.41	10.24 ± 0.06	−0.02
^{18}O	11.94	7.77	8.80 ± 0.15	0.12
^{23}Na	58.38	35.03	37.73 ± 0.14	0.07
^{40}Ca	465.5	257.9	252.5 ± 0.6	−0.02
^{44}Ca	318	189	179 ± 4	−0.06
^{75}As	1148	679	609 ± 4	−0.11
^{112}Cd	1825	1078	1061 ± 9	−0.02
^{208}Pb	1939	1310	1311 ± 8	0.00

Data are taken from [66], and when more than one measurement is quoted in [66], we use a weighted average: $\overline{\Gamma}/\sigma^2 = \sum_i \Gamma_i/\sigma_i^2$, with $1/\sigma^2 = \sum_i 1/\sigma_i^2$. To illustrate the role played by the RPA correlations, we quote two different theoretical results: (i) Pauli obtained from (52) without including RPA correlations; (ii) the full calculation, including different nuclear effects discussed in [17] and denoted as RPA, since these latter long range correlations turn out to be the most relevant. As commented in the text, the RPA calculation carried out in [17] leads to similar results to that outlined in these lectures. Finally, in the last column we show the relative discrepancies existing between the theoretical predictions given in the third column and data

effects play a very important role in this problem. Indeed, in Table 1 the results calculated with a without the renormalization (RPA) for several nuclei are shown. For medium and heavy nuclei the nuclear renormalization reduces the results in about a factor two and it is essential to produce agreement with the experimental numbers. This is a very interesting process, which evidences the strong nuclear renormalization on top of the weak interaction process, which can be brought under control as we have shown here. Although similar effects due to the spin-isospin polarization of the nucleus also appear in many nuclear processes, sometimes it is more difficult to asses their importance since the nuclear interaction itself can be less controllable. However, it is interesting to mention that these medium polarization effects have been also considered in connection with the problem of Σ-atoms and hypernuclei, Λ-hypernuclei, K^+-nucleus scattering, pionic atoms, π-nucleus scattering a low energies, electro-weak QE cross sections [17, 21–38, 65] … The clean effects of this medium renormalization shown here stress and reinforce the interpretation given for these other phenomena.

Finally, in Fig. 15 we show the outgoing ν_μ energy distribution from muon capture in ^{12}C, which ranges from 70 to 90 MeV. The energy transferred to the daughter nucleus (^{12}B) ranges from 0 to 20 MeV. We also show in the figure the medium polarization effect on the differential decay rate. The shape of the curves in Fig. 15 will significantly change if a proper finite nuclei treatment is carried out, with the appearance of narrow peaks, but providing similar values for the integrated widths [53].

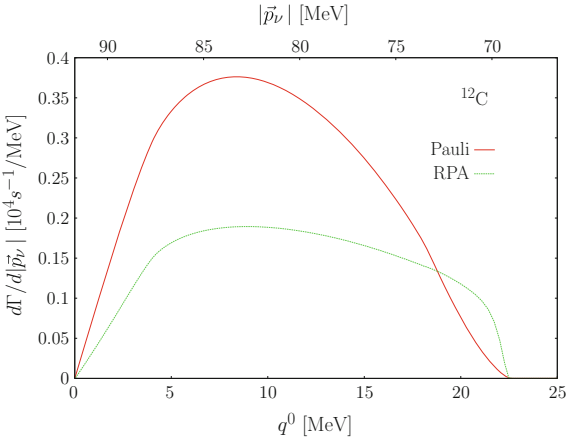

Fig. 15 Inclusive muon capture differential width from ^{12}C, as a function of the outgoing neutrino energy (*top axis*) and of the energy transfer (*bottom axis*). The two calculations are labeled as in Table 1

4 Inclusive Electron-Nucleus Scattering at Intermediate Energies

Inclusive electron scattering, particularly around the QE peak is probably one of the problems that has attracted more attention in nuclear physics. In this section we review on a self-contained many body model, exposed in [30], which provides a complete and successful description of the (e, e') inclusive reaction in a range of energies between 100 MeV and about 500 MeV of the virtual photon. The model incorporates effects which have convincingly proved to be relevant in previous works (meson exchange currents, RPA correlations, final state interaction, etc.), but also it incorporates Delta–hole (Δh) and two particle-hole excitations, additional to the particle–hole excitations. This fact allows to simultaneously study the quasielastic peak, the Δ peak and the "dip" region between the two peaks in the inclusive (e, e') cross section. The model constitutes a generalization of the work performed for real photons in [24] to virtual ones, and it will be extended to study neutrino induced reactions in Sect. 5. Such many body scheme provides an adequate framework to disentangle the MiniBooNE nucleon axial mass puzzle.

4.1 Formalism

We present a covariant many body formalism to evaluate the (e, e') cross section. For this purpose we evaluate the electron self-energy for an electron moving in infinite nuclear matter. Diagrammatically this is depicted in Fig. 16. The electron disappears from the elastic flux, by inducing $1p1h, 2p2h...$ excitations or creating pions, etc., at a rate given by

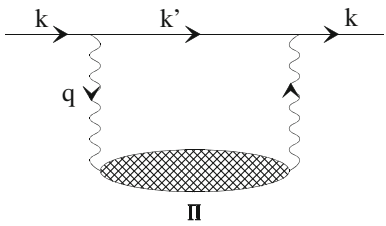

Fig. 16 Diagrammatic representation of the electron self-energy in nuclear matter

$$\Gamma(k) = -2\frac{m_e}{E_e}\mathrm{Im}\Sigma. \tag{57}$$

where $\mathrm{Im}\Sigma$ is the imaginary part of the electron self-energy. This latter magnitude can be readily evaluated from the diagram of Fig. 16 and we find:

$$\Sigma_r(k) = ie^2\int \frac{d^4q}{(2\pi)^4}\bar{u}_r(k)\gamma_\mu\frac{(\not{k}' + m_e)}{k'^2 - m_e^2 + i\varepsilon}\gamma_\nu u_r(k)\frac{\Pi_\gamma^{\mu\nu}(q)}{(q^2 + i\varepsilon)^2} \tag{58}$$

where $\Pi_\gamma^{\mu\nu}$ is the virtual photon self-energy. Equation (58) displays explicitly the electron propagator (fraction after γ_μ) and the photon propagator $(q^2 + i\varepsilon)^{-1}$ which appears twice. By averaging over the spin of the electron, r, we find

$$\Sigma(k) = \frac{ie^2}{2m_e}\int \frac{d^4q}{(2\pi)^4}\frac{L_{\mu\nu}\Pi_\gamma^{\mu\nu}(q)}{q^4}\frac{1}{(k'^2 - m_e^2 + i\varepsilon)} \tag{59}$$

and since we are interested in the imaginary part of Σ we can obtain it by following the prescription of the Cutkosky's rules. In this case we cut with a straight vertical line the intermediate e' state and those implied by the photon polarization (shaded region). Those states are then placed on shell by taking the imaginary part of the propagator, self-energy, etc. Thus, we obtain

$$\mathrm{Im}\Sigma(k) = \frac{2\pi\alpha}{m_e}\int \frac{d^3q}{(2\pi)^3}\left(\mathrm{Im}\Pi_\gamma^{\mu\nu}L_{\mu\nu}(k,k')\right)\frac{1}{q^4}\frac{1}{2E_e(\mathbf{k}')}\Theta(q^0) \tag{60}$$

The relationship of $\mathrm{Im}\Sigma$ to the (e, e') cross section is easy: $\Gamma dtdS$ provides a probability times a differential of area, which is a contribution to a cross section. Hence we find

$$d\sigma = \Gamma(k)dtdS = -\frac{2m_e}{E_e}\mathrm{Im}\Sigma dl\, dS = -\frac{2m_e}{|\mathbf{k}|}\mathrm{Im}\Sigma d^3r \tag{61}$$

and hence the nuclear cross section is given by

$$\sigma = -\int d^3r \frac{2m_e}{|\mathbf{k}|} \mathrm{Im}\Sigma(k, \rho(\mathbf{r})) \tag{62}$$

where we have substituted Σ as a function of the nuclear density at each point of the nucleus and integrate over the whole nuclear volume. Equation (62) assumes the LDA, which is an excellent approximation for volume processes like here, hence we are neglecting the electron screening and using implicitly plane waves for the electrons (corrections to account for the small distortion are usually done in the experimental analysis of the data). Thus, we get

$$\frac{d^2\sigma}{d\Omega'_e dE'_e} = -\frac{\alpha}{q^4}\frac{|\mathbf{k}'|}{|\mathbf{k}|}\frac{1}{(2\pi)^2}\int d^3r \left(\mathrm{Im}\Pi^{\mu\nu}_\gamma L_{\mu\nu}\right) \tag{63}$$

which gives us the (e, e') differential cross section in terms of the imaginary part of the photon self-energy. If one compares (63) with the general expression for the inclusive (e, e') cross section [67]

$$\frac{d^2\sigma}{d\Omega'_e dE'_e} = \frac{\alpha^2}{q^4}\frac{|\mathbf{k}'|}{|\mathbf{k}|}L^{\mu\nu}W_{\mu\nu} \tag{64}$$

we find

$$W^{\mu\nu} = -\frac{1}{\pi e^2}\int d^3r \frac{1}{2}\left(\mathrm{Im}\Pi^{\mu\nu} + \mathrm{Im}\Pi^{\nu\mu}\right) \tag{65}$$

By choosing $\mathbf{q}$ in the z direction and using gauge invariance one can write the cross section in terms of the longitudinal and transverse structure functions W_L, W_T as

$$\frac{d^2\sigma}{d\Omega'_e dE'_e} = \left(\frac{d\sigma}{d\Omega}\right)_{Mott}\left(-\frac{q^2}{|\mathbf{q}|^2}\right)\left\{W_L(\omega, |\mathbf{q}|) + \frac{W_T(\omega, |\mathbf{q}|)}{\varepsilon}\right\} \tag{66}$$

where $q^2 = \omega^2 - |\mathbf{q}|^2$

$$\left.\frac{d\sigma}{d\Omega}\right|_{Mott} = \frac{\alpha^2\cos^2_e(\theta/2)}{4E_e^2\sin^4_e(\theta/2)} \tag{67}$$

$$W_L = -\frac{q^2}{\omega^2}W^{zz} = -\frac{q^2}{|\mathbf{q}|^2}W^{00} \tag{68}$$

$$W_T = W^{xx} \tag{69}$$

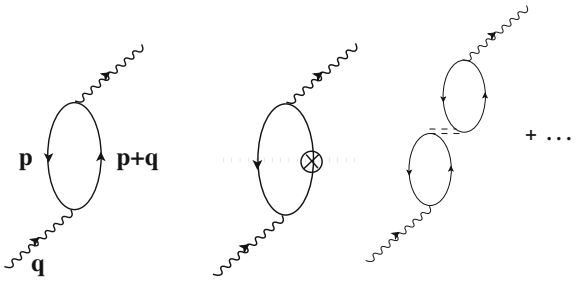

Fig. 17 *Left* Photon self-energy diagram for the $1ph$ excitation driven by the virtual photon. *Middle* Insertion of the nucleon self-energy on the nucleon line of the particle state. *Right* Diagrammatic representation of the polarization effects in the $1ph$ excitation

Hence we can write W_L and W_T in terms of the photon self-energy as

$$W_L = \frac{q^2}{\pi e^2 |\mathbf{q}|^2} \int d^3r \, \mathrm{Im}\Pi^{00}(q, \rho(\mathbf{r})) \tag{70}$$

$$W_T = -\frac{1}{\pi e^2} \int d^3r \, \mathrm{Im}\Pi^{xx}(q, \rho(\mathbf{r})) \tag{71}$$

where we see that we only need the components Π^{00} and Π^{xx} of the virtual photon self-energy.

4.2 Virtual Photon Self-Energy in Nuclei

4.2.1 One Particle—One Hole Contribution: Quasielastic Peak

Unlike the case with real photons, a virtual photon can be absorbed by one nucleon leading to the QE peak of the response function. Thus, we begin by evaluating $\Pi^{\mu\nu}$ for the $1ph$ excitation driven by the virtual photon, as depicted in the first many body diagram of Fig. 17. The imaginary photon self-energy associated to this diagram is given by the well known result,

$$Im\Pi^{\mu\nu} = \frac{e^2}{2} Im\bar{U}(q, \rho) A^{\mu\nu} \tag{72}$$

where $\bar{U}(q, \rho)$ is the Lindhard function, which plays the role of a particle-hole propagator, as discussed previously, ρ is the density and

$$A^{00} = \frac{1}{M_N^2}\left\{\frac{1}{1-\frac{q^2}{4M_N^2}}\left[G_E^2(q) - \frac{q^2}{4M_N^2}G_M^2(q)\right]\frac{1}{2}(2p^0+q^0)^2 - \frac{1}{2}\mathbf{q}^2 G_M^2(q)\right\} \tag{73}$$

$$A^{xx} = \frac{1}{M_N^2}\left\{\frac{1}{1-\frac{q^2}{4M_N^2}}\left[G_E^2(q) - \frac{q^2}{4M_N^2}G_M^2(q)\right]\frac{2}{5}k_F^2 - \frac{1}{2}q^2 G_M^2(q)\right\} \tag{74}$$

where $p^0 = M_N + \frac{3}{5}\frac{k_F^2}{2M_N}$, with k_F the Fermi momentum and G_E, G_M are the Sachs form factors [67, 68]. In the above expression, the average over the Fermi momentum has be done keeping terms up to q^2/M_N^2. The main corrections to the bare ph excitation studied above are:

(A) *Spectral function effects*
It is well known that there are important effects induced by the interaction felt by each of the individual nucleons with the rest of the nucleons of the nucleus. This produces a change of the dispersion relation of the nucleon inside of the nuclear environment. In the present framework, it can be taken into account by dressing up the nucleon propagator of the particle and hole states in the ph excitation, as depicted in the middle panel of Fig. 17 for the particle propagator. Thus, following the Dyson equation, the free particle nucleon propagator entering in the Lindhard function of (72) should be replaced by a renormalized nucleon propagator including the nucleon self-energy in the medium,

$$G(p^0, \mathbf{p}) = \frac{1}{p^0 - \frac{\mathbf{p}^2}{2M_N} - \Sigma(p^0, \mathbf{p})} \tag{75}$$

where $\sum(p^0, \mathbf{p})$ is the nucleon self-energy. Alternatively one can use the spectral function representation [39]. We use the spectral functions calculated in [27], but since the imaginary part of the nucleon self-energy for the hole states is much smaller than that of the particle states, we make the approximation of setting to zero $\mathrm{Im}\Sigma$ for the hole states. This was found to be a good approximation in [69]. The effect of the use of the spectral functions is a quenching of the quasielastic peak and a spreading of the strength at higher energy as can be seen in Fig. 18. Similar effects were found in [70].

(B) *Polarization (RPA) effects in the QE contribution*
We take now into account polarization effects in the $1p1h$ excitation, substituting it by an RPA response as shown diagrammatically in the last diagram depicted in Fig. 17, and showed in some more detail in Fig. 11. For that purpose we use an effective interaction of the Landau-Migdal type

$$\begin{aligned} V &= c_0\left\{f_0(\rho) + f_0'(\rho)\boldsymbol{\tau}_1\boldsymbol{\tau}_2 + g_0(\rho)\boldsymbol{\sigma}_1\boldsymbol{\sigma}_2\right\} \\ &+ \left[V_t\left(\delta_{ij} - \frac{q^i q^j}{\mathbf{q}^2}\right) + V_l\frac{q^i q^j}{\mathbf{q}^2}\right](\boldsymbol{\sigma}_1^i\boldsymbol{\sigma}_2^j)\boldsymbol{\tau}_1\boldsymbol{\tau}_2 \end{aligned} \tag{76}$$

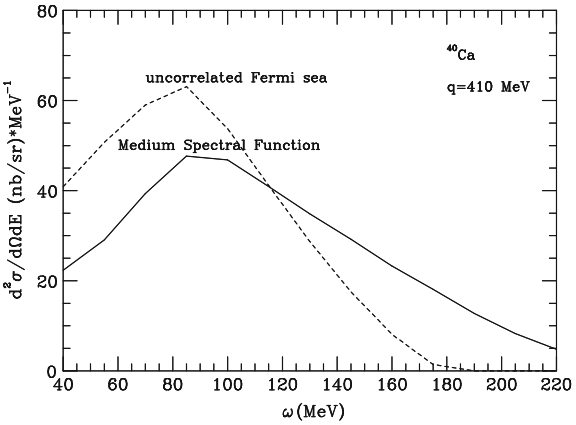

Fig. 18 Effect of the use of the spectral function in the evaluation of the Lindhard function

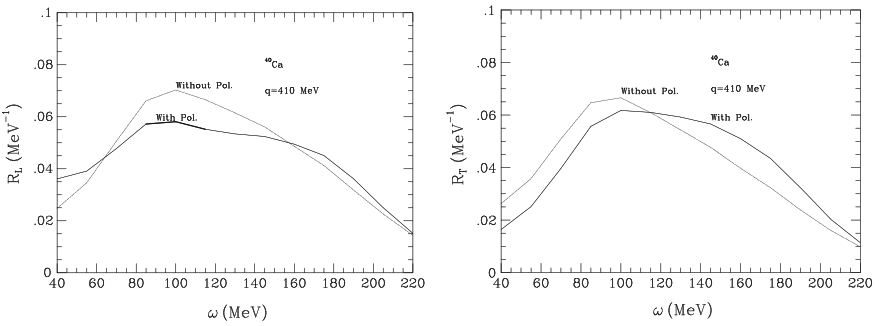

Fig. 19 Polarization (RPA) effect in the evaluation of R_L (*left*) and R_T (*right*)

with the modified $\pi + \rho$ interaction in the $\sigma\sigma\tau\tau$ sector given in (42) and (43), and we take the parametrization for the rest of coefficients from [71]. RPA effects on R_L and R_T ($R_L = -\frac{|\mathbf{q}|^2}{q^2} W_L$ and $R_T = 2W_T$) are shown in Fig. 19. The net effect in the cross section is a quenching in the QE peak and a spreading of the strength at higher energies.

4.2.2 Pion Production Contribution

In this subsection, we construct a self-energy diagram for the photon which contains pion production in the intermediate states. This is readily accomplished by taking the amplitude of the $\gamma^* N \to \pi N$ process (γ^* will stand from now on for the virtual photon) and folding it with itself. One gets then the diagram of the left panel of Fig. 20 where the circle stands for the elementary amplitude $\gamma^* N \to \pi N$.

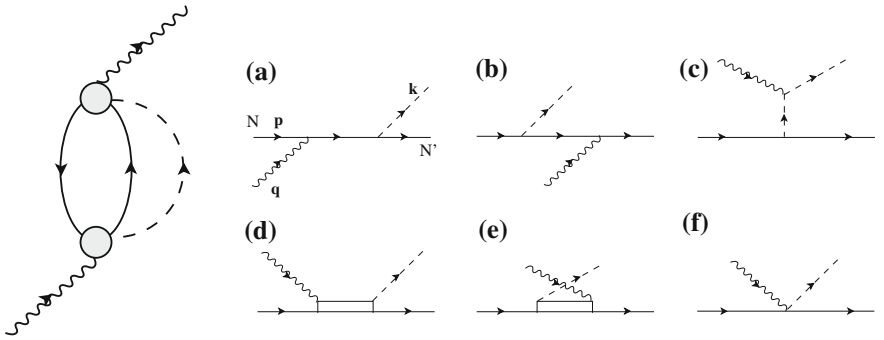

Fig. 20 *Left* Photon self-energy obtained by folding the $\gamma^* N \to \pi N$ amplitude. *Right* Feynman diagrams considered for the $\gamma^* N \to \pi N$ reaction

- **The $eN \to eN\pi$ reaction**. Thus, the first necessary ingredient to study the pion contribution to the (e, e') reaction is an accurate model for the $\gamma^* N \to \pi N$ reaction in the vacuum. For such process, we essentially use the model for the $eN \to eN\pi$ reaction derived in [72]. The basic vertices are the coupling of the photon and the pion to the nucleon and to the $N\Delta$ transition, plus the Kroll Ruderman term, and the coupling of the photon to the pion. The Kroll Ruderman contribution appears as a gauge invariant term through minimal substitution when a pseudovector πNN coupling is used. The Feynman diagrams considered in the model of [72] are depicted in the right panel of Fig. 20. They are the nucleon pole direct (NP) term (a), the nucleon pole crossed (NPC) term (b), the pion pole (PP) term (c), the delta pole direct (DP) term (d), delta pole crossed (DPC) term (e) and the Kroll Ruderman (KR) term (f). The expressions for these amplitudes are obtained by doing the non-relativistic reduction of the relativistic amplitudes of [72]. The model satisfies gauge invariance and unitarity is restored by means of a procedure suggested in [73] and also applied recently with great success to neutrino induced reactions in [74]. Though simple, the model of the right panel of Fig. 20 provides a reasonable description of the $eN \to eN\pi$ differential cross section for all energy and angular variables of the outgoing electron and pion accessible to experiments involving nucleon energies below 500 MeV.[7]

Thus, in the left panel of Fig. 20 the circle stands for any of the 6 terms of the elementary model for $\gamma^* N \to \pi N$. The photon self-energy corresponding to this diagram turns out actually to sum up the contribution of the 36 diagrams implicit in the figure. The lines going up and down follow the standard many body nomenclature and stand for particle and hole states respectively. After a little of algebra, one finds [30]

$$\mathrm{Im}\Pi^{\mu\nu} = \int \frac{d^3k}{(2\pi)^3} \mathrm{Im}\bar{U}_{NN'}(q-k) \frac{\theta(q^0 - \omega(\mathbf{k}))}{2\omega(\mathbf{k})} \frac{1}{2} Tr^{Spin}(T^\mu T^{\dagger\nu}_{NN'}) \Big|_{k^0=\omega(\mathbf{k})} \quad (77)$$

[7] See [30] for more details, both of the model and its comparison to experimental data.

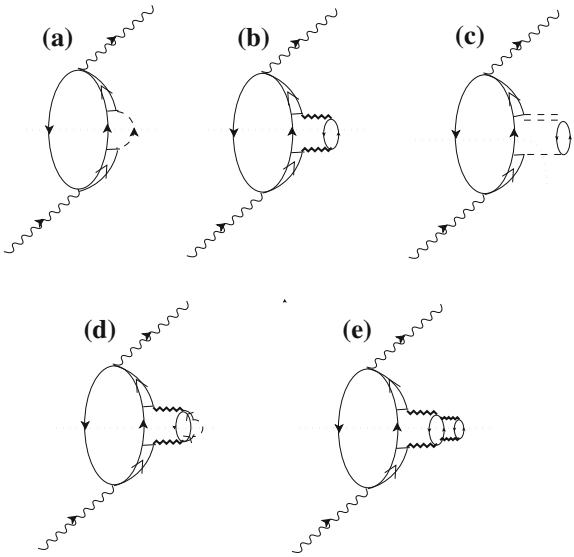

Fig. 21 Diagrammatic representation of the Δh photo-nuclear excitation term

where $\bar{U}_{N,N'}$ is the Lindhard function defined in asymmetric nuclear matter, θ is the Heaviside function and T^{μ} is the amplitude for the $\gamma^* N \to \pi N$ process. There is an interesting test to (77). Indeed, in the limit of small densities $Im\bar{U}_{NN'}(q) \simeq -\pi\rho_N \delta(q^0 - \frac{\mathbf{q}^2}{2M_N})$. Substituting this into (77) one easily obtains that $\sigma_{eA} = \sigma_{ep} Z + \sigma_{en} N$, the strict impulse approximation.[8] By performing the integral in (77) one accounts for Pauli blocking and in an approximate way for Fermi motion. Other corrections due to medium polarization will be also included.

4.2.3 The Δ Excitation Term

One of the terms implicit in (77) is the one where one picks up the Δ excitation term both in T^{μ} and $T^{\dagger\nu}$. This term is depicted diagrammatically in Fig. 21a and, like in pion-nuclear and photo-nuclear reactions at intermediate energies, plays a major role in this reaction as can be appreciated in Fig. 22. There, we show the contribution (solid line) of the Δ piece for the ^{12}C nucleus (experimental data points are from [75]). We can see that most of the experimental strength in the Δ region is provided by this Δ excitation term, but there is still some strength missing. The study of this missing strength will occupy the next subsection.

Given the importance of the Δ contribution, it is necessary to treat it with special care and it has been the subject of a lot of work [76–84]. Among other dynamical features discussed in the original work of [30], one which plays a special role is to consider that in a nuclear medium the Δ is renormalized and it acquires a

[8] The elementary pion production cross sections σ_{ep} and σ_{en} can be found for instance in [68].

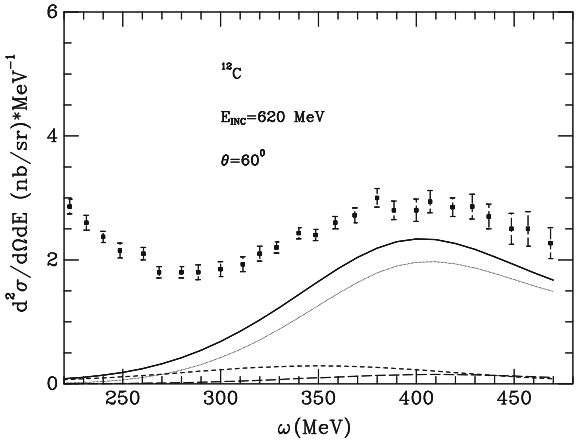

Fig. 22 Contribution of the Δ piece to the (e, e') cross section in ^{12}C. Experimental data from [75]. Besides the *upper solid line*, which stands for the total contribution, looking from up to down at about $\omega = 350$ MeV, the next line corresponds to pion production, the following one is two nucleon absorption and the lowest one three body absorption

self-energy Σ_Δ. This self-energy accounts for the diagrams depicted in Fig. 21, where the double dashed line stands for the effective spin-isospin interaction of (42), while the serrated line accounts for the induced interaction (45). As discussed in Sect. 2.3, the effective spin-isospin interaction is originated by a pion exchange in the presence of short range correlations and includes ρ-exchange as well. The induced interaction accounts for the series of diagrams depicted in Fig. 11. Σ_Δ was evaluated in [85], where a useful analytical parametrization of the numerical results is given that we use here. The imaginary part is parametrized as

$$Im\Sigma_\Delta = -\left\{C_Q(\rho/\rho_0)^\alpha + C_{A_2}(\rho/\rho_0)^\beta + C_{A_3}(\rho/\rho_0)^\gamma\right\} \tag{78}$$

where the different coefficients are given in [85] as a function of the energy. The separation of terms in (78) is useful because the term C_Q comes from the diagrams (c) and (d) of Fig. 21 when the lines cut by the dotted line are placed on shell, and hence the term is related to the (γ^*, π) channel, while C_{A_2}, C_{A_3} come from the diagrams (b) and (e) and are related to two and three body absorption. Hence, the separation in this formula allows us to separate the final cross section into different channels. To get an idea of the size of each of these contributions, in Fig. 22, the total contribution of the Δ piece is split into the different open channels. Yet, we should mention that the RPA sum of Δh excitations, shown in Fig. 23, is also taken into account in the model.

4.2.4 Two Body Photo-Absorption: 2p2h Nuclear Excitations

Let us go back to the generic diagram of pion electro-production of the left panel of Fig. 20. Let us take the pion line and allow the pion to excite a ph. This leads us to the left diagram of Fig. 24. This is still a generic diagram which actually contains 36 diagrams when in the shaded circle we put each one of the terms of the $\gamma^* N \to \pi N$

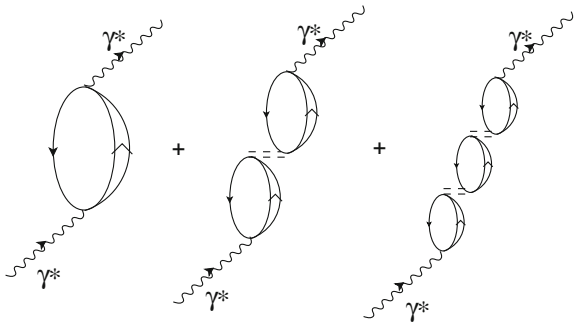

Fig. 23 Irreducible pieces in the Δh channel from the Δh interaction

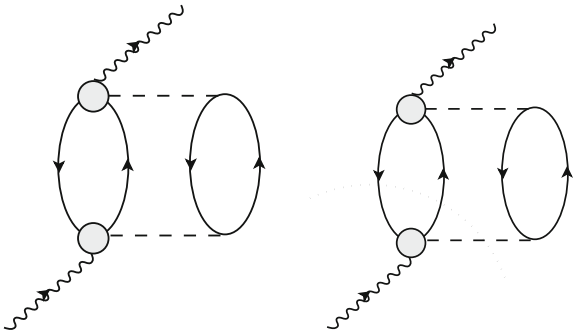

Fig. 24 *Left* Photon self-energy obtained from the one in Fig. 20 when the pion is allowed to excite a ph. *Right* Same as the *left panel* and showing the cut which places one ph and the pion on shell

amplitude of the right panel of Fig. 20. One can see that the diagrams in the left panel of Fig. 24 contribute to ImΠ according to Cutkosky's rules when we cut by a horizontal line and the $2p2h$ are placed on shell. Thus, we obtain

$$\mathrm{Im}\Pi^{(2)\,\mu\nu} = -\sum_{NN'}\int \frac{d^4k}{(2\pi)^4}\Theta(q^0-k^0)Im\bar{U}_{NN'}(q-k)\Theta(k^0)U_\lambda(k)$$
$$\times\ D_\pi^2(k)\frac{f_{\pi NN}^2}{m_\pi^2}\mathbf{k}^2F_\pi^4(k)S_\alpha Tr^{Spin}(T^\mu T^{\dagger\nu})_{NN'} \tag{79}$$

where U_λ is the Lindhard function for ph by an object of charge λ: this is, twice $\bar{U}_{p,n}$ or $\bar{U}_{p,n}$ for the excitation by a charged pion or $\bar{U}_{p,p}+\bar{U}_{n,n}$ for the excitation by a neutral pion and $\mathbf{k}$ is the pion momentum. The factor $F_\pi^4(k)$, where F_π is the pion form factor appears because now the pions are off shell. The factor S_α is the symmetry factor: unity for all diagrams except for the symmetric ones, for which it takes the value 1/2.

The cut which places the two ph on shell in the left diagrams of Fig. 24 is not the only possible one. In the right panel of Fig. 24 we show a different cut (dotted line) which places one ph and the pion on shell. This contribution is taken into account in the Δ excitation term by means of the term C_Q. As done for real photons in [24],

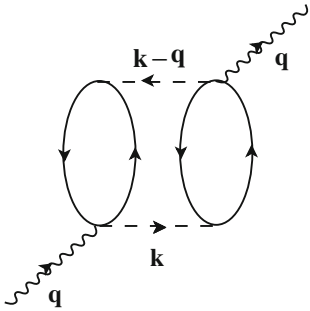

Fig. 25 Feynman diagram related to the KR term of Fig. 20f with outgoing photon from the second nucleon

we neglect this contribution in the other terms, because at low energies where the background pieces are important, the (γ^*, π) channel is small and at high energies where the (γ^*, π) contribution is important, this channel is dominated by the Δ excitation and there this correction is taken into account.

We have also considered two body diagrams where each photon couples to different bubbles: As found in [24] only one of them is relevant, the one in Fig. 25, which involves the KR term alone and which we take into account.

The contribution of this term is roughly 1/2 of the $KR \times KR$ term in the generic diagram of Fig. 24 and it can be found in [30].

In the model developed in [30], some contributions related to the $(\gamma^*, 2\pi)$ channel are also considered. The contribution of these terms below $\omega = 350$ MeV is very small. Their importance increases with the energy and at $\omega = 450$ MeV they account for about 1/5 of the cross section, as found for real photons.

4.2.5 Polarization (RPA) Effects and Short Range Correlations

In the diagrams of Fig. 24 we can consider the ph as just the first order of a series of the RPA excitations through ph and Δh excitations. If one replaces the ph by the RPA series, one is led to the terms implicit in Fig. 26. A similar series would appear for the case of the (γ, π) process depicted in Fig. 20. In practical terms this is done in a simple way by having a bookkeeping of both the spin longitudinal and spin transverse parts and replacing

$$ImU_N \to a \frac{ImU_N}{|1 - U_\lambda(q) V_l|^2} + b \frac{ImU_N}{|1 - U_\lambda V_t|^2} \tag{80}$$

where a, b measure the strength of the longitudinal and transverse parts.

Note that short range correlations in the baryon-baryon $p-$wave interaction terms are included in the effective V_l and V_t potentials, originated from π and ρ exchanges,

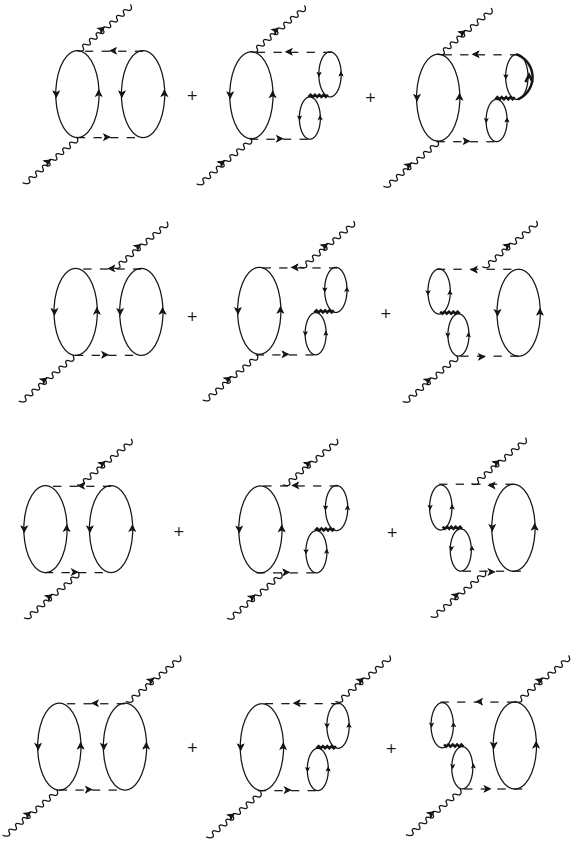

Fig. 26 Terms of the KR and pion pole block implicit in Fig. 24 showing the medium polarization through RPA ph and Δh excitations induced by the pion

respectively. As discussed in Sect. 2.3, the method to introduce the effects of correlations is to substitute a two nucleon amplitude $V(q)$ by

$$V(\mathbf{q}) \to \frac{1}{(2\pi)^3} \int d^3k V(\mathbf{k}) \Omega(\mathbf{q} - \mathbf{k}) \tag{81}$$

where $\Omega(\mathbf{p})$ is the Fourier transform of a nuclear correlation function.

4.3 Results

Let us first discuss results in the quasielastic peak. Figure 27 shows results for R_L and R_T for ^{12}C and compare them to the data of [86]. The lower line shows the results obtained with the medium spectral function, while the upper one includes also the rest of the effects discussed in the former section. In Fig. 28, we show results for

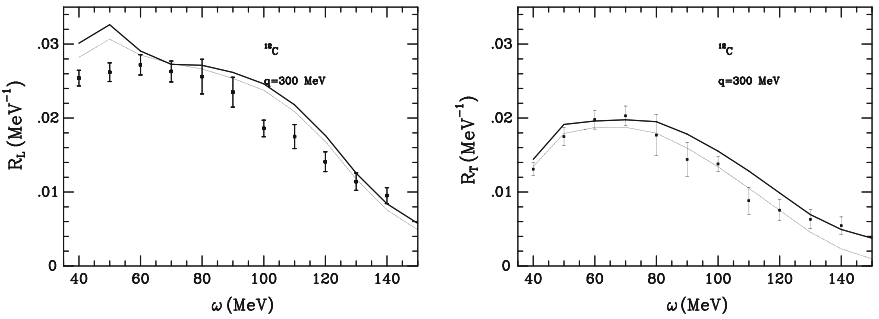

Fig. 27 Calculation of R_L and R_T for ^{12}C. The *lower line* in the high energy region corresponds to the result obtained with the contribution of the $1p1h$ excitation using medium spectral functions. The *upper line* is the result when one adds the rest of contributions. Experimental data from [86]

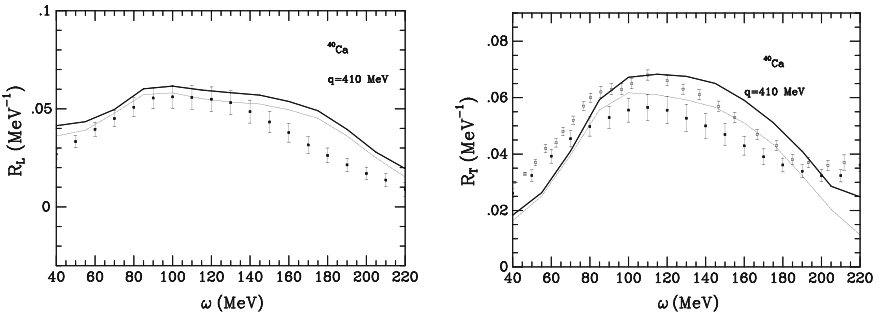

Fig. 28 Calculation of R_L and R_T for ^{40}Ca. Same meaning of the lines as in Fig. 27. Experimental data from [87, 88] and [89, 90] (upper points of R_T)

^{40}Ca compared to the data of [87–90]. As one can see, we find a good agreement with the reanalysis of [87, 88]. Finally let us see the global results including the quasielastic peak, the dip region and the delta region. They can be seen in Figs. 29 and 30 for the nuclei of ^{12}C and ^{208}Pb, respectively. The global agreement is good and the three regions are well reproduced (a bit overestimated for ^{208}Pb). In the left panel of Fig. 29 we also show with a dotted line the results for pion production. In Fig. 30 instead we show with a dotted line the results for the $1p1h$ excitation alone.

4.4 Conclusions

We have reviewed a microscopic many body model of the (e, e') reaction below $\omega = 500-600$ MeV. The model has no free parameters. All the input consists of basic couplings of photons to nucleons and isobars, and some phenomenological inputs, as correlations, which has been tested in former pionic reactions.

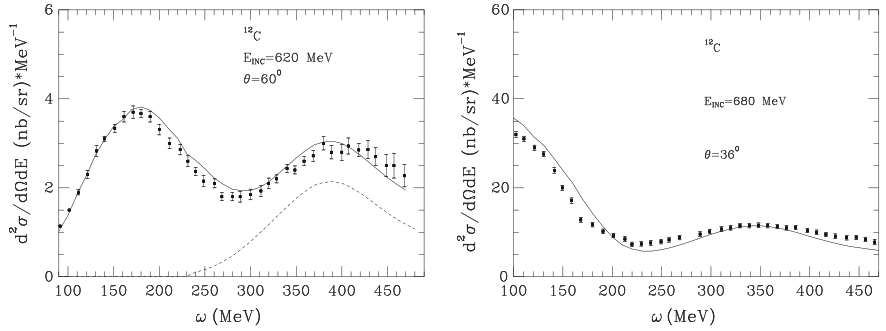

Fig. 29 Inclusive (e, e') cross section for ^{12}C (experimental data from [75]). *Left* $E_e = 620$ MeV and $\theta_e = 60°$. The *dotted line* corresponds to the pion production contribution. *Right* $E_e = 680$ MeV and $\theta_e = 36°$

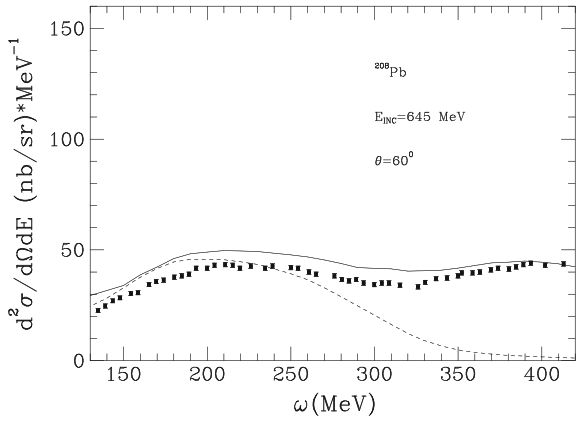

Fig. 30 Inclusive (e, e') cross section for ^{208}Pb. $E_e = 645$ MeV and $\theta_e = 60°$. The *dotted line* corresponds to the $1p1h$ excitation contribution. Experimental data from [91]

The model is suited to study the inclusive (e, e') reaction from the quasielastic peak up to the Δ peak, passing through the dip region. Although many studies have been devoted to particular energy regions of the spectrum, this is the first work, to our knowledge, which ranges this wide energy spectrum. The $1N$ knockout channel, the virtual photon absorption by pairs or trios of particles, the pion production plus exchange currents mechanisms tied to the $(\gamma^*, 2\pi)$ channel and which contribute to $(\gamma^*, NN\pi)$ or (γ^*, NNN) channels are explicitly accounted for in the model. Besides, effects which have been found important in earlier works, like polarization, renormalization of Δ properties in a nuclear medium, FSI effects through the use of spectral functions and meson exchange currents are also considered.

The model can be also used as starting point to evaluate differential cross sections for the $(e, e'N)$, $(e, e'NN)$, $(e, e'\pi)$ and $(e, e'N\pi)$ reactions [92]. There, a Monte Carlo simulation method, in which the probabilities for the different steps have been evaluated microscopically before using quantum mechanical many body techniques, is used to deal with the multichannel problem in the final state of the (e, e') reaction.

5 Inclusive Neutrino-Nucleus Scattering at Intermediate Energies

The inclusive cross section for the process $\nu_\ell(k) + A_Z \to \ell^-(k') + X$ is determined by the W gauge boson selfenergy in the nuclear medium [17, 21], and in particular for the different modes in which it can be absorbed.[9] The formalism used in these two references is an extension of that reviewed in the previous section for the case of inclusive electron-nucleus scattering. The major differences arise from the contributions due to the axial interaction of the intermediate gauge boson (W or Z) with nucleons and pions, and we refer the reader to these two references for further details. We will focus here in the so-called MiniBooNE M_A puzzle.

5.1 MiniBooNE M_A Puzzle

The most relevant W gauge boson absorption modes in nuclei are: the absorption by one nucleon, or by a pair of correlated nucleons that are exchanging virtual mesons (π, ρ, ...), or the excitation of a Δ or a higher energy resonance, etc. (see Fig. 31). As mentioned in the introduction, in most theoretical works QE is used for processes where the gauge boson W is absorbed by just one nucleon, which together with a lepton is emitted (see Fig. 31a). In what follows, we will refer to this contribution as *genuine* QE. However, the recent MiniBooNE CCQE data [3] include events in which only a muon is detected (QE-like events). This data selection is adopted because ejected nucleons are not detected in that experiment. As already discussed in the introduction of this chapter, the QE-like sample does not include events with pions coming off the nucleus, since they will give rise to additional leptons after their decay (see Fig. 31c). However, this event-sample includes multinucleon events, as those displayed in Fig. 31e, where the gauge boson is absorbed by two interacting nucleons (in the many body language, this amounts to the excitation of a 2p2h nuclear component). These mechanisms populate the so called dip region in electron scattering (see Sect. 4.2.4) located between the QE and the Δ peaks (see Fig. 29). On the other hand, other events like real pion production followed by its absorption should be also included in the QE-like sample, though the MiniBooNE analysis Monte Carlo corrects for those. Here, there is a subtlety that is worth to comment in some detail. Let us pay attention to processes like the one depicted in the bottom panel of Fig. 31c, but when the pion is off-shell instead of being on the mass-shell. In any of these processes, the *virtual* pion, that is produced in the first step, will be necessarily absorbed by a second nucleon, and thus the process should be classified/cataloged as a two nucleon W absorption mechanism (Fig. 31e). Hence, events originated by these kind of processes, which populate the dip region, do not contribute to the genuine QE cross section, but they do to the cross section measured

[9] Neutral current driven QE processes were studied in [65].

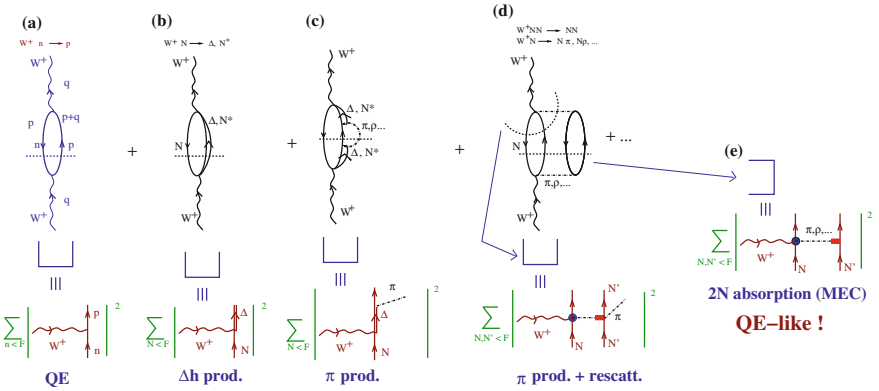

Fig. 31 Diagrammatic representation of some diagrams contributing to the W-selfenergy and their connection with different absorption modes of the gauge boson in the nuclear medium

in the MiniBooNE experiment. After this discussion, we draw a first important conclusion: the MiniBooNE CCQE data [3] cannot be directly compared to most of the previous theoretical calculations, in which only the one-body genuine QE contribution was usually considered. This was first pointed out by M. Martini et al. [19, 20]. Indeed, the absolute values of the CCQE cross section reported in [3] are too large as compared to the consensus of theoretical predictions for the genuine QE contribution [15]. Thus, the cross section per nucleon on ^{12}C is clearly larger than for free nucleons, and a fit, using a relativistic Fermi gas model, to the data led to an axial mass, $M_A = 1.35 \pm 0.17$ GeV [3] , much larger than the previous world average (≈ 1.03 GeV). Similar results have been later obtained analyzing MiniBooNE data with more sophisticated treatments of the nuclear effects that work well in the study of electron scattering [13, 93, 94].

In what follows, we present results from a microscopic calculation [17, 21] of the CCQE-like 2D cross section $d\sigma/dT_\mu d\cos\theta_\mu$. There are no free parameters in the description of nuclear effects, since they were fixed in previous studies of photon, electron, and pion interactions with nuclei [24, 30, 34, 35]. We approximate the CCQE-like cross section by the sum of the genuine QE contribution (Fig. 31a) and that induced by 2p2h mechanisms (Fig. 31e), for which the gauge boson is being absorbed by two or more nucleons without producing pions.

5.2 RPA Effects in QE Processes

The genuine QE contribution was studied in [17] incorporating several nuclear effects.[10] The main one is the medium polarization (RPA), that accounts for the

[10] Theoretical uncertainties of the model are estimated in [95], where the deviations of the predictions of the many body framework of [17] from those obtained within a simple Fermi gas model are also quantified.

change of the electroweak coupling strengths, from their free nucleon values, due to the presence of strongly interacting nucleons. Indeed, the quenching of axial current is a well-established phenomenon. Muon capture in nuclei, reviewed in Sect. 3, constitutes a clear example of these strong renormalization effects. The RPA re-summation accounts for the medium polarization effects in the 1p1h contribution (Fig. 31a) to the W selfenergy by substituting it by a collective response as shown diagrammatically in the top left panel of Fig. 32. The underline physics is the same as that discussed above in the study of muon capture in nuclei (Fig. 13) or the inclusive electron scattering reaction at the QE (right panel of Fig. 17) and Δ (Fig. 23) peaks and in the dip region (Fig. 26). Evaluating these effects, requires of an in medium baryon-baryon effective force, that within our model includes Δ-hole degrees of freedom, short range correlations and explicit π and ρ meson exchanges in the vector-isovector channel, as depicted in Fig. 11 and discussed in Sect. 2.3. RPA effects are important, as can be also appreciated in Fig. 32. In the top right panel, we show results [18] for the genuine QE contribution from our model (labeled as IFIC) for the CC quasielastic $\nu_\mu - {}^{12}$C double differential cross sections convoluted with the MiniBooNE flux. There, we also display results from the model of M. Martini et al. (labeled as Lyon) taken from [96]. The predictions of both groups for this genuine QE contribution, with and without RPA effects, turn out to be in a quite good agreement. We would finally like to remark that the RPA corrections strongly decrease as the neutrino energy increases, while they strongly modify the q^2-differential distributions at low neutrino energies, as can be appreciated in the left and right bottom panels of Fig. 32, respectively.

5.3 2p2h Mechanisms

Two body absorption or multinucleon mechanisms, together with the important Δ resonance contributions were studied in great detail in [21]. The model is fully microscopical and includes one, two, and even three-nucleon mechanisms, as well as the excitation of Δ isobars. The scheme runs in parallel to that outlined in Sects. 4.2.3–4.2.5 for the case of the inclusive electron scattering. As mentioned above, axial driven interaction mechanisms need to be considered now, together with the interferences of these new terms with those mediated by the vector current. The microscopic evaluation of the set of equivalent diagrams to those depicted in Figs. 20, 24, 25 and 26 requires a realistic model for the $WN \to N\pi$ reaction in the free space.

Theoretical studies of weak pion production off the nucleon at intermediate energies (see for instance the pioneering works of [97–99]) have highlighted the important role of baryon resonance excitation, predominantly the $\Delta(1232)3/2^+$. The weak nucleon-to-$\Delta(1232)$ transition current can be written in terms of vector and axial form factors, C_{3-5}^V and C_{3-6}^A in the notation of [99], for which is usual to employ empirical parametrizations. The role of heavier resonances has also been investigated although the available experimental information about the axial sector is very limited. Among these states, only the $N(1520)3/2^-$ appears to be relevant for neutrino

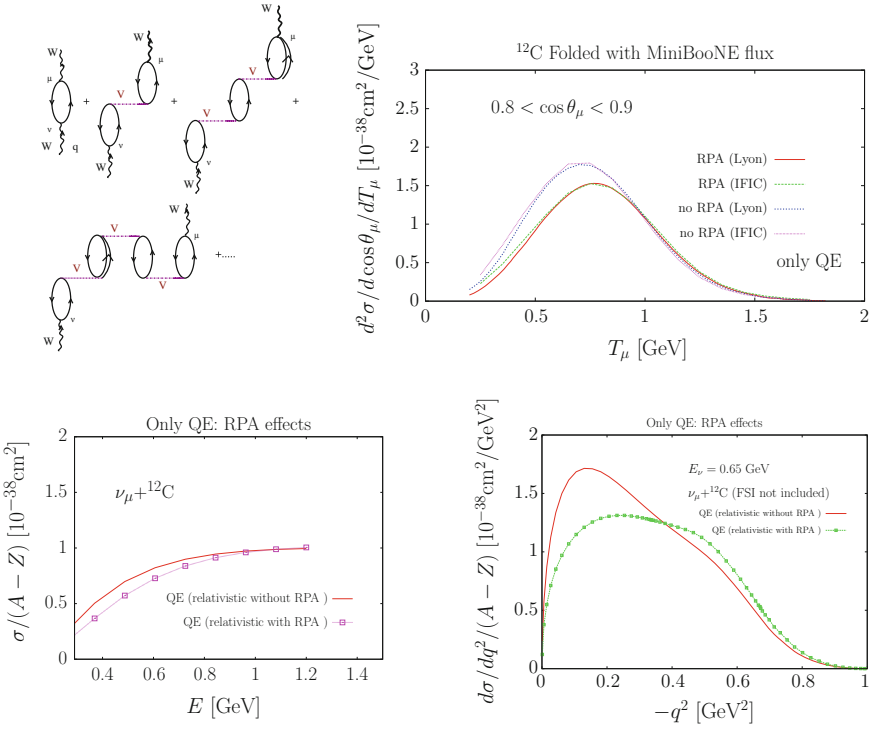

Fig. 32 *Top left* Set of irreducible diagrams responsible for the polarization (RPA) effects in the 1p1h contribution to the W self-energy. *Top right* MiniBooNE flux-averaged $\nu_\mu - ^{12}$C double differential cross section per neutron for $0.8 < \cos\theta_\mu < 0.9$ as a function of the muon kinetic energy. The *bottom plots* correspond to different theoretical predictions for muon neutrino CCQE total cross section off ^{12}C as a function of the neutrino energy (*left*) and q^2 (*right*), obtained from the relativistic model of [17]. In all cases $M_A \sim 1.05\,\text{GeV}$

energies below 1.5 GeV [100]. Non resonant electroweak amplitudes have also been extensively considered, similar to those shown in Fig. 20 for the case of electrons. As pointed out in [101], these terms are not only demanded but, close to threshold, fully fixed by chiral symmetry. Away from threshold, these amplitudes are usually modeled using phenomenologically parametrized nucleon form factors, introduced in a way that respects both the conservation of the vector current and the partial conservation of the axial current (PCAC). The evaluation of the multinucleon mechanisms carried out in [21] uses the model derived in [101], where non-resonant amplitudes evaluated from the leading contributions of the SU(2) chiral Lagrangian, supplemented with empirical parametrizations of the nucleon form factors, were considered alongside with the $\Delta(1232)$ excitation. The vector form factors in the $N\Delta$ vertex come from helicity amplitudes extracted in the analysis of electron scattering data [102]. The vector current part of the model reduces to that used in Sect. 4 and depicted in the right panel of Fig. 20. The most important among the axial form factors is C_5^A, which

appears at leading order in an expansion of the hadronic tensor in the four-momentum transfer q^2. Assuming the pion pole dominance of the pseudoscalar form factor C_6^A, it can be related to C_5^A owing to PCAC. For the sub-leading $C_{3,4}^A$ form factors, the Adler's parametrizations [97, 98] were adopted: $C_3^A = 0$, $C_4^A = -C_5^A/4$. The available bubble-chamber data on pion production induced by neutrinos on deuterium, taken at Argonne and Brookhaven National Laboratories (ANL and BNL) [103, 104] are quite insensitive to the values of these form factors [105]. With the aim of extending the model of [101] towards higher energies, the $N(1520)$ intermediate state was added in [106] using the transition form factors introduced in [100]. A simultaneous fit to both ANL and BNL data samples including independent overall flux normalization uncertainties for each experiment, as suggested in [107], and considering deuterium-target corrections obtained $C_5^A(0) = 1.00 \pm 0.11$ [105], 2σ below the Goldberger-Treiman's theorem (GTT) prediction. The model has been recently improved by imposing in [74] by Watson's theorem [108] to the dominant vector and axial multipoles, which has led to new $C_5^A(0)$ values in better agreement with the prediction from the off-diagonal GTT.

The consideration of the 2p2h nuclear excitations in [21], using the model of [101, 105] for the $WN \to N\pi$ reaction, allows to describe [18] the MiniBooNE CCQE-like flux averaged 2D cross section $d\sigma/dT_\mu/d\cos\theta_\mu$ [3] with values of M_A around 1 GeV. This can be seen in Fig. 33, where we also show results for antineutrinos. This is reassuring from the theoretical point of view and more satisfactory than the situation envisaged by some other works that described these CCQE-like data in terms of a larger value of M_A of around 1.3–1.4 GeV (see the discussion in [9]), difficult to accommodate with our current knowledge on the nucleon axial radius. However, not only multinucleon mechanisms, but also RPA corrections turn out to be essential to obtain axial masses consistent with the world average. This can be appreciated in Fig. 34, where we see that RPA strongly decreases the cross section at low energies, while multinucleon mechanisms accumulate their contribution at low muon energies and compensate for that depletion. Therefore, the final picture is that of a delicate balance between a dominant single nucleon scattering, corrected by collective effects, and other mechanisms that involve directly two or more nucleons. Both effects can be mimicked by using a large M_A value (red lines in the neutrino panels of Fig. 33).The work of [96] also include multinucleon mechanisms and find a good description of the 2D MiniBooNE data. The findings of [96] corroborate the relevant role played by the 2p2h mechanisms to describe the MiniBooNE data. However the models used in [18] and [96] differ differ considerably in the size (about a factor of two) of the multinucleon effects. There exist indeed some important differences which amount to a more comprehensive inclusion of mechanisms in the scheme presented here and some approximations used in the calculations of [96]. A more detailed discussion on these differences can be found in [21, 110]. We would also like to point out that the simple phenomenological approach adopted in [111] to account for the 2p2h effects also reinforces the picture that emerges from [18, 96]. Yet, a partial microscopical calculation of the 2p2h contributions to the CCQE cross section has been also presented in [112] and [113], for neutrino and antineutrino

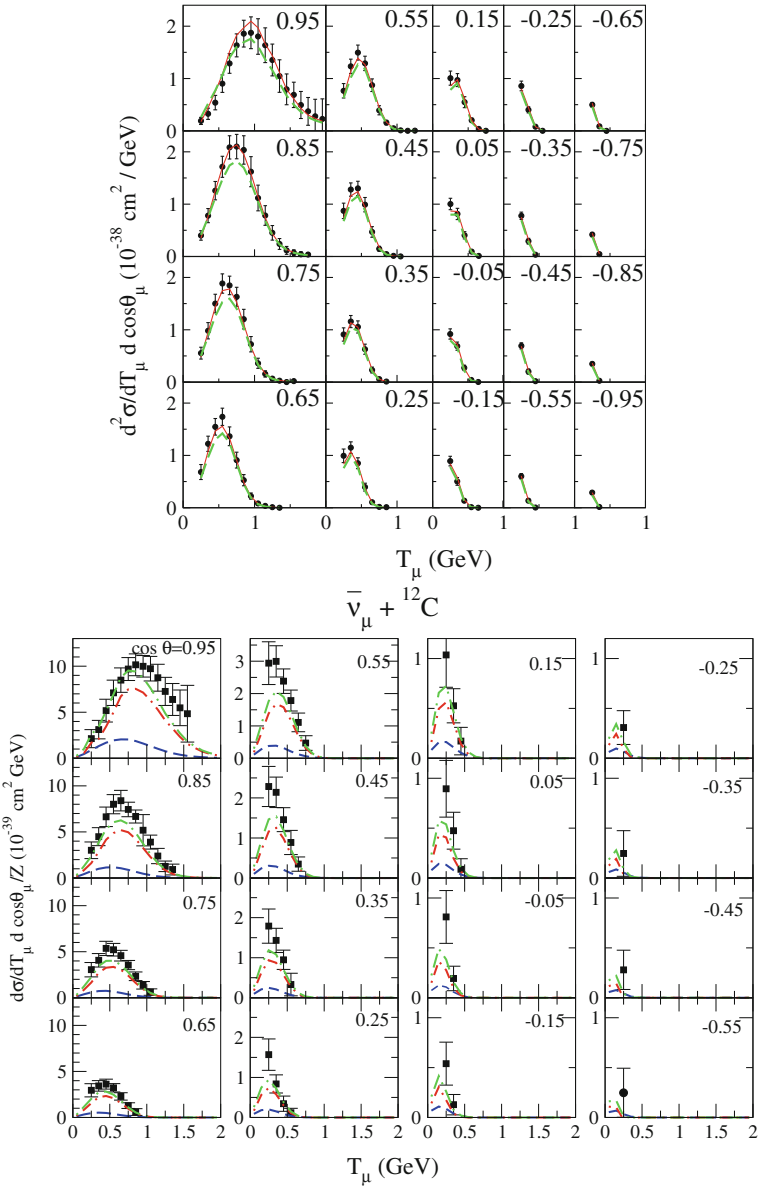

Fig. 33 *Top* (*Bottom*) Muon angle and energy neutrino (antineutrino) distribution $d\sigma/dT_\mu/d\cos\theta_\mu$ per neutron (proton) on a ^{12}C target folded with the MiniBooNE ν_μ ($\bar{\nu}_\mu$) flux. *Different panels* correspond to the various angular bins (labeled by the central value of the cosinus). Data are taken from [3, 6], with errors that only account for the shape uncertainties. The *green-dashed lines* are the full model predictions including QE (relativistic and with RPA) and 2p2h mechanisms from [18, 109] (calculated with $M_A = 1.05$ GeV). Red-solid lines in the top panels (ν) stand for the best fit ($M_A = 1.32$ GeV) results from the model without RPA and without multinucleon mechanisms. Finally in the *bottom panels* ($\bar{\nu}$) the *red-dash-dotted curve* corresponds to QE and the *blue-dashed curve* to 2p2h events

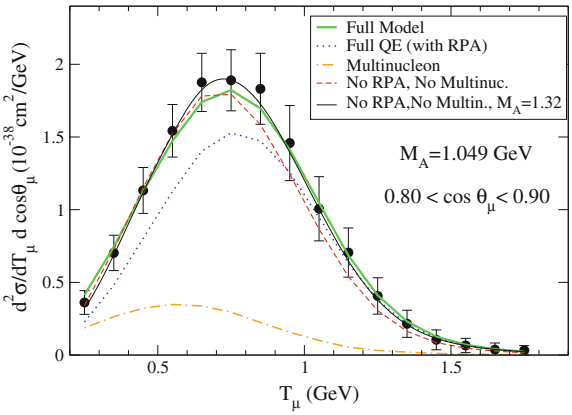

Fig. 34 $\nu_\mu + {}^{12}$C cross sections. Muon angle and energy distribution per neutron for the $0.80 < \cos\theta_\mu < 0.90$ bin (see [18]). All theoretical results have been obtained with the model of [17, 21] and $M_A = 1.05$ GeV, except those corresponding to the $M_A = 1.32$ GeV curve that have been also re-scaled by an overall factor 0.9, as obtained in the analysis of [18]

induced reactions, respectively. In these works, the contribution of the vector meson exchange currents in the 2p2h sector is added to the QE neutrino or antineutrino cross section predictions deduced from a phenomenological model based on the super-scaling behavior of electron scattering data. In [114], and for the neutrino case, the SuSA+2p2h results were also compared with those obtained from a relativistic mean field approach. Although, all these schemes do not account for the axial part of the 2p2h effects yet, their results also corroborate that 2p2h meson exchange currents play an important role in both CCQE-like neutrino and antineutrino scattering, and that they may help to resolve the controversy on the nucleon axial mass raised by the recent MiniBooNE data.

A final remark concerns to the importance of 2p2h effects in antineutrino reactions as compared to neutrino ones. In the model presented here the relative importance of the 2p2h channel is somehow larger for antineutrinos [109]. A similar trend, although with a stronger reduction, has been found by Amaro et al. [113] in the SuSA approximation. However, other works like [115], which reaches agreement with MiniBooNE QE neutrino data by modifying the magnetic form factors of the bound nucleons, and [20] lead to an enhancement of the effect for antineutrino induced reactions.

5.4 Neutrino–Energy Reconstruction and the Shape of the CCQE-Like Total Cross Section

The relevance of the multinucleon mechanisms has some unwanted consequences. Obviously, the neutrino energy reconstruction, based on the QE kinematics is not so reliable [14, 116–118] and that implies larger systematic uncertainties in the neutrino oscillation experiments analysis. In general, the energy of the neutrino that has originated an event is unknown, and it is common to define a reconstructed neutrino energy $E_{\rm rec}$, obtained from the measured angle (θ_ℓ) and three-momentum ($\mathbf{p}_\ell$) of the outgoing charged lepton ℓ, as

$$E_{\rm rec} = \frac{M_N E_\ell - m_\ell^2/2}{M_N - E_\ell + |\mathbf{p}_\ell| \cos\theta_\ell} \tag{82}$$

which will correspond to the energy of a neutrino that emits a lepton, of mass m_ℓ and energy E_ℓ, and a gauge boson W that is being absorbed by a nucleon of mass M_N at rest. The usual reconstruction procedure assumes that we are dealing with a genuine quasielastic event on a nucleon at rest.

Each event contributing to the flux averaged double differential cross section $d\sigma/dE_\ell d\cos\theta_\ell$ defines unambiguously a value of $E_{\rm rec}$. The actual ("true") energy, E, of the neutrino that has produced the event will not be exactly $E_{\rm rec}$. Actually, for each $E_{\rm rec}$, there exists a distribution of true neutrino energies that could give rise to events whose muon kinematics would lead to the given value of $E_{\rm rec}$. In the case of genuine QE events, this distribution is sufficiently peaked around the true neutrino energy to make the algorithm in (82) accurate enough to study the neutrino oscillation phenomenon [119] or to extract neutrino flux unfolded CCQE cross sections from data (assuming that the neutrino flux spectrum is known) [14, 117]. However, and due to the large importance of the 2p2h events, in the case of CCQE-like events, there are appear a long tail in the distribution of true energies associated to each $E_{\rm rec}$ that makes unreliable the use of (82). The effects of the inclusion of multinucleon processes on the energy reconstruction have been investigated within the present model in [14], finding results in a qualitative agreement with those described in [117]. In [14], it is also studied in detail the ^{12}C unfolded neutrino CCQE-like cross section published in [3]. Indeed, it is shown there, that it is not a very clean observable, because the unfolding procedure itself is model dependent and assumes that the events are purely QE. Moreover, it is also shown the MiniBooNE published cross section differs from the real one $\sigma(E)$. This is illustrated in Fig. 35, where different predictions from the present model, together with the CCQE-like MiniBooNE data are depicted. The theoretical results are obtained from the relativistic models of [17] and [21], for the genuine QE and multinucleon contributions, respectively. In al cases M_A is set to 1.05 GeV. First, we see that the theoretical prediction $\sigma^{\rm QE+2p2h}$ does not correctly reproduce the neutrino-energy shape of the published data. The 2p2h contributions clearly improve the description of the data, which are totally missed by the QE prediction. Though the model provides a reasonable description, we observe

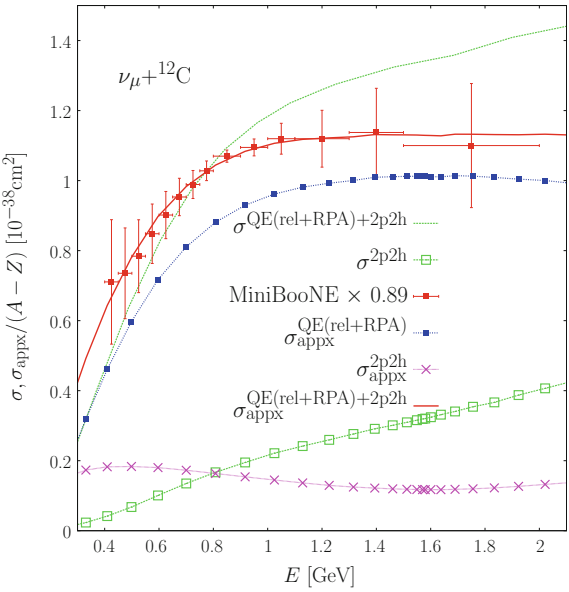

Fig. 35 ν_μ+^{12}C cross sections. Theoretical (σ) and approximate (σ_{appx}) CCQE-like integrated cross sections as a function of the ν energy (see [14]). The MiniBooNE data [3] and errors (*shape)* have been re-scaled by a factor 0.9, as a result of the analysis carried out in [18]. All theoretical results have been obtained with the model of [17, 21] and $M_A = 1.05$ GeV

a sizable excess of low energy neutrinos in the data. The unfolding procedure used in [3] (see [14] for some details) does not appreciably distort the genuine QE events, and as can be appreciated in Fig. 35, $\sigma_{\rm appx}(E)$ is an excellent approximation to the real $\sigma(E)$ cross section in that case. However, the situation is drastically different for the 2p2h contribution. It turns out that $\sigma^{\rm 2p2h}_{\rm appx}(E)$ (result obtained after the unfolding procedure) is a poor estimate of the actual multinucleon mechanism contribution $\sigma^{\rm 2p2h}(E)$. We also observe in Fig. 35 that the MiniBooNE CCQE-like data compare rather well with $\sigma_{\rm appx}$, quantity obtained after implementing the unfolding procedure presumably carried out in [3], but that however, appreciably differs from the actual cross section σ. Therefore, we conclude the MiniBooNE unfolded cross section exhibits an excess (deficit) of low (high) energy neutrinos, which is an artifact of the unfolding process that ignores multinucleon mechanisms.

5.5 *Concluding Remarks*

In summary, we have analyzed the MiniBooNE CCQE double differential cross-section data using the theoretical model of [17, 21, 65]. The model, that starts from a relativistic local Fermi gas description of the nucleus, includes RPA correlations and multinucleon effects. The same model is quite successful in the analysis of nuclear reactions with electron, photon and pion probes and contains no additional free parameters. RPA and multinucleon knockout have been found to be essential for the description of the data. The main conclusion is that MiniBooNE data are

fully compatible with former determinations of the nucleon axial mass, both using neutrino and electron beams in contrast with several previous analyses. Besides, we have found that the procedure commonly used to reconstruct the neutrino energy for quasielastic events from the muon angle and energy could be unreliable for a wide region of the phase space, due to the large importance of multinucleon events.

6 Conclusions

We have studied different problems of Nuclear Physics, apparently disconnected, but with a common link in their sensitivity to the spin-isospin part of the baryon-baryon interaction and to the peculiar way that this interaction is modified in a nuclear medium. We have reviewed the problem of the muon capture in nuclei, and have addressed the main features of the inclusive electron and neutrino-nucleus interaction at intermediate energies. In particular we have studied and offered a solution to the so-called MiniBooNE nucleon axial mass puzzle. The framework to deal with these problems has been Many Body Quantum Field Theory, which proves to be an ideal method to calculate efficiently and reliably most nuclear magnitudes, and which offers, through its diagrammatic method, an intuitive picture of the physical meaning of the magnitudes which are calculated.

Many other topics could have also been included, pion-nucleus reactions, scattering K^+-nucleus, Λ, $\Sigma-$hypernuclei, $\bar{p}$ annihilation in nuclei... with similar conclusions and success, but for reasons of space have not been considered here.

Acknowledgments This research has been supported by the Spanish Ministerio de Economía y Competitividad and European FEDER funds under the contracts FIS2011-28853-C02-02, FIS2014-51948-C2-1-P, FIS2014-57026-REDT and SEV-2014-0398 (MINECO), by Generalitat Valenciana under contract PROMETEOII/2014/0068 and by the EU HadronPhysics3 project, grant agreement no. 283286.

References

1. E. Fernandez-Martinez, D. Meloni, Importance of nuclear effects in the measurement of neutrino oscillation parameters. Phys. Lett. **B697**, 477–481 (2011). doi:10.1016/j.physletb.2011.02.043
2. Y. Nakajima et al., Measurement of inclusive charged current interactions on carbon in a few-GeV neutrino beam. Phys. Rev. **D83**, 012, 005 (2011). doi:10.1103/PhysRevD.83.012005
3. A. Aguilar-Arevalo et al., First measurement of the Muon neutrino charged current quasielastic double differential cross section. Phys. Rev. **D81**, 092, 005 (2010). doi:10.1103/PhysRevD.81.092005
4. A. Aguilar-Arevalo et al., Measurement of neutrino-induced charged-current charged pion production cross sections on mineral oil at $E_\nu \sim 1$ GeV. Phys. Rev. **D83**, 052, 007 (2011). doi:10.1103/PhysRevD.83.052007

5. A. Aguilar-Arevalo et al., Measurement of ν_μ-induced charged-current neutral pion production cross sections on mineral oil at $E_\nu \in 0.5 - 2.0$ GeV. Phys. Rev. **D83**, 052, 009 (2011). doi:10.1103/PhysRevD.83.052009
6. A. Aguilar-Arevalo et al., First measurement of the Muon anti-neutrino double-differential charged current quasi-elastic cross section. Phys. Rev. **D88**, 032, 001 (2013). doi:10.1103/PhysRevD.88.032001
7. L. Alvarez-Ruso, Y. Hayato, J. Nieves, Progress and open questions in the physics of neutrino cross sections at intermediate energies. New J. Phys. **16**, 075, 015 (2014). doi:10.1088/1367-2630/16/7/075015
8. H. Gallagher, G. Garvey, G.P. Zeller, Neutrino-nucleus interactions. Ann. Rev. Nucl. Part. Sci. **61**, 355–378 (2011). doi:10.1146/annurev-nucl-102010-130255
9. J.G. Morfin, J. Nieves, J.T. Sobczyk, Recent developments in neutrino/antineutrino—nucleus interactions. Adv. High Energy Phys. **2012**, 934, 597 (2012). doi:10.1155/2012/934597
10. A. Bodek, S. Avvakumov, R. Bradford, H.S. Budd, Vector and axial nucleon form factors: a duality constrained parameterization. Eur. Phys. J. **C53**, 349–354 (2008). doi:10.1140/epjc/s10052-007-0491-4
11. V. Bernard, N. Kaiser, U.G. Meissner, Measuring the axial radius of the nucleon in pion electroproduction. Phys. Rev. Lett. **69**, 1877–1879 (1992). doi:10.1103/PhysRevLett.69.1877
12. V. Lyubushkin et al., A study of quasi-elastic muon neutrino and antineutrino scattering in the NOMAD experiment. Eur. Phys. J. **C63**, 355–381 (2009). doi:10.1140/epjc/s10052-009-1113-0
13. O. Benhar, P. Coletti, D. Meloni, Electroweak nuclear response in quasi-elastic regime. Phys. Rev. Lett. **105**, 132, 301 (2010). doi:10.1103/PhysRevLett.105.132301
14. J. Nieves, F. Sanchez, I. Ruiz Simo, M. Vicente Vacas, Neutrino energy reconstruction and the shape of the CCQE-like total cross section. Phys. Rev. **D85**, 113, 008 (2012). doi:10.1103/PhysRevD.85.113008
15. S. Boyd, S. Dytman, E. Hernandez, J. Sobczyk, R. Tacik, Comparison of models of neutrino-nucleus interactions. AIP Conf. Proc. **1189**, 60–73 (2009). doi:10.1063/1.3274191
16. R.J. Blin-Stoyle, Fundamental Interactions and the Nucleus (1973)
17. J. Nieves, J.E. Amaro, M. Valverde, Inclusive quasi-elastic neutrino reactions. Phys. Rev. **C70**, 055, 503 (2004). doi:10.1103/PhysRevC.70.055503, 10.1103/PhysRevC.72.019902
18. J. Nieves, I. Ruiz Simo, M. Vicente Vacas, The nucleon axial mass and the MiniBooNE quasielastic neutrino-nucleus scattering problem. Phys. Lett. **B707**, 72–75 (2012). doi:10.1016/j.physletb.2011.11.061
19. M. Martini, M. Ericson, G. Chanfray, J. Marteau, A unified approach for nucleon knock-out, coherent and incoherent pion production in neutrino interactions with nuclei. Phys. Rev. **C80**, 065, 501 (2009). doi:10.1103/PhysRevC.80.065501
20. M. Martini, M. Ericson, G. Chanfray, J. Marteau, Neutrino and antineutrino quasielastic interactions with nuclei. Phys. Rev. **C81**, 045, 502 (2010). doi:10.1103/PhysRevC.81.045502
21. J. Nieves, I. Ruiz Simo, M. Vicente Vacas, Inclusive charged–current neutrino–nucleus reactions. Phys. Rev. **C83**, 045, 501 (2011). doi:10.1103/PhysRevC.83.045501
22. C. Albertus, J.E. Amaro, J. Nieves, What does free space Lambda-Lambda interaction predict for Lambda-Lambda hypernuclei? Phys. Rev. Lett. **89**, 032, 501 (2002). doi:10.1103/PhysRevLett.89.032501
23. C. Albertus, J.E. Amaro, J. Nieves, Pionic decay of Lambda hypernuclei in a continuum shell model. Phys. Rev. **C67**, 034, 604 (2003). doi:10.1103/PhysRevC.67.034604
24. R. Carrasco, E. Oset, Interaccion of real photons with nuclei from 100-MeV to 500-MeV. Nucl. Phys. **A536**, 445–508 (1992). doi:10.1016/0375-9474(92)90109-W
25. P. Fernandez de Cordoba, J. Nieves, E. Oset, M. Vicente-Vacas, Coherent pion production in the (He-3, t) reaction in nuclei. Phys. Lett. **B319**, 416–420 (1993). doi:10.1016/0370-2693(93)91744-8
26. P. Fernandez de Cordoba, E. Oset, Projectile and target delta excitation in the (He-3, t) and (He-3, He-3) reactions. Nucl. Phys. **A544**, 793–810 (1992). doi:10.1016/0375-9474(92)90541-Q

27. P. Fernandez de Cordoba, E. Oset, Semi phenomenological approach to nucleon properties in nuclear matter. Phys. Rev. **C46**, 1697–1709 (1992). doi:10.1103/PhysRevC.46.1697
28. P. Fernandez de Cordoba, Y. Ratis, E. Oset, J. Nieves, M.J. Vicente-Vacas, B. Lopez-Alvaredo, F. Gareev, Projectile delta excitation in alpha—proton scattering. Nucl. Phys. **A586**, 586–606 (1995). doi:10.1016/0375-9474(94)00815-5
29. C. Garcia-Recio, J. Nieves, E. Oset, Pion cloud contribution to K+ nucleus scattering. Phys. Rev. **C51**, 237–251 (1995). doi:10.1103/PhysRevC.51.237
30. A. Gil, J. Nieves, E. Oset, Many body approach to the inclusive (e, e-prime) reaction from the quasielastic to the delta excitation region. Nucl. Phys. **A627**, 543–598 (1997). doi:10.1016/S0375-9474(97)00513-7
31. S. Hirenzaki, P. Fernandez de Cordoba, E. Oset, Roper excitation in alpha—proton scattering. Phys. Rev. C **53**, 277–284 (1996). doi:10.1103/PhysRevC.53.277
32. S. Hirenzaki, J. Nieves, E. Oset, M. Vicente-Vacas, Coherent pi0 electroproduction. Phys. Lett. B **304**, 198–202 (1993). doi:10.1016/0370-2693(93)90282-M
33. J. Nieves, E. Oset, Pionic decay of lambda hypernuclei. Phys. Rev. **C47**, 1478–1488 (1993). doi:10.1103/PhysRevC.47.1478
34. J. Nieves, E. Oset, C. Garcia-Recio, A theoretical approach to pionic atoms and the problem of anomalies. Nucl. Phys. **A554**, 509–553 (1993). doi:10.1016/0375-9474(93)90245-S
35. J. Nieves, E. Oset, C. Garcia-Recio, Many body approach to low-energy pion nucleus scattering. Nucl. Phys. **A554**, 554–579 (1993). doi:10.1016/0375-9474(93)90246-T
36. E. Oset, P. Fernandez de Cordoba, J. Nieves, A. Ramos, L.L. Salcedo, A review on mesonic decay of lambda hypernuclei. Prog. Theor. Phys. Suppl. **117**, 461–476 (1994). doi:10.1143/PTPS.117.461
37. E. Oset, P. Fernandez de Cordoba, L.L. Salcedo, R. Brockmann, Decay modes of Σ and Λ hypernuclei. Phys. Rept. **188**, 79 (1990). doi:10.1016/0370-1573(90)90091-F
38. E. Oset, H. Toki, W. Weise, Pionic modes of excitation in nuclei. Phys. Rept. **83**, 281–380 (1982). doi:10.1016/0370-1573(82)90123-5
39. A.L. Fetter, J.D. Walecka, *Quantum Theory of Many-Particle Systems*. Dover (2003)
40. R.D. Mattuck, *A Guide to Feynman Diagrams in the Many Body Problem*, 2d edn. (1976)
41. F. Mandl, G. Shaw, Quantum field theory (1985), http://eu.wiley.com/WileyCDA/WileyTitle/productCd-0471496839.html
42. C. Itzykson, J.B. Zuber, Quantum field theory (1980), http://dx.doi.org/10.1063/1.2916419
43. M. Ericson, Nuclear critical opalescence. Nucl. Phys. **A335**, 309–314 (1980). doi:10.1016/0375-9474(80)90186-4
44. J.D. Bjorken, S.D. Drell, *Relativistic Quantum Fields* (1965)
45. W.M. Alberico, M. Ericson, A. Molinari, Quenching and hardening in the transverse quasi-elastic peak. Nucl. Phys. **A379**, 429 (1982). doi:10.1016/0375-9474(82)90007-0
46. A. Faessler, F. Fernandez, G. Lubeck, K. Shimizu, The quark model and the nature of the repulsive core of the nucleon nucleon interaction. Phys. Lett. **B112**, 201–205 (1982). doi:10.1016/0370-2693(82)90961-3
47. M. Oka, K. Yazaki, Nuclear force in a quark model. Phys. Lett. **B90**, 41–44 (1980). doi:10.1016/0370-2693(80)90046-5
48. K. Holinde, Two nucleon forces and nuclear matter. Phys. Rept. **68**, 121–188 (1981). doi:10.1016/0370-1573(81)90188-5
49. G.E. Brown, A.D. Jackson, *The Nucleon-Nucleon Interaction* (1979)
50. G.E. Brown, *Many Body Problems* (1972)
51. H.C. Chiang, E. Oset, P. Fernandez de Cordoba, Muon capture revisited. Nucl. Phys. **A510**, 591 (1990). doi:10.1016/0375-9474(90)90350-U
52. H. Primakoff, Theory of muon capture. Rev. Mod. Phys. **31**, 802–822 (1959). doi:10.1103/RevModPhys.31.802
53. J.E. Amaro, C. Maieron, J. Nieves, M. Valverde, Equivalence between local fermi gas and shell models in inclusive muon capture from nuclei. Eur. Phys. J. **A24**, 343–353 (2005). doi:10.1140/epja/i2005-10034-2

54. N. Auerbach, B.A. Brown, Weak interaction rates involving C-12, N-14, and O-16. Phys. Rev. **C65**, 024, 322 (2002). doi:10.1103/PhysRevC.65.024322
55. A.C. Hayes, I.S. Towner, Shell model calculations of neutrino scattering from C-12. Phys. Rev. **C61**, 044,603 (2000). doi:10.1103/PhysRevC.61.044603
56. N. Jachowicz, K. Heyde, J. Ryckebusch, S. Rombouts, Continuum random phase approximation approach to charged current neutrino nucleus scattering. Phys. Rev. **C65**, 025, 501 (2002). doi:10.1103/PhysRevC.65.025501
57. C.W. Kim, S.L. Mintz, Total neutrino scattering cross-sections and total muon capture rates in nuclei. Phys. Rev. **C31**, 274–277 (1985). doi:10.1103/PhysRevC.31.274
58. E. Kolbe, K. Langanke, G. Martinez-Pinedo, P. Vogel, Neutrino nucleus reactions and nuclear structure. J. Phys. **G29**, 2569–2596 (2003). doi:10.1088/0954-3899/29/11/010
59. E. Kolbe, K. Langanke, P. Vogel, Muon capture, continuum random phase approximation and in-medium renormalization of the axial vector coupling constant. Phys. Rev. **C50**, 2576–2581 (1994). doi:10.1103/PhysRevC.50.2576
60. E. Kolbe, K. Langanke, P. Vogel, Muon capture on nuclei with N > Z, random phase approximation, and in-medium renormalization of the axial vector coupling constant. Phys. Rev. **C62**, 055, 502 (2000). doi:10.1103/PhysRevC.62.055502
61. N.C. Mukhopadhyay, Nuclear muon capture. Phys. Rept. **30**, 1–144 (1977). doi:10.1016/0370-1573(77)90073-4
62. N.C. Mukhopadhyay, H.C. Chiang, S.K. Singh, E. Oset, Inclusive muon capture in light nuclei. Phys. Lett. B **434**, 7–13 (1998). doi:10.1016/S0370-2693(98)00790-4
63. J. Navarro, J. Bernabeu, J.M.G. Gomez, J. Martorell, Total muon capture rates for N=Z nuclei in the 1P shell. Nucl. Phys. A **375**, 361–380 (1982). doi:10.1016/0375-9474(82)90019-7
64. V.G. Nguyen, N. Auerbach, A.Z. Mekjian, Selfconsistent random phase approximation calculations of muon capture rates. Phys. Rev. Lett. **46**, 1444–1447 (1981). doi:10.1103/PhysRevLett.46.1444
65. J. Nieves, M. Valverde, M. Vicente Vacas, Inclusive nucleon emission induced by quasi-elastic neutrino-nucleus interactions. Phys. Rev. **C73**, 025, 504 (2006). doi:10.1103/PhysRevC.73.025504
66. T. Suzuki, D.F. Measday, J.P. Roalsvig, Total nuclear capture rates for negative muons. Phys. Rev. **C35**, 2212 (1987). doi:10.1103/PhysRevC.35.2212
67. P.J. Mulders, Modifications of nucleons in nuclei and other consequences of the quark substructure. Phys. Rept. **185**, 83–169 (1990). doi:10.1016/0370-1573(90)90086-H
68. E. Amaldi, S. Fubini, G. Furlan, Pion electroproduction. Electroproduction at low-energy and hadron form-factors. Springer Tracts Mod. Phys. **83**, 1–162 (1979). doi:10.1007/BFb0048209
69. C. Ciofi degli Atti, S. Liuti, S. Simula, Nucleon spectral function in complex nuclei and nuclear matter and inclusive quasielastic electron scattering. Phys. Rev. **C41**, R2474–R2478 (1990). doi:10.1103/PhysRevC.41.R2474
70. J.E. Amaro, A.M. Lallena, J. Nieves, Radiative pion capture in nuclei: a continuum shell model approach. Nucl. Phys. **A623**, 529–547 (1997). doi:10.1016/S0375-9474(97)00187-5
71. J. Speth, V. Klemt, J. Wambach, G. Brown, The influence of the π and ρ exchange potential on magnetic properties of nuclei. Nucl. Phys. **A343**, 382–416 (1980). doi:10.1016/0375-9474(80)90660-0
72. S. Nozawa, T.S.H. Lee, Electroproduction of pions on the nucleon. Nucl. Phys. **A513**, 511–542 (1990). doi:10.1016/0375-9474(90)90396-4
73. M. Olsson, Solutions of the multichannel unitarity equations describing the addition of a resonance and background: application to a pole model of photoproduction. Nucl. Phys. **B78**, 55 (1974). doi:10.1016/0550-3213(74)90115-1
74. L. Alvarez-Ruso, E. Hernandez, J. Nieves, M.J.V. Vacas, Watson's theorem and the $N\Delta(1232)$ axial transition. Phys.Rev. **D93**, 014016 (2016). doi:10.1103/PhysRevD.93.014016
75. P. Barreau et al., Deep Inelastic electron scattering from carbon. Nucl. Phys. **A402**, 515–540 (1983). doi:10.1016/0375-9474(83)90217-8
76. J.E. Amaro, M.B. Barbaro, J.A. Caballero, T.W. Donnelly, A. Molinari, Relativistic effects in electromagnetic nuclear responses in the quasielastic delta region. Nucl. Phys. **A657**, 161–186 (1999). doi:10.1016/S0375-9474(99)00334-6

77. J.E. Amaro, M.B. Barbaro, J.A. Caballero, T.W. Donnelly, A. Molinari, Gauge and Lorentz invariant one pion exchange currents in electron scattering from a relativistic fermi gas. Phys. Rept. **368**, 317–407 (2002). doi:10.1016/S0370-1573(02)00195-3
78. M. Anghinolfi et al., Quasielastic and inelastic inclusive electron scattering from an oxygen jet target. Nucl. Phys. **A602**, 405–422 (1996). doi:10.1016/0375-9474(96)00093-0
79. E. Bauer, On the role of the delta (1232) on the transverse nuclear response in the (e, e-prime) reaction. Nucl. Phys. **A637**, 243–279 (1998). doi:10.1016/S0375-9474(98)00235-8
80. G. Chanfray, J. Delorme, M. Ericson, A. Molinari, Quasielastic delta excitation in the charge response of the nucleus. Nucl. Phys. **A556**, 439–452 (1993). doi:10.1016/0375-9474(93)90371-4
81. D.B. Day et al., Inclusive electron nucleus scattering at high momentum transfer. Phys. Rev. **C48**, 1849–1863 (1993). doi:10.1103/PhysRevC.48.1849
82. M.J. Dekker, P.J. Brussaard, J.A. Tjon, Relativistic meson exchange currents in the dip region. Phys. Lett. **B266**, 249–254 (1991). doi:10.1016/0370-2693(91)91034-S
83. V. Gadiyak, V. Dmitriev, Nuclear response in electron scattering at high momentum transfer. Nucl. Phys. **A639**, 685–704 (1998). doi:10.1016/S0375-9474(98)00242-5
84. J.W. Van Orden, T.W. Donnelly, Mesonic processes in deep inelastic electron scattering from nuclei. Ann. Phys. **131**, 451–493 (1981). doi:10.1016/0003-4916(81)90038-5
85. E. Oset, L. Salcedo, Δ selfenergy in nuclear matter. Nucl. Phys. **A468**, 631–652 (1987). doi:10.1016/0375-9474(87)90185-0
86. A. Dellafiore, F. Lenz, F.A. Brieva, Particle-hole calculation of the longitudinal response function of C-12. Phys. Rev. **C31**, 1088–1104 (1985). doi:10.1103/PhysRevC.31.1088
87. J. Jourdan, Longitudinal response functions: the coulomb sum revisited. Phys. Lett. B **353**, 189–195 (1995). doi:10.1016/0370-2693(95)00581-5
88. J. Jourdan, Quasielastic response functions: the coulomb sum revisited. Nucl. Phys. A **603**, 117–160 (1996). doi:10.1016/0375-9474(96)00143-1
89. Z. Meziani, P. Barreau, M. Bernheim, J. Morgenstern, S. Turck-Chieze et al., Coulomb sum rule for Ca-40, Ca-48, and Fe-56 for |q (Vector)| = 550-MeV/c. Phys. Rev. Lett. **52**, 2130–2133 (1984). doi:10.1103/PhysRevLett.52.2130
90. Z.E. Meziani et al., Transverse response functions in deep inelastic electron scattering for CA-40, CA-48, and FE-56. Phys. Rev. Lett. **54**, 1233–1236 (1985). doi:10.1103/PhysRevLett.54.1233
91. A. Zghiche et al., Longitudinal and transverse responses in quasielastic electron scattering from Pb-208 and He-4. Nucl. Phys. **A572**, 513–559 (1994). doi:10.1016/0375-9474(94)90399-9. [Erratum: Nucl. Phys. A584,757(1995)]
92. A. Gil, J. Nieves, E. Oset, Inclusive (e, e-prime N), (e, e-prime N N), (e, e-prime pi): reactions in nuclei. Nucl. Phys. **A627**, 599–619 (1997). doi:10.1016/S0375-9474(97)00515-0
93. A. Butkevich, Analysis of flux-integrated cross sections for quasi-elastic neutrino charged-current scattering off ^{12}C at MiniBooNE energies. Phys. Rev. **C82**, 055, 501 (2010). doi:10.1103/PhysRevC.82.055501
94. C. Juszczak, J.T. Sobczyk, J. Zmuda, On extraction of value of axial mass from MiniBooNE neutrino quasi-elastic double differential cross section data. Phys. Rev. **C82**, 045, 502 (2010). doi:10.1103/PhysRevC.82.045502
95. M. Valverde, J.E. Amaro, J. Nieves, Theoretical uncertainties on quasielastic charged-current neutrino-nucleus cross sections. Phys. Lett. **B638**, 325–332 (2006). doi:10.1016/j.physletb.2006.05.053
96. M. Martini, M. Ericson, G. Chanfray, Neutrino quasielastic interaction and nuclear dynamics. Phys. Rev. **C84**, 055, 502 (2011). doi:10.1103/PhysRevC.84.055502
97. S.L. Adler, Photoproduction, electroproduction and weak single pion production in the (3,3) resonance region. Ann. Phys. **50**, 189–311 (1968). doi:10.1016/0003-4916(68)90278-9
98. J. Bijtebier, A comparison between Salin's and Adler's models for neutrino $\nu N \to \mu N^*$ reactions. Nucl. Phys. **B21**, 158–172 (1970)
99. C. Llewellyn Smith, Neutrino reactions at accelerator energies. Phys. Rept. **3**, 261–379 (1972). doi:10.1016/0370-1573(72)90010-5

100. T. Leitner, O. Buss, L. Alvarez-Ruso, U. Mosel, Electron- and neutrino-nucleus scattering from the quasielastic to the resonance region. Phys. Rev. **C79**, 034, 601 (2009). doi:10.1103/PhysRevC.79.034601
101. E. Hernandez, J. Nieves, M. Valverde, Weak pion production off the nucleon. Phys. Rev. **D76**, 033, 005 (2007). doi:10.1103/PhysRevD.76.033005
102. O. Lalakulich, E.A. Paschos, Resonance production by neutrinos. I. J = 3/2 resonances. Phys. Rev. **D71**, 074, 003 (2005). doi:10.1103/PhysRevD.71.074003
103. T. Kitagaki, H. Yuta, S. Tanaka, A. Yamaguchi, K. Abe et al., Charged current exclusive pion production in neutrino deuterium interactions. Phys. Rev. **D34**, 2554–2565 (1986). doi:10.1103/PhysRevD.34.2554
104. G. Radecky, V. Barnes, D. Carmony, A. Garfinkel, M. Derrick et al., Study of single pion production by weak charged currents in low-energy neutrino *d* interactions. Phys. Rev. **D25**, 1161–1173 (1982). doi:10.1103/PhysRevD.25.1161, 10.1103/PhysRevD.26.3297
105. E. Hernandez, J. Nieves, M. Valverde, M. Vicente Vacas, N-Delta(1232) axial form factors from weak pion production. Phys. Rev. **D81**, 085, 046 (2010). doi:10.1103/PhysRevD.81.085046
106. E. Hernández, J. Nieves, M.J.V. Vacas, Single π production in neutrino nucleus scattering. Phys. Rev. **D87**, 113, 009 (2013). doi:10.1103/PhysRevD.87.113009
107. K. Graczyk, D. Kielczewska, P. Przewlocki, J. Sobczyk, C(5)**A axial form factor from bubble chamber experiments. Phys. Rev. **D80**, 093, 001 (2009). doi:10.1103/PhysRevD.80.093001
108. K.M. Watson, The effect of final state interactions on reaction cross-sections. Phys. Rev. **88**, 1163–1171 (1952). doi:10.1103/PhysRev.88.1163
109. J. Nieves, I. Ruiz Simo, M. Vicente Vacas, Two particle-hole excitations in charged current quasielastic antineutrino-nucleus scattering. Phys. Lett. **B721**, 90–93 (2013). doi:10.1016/j.physletb.2013.03.002
110. M. Martini, Two particle-two hole excitations in charged current quasielastic neutrino-nucleus interactions. J. Phys. Conf. Ser. **408**, 012, 041 (2013)
111. O. Lalakulich, K. Gallmeister, K. Mosel, Many-body interactions of neutrinos with nuclei—observables. Phys. Rev. **C86**, 014, 614 (2012). doi:10.1103/PhysRevC.86.014614
112. J. Amaro, M. Barbaro, J. Caballero, T. Donnelly, C. Williamson, Meson-exchange currents and quasielastic neutrino cross sections in the superscaling approximation model. Phys. Lett. **B696**, 151–155 (2011). doi:10.1016/j.physletb.2010.12.007
113. J. Amaro, M. Barbaro, J. Caballero, T. Donnelly, Meson-exchange currents and quasielastic antineutrino cross sections in the superscaling approximation. Phys. Rev. Lett. **108**, 152, 501 (2012). doi:10.1103/PhysRevLett.108.152501
114. J. Amaro, M. Barbaro, J. Caballero, T. Donnelly, J. Udias, Relativistic analyses of quasielastic neutrino cross sections at MiniBooNE kinematics. Phys. Rev. **D84**, 033, 004 (2011). doi:10.1103/PhysRevD.84.033004
115. A. Bodek, H. Budd, M. Christy, Neutrino quasielastic scattering on nuclear targets: parametrizing transverse enhancement (Meson exchange currents). Eur. Phys. J. **C71**, 1726 (2011). doi:10.1140/epjc/s10052-011-1726-y
116. O. Lalakulich, U. Mosel, Energy reconstruction in quasielastic scattering in the MiniBooNE and T2K experiments. Phys. Rev. **C86**, 054, 606 (2012). doi:10.1103/PhysRevC.86.054606
117. M. Martini, M. Ericson, G. Chanfray, Neutrino energy reconstruction problems and neutrino oscillations. Phys. Rev. **D85**, 093, 012 (2012). doi:10.1103/PhysRevD.85.093012
118. M. Martini, M. Ericson, G. Chanfray, Energy reconstruction effects in neutrino oscillation experiments and implications for the analysis. Phys. Rev. **D87**, 013, 009 (2013). doi:10.1103/PhysRevD.87.013009
119. D. Meloni, M. Martini, Revisiting the T2K data using different models for the neutrino-nucleus cross sections. Phys. Lett. **B716**, 186–192 (2012). doi:10.1016/j.physletb.2012.08.007

Hadrontherapy

Dieter Schardt

Abstract In comparison to photon or electron beams used in conventional radiation therapy, high-energy proton- and heavy-ion beams offer favorable conditions for the treatment of deep-seated local tumors. Their physical depth-dose distribution in tissue is characterized by a small entrance dose and a distinct maximum (Bragg peak) near the end of range with a sharp fall-off at the distal edge. The well-defined range and the small lateral beam spread make it possible to deliver the dose with millimetre precision. Heavy ions, in addition, have an enhanced biological effectiveness in the Bragg peak region which is caused by the dense ionization and the resulting reduced cellular repair rate and make them very attractive for the treatment of radio-resistant local tumors. The article gives an introduction to hadrontherapy, including remarks on the history, basic physical and radiobiological principles, techniques of beam delivery and dose verification, and clinical experiences.

1 Introduction

Radiotherapy plays an important role in the treatment of cancer. Nowadays it is the most frequently and most successfully applied form of therapy after surgery and more than 50 % of all patients with localized malignant tumors are treated with radiation. In radiotherapy the key problem is to deliver the dose in such a way that ideally the intended target volume (covering the tumor region) receives 100 % of the planned dose needed to kill all cancer cells in the tumor, while the surrounding normal tissue does not receive any dose. This can not be achieved in practice because of the unavoidable dose deposited in the entrance channel of the irradiation, but in the past 60 years significant progress has been made to better understand the biological effectiveness of radiation and to improve the dose deposition towards the ideal and to increase thereby the tumor control rate for potentially curable cases.

D. Schardt (✉)
Biophysics Department, GSI Helmholtzzentrum für
Schwerionenforschung GmbH, Planckstr. 1, 64291 Darmstadt, Germany
e-mail: d.schardt@gsi.de

J.-E. García-Ramos et al. (eds.), *Basic Concepts in Nuclear Physics: Theory, Experiments and Applications*, Springer Proceedings in Physics 182,
DOI 10.1007/978-3-319-21191-6_2

These achievements would not have been possible without the strong and fruitful interdisciplinary collaboration of scientists in the fields of oncology and radiation medicine, radiation biology, accelerator technology and engineering, as well as atomic and nuclear physics

The application of high-energy beams of **heavy charged particles** to radiotherapy was first considered in 1946 by Robert R. Wilson. He had worked in the Manhattan Project in Los Alamos and soon after the end of World war II decided to go back to Berkeley, where he found an inspiring academic research environment around Ernest Lawrence and collaborators. In the course of the design of a new cyclotron he started to investigate the range of 150 MeV protons and the stopping characteristics in various shielding materials. But, as he explains himself [53], he went on and studied the stopping characteristics in more detail and found "…the Bragg curve came up slowly and then came down very sharply which would make them very interesting for medical applications". In his classical paper entitled "*Radiological use of fast protons*" [51] he recognized the potential benefits of proton beams and predicted "…that precision exposures of well defined small volumes within the body will soon be feasible". Moreover he predicted that "…the intense specific ionization of alpha particles will make them the most desirable therapeutically" and "…heavier nuclei, such as very energetic carbon ions, may eventually become therapeutically practically".

Two years later the 184 in. synchrocyclotron at LBL Berkeley became available for experiments and the physical and radiobiological properties of proton beams were thoroughly investigated by Tobias and co-workers [46]. Patient treatments started in 1954 at LBL Berkeley, first with protons and later with helium beams. At the Harvard Cyclotron Lab (USA) more than 9000 patients were treated with proton beams (1961–2002), and also in Europe proton therapy begun in the 1950 s and 1960 s at laboratories in Uppsala (Sweden), Moscow and St. Petersburg.

Radiotherapy with heavier ions was initiated by Tobias and co-workers at the BEVALAC facility at LBL. Many interesting facts about the development of hadrontherapy can be found in [32]. At LBL most of the patient treatments (1975–1992) with heavy ions were performed with ^{20}Ne ions (670 MeV/u) which at that time appeared to be most attractive because of their high relative biological effectiveness (RBE) combined with a low oxygen enhancement ratio (OER) in the treatment target volume (see e.g. Review articles [18, 30]). The beams were delivered to the patients by passive beam shaping systems, including scattering devices and wobbler magnets for broadening the beam and a number of passive elements like ridge filter, range modulator, collimator and bolus [5]. Until its closure in 1992 the BEVALAC was the only facility worldwide using heavy ions for the treatment of localized deep-seated tumors. In 1994 the heavy-ion medical accelerator HIMAC [11] dedicated to radiotherapy started with carbon ions at NIRS Chiba (Japan), using similar technical concepts as those pioneered at Berkeley. In Europe first treatments with ^{12}C ions started at GSI Darmstadt in 1997.

It is amazing to see that Robert Wilson's predictions have all been verified. Besides the great success of using proton beams for cancer therapy, carbon ions have shown to be an effective treatment modality as high-LET radiation with more than 10,000

patients treated worldwide (mainly in Japan). Helium ions indeed seem to be therapeutically very promising as they offer a good compromise between high-LET and low-LET radiation, combined with favorable physical characteristics (much less scattering than protons). Clinical trials with He-ions are under preparation at the HIT facility in Heidelberg. At present only proton and carbon ion beams are used in hadrontherapy worldwide. The physical and radiobiological characteristics of these beams will be discussed in the next chapters.

2 Physical Characterization of Ion Beams in Radiotherapy

2.1 Depth-Dose Profile (Bragg Curve)

The major physical advantage of heavy charged particles as compared to photons is their characteristic depth-dose profile—the well known Bragg curve—named after Sir William Henry Bragg who investigated the energy deposition of α-particles from a radium source in air at the beginning of the last century [2]. Whereas the photon dose decreases exponentially with penetration depth according to the absorption law for electromagnetic radiation, the depth-dose profile of heavy charged particles exhibits a flat plateau region with low dose and a distinct peak near to the end of range of the particles, the so-called 'Bragg peak' (Fig. 1).

This is a consequence of the interaction mechanism of the particles in the slowing-down process as described by the Bethe-formula which shows a $1/\beta^2$ dependence of the specific energy loss dE/dx. The interaction of the projectiles (ions) with the absorbing medium is governed by inelastic collisions with the atomic electrons of the absorber material. At high velocities $\beta(\equiv v/c)$ the projectiles loose small amounts of energy in a large number of such collisions. The specific energy loss is at a maximum (Bragg peak) when the projectile reaches the Bohr velocity $v_B = e^2/\hbar$. This characteristic behavior of heavy charged particles was first investigated theoretically

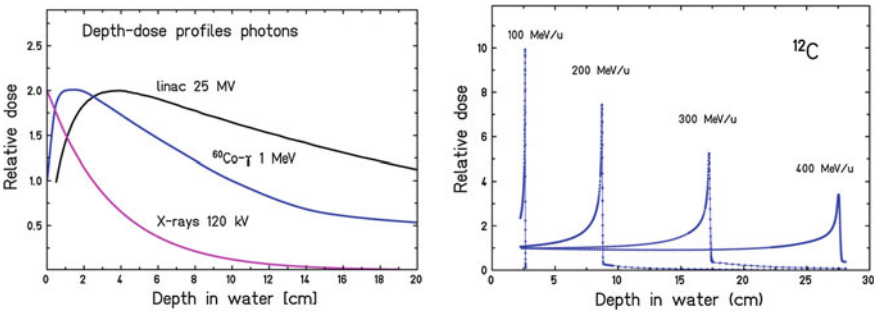

Fig. 1 Comparison of depth-dose profiles in water for photons and high-energy carbon ions. The Bragg curves for ^{12}C ions were measured at GSI

by Niels Bohr by considering the energy loss per unit path length (dE/dx) in a semi-classical treatment [3]. In the following only the basic steps are briefly sketched, more details can be found in the book *Experimental Nuclear Physics* by E. Segré. We consider an ion (projectile) with atomic number Z_p moving with velocity $\vec{v}$ and at a distance r(t) of an atomic electron of the absorber. The Coulomb force acting between the ion and electron is given by

$$\left|\vec{F}\right| = \frac{Z_p \cdot e^2}{r^2} \tag{1}$$

assuming the electron to be free and at rest and a short interaction time (non-adiabatic conditions). For symmetry reasons only the vertical component of the momentum transfer to the electron has to be considered:

$$\Delta p_\perp = \int_{-\infty}^{\infty} F_\perp dt = \int_{-\infty}^{\infty} F_\perp \frac{dx}{v} \tag{2}$$

The integral can be solved using the Gaussian theorem, resulting in

$$\Delta p_\perp = \frac{2Z_p e^2}{b \cdot v}$$

where b denotes the impact parameter. The energy transferred to one electron is

$$\Delta E = \frac{(\Delta p_\perp)^2}{2m_e} = \frac{2}{m_e} \cdot \left[\frac{Z_p e^2}{bv}\right]^2 \tag{3}$$

From these relations it is clear that the transferred momentum and hence the energy loss of the ion gets large when the velocity is small, due to the longer interaction time.

Summing up the contributions of all interactions with atomic electrons by integration over the impact parameter from 0 to infinity leads to a divergent integral. Bohr solved this problem by replacing the boundaries by the limiting values $b_{\min} = \hbar/(\gamma m_e v)$ and $b_{\max} = \gamma \cdot v/\langle \nu \rangle$ resulting in the classical formula [3]:

$$-\frac{dE}{dx} = 4\pi \cdot n_e \cdot \frac{Z_p^2 e^4}{m_e v^2} \cdot \ln\left[\frac{m_e v^2 \gamma^2}{\hbar \cdot \langle \nu \rangle}\right] \tag{4}$$

with γ the Lorentz factor and $\hbar \cdot \langle \nu \rangle$ corresponding to the mean ionization potental I in the Bethe-formula (see (6)). The electron density n_e of the absorber material can be calculated by

$$n_e = \frac{N_A \cdot Z_T \cdot \rho}{A_T \cdot M_u} \tag{5}$$

with Z_T, A_T and ρ denoting the atomic number, mass number and density of the absorber (target) material, N_A the Avogadro number and M_u the molar mass constant.

In 1930 Hans Bethe treated the problem quantum-mechanically and arrived in 1932 at the relativistic formula ('Bethe-Formula'):

$$-\frac{dE}{dx} = 4\pi \frac{Z_p^2 e^4}{m_e c^2 \beta^2} \cdot n_e \cdot \ln\left[\frac{2m_e c^2 \beta^2}{I \cdot (1-\beta^2)}\right] - \beta^2 \tag{6}$$

The specific energy loss dE/dx or 'stopping power' according to (6) is shown in Fig. 2 as a function of energy for protons and ^{12}C ions passing through water.

Due to the $1/\beta^2$ dependence the energy loss increases with decreasing particle energy. At high velocities the atomic electrons are completely stripped off and the projectile charge is equal to the atomic charge number Z_p. At lower velocities (for light ions below about 10 MeV/u), the mean charge state decreases due to the interplay of ionization and recombination processes and Z_p in (6) has to be replaced by the effective charge Z_{eff}, which can be described by the empirical Barkas-Formula [1]:

$$Z_{eff} = Z_p \cdot \left[1 - \exp(-125\beta \cdot Z_p^{-2/3})\right] \tag{7}$$

The maximum energy-loss rate, corresponding to the Bragg peak, is reached at a projectile velocity of

$$v_p \approx Z_p^{2/3} \cdot v_0 \tag{8}$$

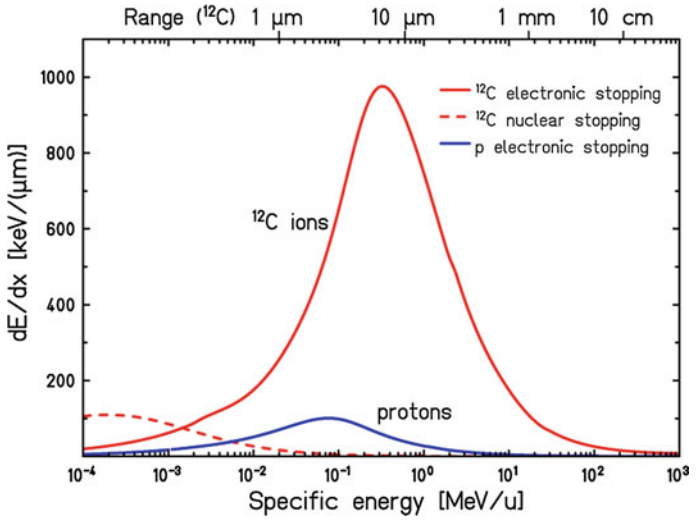

Fig. 2 Specific electronic energy loss of protons and ^{12}C ions in water. Note the logarithmic energy scale. The *dashed line* indicates the contribution of nuclear stopping. Residual ranges for ^{12}C ions are given on the *top*

where $v_0 = e^2/\hbar$ is the Bohr velocity and the corresponding $\beta = e^2/(\hbar c) = 1/137$. For ^{12}C ions this maximum occurs at a specific energy of about 350 keV/u. At still lower projectile energies $E_p < 10$ keV/u elastic collisions with target nuclei begin to contribute significantly to the energy loss and dominate the stopping process at the very end of the particle path (the last few μm). The corresponding dose contribution is, however, very small and can be neglected here.

The dose deposited in tissue is the most important physical quantity in radiotherapy. It is defined by the term *absorbed dose* (unit Gray [Gy = J/kg]) as the mean energy $d\varepsilon$ deposited by ionizing radiation in a mass element dm or volume element V with mass density ρ:

$$D = \frac{d\varepsilon}{dm} = \frac{1}{\rho}\frac{d\varepsilon}{dV} \tag{9}$$

For a parallel beam with particle fluence F the dose deposited in a thin slice of the absorber material can be written as:

$$D\left[\mathrm{Gy}\right] = 1.6 \cdot 10^{-9} \cdot \frac{dE}{dx}\left[\frac{\mathrm{keV}}{\mu\mathrm{m}}\right] \cdot F\left[\mathrm{cm}^{-2}\right] \cdot \frac{1}{\rho}\left[\frac{\mathrm{cm}^3}{g}\right] \tag{10}$$

As an example, the energy deposition of a *single* ^{12}C ion with an initial specific energy of 270 MeV/u as a function of depth in water is shown in Fig. 3 (dashed line), using the same data according to the Bethe-formula as in Fig. 2.

The energy deposition is characterized by a very sharp peak near the end of range of the ion, with a peak-to-entrance ratio of about 60. One has to keep in mind, however, that the energy loss along the penetration path is composed of a large

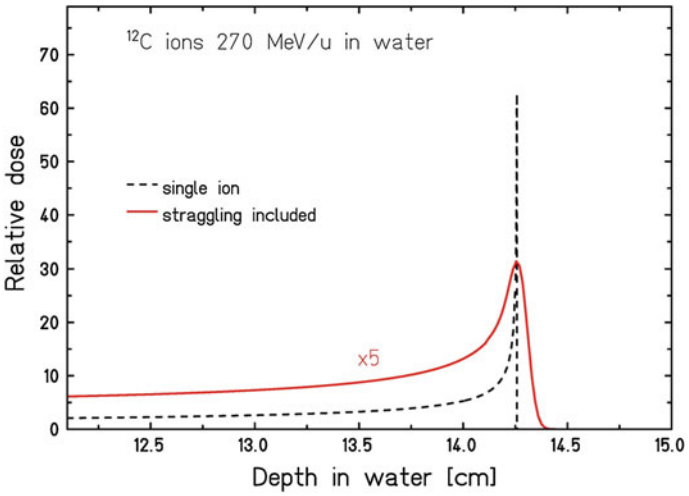

Fig. 3 Energy deposition of 270 MeV/u ^{12}C ions with a range of 14.25 cm in water for a *single ion* (*dashed line*) and an ion beam as used in therapy treatments (*solid line*)

number of single statistical processes. For an ion beam consisting of many ions (of the order of 10^8 or more) this leads to fluctuations in the energy loss and range for each individual ion, known as energy-loss-straggling and range-straggling. As a consequence, the extremely sharp peak of a single ion is smeared out and the peak-to-entrance ratio is significantly reduced (solid line in Fig. 3). This effect represents the main contribution for the observed width of the Bragg peak. Also the energy definition $\Delta E/E$ of accelerated beams contributes to the width, but it is typically of the order of 10^{-3}or better and can be noticed only at low energies where the straggling effects are smaller and the Bragg peaks may become very sharp.

The Bragg curve for a therapeutic ion beam shows an excellent dose profile (with a peak-to-entrance ratio of 5:1 in the example shown in Fig. 3) in comparison with the exponential dose fall-off for X-rays. This represents the major advantage of ion beams for the treatment of deep-seated local tumors.

2.2 Lateral Beam Spread

The lateral spread of proton or ion beams passing through an absorber is mainly caused by Coulomb scattering and is well described by the Molière-Theory [25]. For small angles the higher-order terms in Molière's solution can be neglected and the angular distribution can be approximated by a Gaussian function with a standard deviation given in [10]:

$$\sigma_\theta[rad] = \frac{14.1\,\text{MeV}}{\beta pc} \cdot Z_p \cdot \sqrt{d/L_{rad}} \cdot \left[1 + \frac{1}{9} \cdot \log_{10}(d/L_{rad})\right] \qquad (11)$$

The absorber material is characterized by the thickness d and the radiation length L_{rad}. Values of L_{rad} for common materials can be found in [47] and can be easily computed for compounds. In practice two different sources of angular beam spreading have to be considered: (a) scattering caused by materials in front of the patient (e.g., vacuum exit window, beam monitor, beam shaping devices) and (b) scattering in the patient's tissue between entrance point and stopping depth. The contributions of these two sources depend on the particle type and energy and are illustrated in Fig. 4 for a typical treatment beamline.

At low energies (a) represents the dominant contribution because even a small angular spread translates in a significant broadening of the beam spot due to the travelling distance of typically 0.5–1.0 m before entering the patient. This is critical in particular for protons. Therefore the material in the beam path in front of the patient should be kept as thin as possible, not contain heavy elements, and be located as close as possible towards the patient. At higher energies contribution (a) becomes less important or even negligible while (b) increases due to the larger penetration depths in tissue. Moreover, the calculations shown in Fig. 4 demonstrate the much smaller beam spread of ^{12}C ions compared to protons. This allows a better dose conformation

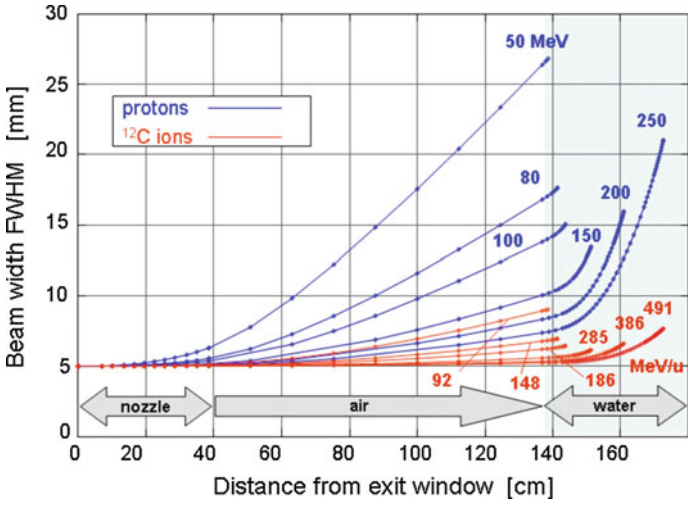

Fig. 4 Calculated spread of proton and ^{12}C ion beams in the nozzle, air gap and water (representing the patient's tissue) for a typical treatment beamline (U. Weber, GSI Darmstadt)

to the planned treatment volume (with a sharp dose fall-off at the boundaries) and is a special advantage for treating tumors located very near to critical organs.

2.3 Nuclear fragmentation

So far we considered the stopping of heavy charged particles in an absorber medium which is governed by inelastic collisions of the projectile with atomic electrons. However, also nuclear reactions along the penetration path may occur and cause a significant alteration of the radiation field. This holds in particular for heavier ions such as ^{12}C which may break up (e.g. into three α-particles) in nuclear reactions, producing thereby lighter fragments at high energies. Proton beams also get attenuated by nuclear reactions, leading amongst others to the production of secondary neutrons emitted mainly in forward direction. In the following we will consider the effects for heavy-ion beams in more detail.

At energies of several hundred MeV/u which are required for radiotherapy the most frequent nuclear interactions are peripheral collisions where the beam particles loose one or several nucleons. These reactions are well described by the so-called abrasion-ablation model according to [44] as illustrated in Fig. 5.

The total reaction cross sections at high energies (>100 MeV/u) can be well described by semi-empirical geometrical models and are almost constant over a wide energy range. Typical values (for water target) are about 350 mb for 200 MeV protons and 1400 mb for 380 MeV/u ^{12}C ions. These values correspond to mean free

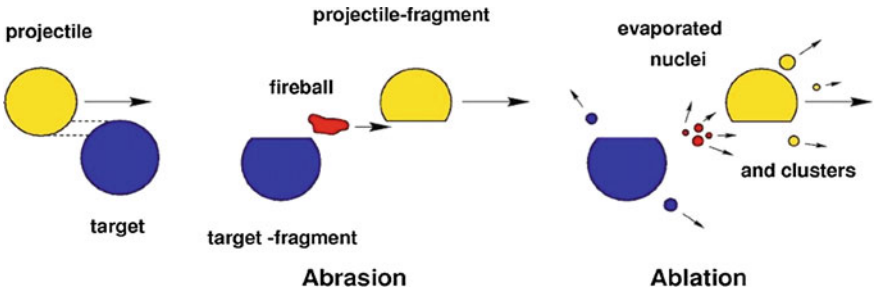

Fig. 5 Illustration of the Abrasion-ablation model [44]

path lengths in water of about 85 cm for protons and 21 cm for ^{12}C ions. This means that e.g. at a depth of 10 cm in water about 11 % of the initial proton flux was lost by nuclear reactions, while this number is much higher (38 %) for ^{12}C ions.

The projectile-fragments continue travelling with nearly the same velocity and direction. These nuclear reactions lead to an attenuation of the primary beam flux and a build-up of lower-Z fragments with increasing penetration depth. Recent experiments [9] at GSI studying the build-up functions of secondary charged particles were performed at ^{12}C beam energies of 200 and 400 MeV/u, using a $\Delta E - E$ scintillator telescope and time-of-flight (TOF) techniques. The experimental set-up is shown in Fig. 6.

In these experiments the nuclear charge Z_f of secondary fragments was identified by combining energy loss and time-of-flight (TOF) measurements (Fig. 7). Energy spectra and yields were recorded at lab angles of 0°–10° and at seven different water depths corresponding to the entrance channel, the Bragg peak region and the tail of the Bragg curve. The results include energy- and angular-distributions, fragment yields and attenuation of the primary carbon projectiles at all measured depths. As

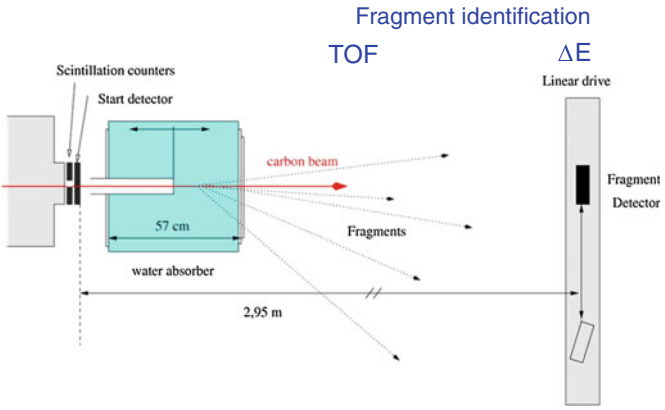

Fig. 6 Experimental setup for fragmentation measurements at GSI Darmstadt [9]

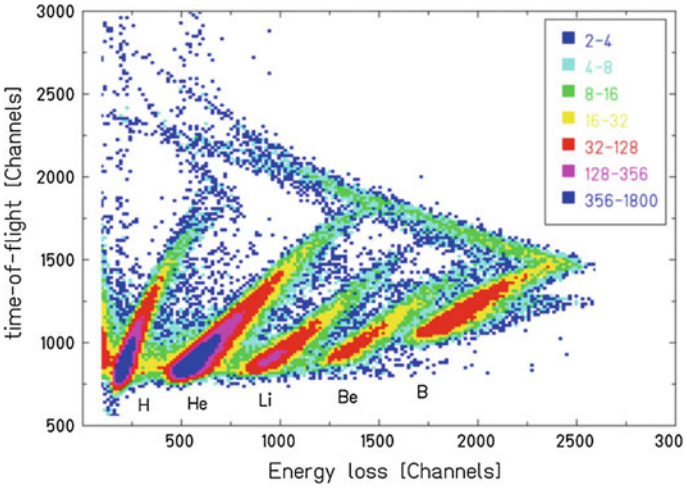

Fig. 7 Two-dimensional scatter plot of time-of-flight versus energy loss from 400 MeV/u ^{12}C ions fully stopped in a 31.1 cm thick water target. The detection angle was 0° with respect to the beam axis [9]

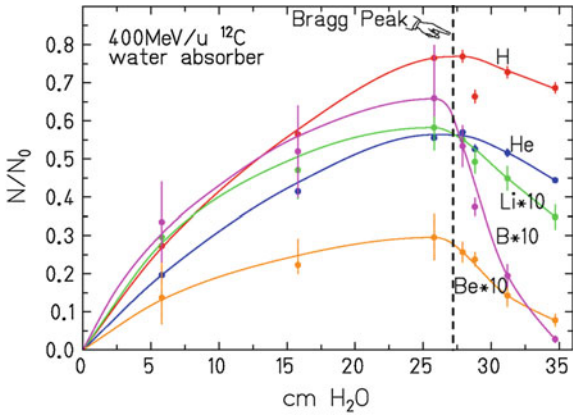

Fig. 8 Build-up of secondary fragments in water. The data points were obtained by integration of the angular distributions measured at each depth [9]

an example, build-up functions and angular distributions for primary 400 MeV/u ^{12}C ions passing through a water absorber of variable thickness are shown in Fig. 8.

As a consequence of nuclear fragmentation a rather complex radiation field is produced and leads to significant alterations which can also be observed in the shape of the Bragg curves. Since the range of the particles (at same velocity) scales with A/Z^2 and therefore lower-charge fragments have a correspondingly longer range, the depth-dose profile of heavy-ion beams shows a characteristic fragment tail beyond the Bragg peak. The Bragg curve displayed in Fig. 9 for a 330 MeV/u ^{12}C beam with the Bragg peak at about 20 cm depth of water exhibits a significant contribution of secondary fragments to the total dose. In the tail behind the Bragg peak first heavier fragments like B, Be, Li-ions contribute most of the dose, while the long range

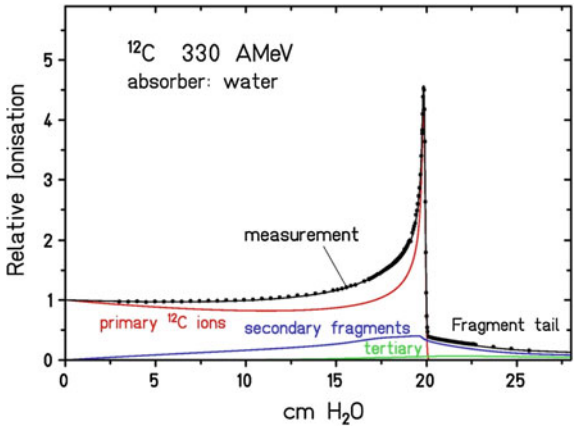

Fig. 9 Measured Bragg curve of 330 MeV/u ^{12}C ions in water and calculated contributions of primary ions, secondary and tertiary nuclear fragments [45]

tail is caused essentially by protons and α-particles. Of course, these fragmentation effects get more important with increasing depth due to the loss of primary ions and increasing production of fragments. The production of secondary fast neutrons was studied in detail by similar experiments using a BaF_2 scintillation detector [7]. It was found that the number of neutrons per primary ^{12}C ion stopping in water is $0.54 \pm 20\,\%$. Although this number is much higher compared to protons (0.025), the neutron doses are comparable and of the order of a few mSv per GyE delivered in the treatment. This is explained by the fact that a much higher number of protons (more than a factor 20) is needed to produce the same dose as carbon ions (Z^2 factor in 6).

Concluding this chapter we can summarize the physical characteristics of heavy charged particles in radiotherapy as follows:

- The 'inverted' depth-dose profile (Bragg curve) of heavy charged particles offers excellent conditions for the treatment of deep-seated localized tumors
- The position in depth of the Bragg peak can be shifted by changing the kinetic energy of the particles and perfectly optimized to the treatment plan
- The lateral beam spread caused by Coulomb scattering is much smaller for heavy ions like ^{12}C than for protons, especially for large penetration depths
- Nuclear fragmentation reactions lead to a complex radiation field in the patient's tissue, especially for heavy ions, resulting in a characteristic dose tail beyond the Bragg peak. For protons such effects are much less significant.

3 Biological Effectiveness of Ion Beams

The effects of radiation on biological systems such as living cells have been investigated in innumerable radiobiological experiments since long time. In many of these studies the cell survival was measured as a function of the absorbed dose, defining

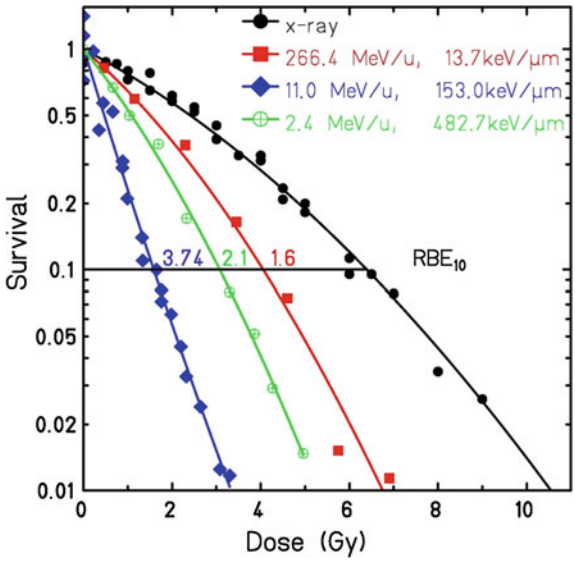

Fig. 10 Experimental dose-effect curves of CHO-cells for irradiations with X-rays and ^{12}C ions at different energies corresponding to different LET-values [52]

cell death as a complete loss of the proliferation capacity. The resulting dose-effect curves show characteristic slopes which can be understood in terms of the biological effectiveness of the applied radiation. As an example, survival curves of Chinese Hamster cells (CHO), a standard mammalian cell line, are shown in Fig. 10 for different types of radiation. The dose-effect curve for X-rays shows a non-linear behavior in form of a shoulder (survival S is plotted in log-scale vs. dose Din linear scale). At low doses the radio-sensitivity is small because most of the damage can be repaired. At higher doses the sensitivity increases and the slope of the curves decreases more and more steeply. This can be expressed by a linear-quadratic expression:

$$S = \exp(-\alpha D + \beta D^2) \tag{12}$$

where the coefficient α describes the slope at small doses and gives the initially produced irreparable damage, and β the influence of repair which is important at higher doses. The ratio α/β is therefore a measure for the repair capacity of the cells and takes typical values of 1–3 Gy for cells with high repair potential and close to 10 Gy for repair-deficient cells. For ^{12}C ions the slope of the dose-effect curves depends strongly on the energy of the particles. At high energies the curves are steeper than the X-ray curve but still exhibit a small shoulder. At lower energies the survival curves become steeper, indicating a greater effectiveness of the particles. At an ion energy of 11 MeV/u the survival curve shows a purely exponential slope.

As a measure for the effectiveness the factor RBE (Relative Biological Effectiveness) was introduced as the ratio between X-ray dose and ion dose which are required to produce the same effect:

$$RBE = \frac{D_X}{D_{ion}} \Big|_{Isoeffect} \tag{13}$$

As can be seen from Fig. 10, the RBE values for ^{12}C ions at 10 % survival level increase from 1.6 at 266 MeV/u to 3.7 at 11 MeV/u. This behavior can be easily understood in terms of the energy-LET relation (Bethe-Formula), i.e. at low energies (near the Bragg peak) the local energy deposition and hence the irreparable damage are much higher than at high energies. Surprisingly, at still lower ion energies RBE does not further increase but decreases again (see data for 2.1 MeV/u). This can be explained by two different effects: (1) if the dose deposited by a single ion is much higher than necessary to kill the cell, the energy is wasted and leads to a saturation effect ('overkill'), and (2) at very low energy, i.e. high LET, the fluences required for doses of a few Gy become very small (see 10) and a certain fraction of the cells may not be hit at all, thus again decreasing the effectiveness.

Since the discovery of the DNA and the genetic code in 1953 it became clear that the DNA molecule in the cell nucleus represents the sensitive radiation target. The existence of genes as a unit of heredity inside of cells was known long before from biological experiments which showed radiation-induced mutation in flies. These results had attracted also the interest of physicists like Max Delbrück, who had suggested already in 1935 the nature of genes as macromolecules, and Erwin Schrödinger following these ideas in his famous lecture "What is life?" [40].

Various possible damages of the DNA are schematically illustrated in Fig. 11. The most critical lesion is the double strand break which leads to cell death or mis-repair

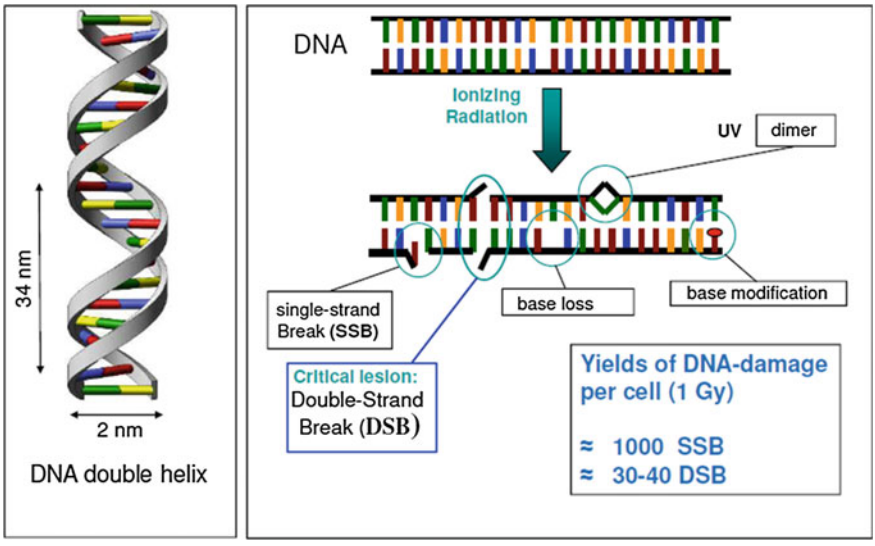

Fig. 11 DNA-damage induced by ionizing radiation [37]

and cancerogenesis. The yields of DNA-damage are rough estimates illustrating the order of magnitude [37].

The higher biological effectiveness of ion beams can be explained by the microscopic structure of particle tracks and their interaction with the DNA molecule. As discussed above, the interaction of energetic ions with the tissue is governed by inelastic collisions with the atomic electrons. Since the ion/electron mass ratio is very large, the ions are moving on practically straight trajectories through the tissue. Delta-electrons are emitted mainly in forward direction and those emitted at larger angles have comparatively low energies and short ranges (due to the collision kinematics). The *local* dose inside these particle 'tracks' can reach values up to a few thousand Gy, but decreases extremely steeply ($\sim 1/r^2$) with the radial distance r down to the order of 1 Gy at about 1 μm. This means that the dose deposition of an ion passing through a cell is highly concentrated in the track core whereas other regions of the cell do not receive any dose. This is in contrast to the dose deposition of sparsely ionizing radiation like photons or electrons, where the dose deposition is almost homogeneous in the region of a cell because it is the result of many ionizing events which are statistically distributed over the whole volume.

For fast protons the local δ-electron density along their tracks is relatively small, their biological effectiveness is not very different from photons (RBE close to 1). For ^{12}C ions, due to the Z^2 factor in the Bethe-formula, the local dose deposition and ionization density is much higher, especially at low energies near the Bragg peak. This is illustrated in Fig. 12 by Monte-Carlo simulations [19] showing the trajectories of individual δ-electrons of protons and ^{12}C ions at various energies. While proton irradiation leads mostly to reparable DNA-damage, the probability for multiple damage of the DNA molecule (double strand breaks) and cell death is much higher for ^{12}C ions, especially at the end of their track.

The elevated biological effectiveness of ion beams is of greatest importance for therapy applications and has to be correctly implemented into the treatment planning procedures. The fact that RBE depends on many different parameters such as the biological end point, dose, particle type, and energy, composition of the radiation field as well as the tissue under consideration poses however a big challenge. Therefore RBE-values are different for every location in the treatment volume. This is most important when the radiation dose is applied by beam scanning and the RBE varies from pixel to pixel. At GSI Darmstadt a model was developed for calculating the RBE value at any position in the irradiation field. The so-called Local Effect Model (LEM) [38, 39] relates the response of biological systems following ion irradiation to the corresponding response after photon irradiation. It assumes that the biological effect of irradiation is entirely determined by the spatial local dose distribution inside the cell nucleus. The basic principle is to convolute the radial dose distribution of the ion tracks with the non-linear photon dose effect curve (Fig. 13).

The accumulated local dose in the cell nucleus from different ion tracks is calculated for small sub-volumes individually using a track structure model. With knowledge of the deposited dose, the resulting biological damage is extrapolated from data of photon experiments for each sub-volume and integrated over the entire cell nucleus. This procedure was implemented into the treatment planning code TRiP

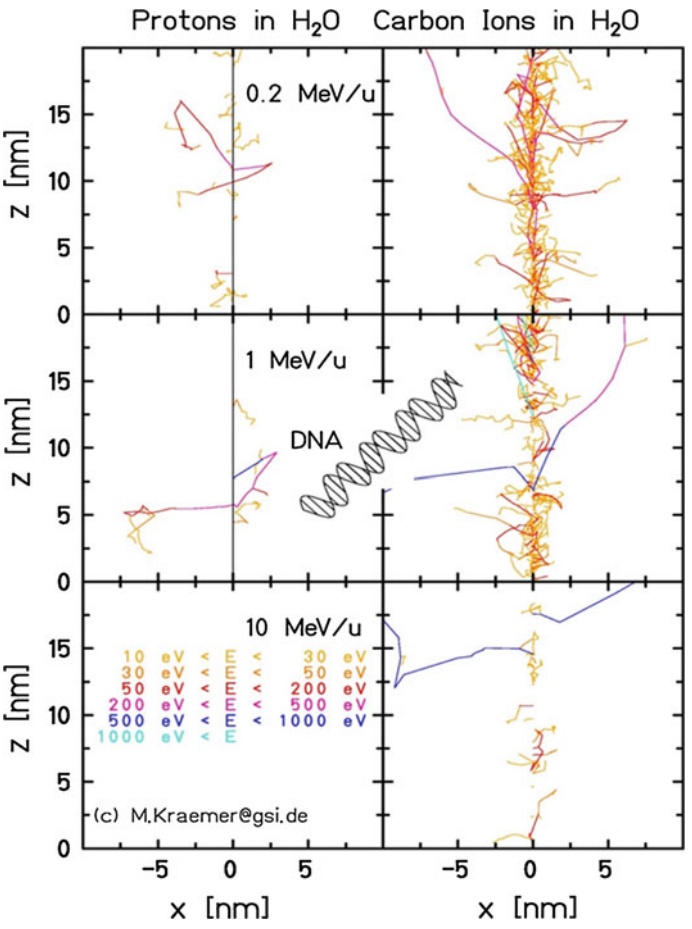

Fig. 12 Monte-Carlo simulations [19] showing individual tracks of δ-electrons produced by energetic protons and ^{12}C ions penetrating tissue. The particles enter at x = 0 and move along the z-axis

[20] which was successfully applied for the preparation of treatment plans for all patients treated within the pilot project at GSI.

Concluding this chapter we can state that heavy ions like ^{12}C, besides their favorable depth-dose profile, exhibit an elevated biological effectiveness (or cell killing power) which represents an important advantage for the treatment of radio-resistant tumors. The biological effectiveness generally increases with the atomic number Z of the projectile and is much higher in the Bragg peak region than in the entrance channel. In numerous radiobiological investigations carried out over the last decades it has been found that ^{12}C ions seem to be a good compromise with respect to the biological effectiveness in the tumor volume and with acceptable tolerance of the normal tissue which has to be traversed. These findings were confirmed already by

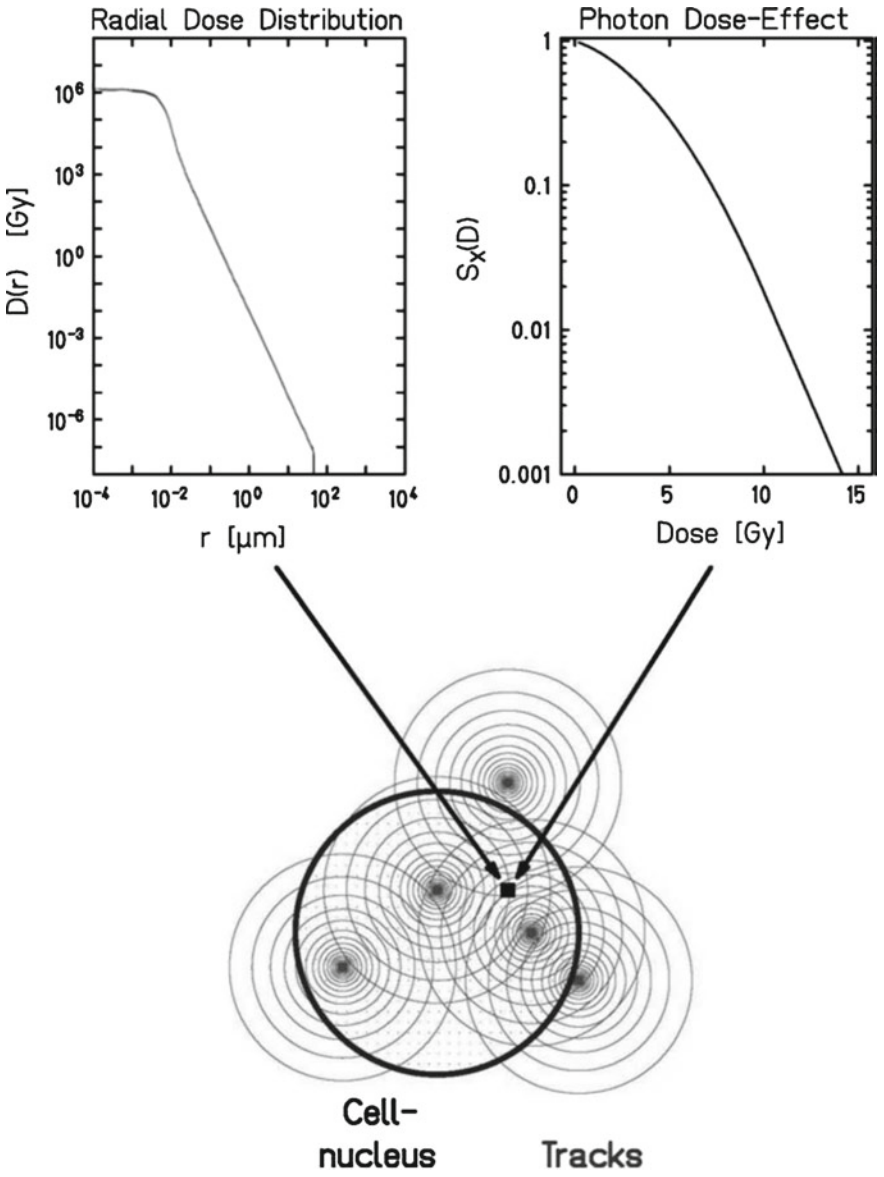

Fig. 13 Principle of the Local Effect Model (LEM) [38]

the first ^{12}C ion treatments within the pilot project (1993–2008) at GSI, where 440 patients, most of them with radio-resistant tumors in the skull base, were successfully treated with tumor control rates up to 90 % [43]. A number of new clinical studies currently being performed at the clinical center HIT (Heidelberg/Germany)

show promising results, see e.g. [14]. Moreover, the HIT facility offers the unique possibility to perform both proton and ^{12}C ion treatments under the same (technical) irradiation conditions, using a beam scanning delivery system for delivering a highly tumor-conform dose deposition.

4 Accelerators and Beam Delivery Systems

Proton and ion beam therapy require powerful accelerators in order to reach clinically relevant particle ranges in tissue up to 30 cm. The range of ions with the same specific energy (in MeV/u) scales with the factor A/Z^2. For protons and He-ions energies up to 250 MeV/u are required, for ^{12}C ions 430 MeV/u, for heavier ions like ^{16}O more than 500 MeV/u (Fig. 14). These energies correspond to magnetic rigidities $B\rho$ of 2.3 Tm for protons and 6.6 Tm for ^{12}C ions.

Today most therapy facilities offering exclusively protons are operated with cyclotrons, while all facilities with ^{12}C ions are using synchrotron accelerators. Cyclotrons are considered as easy to operate, highly reliable, and compact machines. They offer continuous beam (ideal for beam scanning) and extremely stable and regulable intensities, but no energy variation, i.e. only by means of passive degraders in the beam line. Synchrotrons, on the other hand, offer fast energy variation (from pulse to pulse), but need an injector and a delicate extraction system and are more complex in operation.

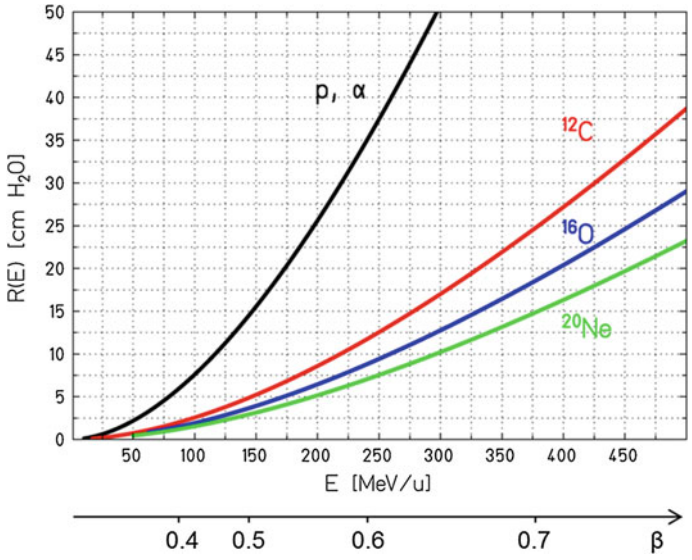

Fig. 14 Range-energy relation and velocity $\beta = v/c$ for protons and light ions in water

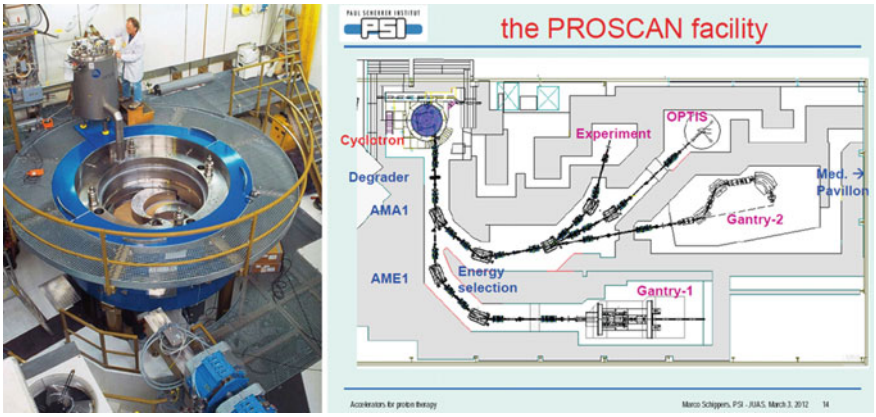

Fig. 15 Layout of the PROSCAN-Facility at PSI in Villigen (Switzerland). The left part shows the super-conducting cyclotron during maintenance [35]

Super-conducting cyclotrons (only 2–3 m in diameter) need very little floor space and are thus ideally suited for integration in the hospital. As an example the layout of the proton therapy facility PROSCAN is shown in Fig. 15. Fast energy variation required for the spot-scanning technique is accomplished here with a carbon wedge degrader system followed by a cleaning and analyzing section, accepting however significant beam losses and related activation problems. By this arrangement fast neutrons produced in the degrader and emerging mainly in forward direction do not reach the patient treatment area. The treatment beam is sent to two Gantry systems and delivered by the spot-scanning techniques developed at PSI.

The synchrotron solution was chosen for all heavy-ion therapy centres presently in operation or under construction. Nonetheless, there are ongoing efforts for the design of cyclotrons for heavy-ion therapy as well. The problem of the higher magnetic rigidities for heavy ions might be overcome by superconducting cyclotrons. Compact accelerators for modern carbon-ion therapy centres such as the HIBMC Hyogo, Japan (designed by Mitsubishi) or Heidelberg Ion Therapy centre (HIT) Heidelberg, Germany (GSI Design) combine injection linacs less than 10 m long with synchrotron rings of 20–30 m diameter.

Particle beams provided by cyclotron or synchrotron accelerators are typically narrow, pencil-like beams centred at the axis of the beam tube. An important task which is performed by the so-called beam delivery system is to distribute the beam over the planned target volume (PTV) accurately and homogeneously with the desired dose distribution. Two different basic strategies were followed which in their extreme forms are represented by (i) the fully passive systems with fixed beam modulation or (ii) the fully active beam scanning systems. In the first case, the particle beam is adapted in three dimensions to the target volume only by passive non-variable field shaping elements. In the second case, the target volume is dissected in small volume elements (voxels) and a fine pencil-like beam is used to fill the voxels with the

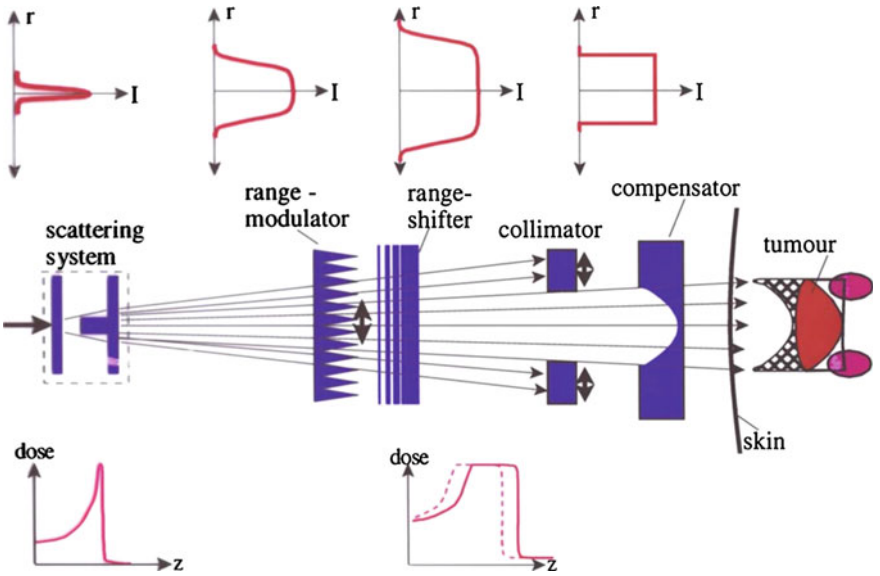

Fig. 16 Principle of fully passive beam delivery system (see e.g. [5])

appropriate dose, ideally without any material in the beam path. Many other solutions in between these two extremes are possible and were discussed in [5]. The principle of a fully passive system is shown in Fig. 16. The initially narrow beam delivered by the accelerator is first broadened by a scattering device, normally a double-scattering system which generates a flat transversal profile in a most efficient way. The pristine Bragg peak is spread out by a range modulator in order to cover the entire length of the target volume. The whole spread-out Bragg peak (SOBP) can be shifted in depth by absorber plates (range shifter). The following two devices are patient specific and need to be precisely fabricated: the collimator cuts out the field area defined by the largest target contour as seen in beam's eye view, preventing particles outside the field to pass through. The range compensator adjusts the distal depth pattern, taking into account also the complex tissue composition. A major limitation of the fully passive modulation system is the fixed width of the SOBP, which may result in significant dose deposition outside the target volume, e.g. in the proximal part when the particle range is adjusted to the distal contours (as shown in Fig. 16).

In the early 1990s a new beam delivery technique was developed almost in parallel at PSI (Switzerland) and at GSI (Germany). Both the spot scanning system (PSI) [29] and the raster scanning system (GSI) [8] represent fully active techniques in the sense that no passive elements are used in order to adapt the dose deposition optimally to the target volume. The basic principle of the raster scanning system is shown in Fig. 17. In contrast to the passive systems there is no scattering device, but the fine pencil-like beam is moved in horizontal and vertical direction by fast magnetic deflection magnets. The treatment dose is delivered slice by slice, each slice corresponding to

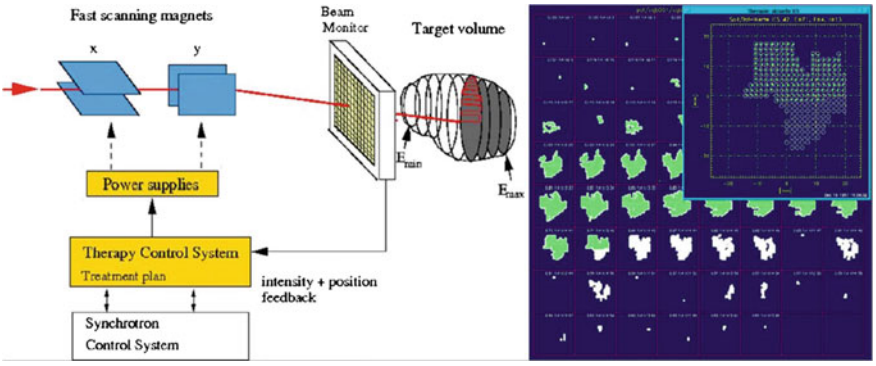

Fig. 17 Principle of the intensity-controlled raster scanning system at GSI [8]. The position of the beam and the number of ions (corresponding to the dose) are recorded in real-time by large-area parallel-plate ion chambers and multi-wire chambers

constant beam energy. The scan path within one slice follows a meander-like line connecting all points of a dense grid. The spacing between adjacent raster points is typically 2 mm and much smaller than the beam-spot. This makes the system more robust since many grid points contribute to the covering of a small area.

When the desired dose in one voxel is reached (this is controlled by the beam monitor system in front of the patient), the beam is moved to the next voxel. After completion of one slice the synchrotron beam extraction is instantly interrupted and the beam energy for the next slice is selected and delivered with the next synchrotron pulse. The scanning control system is linked with the accelerator control system and requests the appropriate beam parameters for each slice irradiation during execution of the treatment plan. With this system it is possible to adapt the dose distribution to any complex shape of the target volume, individually for each patient and without any patient-specific hardware.

5 Treatment Planning

The first step of treatment planning for any radiation therapy modality is to define and delineate the target volume on the basis of modern imaging techniques. X-ray CT provides quantitative information about the anatomical structures by recording photon attenuation images with a typical pixel resolution of 1 mm and slice thickness of 3 mm. Native CT data (without contrast agents) are essential for calculating the particle range and dose deposited in tissue and have to be recorded under the same conditions and with the same fixation aids (e.g. head mask) as used later in the treatment. Magnetic resonance imaging (MRI) and Positron-Emission-Tomography (PET) are often applied in combination with CT to allow for a better definition of the target volume and organs at risk.

The following steps of preparation are needed before the treatment can start:

- definition and delineation of the target volume (CT, MRI, PET)
- transformation of patient CT-data to water-equivalent path-length of ions
- Treatment planning:
  - find best entrance ports
  - optimization of absorbed dose [Gy] based on physical model
  - heavy ions: biological optimization (incl. RBE, biol. model)
- Verification of planned dose distribution in water phantom
- Patient positioning/verification
- Irradiation.

To calculate the dose deposition including the exact position of the Bragg peak in heterogeneous tissue, the relationship between CT numbers (given in Hounsfield units) and stopping power has to be established. The concept of water-equivalent path length (WEPL) is used to relate the traversal of an ion through a given CT voxel to the corresponding ion path length in water. There is no simple functional relationship between CT number and stopping power or WEPL, but in a first step it can be approximated by linear sections. The CT-WEPL relationship has been carefully investigated and verified experimentally by measuring pairs of CT numbers and stopping powers for animal tissue samples [23, 33, 34].

For passive beam delivery systems, treatment planning is equivalent in optimizing a set of beam shaping elements and preparing patient-specific hardware for each individual case [5]. It is a major advantage of fully active scanning beam devices that patient-specific beam shaping elements are not needed at all. Since the pristine Bragg peaks are relatively narrow, the irradiation of extended target volumes requires the superposition of a number of Bragg curves in order to move the position of the Bragg peak in depth over the whole target volume (Fig. 18). With passive delivery systems this is achieved by range shifters and ridge-filters located in front of the patient, while scanning systems can be combined with an active energy variation by the accelerator control system.

For protons the optimization commonly is restricted to absorbed dose only, applying a constant RBE value of 1.0–1.1 [12, 26], but the need of better consideration of RBE for protons is still under discussion [16]. For heavy-ion therapy the biological effective dose has to be optimized, which is a difficult task in view of the manifold dependencies of RBE and the complex radiation field. Considering the fact that RBE increases significantly towards the end of range of the ions, the absorbed dose has to be lowered correspondingly in order to obtain a uniform biological effective dose over the planned target volume (see Fig. 19). For passive delivery systems this requires patient-specific complex beam shaping elements such as rotating propellers in order to modulate the SOBP.

A major improvement was achieved by the development of intensity-modulated particle therapy (IMPT), using beam scanning techniques (see above), where the target volume is irradiated point by point. With such systems any prescribed dose can be assigned to each voxel separately. This was a prerequisite for the development of

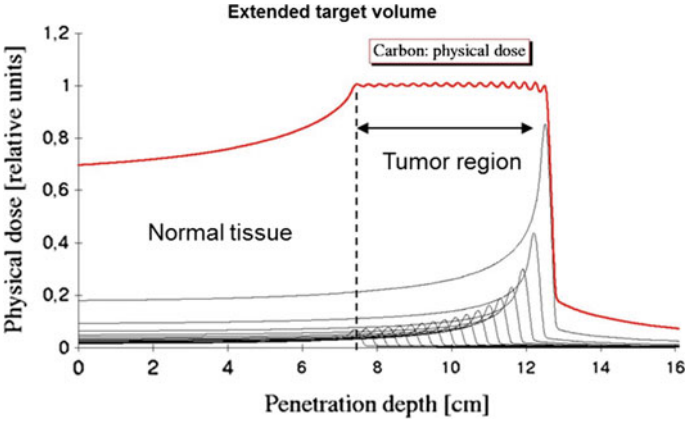

Fig. 18 Superposition of Bragg curves for the irradiation of an extended target volume with constant dose (M. Krämer, U. Weber GSI)

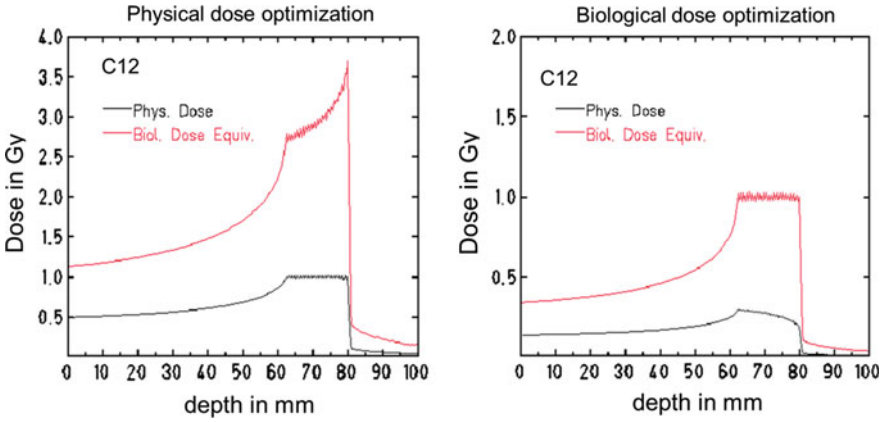

Fig. 19 Correspondent of absorbed dose for 1 Gy physical dose (*left*) and 1 Gy (RBE) biological effective dose in a planned target volume at 60–80 mm in depth (M. Krämer GSI)

the *Biological Treatment Planning System* (TRiP) for ^{12}C ions at GSI Darmstadt [20, 21]. Using the Local Effect Model (LEM), the local RBE can be calculated for any position in the treatment volume. However, this requires not only knowledge of the absorbed dose at each position (voxel), but also the composition of the radiation field at each point, since RBE depends on LET which in turn depends on the characteristics of the particle field. The latter information (e.g. the energy spectra of the primary ^{12}C ions, secondary fragment yields, energy spectra and angular distributions) has to be provided by a physical model characterizing the beam and its interaction with tissue. The first step then is an optimization of the absorbed dose (physical dose) in order to reach highest conformation of the treatment dose to the planned target volume (PTV). In a second step, the biological optimization is performed by a complex iteration

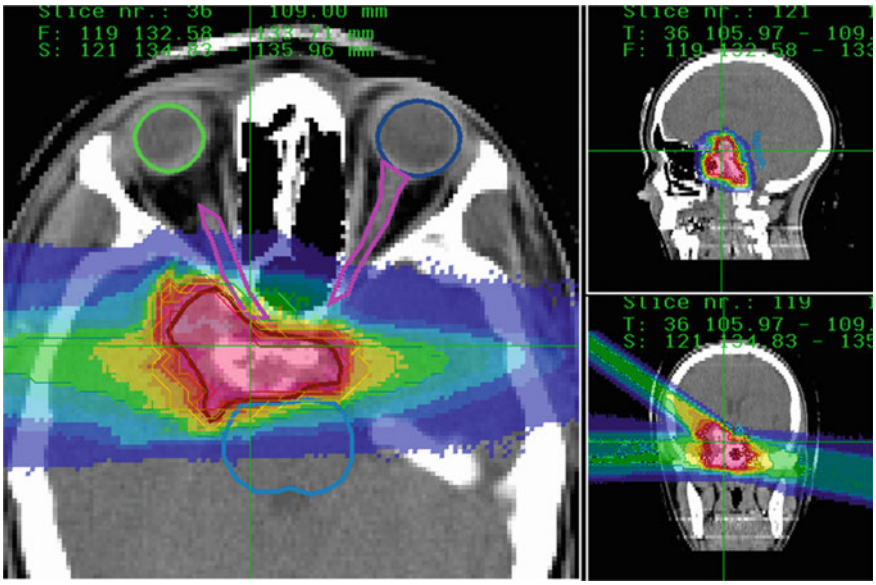

Fig. 20 Biologically effective dose distribution optimized with the treatment planning system TRiP [20] for a skull base tumor treated at GSI Darmstadt. With three fields an excellent sparing of critical organs (brain stem and optical nerves) is achieved. (Figure courtesy of O. Jäkel, DKFZ Heidelberg)

procedure, which finally results in a uniform deposition of the desired biologically effective dose over the PTV and produces all machine settings for the accelerator control and scanning system. The treatment plan shown in Fig. 20 represents a typical case of skull base tumors treated at GSI and illustrates the dose conformation and the sparing of organs at risk (here the brain stem and the optic nerves). The treatment planning system TRiP in combination with the planning software 'Voxelplan' (DKFZ Heidelberg), was routinely used for carbon-ion treatments during 1997–2008 and has proven to be a reliable tool for heavy-ion therapy with scanning beams.

6 Dose Verification Techniques

Verification of the absolute dose and the spatial dose distribution in a phantom prior to the patient treatment is an important part of quality assurance (QA). In conventional radiotherapy with photon or electron beams this is routinely performed using small air-filled ion chambers and a standard water phantom. The same techniques can be applied to proton or heavy ion beams. The dose to water can be written as

$$D_w(P_{eff}) = M_{corr} \cdot N_{w,Co60} \cdot k_Q \tag{14}$$

where P_{eff} denotes the effective point of measurement, i.e., the point in depth to which the measured dose refers, M_{corr} is the measured charge in the air cavity corrected for deviations from the reference conditions, $N_{w,Co60}$ is the ^{60}Co calibration factor, and k_Q is a calculated beam quality correction factor which takes into account the stopping power ratios of water to air and specific correction factors for charged particles.

In static irradiation fields the dose distribution can be verified by moving a single small ion chamber successively to different locations in the water phantom. Dose measurements with a single ionization chamber placed in a water phantom would, however, be ineffective for scanning systems, as each measurement would require repeated complete applications of the treatment field. Instead dedicated systems were developed, consisting of many ion chambers mounted in a block structure, which permits to measure the dose at many different locations simultaneously [17]. For further details about dosimetry techniques for proton and ion beams see e.g. [13, 36].

The biological effective dose, however, can only be verified in radiobiological measurements with living cells. For this purpose, numerous cell survival experiments with a mammalian cell line (CHO) have been carried out at GSI Darmstadt. The cells were irradiated in a therapy-like scenario using a cylindrical head phantom, which allowed to place the cell cultures at selected positions in 3 dimensions.

These measurements confirmed the validity of the LEM and its applicability for complex target volumes with surrounding organs at risk. The example shown in Fig. 21 demonstrates the good agreement of the measured cell survival data with the prediction of the biological planning with TRiP, including the LEM calculations. As explained above the constant biological effect in the planned target volume is obtained by decreasing the physical dose towards the distal zone.

6.1 In-vivo treatment monitoring

Radiation therapy with heavy ions such as ^{12}C or ^{16}O offers the unique possibility of in-vivo monitoring of the treatment irradiation. This yields an independent experimental verification of correct treatment planning and beam delivery, especially the monitoring of the ion ranges in tissue which is invaluable for treating tumors near critical structures. The principle of the measurement is sketched in Fig. 22.

Along the penetration path in tissue a small fraction of the primary ^{12}C ions undergoes a peripheral nuclear reaction and continues travelling as ^{11}C fragment with about the same velocity (c.f. Fig. 5). As they have the same nuclear charge they reach almost the same depth as the primary ions (^{11}C ions have a little shorter range than ^{12}C because of the lower mass number). The spatial distribution of the β^+-activity of the ^{11}C ions can be obtained by coincident recording of the annihilation radiation in two opposite detector heads and applying tomographic reconstruction algorithms. The β^+-activity distribution is then compared to the expected distribution which is calculated based on the patient CT-data, the treatment plan and the actual

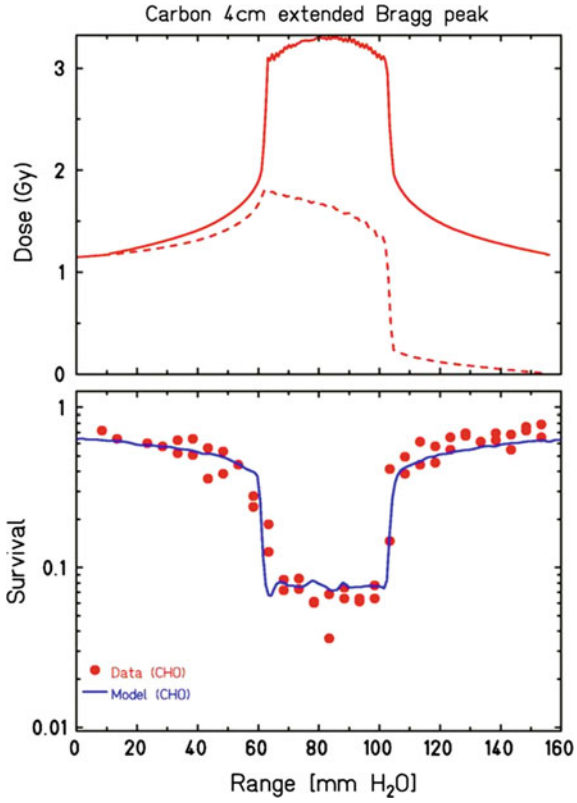

Fig. 21 Biological verification of a treatment plan with two opposing fields of ^{12}C ions calculated with the treatment planning code TRiP (solid line). The profiles of the two fields were optimized in order to obtain a constant biological effect at 80–100 mm depths in water. This was verified experimentally by cell survival measurements (data points) [22]

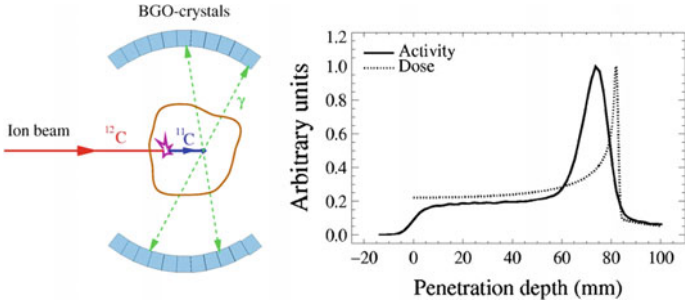

Fig. 22 Principle of in-vivo and in-situ range verification by PET-techniques [6, 27]. The correlation between depth-dose profile and β-activity distribution is shown in the right part

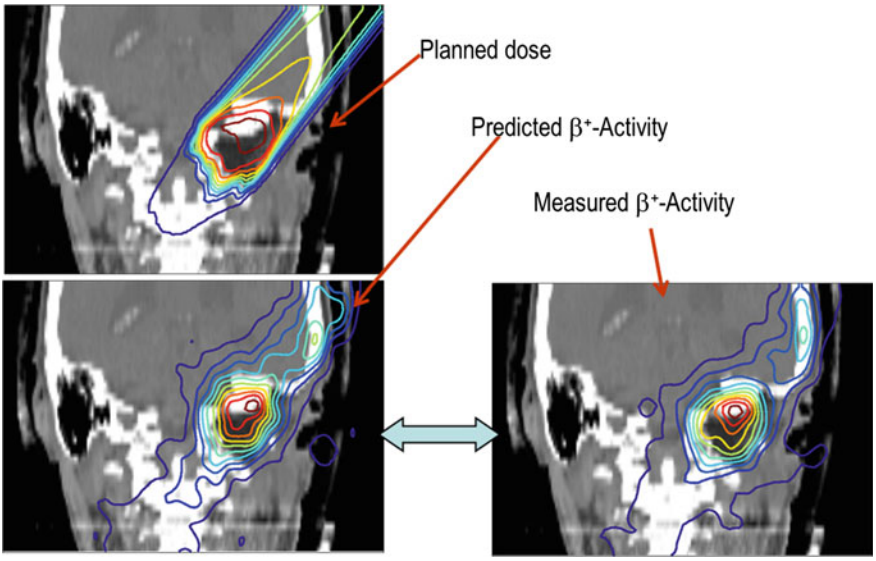

Fig. 23 Comparison of the measured β^+-activity distribution with the expected distribution calculated on the basis of the treatment plan [6]

irradiation conditions (Fig. 23). Superposition of the measured and calculated β^+-activity distributions then reveals possible differences with an accuracy of about 2–3 mm. This method has proven to be a valuable tool for the quality assurance of heavy-ion therapy and was routinely applied during all patient treatments at GSI.

Optimum performance is obtained with an in-beam PET camera mounted at the patient position as in the pilot project at GSI. In this way, the alteration of the intrinsic spatial β^+-activity distribution by metabolism or blood flow (wash-out effect) can be minimized and the contribution of short-lived positron-emitters like ^{10}C ($T_{1/2} = 19\,s$) can be fully exploited. On the other hand, space limitations in clinical facilities may not allow mounting a PET camera directly at the irradiation position. In this case PET-verification can be applied off-line by transporting the patient immediately after the treatment session to a PET-system in a neighbouring room and recording the β^+-activity of mainly ^{11}C ($T_{1/2} = 20\,min$) from a primary ^{12}C beam. The wash-out effect will then be more pronounced, but the off-beam PET verification can be performed with a full PET-ring which is a great advantage because of the small activity level and generally low counting statistics. The PET verification method can also be applied in proton therapy, but the correspondence between depth-dose distribution (Bragg cuve) and the β^+-activity distribution is less favourable for protons as it originates only from target fragments. A comprehensive discussion of in-vivo PET verification with ^{12}C ions and protons both in-beam and off-beam can be found in [28].

An interesting alternative to the application of PET techniques for in vivo range and dose monitoring in proton- or heavy-ion therapy might be the utilization of *prompt* photon or particle radiation. In fragmentation reactions occurring along the

stopping path of the primary particles prompt photons are emitted by excited nuclei as well as secondary protons, α-particles, and neutrons which have long ranges and can be detected outside of the patient's body. Since this radiation is emitted promptly, i.e. typically within less than 1 ns after the nuclear reaction, the spatial information is not affected by physiological processes unlike the PET method. As was demonstrated for proton beams of 100–200 MeV stopping in a water phantom, the intensity of prompt photons emitted orthogonally to the beam direction exhibits a peak structure which is correlated with the Bragg peak [24]. In comparison to the β^+-activity distribution shown in Fig. 22, however, the depth profile of the photon emission is much broader and hence the correlation with the Bragg peak position less pronounced. In a recent comprehensive study of prompt gamma yields from stopping proton and carbon ion beams it was found that the gamma yield for carbon ions is about a factor 5 higher than for protons with the same range in water [31]. Extrapolation of these data to real treatment scenarios support the feasibility of prompt-gamma monitoring in particle therapy, but further investigations are needed to evaluate the full potential of this technique.

7 Clinical Facilities and Experiences

From 1954 to end of the year 2014 about 137,000 patients were treated with particle therapy, most of them with protons (86 %) and with ^{12}C ions (14 %) [15]. From the 1980s on the number of patients started to increase significantly from few thousands per year to more than 120,000 per year. In parallel, the number of clinical particle therapy facilities grew up to 48 facilities today. This is an impressive development reflecting the progress in cancer research and particle therapy technology.

At the early stage of particle therapy the treatment irradiations were performed in the experimental environment of nuclear research centres, using particle accelerators which were not optimized for the requirements of particle therapy. The design of clinical facilities, however, has to focus on reliability of the machine operation and extreme care in beam control, which are key issues for operation in a clinical environment and patient safety. From about 1990 on this situation changed when the first dedicated clinical proton therapy facilities came into operation in USA and Japan. Proton therapy is most widely distributed in USA (15 facilities) and Japan (9 facilities).

Considering heavier ions, the BEVALAC (Berkeley/California) for a long time was the only machine worldwide capable of accelerating heavy ions to kinetic energies of several hundred MeV/u as required for radiotherapy. It mainly served as a forefront tool for nuclear physics experiments at high energies. Until its closure (1992) 433 patients were treated with ^{20}Ne beams. After this exciting pioneering era no more heavy-ion therapy facility was built in USA. In Japan the first dedicated medical heavy-ion therapy facility HIMAC (Heavy Ion Medical Accelerator) at Chiba (Japan) came into operation in 1994. Today Japan is leading in heavy-ion

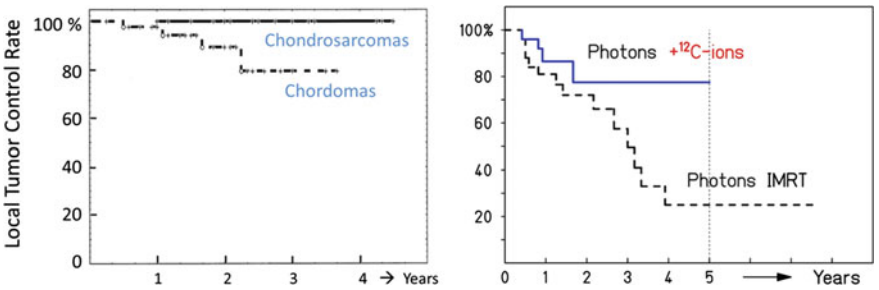

Fig. 24 Local tumor control rates for patients treated with ^{12}C ions at GSI Darmstadt (redrawnfrom [41, 42])

therapy having four facilities in operation and another one (i-Rock, Yokohama) under construction.

While the Japanese particle therapy centres implemented passive beam delivery systems very similar to those developed at Berkeley, two facilities in Europe started to treat patients with new irradiation techniques: PSI (Switzerland) with the 'spot scanning system' (1996) and GSI Darmstadt with the 'raster scanning system' (1997). Such systems permitted treatments with better conformity of the planned target volume and better sparing of critical structures. The experiences gained in the pilot project at GSI (1997–2008) entered into the construction of the dedicated clinical facility HIT (Heidelberg Ion Therapy) which started patient treatments in 2009. Another heavy-ion facility, the CNAO centre in Pavia (Italy) started patient treatments in 2012, and in Austria the MedAustron facility is expected to start treatments in 2016.

The most important criteria for the clinical assessment of radiation treatment are the tumor control rate, survival rate, side effects and toxicity. Tumor control is commonly defined as the absence of tumor growth up to 5 years after the treatment. Such data can be obtained in clinical studies with patients recruited according to certain selection criteria such as tumor type or tumor site. Some of the first clinical results obtained with ^{12}C treatments at GSI are shown in Fig. 24.

These data represent the first 152 patients which were treated with ^{12}C ions at GSI Darmstadt [41]. The patients suffered from slowly growing radio-resistant tumors such as chordomas and chondrosarcomas. Those indications in the skull base were chosen for the first trials because the patient's head can be immobilized very accurately with full mask techniques. This is important in order to take full advantage of the high precision of dose application in ion therapy. The treatments resulted in 3-year tumor control rates of 100 % for chondrosarcomas and 81 % for chordomas. The encouraging results were recently confirmed in a long-term study with 10 years follow-up [49]. An example demonstrating the tumor regression in the MRI image is shown in Fig. 25. These first results were comparable or better than those obtained in proton therapy and clearly superior than those known from conventional therapy.

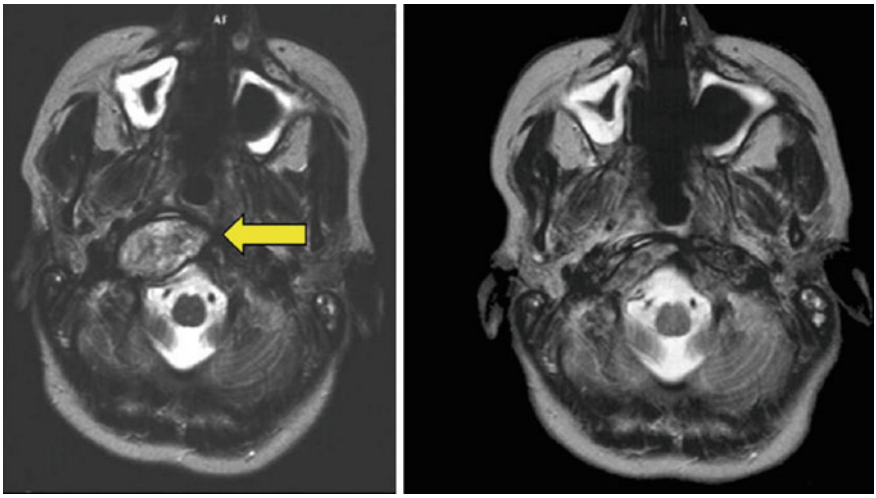

Fig. 25 Axial MRI scan of a skull base chordoma prior to carbon ion therapy (*left*) and tumor regression 6 weeks after irradiation (*right*) [36]

In the second example shown in Fig. 24 (right part) for adenoid-cystic carcinoma, 29 patients were treated with photon IMRT only and 35 patients treated with photon IMRT and a boost irradiation with ^{12}C ions. This latter group shows a significant improvement with 77 % tumor control compared to 25 % without carbon boost irradiation [42]. Moreover, much smaller side effects were observed as compared to conventional therapy. Chordoma and chondrosarcoma treatments of young patients (age < 21 y) with ^{12}C ions (60 GyE total median dose) at GSI were very well tolerated [4].

Many more patients were treated with ^{12}C ions in Japan (since 1994 more than 10,000 patients). The clinical results confirmed the improved tumor control rates for the tumor types studied at GSI and gave excellent results also for other indications such as prostate, lung and liver tumors [48].

As a result of the promising clinical results obtained in proton and carbon ion therapy, the plans for new clinical centres have recently received a substantial boost [15]. In the near future four large clinical facilities in Europe (HIT Heidelberg, MIT Marburg, CNAO Pavia and MedAustron (Wiener Neustadt) will offer both proton- and heavy-ion therapy with scanning systems. This will permit meaningful comparisons between proton and heavy ion treatments [50]. Furthermore, treatments with other ions such as ^{4}He or ^{16}O are under preparation at HIT. Helium ions offer higher LET and slightly increased RBE values, but significantly reduced lateral scattering as compared to protons and therefore might be an interesting option. Oxygen ions may be seen as an alternative between carbon and neon ions (used at LBL Berkeley) for the treatment of highly radio-resistant tumors such as glioblastoma.

In proton therapy significant progress was made in the design and construction of very compact superconducting cyclotrons with only few meters diameter. Such

machines, combined with beam scanning and Gantry-system are nowadays available at relatively low cost, facilitating substantially their integration into existing hospital environment.

References

1. H.W. Barkas, *Nuclear Research Emulsions*, vol. 1 (Academic, New York, 1963)
2. W. Bragg, R. Kleeman, On the α-particles of radium and their loss of range in passing through various atoms and molecules. Phil Mag **10**, 318–340 (1905)
3. N. Bohr, On the theory of the decrease of velocity of moving electrified particles on passing through matter. Phil. Mag. **25**, 10–31 (1913)
4. S. Combs et al., Carbon ion radiotherapy for pediatric patients and young adults treated for tumors of the skull base. Cancer **115**, 1348–1355 (2009)
5. W.T. Chu et al., Instrumentation for treatment of cancer using proton and light-ion beams. Rev. Sci. Instrum. **64**, 2055–2122 (1993)
6. W. Enghardt et al., Charged hadron tumour therapy monitoring by means of PET. Nucl. Instr. Meth. Phys. Res. A **525**, 284–288 (2004)
7. K. Gunzert-Marx et al., Secondary beam fragments produced by 200 MeV/u ^{12}C ions in water and their dose contributions in carbon ion radiotherapy. New J. Phys. **10**, 075003 (2008)
8. T. Haberer et al., Magnetic scanning system for heavy ion therapy. Nucl. Instr. Meth. Phys. Res. A **330**, 296–305 (1993)
9. E. Haettner et al., Experimental study of nuclear fragmentation of 200 and 400 MeV/u ^{12}C ions in water for applications in particle therapy. Phys. Med. Biol. **58**(23), 8265–8279 (2013)
10. V.L. Highland, Some practical remarks on multiple scattering. Nucl. Instr. Meth. Phys. Res. **129**, 497–499 (1975)
11. Y. Hirao et al., Heavy-ion synchrotron for medical use—HIMAC project at NIRS Japan. Nucl. Phys. A **538**(1992), 541c–550c (1992)
12. ICRU, ICRU Report 78. Prescribing, recording and reporting proton-beam therapy. J. ICRU **7**(2) (2007)
13. O. Jäkel, in *Radiotherapy with Protons and Ion Beams*, ed. by C. Alonso, M.V. Andrés, J. Garcia-Ramos, F. Pérez-Bernal. La Rábida 2009 International Scientific meeting on Nuclear Physics, AIP Conference Proceedings 1231 (2009)
14. A.D. Jensen et al., COSMIC: A regimen of intensity modulated radiation therapy plus dose-escalated, raster-scanned carbon ion boost for malignant salivary gland tumors: results of the prospective phase 2 trial. Int. J. Radiat. Oncol. Biol. Phys. **93**(1), 37–46 (2015)
15. M. Jermann, Particle therapy statistics in 2013. Int. J. Part. Ther. **1**, 40–43 (2014)
16. B. Jones, Towards achieving the full clinical potential of proton therapy by inclusion of LET and RBE models. Cancers **7**, 460–480 (2015)
17. C.P. Karger et al., A system for three-dimensional dosimetric verification of treatment plans in intensity-modulated radiotherapy with heavy ions. Med. Phys. **26**, 2125–2132 (1999)
18. G. Kraft, Tumor therapy with heavy charged particles. Prog. Part. Nucl. Phys. **45**, S473–S544 (2000)
19. M. Krämer, Calculations of heavy-ion track structure. Nucl. Instr. Meth. Phys. Res. B **105**, 14–20 (1995)
20. M. Krämer et al., Treatment planning for heavy-ion radiotherapy: Physical beam model and dose optimization. Phys. Med. Biol. **45**, 3299–3317 (2000)
21. M. Krämer, M. Scholz, Treatment planning for heavy-ion radiotherapy: calculation and optimization of biologically effective dose. Phys. Med. Biol. **45**, 3319–3330 (2000)
22. M. Krämer et al., Biological dosimetry of complex ion radiation fields. Phys. Med. Biol. **48**, 2063–2070 (2003)

23. N. Matsufuji et al., Relationship between CT number and electron density, scatter angle and nuclear reaction for hadron-therapy treatment planning. Phys. Med. Biol. **43**, 3261–3275 (1998)
24. C.H. Min et al., Determination of distal dose edge location by measuring right-angled prompt-gamma rays from a 38-MeV proton beam. Nucl. Instrum. Meth. Phys. Res. A **580**, 562–565 (2007)
25. G. Molière, Theorie der Streuung schneller geladener Teilchen II, Mehrfach- und Vielfach-streuung. Z. Naturforsch. **3a**, 78–97 (1948)
26. H. Paganetti et al., Relative biological effectiveness (RBE) values for proton beam therapy. Int. J. Radiat. Oncol. Biol. Phys. **53**, 407–421 (2002)
27. K. Parodi et al., Experimental study on the feasibility of in-beam PET for accurate monitoring of proton therapy. IEEE Trans. Nucl. Sci. **52**, 778–786 (2005)
28. K. Parodi et al., Comparison between in-beam and offline positron emission tomography imaging of proton and carbon ion therapeutic irradiation at synchrotron- and cyclotron-based facilities. Int. J. Radiat. Oncol. Biol. Phys. **71**, 945–956 (2008)
29. E. Pedroni et al., The 200-MeV proton therapy project at the Paul Scherrer Institute: conceptual design and practical realization. Med. Phys. **22**, 37–53 (1995)
30. P.L. Petti, A.J. Lennox, Hadronic radiotherapy. Ann. Rev. Nucl. Part. Sci. **44**, 155–197 (1994)
31. M. Pinto et al., Absolute prompt-gamma yield measurements for ion beam therapy monitoring. Phys. Med. Biol. **60**, 565–594 (2015)
32. M.R. Raju, Advances in hadrontherapy, International Congress Series No. 1077 (Elsevier Science, New York, 1994), pp. 67–79
33. E. Rietzel et al., Range accuracy in carbon ion treatment planning based on CT-calibration with real tissue samples. Radiat. Oncol. **2**, 14 (2007)
34. B. Schaffner, E. Pedroni, The precision of proton range calculations in proton radiotherapy treatment planning: experimental verification of the relation between CT-HU and proton stopping power. Phys. Med. Biol. **43**, 1579–1592 (1998)
35. J.M. Schippers et al., The SC cyclotron and beam lines of PSI's new proton therapy facility PROSCAN. Nucl. Instr. Meth. Phys. Res. B **261**, 773–776 (2007)
36. D. Schardt et al., Heavy-ion tumor therapy: Physical and radiobiological benefits. Rev. Mod. Phys. **82**, 383–425 (2010)
37. M. Scholz, Effects of ion radiation on cells and tissues. Adv. Polym. Sci. **62**, 96–155 (2003)
38. M. Scholz et al., Computation of cell survival in heavy ion beams for therapy. The model and its approximation. Radiat. Environ. Biophys. **36**, 59–66 (1997)
39. M. Scholz, G. Kraft, Calculation of heavy ion inactivation probability based on track structure, X-ray sensitivity and target size. Radiat. Prot. Dosim. **52**, 29–33 (1994)
40. E. Schrödinger, *What is Life?* (Cambridge University Press, Cambridge, 1944)
41. D. Schulz-Ertner et al., Results of carbon ion radiotherapy in 152 patients. Int. J. Radiat. Oncol. Biol. Phys. **58**, 631–640 (2004)
42. D. Schulz-Ertner et al., Therapy strategies for locally advanced adenoid cystic carcinomas using modern radiation therapy techniques. Cancer **104**, 338–344 (2005)
43. D. Schulz-Ertner et al., Effectiveness of carbon ion radiotherapy in the treatment of skull-base chordomas. Int. J. Radiat. Oncol. Biol. Phys. **68**, 449–457 (2007)
44. R. Serber, Nuclear reactions at high energies. Phys. Rev. **72**(11), 1114–1115 (1947)
45. L. Sihver et al., Depth-dose distributions of high-energy carbon, oxygen and neon beams in water. Jpn. J. Med. Phys. **18**(1), 1–21 (1998)
46. C.A. Tobias, Heavy charged particles in cancer therapy. Radiobiology and Radiotherapy, Institute Monograph No. 24 (1967)
47. Y.S. Tsai, Pair production and bremsstrahlung of charged leptons. Rev. Mod. Phys. **46**, 815–851 (1974)
48. H. Tsujii et al., Clinical advantages of carbon-ion radiotherapy. New. J. Phys. **10**, 075009 (2008)
49. M. Uhl et al., High control rate in patients with chondrosarcoma of the skull base after carbon ion therapy: first report of long-term results. Cancer **120**(10), 1579–1585 (2014a)
50. M. Uhl et al., Comparing the use of protons and carbon ions for treatment. Cancer J. **20**(6), 433–439 (2014b)

51. R.R. Wilson, Radiological use of fast protons. Radiology **47**, 487–491 (1946)
52. W.K. Weyrather et al., RBE for carbon track-segment irradiation in cell lines of differing repair capacity. Int. J. Radiat. Biol. **75**, 1357–1364 (1999)
53. R.R. Wilson, Advances in Hadrontherapy, International Congress Series No. 1144, (Elsevier Science, New York, 1997), pp. ix–xiii

Gamma-Ray Spectroscopy of Neutron-Rich Nuclei Populated via Multinucleon-Transfer Reactions

Jose Javier Valiente-Dobón

Abstract The methods of γ-ray spectroscopy applied to the study of neutron-rich nuclei populated via multinucleon-transfer reactions are discussed, starting from its basic principles. The latest major developments of γ-ray detector arrays, with a special emphasis on the state-of-the-art γ-ray tracking spectrometer AGATA, are also presented. Examples are taken from various experiments that illustrate the power of γ-ray arrays in the advancement of the knowledge of exotic neutron-rich nuclei.

Keywords Gamma spectroscopy · Gamma-ray spectroscopy via multinucleon transfer reactions · In-beam gamma-ray spectroscopy of neutron-rich nuclei · Lifetime measurements

1 Introduction

Nuclear structure physics has as a main objective the study of the nature and of the phenomenology of nucleon-nucleon interaction in the nuclear medium. Gamma-ray spectroscopy represents one of the most powerful methods to study nuclear structure since a large fraction of the de-excitation of the excited nuclear levels goes via γ emission. The precise measurement of the γ rays emitted from excited nuclear levels can provide a large amount of information of the nuclear structure of the specific nucleus under study. One obtains not only the γ-ray transition energy between two excited levels, but also: (i) the lifetime of an excited state that can give the reduced transition matrix elements, (ii) the angular distributions that can give the multipolarity of the transition and (iii) the polarisation that can provide information on the electric or magnetic character of the transition. Needless to say, over the five decades of developments on in-beam γ-ray spectroscopy, different methods have been used to measure all these parameters and thus to infer the nature of the nucleon-nucleon interaction.

J.J. Valiente-Dobón (✉)
Istituto Nazionale di Fisica Nucleare, Laboratori Nazionali di Legnaro,
I-35020 Legnaro, Padova, Italy
e-mail: valiente@lnl.infn.it

J.-E. García-Ramos et al. (eds.), *Basic Concepts in Nuclear Physics: Theory, Experiments and Applications*, Springer Proceedings in Physics 182,
DOI 10.1007/978-3-319-21191-6_3

The knowledge of nuclear matter has gone *pari passu* with the technical development of γ-ray spectrometers that the nuclear spectroscopy community has built up over the last five decades. Our starting point is the first in-beam γ-ray spectroscopy experiment performed in the sixties by Morinaga and co-workers [1] where they used an α-particle beam to bombard targets of rare-earth nuclei and the prompt-γ rays where measured with NaI scintillators clustered around the target. Currently, these basic arrays, that were used for high resolution γ-ray spectroscopy have been continuously replaced by more advance γ spectrometers, such as germanium detectors with and without anti-Compton suppression. At present, state-of-the-art γ spectrometers for high-resolution γ spectroscopy are based on γ-ray tracking, such as the European project Advanced Gamma Tracking Array (AGATA) [2, 3] and the U.S.A. counterpart Gamma-Ray Energy Tracking Array (GRETA) [4, 5].

In this paper, the main principles of γ-ray spectroscopy will be discussed followed by a description of the main developments in γ-ray spectroscopy from inorganic scintillators to semiconductor germanium detectors with anti-Compton suppression and finally to the γ-ray tracking arrays. Once these concepts are discussed, the following step will be to give a review on the study of moderately neutron-rich nuclei populated via multinucleon-transfer reactions.

2 Technical Developments in γ Spectroscopy

Gamma radiation is that part of the electromagnetic waves spectrum with frequencies higher than 10^{18} Hz, which correspond to 10 keV energy. The energies of interest in nuclear spectroscopy range from a few tens of keV up to around 30 MeV. Therefore, the construction of valuable γ-ray detection systems is governed by the physics of the interaction of γ rays of such energies with matter. There are plenty of textbooks, such as Evans [6] that deal with this topic. Therefore, in the following sections, only the general notions essential to follow our journey towards the latest developments in γ-ray detection systems, will be discussed.

In the early days of discrete γ-ray spectroscopy the detectors used for in-beam studies were just a few inorganic scintillators, such as NaI. This was the case, as was already discussed in the introduction, of the first in-beam experiment by Morinaga and co-workers. Later on, various $\approx 4\pi$ multi-detector arrays based on scintillators were built, such as the Spin Spectrometer [7] at Oak Ridge, the Darmstadt-Heidelberg Crystal Ball [8], both of them based on NaI. An array based on BaF_2 was also built, Chateau de Crystal [9]. At present there are two arrays based on scintillators, fully functional, with large granularity and efficiency; one is the Michigan State University CAESAR [10] based on CsI(Na) and the second one is the DALI2 [11] array at RIKEN based on NaI. All these spectrometers have the advantage of having a high efficiency and are capable of providing high γ-ray multiplicity. However, the main disadvantages of these arrays based on scintillators is the poor energy resolution. Typically NaI presents a Full Width Half Maximum (FWHM) of 8 %, meanwhile BaF_2 presents a FWHM of around 10 % for 1 MeV γ rays. The latest two arrays, CAESAR and DALI2, are used for discrete line γ-ray spectroscopy when

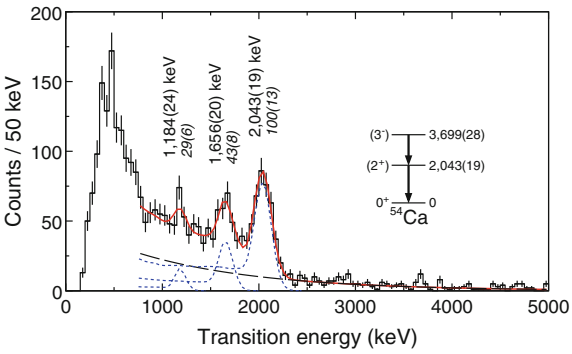

Fig. 1 Doppler-corrected γ-ray spectrum for ^{54}Ca. Three clear peaks can be observed at 1184, 1656 and 2043 keV. Courtesy of D. Steppenbeck, adapted from [12]

the multiplicity of the event is low enough (1–3 γ rays) and therefore the probability that two γ rays with similar energies overlay each other is negligible. Figure 1 shows a typical example of a γ-ray spectrum for these kind of scintillator arrays. It shows the Doppler-corrected γ-ray spectrum taken with DALI2 for the neutron-rich ^{54}Ca after a low-multiplicity knock-out reaction at relativistic energies [12]. Note that this spectrum shows mainly three γ peaks with an energy resolution for the main one $2^+ \rightarrow 0^+$ at 2043 keV of near 200 keV FWHM.

Currently, the PARIS project [13] (Photon Array for studies with Radioactive Ion and Stable beams) aims at constructing a γ-calorimeter with an energy range from 100 keV to 50 MeV, that will be composed of phoswich detectors, consisting of $2 \times 2 \times 2$ $LaBr_3$ optically coupled to $2 \times 2 \times 6$ NaI crystals and read out by a common PMT. The $LaBr_3$ scintillator presents unprecedented energy resolution for scintillator materials, around 3 % [14].

Discrete γ-ray spectroscopy had a major step forward in the early sixties when reversed-biased germanium detectors were developed. At the beginning, Li-drifted detectors Ge(Li) were employed and it was only in the eighties that they were replaced by High-Purity Germanium detectors (HPGe). These detectors present a very good energy resolution of about 0.2 % for 1 MeV γ rays. In the early times it was only possible to grow small crystals. However, nowadays, these detectors can reach, in the best cases, up to a volume of 1 l. A comprehensive description of this kind of detector can be found in many text books, as for example in [15].

HPGe detectors suffer, however, from an unavoidable feature of γ-ray interaction, namely that Compton scattering and pair production that can lead to the incomplete collection of the energy of a γ ray interacting with the crystal. As a result, the peak-to-background ratio in the spectrum is poor. Even for the largest germanium detector crystals, approximately 20 % of the observed counts in the spectrum are in the photopeak, the other 80 % of the counts are distributed in the Compton tail. The initial solution to this problem was the use of a Compton-suppression shield surrounding the Ge detector that could veto those events that released only partially the energy in the active bulk of germanium. Since the mid-eighties the material used was a very dense scintillator called Bismuth Germanium Oxide (BGO). This

enabled Compton-suppressed germanium detectors with high resolving power and with a peak-to-total ratio as good as 50–60 %.

Over the last decades different high-sensitivity arrays of multi detectors were built, most of them being optimised for the measurement of energies and intensities of γ rays in long cascades de-exciting high-spin states and to determine the correlations between the γ rays. The first arrays of germanium detectors with BGO Compton-suppression shields were built in the eighties. One of the earliest of these arrays was TESSA3 [16] at Daresbury laboratory, that presented a total photo-peak efficiency of 0.5 % at 1.3 MeV. It was in the nineties when the largest arrays were built with efficiencies that ranged from a few percent up to 10 %. Some examples of these arrays are GASP [17] (Legnaro, Italy), EUROBALL [18] (Europe) and GAMMASPHERE [19] (U.S.A.), composed of 40, 239 and 110 germanium crystals, respectively. A comprehensive description of these modern arrays can be found in [20].

Nowadays, the concept of Compton-suppressed γ-ray arrays has been overcome by the γ-ray tracking concept. Section 2.1 will be devoted to the discussion of various issues that concern the nature of γ detection that are at the basis of the appearance and evolution of γ-ray arrays such as AGATA [2]. Section 2.2 will be fully devoted to the discussion of γ-tracking arrays and more specifically to the Advanced Gamma Tracking Array (AGATA). Sections 4 and 5 will discuss in-beam γ-ray studies of neutron-rich nuclei populated via multinucleon-transfer reactions performed with anti-Compton suppressed and γ-ray tracking arrays.

2.1 Principles of γ-Ray Detection

Gamma-ray radiation, on the contrary to charged particles, deposits its energy stochastically via discrete events and between these various interactions the distances involved are centimetres (the mean free path of 1 MeV γ ray is 2 cm). The interaction mechanism that a photon can undergo in a solid state detector are restricted to photoelectric absorption, Compton scattering and electron-positron pair production. Figure 2 shows the attenuation for photons in germanium from 1 keV up to 30 MeV. It can be noticed that the photoelectric cross section falls very rapidly with increasing energy. While the energy is increasing we are moving from the regime where the electrons are bound to the situation where the scattering happens on a free electron, where the photoelectric effect is forbidden. The Compton effect takes over as a dominant process in the energy region 0.5–15 MeV that is particularly important for nuclear spectroscopy studies. This is of great importance and is one of the main reasons why anti-Compton shields and later tracking arrays were developed. For the third interaction mechanism, pair production, the threshold for its occurrence happens when the energy of the γ ray is at least twice the electron rest mass $2m_ec^2$ = 1.022 MeV. The γ ray will create an electron-positron pair when interacting with the electromagnetic field of the nucleus. This effect is also important when designing a γ-ray spectrometer since the two positron annihilation photons of 511 keV can escape the crystal.

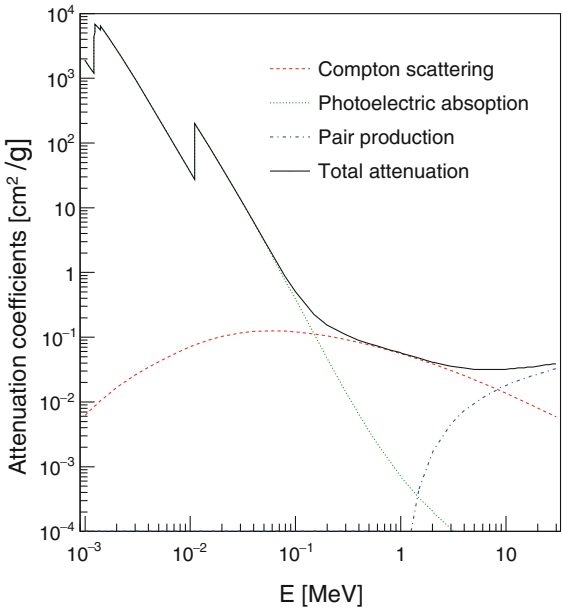

Fig. 2 Attenuation coefficients in germanium for photons from 1 keV up to 30 MeV. The three main processes: photoelectric absorption, Compton scattering, electron-positron pair production are depicted. The *black line* denotes the sum of these three processes. This plot has been created from data in [21]

When designing a γ-ray spectrometer for in-beam studies, other aspects are important besides the nature of the γ radiation itself. These are the multiplicity of γ emission, the average velocities of the emitting nuclei that will originate a Doppler shift of the γ-ray energies and the counting rate. For γ rays emitted by a moving source a Doppler shift of the transition energy is observed. This shifted γ-ray energy and the intrinsic energy are related by:

$$E_\gamma^0 = E_\gamma \frac{1 - \beta \cos\theta}{\sqrt{1-\beta^2}} \tag{1}$$

where E_γ^0 is the transition energy at rest, E_γ is the transition energy in the laboratory, β is the velocity of the moving nucleus and θ is the angle between the velocity vector and the γ ray direction vector in the laboratory, determined by the position of the germanium detector. The FWHM of the γ-ray peak due to the Doppler broadening will depend on the various contributions (θ and β). If one considers these contributions statistically independent, the final contribution can be evaluated through error propagation via partial derivatives of (1) for each of the contributions, as described in the following:

$$\left(\frac{\Delta E_\gamma^0}{E_\gamma^0}\right)^2 = \left(\frac{\beta \sin\theta}{1-\beta\cos\theta}\right)^2 (\Delta\theta)^2 + \left(\frac{\beta - \cos\theta}{(1-\beta\cos\theta)\left(1-\beta^2\right)}\right)^2 (\Delta\beta)^2 + \left(\frac{\Delta E_\gamma}{E_\gamma}\right)^2 \tag{2}$$

Equation 2 shows the three contributions to the final energy resolution ΔE_γ^0, where $\Delta\beta$, $\Delta\theta$ and ΔE_γ are the uncertainty on the velocity, on the detector opening angle and the contribution of the intrinsic energy resolution of the detector, respectively. The γ-ray peak resolution for a moving source will depend mainly from the opening angle of the detector $\Delta\theta$ and the uncertainty on the velocity $\Delta\beta$. Figure 3 shows the different contributions to the Doppler broadening as a function of the angle θ. A γ ray of 1 MeV emitted from a moving source with a $\beta = 30 \pm 5\,\%$ is considered, and a typical intrinsic energy resolution of 2 keV is assumed. Two interesting different cases are shown: a first case for an opening angle of $\Delta\theta = 8°$, which is the typical value for a traditional opening angle for a single germanium detector and a second case with an opening angle of $\Delta\theta = 1.5°$ which is approximately the opening angle expected in γ-ray tracking arrays. One can see the very large difference between these two cases, i.e. between a traditional germanium array composed of single germanium detectors ($\Delta\theta = 8°$) and a tracking array ($\Delta\theta = 1.5°$). In the first case the γ ray peak will have an energy resolution of 45 keV (like a scintillator array), meanwhile in the second case an acceptable energy resolution of 10 keV is obtained.

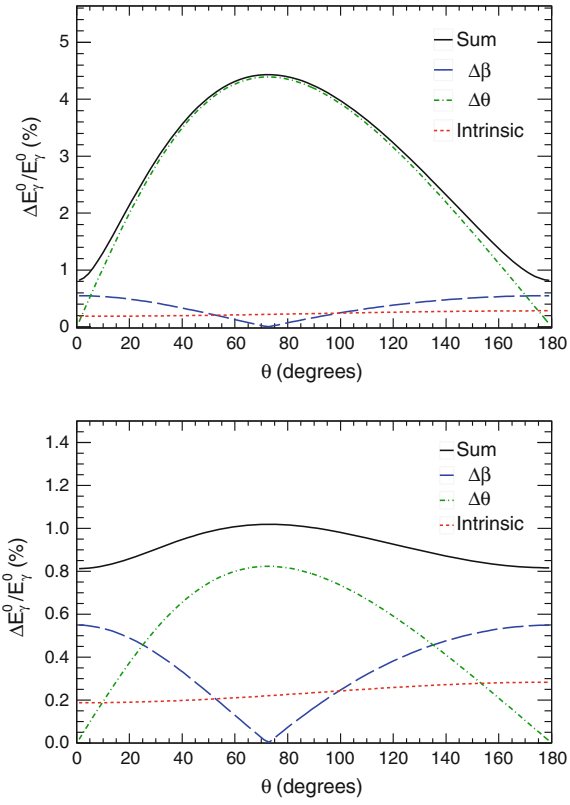

Fig. 3 The *upper graph* shows the various contributions to the Doppler broadening $\left(\frac{\Delta E_\gamma^0}{E_\gamma^0}\right)$ as a function of the angle θ (angle of the photon with respect to the recoil emitting source) for a γ transition of 1 MeV for a typical single germanium detector ($\Delta\theta = 8°$) with an intrinsic energy resolution of 2 keV and a source velocity of $\beta = 30.0 \pm 0.5\,\%$. The *lower graph* shows the same contributions to the Doppler broadening $\left(\frac{\Delta E_\gamma^0}{E_\gamma^0}\right)$ but for a γ-ray tracking array where an opening angle of 1.5° has been assumed

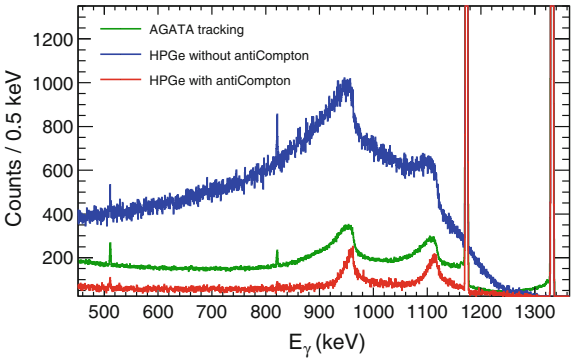

Fig. 4 Simulated γ ray spectrum for a ^{60}Co source for three different cases: (*blue*) GALILEO HPGe detectors without anti-Compton, (*red*) GALILEO HPGe detectors with anti-Compton and (*green*) the γ-ray tracking AGATA

2.2 The AGATA Array

The aim of the AGATA (Advanced GAmma Tracking Array) project is the development of an array of HPGe detectors that can overcome the issues discussed in the previous Sect. 2.1, namely to cope with Doppler effects due to large source velocities at the future facilities for radioactive beams and the high-counting rate at the future high-intensity stable ion beam facilities. A detailed description of AGATA has been published in [2], where all the different aspects of the project are discussed. It is not the scope of this paper to review [2] but to discuss the main advantages of AGATA. With the γ-ray tracking technique [22, 23], anti-Compton shields become unnecessary resulting in a large gain in efficiency while maintaining the spectra quality. The latter can be verified by inspecting Fig. 4 which shows the GEANT4 simulations of the Peak-to-Total (P/T) ratio [24] obtained for a ^{60}Co source for an array of germanium such as GALILEO [25] without anti-Compton shields (blue), GALILEO with its anti-Compton shield (red) and the γ-ray tracking array AGATA (green). The Peak-to-Total (P/T) ratio goes from around 20 % for GALILEO without anti-Compton up to around 50 % for the cases of GALILEO with anti-Compton shield and AGATA.

In addition to the improvement in the quality of the spectra, another advantage of γ-ray tracking arrays is that one can measure with high precision the direction of γ ray emission, which will improve the Doppler energy correction as discussed in the previous Sect. 2.1, see Fig. 3. In order to reach such performance, that is well beyond the standard conventional escape-suppressed arrays, it is necessary to make use of electrically segmented Ge crystals enabling the identification of the individual points of interaction of the γ rays within the volume of the Ge crystals as well as the determination of the deposited energy with high resolution. In addition, digital sampling electronics to extract energy, time, and position information from the signals of the detectors using pulse-shape analysis methods are necessary. The path of the γ rays in the Ge crystals will be reconstructed, making use of tracking algorithms on the position and energy information of the individual interactions, giving finally the full energy of the γ ray hitting the segmented detector, see [2]. AGATA is composed by

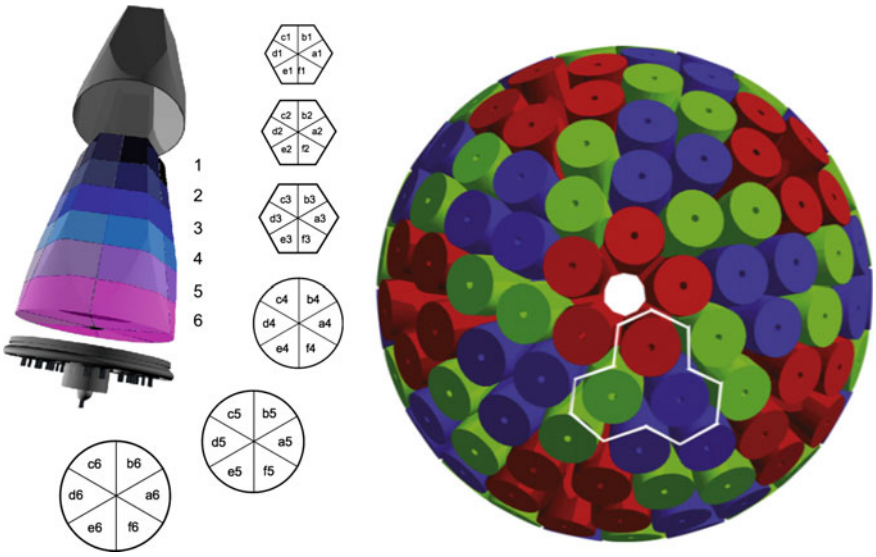

Fig. 5 Crystal geometry of the AGATA HPGe capsules (*left*). Along the crystal axis the external contact is subdivided into six rings labelled *1–6*. Each ring is subdivided into six sectors labelled (*a–f*). Full AGATA with its 180 crystal configuration (*right*). The contour of a Triple Cluster is drawn. The cryostats and the detector encapsulation are not shown. Taken from [2]

an "ensemble" of triple cluster detectors each one combining three different crystal shapes, with each crystal 36-fold segmented. Figure 5 (left) shows one of the crystal geometries with the labelling of the 36 segments, six rings divided in 6 sectors each. On the right of Fig. 5 an image of AGATA is shown when all its 180 crystals will be available, each crystal shape is represented by a different color. The contour of a Triple Cluster is drawn. The cryostats and the detector encapsulation are not shown.

3 Gamma-Ray Spectroscopy via Multinucleon-Transfer Reactions

Historically, nuclei that have been studied in detail via in-beam γ-ray spectroscopy were mainly neutron-deficient isotopes that were populated making use of standard heavy-ion fusion-evaporation reactions. Neutron-rich nuclei have been experimentally more difficult to study in-beam, since they are inaccessible via heavy-ion fusion-evaporation reactions initiated by stable beams. One of the methods that was introduced in the nineties as a mechanism to populate moderately neutron-rich nuclei was the use of multinucleon-transfer reactions [26]. The advent of large γ-ray arrays opened the possibility to perform spectroscopic studies that were previously not possible for these neutron-rich nuclei and at the beginning multinucleon-transfer

reactions were exploited together with γ-ray arrays and thick targets. One of the first experimental studies that showed that it was possible to use few-nucleon transfer reactions to populate neutron-rich nuclei was performed by Broda and co-workers [27]. These initial experiments opened vast areas of knowledge in the neutron-rich side of the Segré Chart. A comprehensive review can be found in [28], some of the most important results obtained with multinucleon-transfer reactions and γ-ray arrays using thick targets are illustrated. Although this technique with thick targets has yielded a large wealth of information on the structure of neutron-rich nuclei, it presents some intrinsic limitations, such as the fact that one can not identify directly the new exotic nucleus produced in the reaction. This is a large limitation because the more exotic nuclei, that present lower cross sections can not be unequivocally identified with the cross-coincidence technique developed by Broda and co-workers for thick target experiments. In addition, the short-lived excited states are emitted while the ion is still moving within the target and therefore no peak structure is visible. Finally, the full integration of the recoils angular range emission, prohibits the measurement of angular distribution and lifetimes.

The development of large-acceptance magnetic spectrometers (large-energy and angular coverage) has paved the road for more sensitive studies of neutron-rich nuclei with thin targets. These spectrometers are very simple devices in terms of the magnetic elements and they might present a very large solid angle, up to 100 *msr*. The large sensitivity of these instruments comes from trajectory reconstruction. To be able to perform an ion-trajectory reconstruction, one needs a detection system that is capable of measuring, besides the atomic number, the position and time information along the path of the ion. Dedicated algorithms have been developed that, from this information, can derive the atomic number Z, mass A and velocity vector β of the

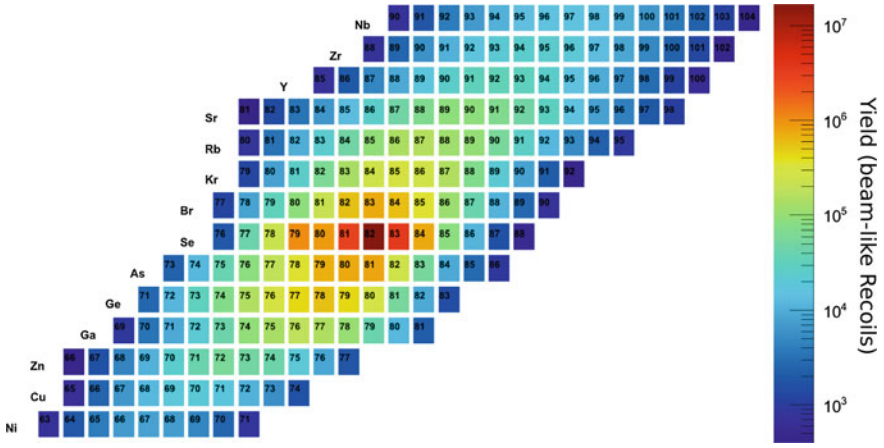

Fig. 6 Yield of the beam-like recoils identified in the PRISMA spectrometer in coincidence with the AGATA demonstrator for the reaction induced by a ^{82}Se beam at an energy of 426 MeV onto a ^{198}Pt target. Adapted from [29]

ion produced in the reaction. These large-acceptance magnetic spectrometers are perfectly suited for multinucleon-transfer reactions where a large number of ions are produced with a broad energy distribution and with cross sections that can span from tenths of milibarn to hundreds of microbarn. Figure 6 shows the yield of the beam-like recoils for the transfer reaction of a ^{82}Se beam at an energy of 426 MeV onto a ^{198}Pt target. It can be noticed that more than 20 nucleons have been transferred between the target and the beam with yields that span more than three orders of magnitude. The coupling of a large-magnetic spectrometer with a large γ-ray array overcomes the aforementioned problems raised with thick targets, see Sects. 4 and 5.

3.1 Multinucleon-Transfer Reactions

In this section a general description of multinucleon-transfer reactions will be given. The starting point will be an introduction to transfer reactions and a brief description of its main characteristics such as cross sections and the grazing angle. It will follow a discussion of the angular momentum selectivity in this kind of reactions. An exhaustive description of multinucleon-transfer processes can be found at [30].

The transfer processes are mainly governed by form factors (spectroscopic information of the colliding nuclei), dynamics of the collision and optimum Q-value considerations (balance of the internal and binding energy in the phase space of the colliding nuclei) [31]. The former expresses the process dependence from the nuclear structure, and in particular from the initial and final wave functions of the transferred nucleons. The latter, on the contrary, takes into account the reaction dynamics and the excitation energy of the reaction products. Depending on the relative relevance of these two parameters, the nucleon transfer process happens in different regimes that most of the times overlap and it will depend strongly from where (in space) and how (acceptance of instruments) the measurement of the reaction products is performed. If the detector is positioned at the grazing angle multinucleon-transfer reactions will be enhanced and in a simplistic view one could say that if the ejectile excitation energy is high enough ($>$20 MeV) the transferred nucleons are in a continuum of quantum states (the density of energy levels increases with increasing energy). The quantum-mechanical amplitude of the nucleon exchanging process is almost only a function of the dynamic factor, and thus do not feel the effects of nuclear structure. As a consequence, the model adopted to describe this reaction is thermodynamical, and the exchange of protons and neutrons is treated as a diffusive process and the transfer between the target and the beam is of statistical character. These reactions are called deep-inelastic reactions or also damped reactions. The name is justified by the fact that, if an high E_{ex} is reached, this occurs thanks to the absorption of a large fraction of the initial kinetic energy of nuclei. On the contrary, if the excitation energy of the ejectiles is not very high ($<$20 MeV), in this case the picked-up or stripped nucleons will be in a discrete energy level. Therefore, the process probability strongly depends on the single particle levels of the involved nuclei, and a statistical approach is not valid. Multinucleon-transfer reactions is the name usually

employed to describe this process. Concluding, in this kind of measurement at a fixed angle of the large-acceptance spectrometer coupled to a γ-ray array the most important parameter to define roughly the reaction regime is the excitation energies of ejectiles. This is, in turn, a function of the initial kinetic energy (i.e. of the colliding beam energy) and of the number of transferred nucleons. For higher kinetic energy and more transferred nucleons, a large final excitation energy can be accessed. In experiments using a large-acceptance spectrometer coupled to a γ-ray array a pure quasi-elastic process can be recognized by a well define peak in Q value. The deep inelastic collisions usually have large transfer of energy with a broad Q-value distribution since a large amount of kinetic energy is dissipated into internal excitation energies of the two emerging fragments. Even if generally there is a difference in the mean energy loss values of the two cases, it is difficult to disentangle them since their overlap may be significant. However, it is expected that deep-inelastic reactions contribute more at more forward angles [32]. Deep inelastic nuclear reactions and multinucleon-transfer reactions have some general features in common:

- The collision preserves the binary character of the system: in fact, the ejectiles are similar to the initial nuclei, having exchanged a few nucleons. Therefore it is possible to distinguish a projectile-like or beam-like ejectile from a target-like ejectile.
- Angular momentum is transferred from the relative orbital motion to the intrinsic spin of the two reaction products.
- The generated ejectiles de-excite primarily through evaporation of light particles such as neutrons, protons and α particles and through γ decay. Heavier fragments decay also via fission.

In a multinucleon-transfer experiment it is very important to know the angle at which the reaction cross section is peaked: in fact, detectors such as those for ion identification should be placed at this angle to obtain the highest possible statistics of multinucleon-transfer events. This angle is called the grazing angle, and it indicates the direction of the ejectiles which are the products of nuclear reaction. It is thus defined as the angle $\theta_{grazing}$ at which the distance of closest approach equals the sum of the nuclear radii, so that the two interacting nuclei are just *touching* each other. The distance of the closest approach d is given by [31]:

$$d = \left(\frac{Z_t Z_p e^2}{4\pi\epsilon_0 E_k}\right) \times \left(1 + \csc\frac{\theta_{grazing}}{2}\right) \tag{3}$$

where Z_t and Z_p are the atomic numbers of the two nuclei involved and E_k is the kinetic energy. The distance of closest approach equals the sum of the nuclear radii, i.e. when the two nuclei are just touching, which can be estimated by the expression,

$$d = 1.2\left(A_t^{1/3} + A_p^{1/3}\right) fm \tag{4}$$

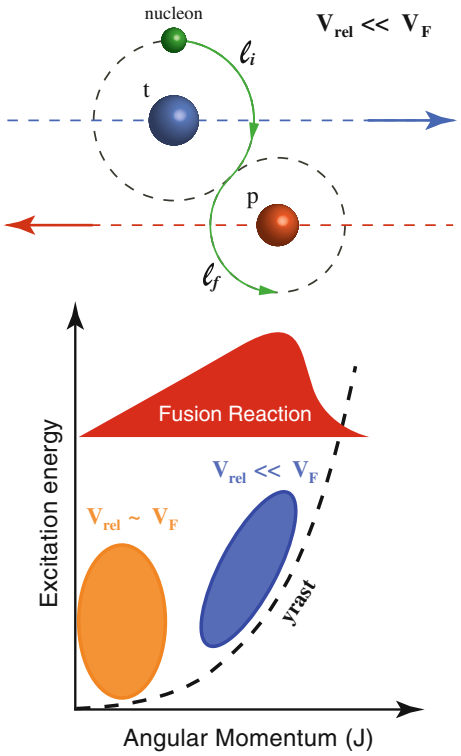

Fig. 7 *Upper panel* Schematic design of the angular momentum transfer in the case of transfer reactions at energies close to the Coulomb barrier. The angular momenta of the orbiting nucleons of the initial $\uparrow \boldsymbol{\ell}_i$ and final state $\downarrow \boldsymbol{\ell}_f$ would be perpendicular to the scattering plane and their projections will have opposite sign. *Lower panel* Schematic representation of the states populated in the plane excitation energy versus angular momentum degrees of freedom for the two regimes discussed in the text: small relative velocities ($E_{rel} < E_F$) and higher transfer energies ($E_{rel} \sim E_F$). The region of population for fusion-evaporation reactions has been depicted for comparison

where A_p is the nuclear mass number for the beam and A_t is the nuclear mass number for the target. By comparing (3) and (4) a straightforward estimate of the grazing angle can be obtained.

The knowledge of entry spin distributions and the related angular momentum population in multinucleon-transfer reactions has a significant bearing on the application of such reactions in the study of medium- to high-spin states in neutron-rich nuclei. In the case of transfer reactions at energies close to the Coulomb barrier, since the relative kinetic energy is very small in comparison to the Fermi kinetic energies ($E_{rel} < E_F$), the transfer of a nucleon happens as it is sketched in Fig. 7 (upper panel), i.e. the angular momenta of the orbiting nucleons of the initial $\boldsymbol{\ell}_i$ and final state $\boldsymbol{\ell}_f$ would be perpendicular to the scattering plane and their projections will have opposite sign. One of the characteristics of transfer reactions among heavy ions is that the spin $\mathbf{s}_{i,f}$ tends to keep its direction in the transfer process [33]. The maximum transfer angular momentum is given by:

$$|\boldsymbol{\ell}_{transfer}| = |\boldsymbol{\ell}_i + \boldsymbol{\ell}_f| = |\boldsymbol{\ell}_i| + |\boldsymbol{\ell}_f| \tag{5}$$

At a higher energies ($E_{rel} \sim E_F$), due to the larger relative angular momentum between the two nuclei, one tends to have a similar population of the states $\boldsymbol{J}_f = \boldsymbol{\ell}_f \pm 1/2$. Therefore, these two regimes will populate two very different regions in an excitation energy versus angular momentum plot, as illustrated in Fig. 7 (lower panel) [34]. The transfer mechanism, due to the angular momentum matching conditions discussed above, makes possible a strong yrast population. Some efforts were made in the study of entry spin distributions in the seventies (e.g. [35]). However, not much was done in the last decades until some recent studies which utilize the power of large-scale γ-ray arrays for channel selection was attacking this problem (e.g. [36, 37]).

4 In-Beam Spectroscopic Studies of Neutron-Rich Nuclei Populated in Multinucleon-Transfer Reactions

The use of multinucleon-transfer reactions has extended our knowledge of the nuclear structure of neutron-rich nuclei. This section will be dedicated to the discussion of the experimental spectroscopic potential of these reactions when a γ-ray array coupled to a large-acceptance magnetic spectrometer and a thin target (ion-γ coincidence technique) are used. This experimental technique overcomes most of the limitations that emerge when using a thick target, namely: (i) the lack of ion-identification, (ii) the possibility to measure very short living states, (iii) the measurement of γ angular distributions and (iv) the possibility to measure lifetimes of nuclear states. The latter point will be discussed in Sect. 5.

The ion-γ coincidence technique is particularly interesting for nuclei moderately neutron-rich that are poorly known or completely unknown, since the mass number A and the atomic number Z can be identified in coincidence with γ rays event-by-event. Figure 8 shows the γ rays in coincidence with the isotopes of Se populated in the multinucleon-transfer reaction ^{198}Pt(^{82}Se; $^{A'}$Se)^{A}Pt. It can be clearly seen the unambiguous identification of the γ transitions belonging to the different isotopes. These γ transitions de-excite mainly yrast states but, as it has been already discussed in Sect. 3, they might de-excite non-yrast states, which are also populated with less probability in such reactions, see [36, 38]

Once the γ rays of a specific nucleus have been identified by the ion-γ coincidence technique, the following step is to build the level scheme and to determine the spin and parity of the nuclear states emitting these γ rays. Angular distributions and also linear polarization measurements of the γ transitions are a powerful tool to firmly establish the spin and parity of the nuclear states [39]. In order to be able to measure γ-ray angular distributions, that will provide the multipolarity of the transition, it is necessary to have a preferential spin alignment of the nuclei. It is well known, since the seventies, that heavy-ion transfer reactions at energies around the Coulomb barrier produce a reduced spin alignment in comparison with fusion-evaporation reactions [40]. However, it has been shown that such alignment is large enough

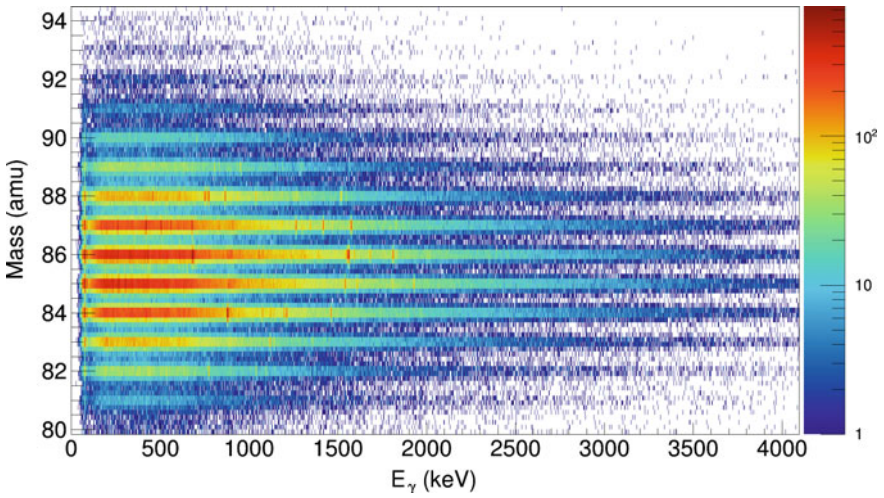

Fig. 8 Matrix of the γ rays versus the mass of the Se isotopes populated via pure neutron transfer channels in a multinucleon-transfer reaction where a beam of ^{82}Se with an energy of 426 MeV impinged on a ^{198}Pt target. The γ rays were identified with AGATA and the mass was measured with PRISMA

to perform detailed angular distributions. For example Montanari and coworkers measured the spin alignment of a low-energy binary multinucleon-transfer reaction at grazing angles (^{48}Ca beam at 282 MeV impinging on a ^{64}Ni target) to be $\alpha_2 = 0.71 \pm 0.13$ as can be seen in Fig. 6 of [41]. The spin alignment in this reaction is perpendicular to the reaction plane that, when a magnetic spectrometer is used, is defined by the magnetic spectrometer itself. Therefore, in multinucleon-transfer reactions there is an asymmetry with respect to the azimuthal angle ϕ, opposite to what happens in fusion-evaporation reactions where a symmetry with respect to the azimuthal angle ϕ is observed. The asymmetry in ϕ can be clearly seen in Fig. 6 of [41]. On the other hand the measurement of the polarization of a γ ray, that will give information on its electric or magnetic character, is measured by exploiting the azimuthal-angle dependence of the Compton scattering differential cross section, for a detailed discussion, see [42]. In the following, an example of an angular distribution and polarization measurement will be discussed.

Figure 9b shows an example of an angular distribution measurement with the γ-ray array CLARA [44] for the case of a stretched $L = 2$ transition such as the $2^+ \rightarrow 0^+$ transition at 1027 keV of ^{50}Ca. The CLARA array consisted in 24 high-purity germanium clover detectors, arranged in a hemisphere with the following polar angles $\theta = 100°$, 130° and 150° with respect to the optical axis of the PRISMA spectrometer. The clover detectors are composed of four germanium crystals mounted in the same cryostat and surrounded by an anti-Compton shield. The three points presented in Fig. 9b correspond to these polar angles. The intensity measured in the three rings was normalized to the one at 100°, after taking into account the efficiency of each ring.

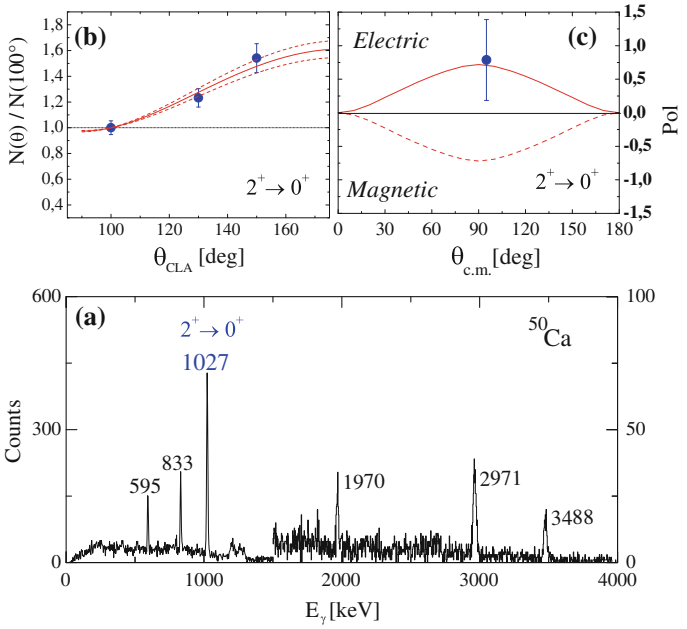

Fig. 9 *Bottom* Gamma spectrum measured in coincidence with ^{50}Ca ions detected in PRISMA. Note that above 1500 keV the scale of the y axis is given on the *right*. Panel **a** Angular distribution of the $2^+ \rightarrow 0^+$ transition at 1027 keV. The *solid line* is the fit by the angular distribution function $W(\theta) = 1 + a_2 P_2(\cos\theta)$, with $a_2 = 0.51 \pm 0.06$. The *dotted lines* give the uncertainty in $W(\theta)$, as follows from the error propagation in the a_2 coefficient. Panel **b** Polarization measurement of the $2^+ \rightarrow 0^+$ transition. *Solid* and *dashed lines* give the expected values for a pure electric or magnetic quadrupole decay. Taken from [43]

The data was fitted using the angular distribution function $W(\theta) = 1 + a_2 P_2(\cos\theta)$, $P_2(\cos\theta)$ being the Legendre polynomial and a_2 the attenuated angular distribution coefficient (solid line). The dotted lines give the uncertainty in $W(\theta)$ following the error propagation in a_2. This technique has been used in various mass regions of neutron-rich nuclei, such as Co, Ge and As isotopes [45, 46]. Figure 9c shows an example of linear polarization P for the $2^+ \rightarrow 0^+$ transition at 1027 keV of ^{50}Ca using the same reaction and the same experimental setup just discussed above. For the polarization measurement, only the most sensitive clover detectors at 100° were used. P is defined as the ratio A_{sym}/Q, with $A_{sym} = (N_\perp - N_\parallel)/(N_\perp + N_\parallel)$, the measured asymmetry in the number of photons scattered, in the clover crystals, perpendicular ($N_\perp$) and parallel ($N_\parallel$) to the emission plane. Q is the polarimeter sensitivity [47]; for the CLARA array the polarimeter sensitivity can be found in Fig. 1 of [41]. For the $2^+ \rightarrow 0^+$ transition at 1027 keV of ^{50}Ca a clear positive asymmetry A_{sym} was measured. This is a strong indication of the electric character of this γ decay, which gave a linear polarization $P = 0.79 \pm 0.6$, as expected for a stretched $2^+ \rightarrow 0^+$ electric transition with ≈70 % spin alignment.

It is evident by now the high potential of multinucleon-transfer reactions to access moderately neutron-rich nuclei and to enlarge to a large extent the nuclear structure information on those nuclei. This technique has been heavily used in the last decades and a wealth of experimental data have been obtained in various regions of the Segré chart by applying the ion-γ coincidence method to the beam-like recoils, see for example [43, 48–52].

One open question still remaining regards the possibility to learn something about the more massive target-like recoils. The following paragraphs will be dedicated to the binary partner method that will explain how it is possible to gain spectroscopic access also to the target-like recoils that typically cannot be identified in atomic number and mass by a large-acceptance magnetic spectrometer.

The binary partner method was developed in order to study heavy neutron-rich nuclei that cannot be accessed otherwise due to their large mass and atomic number. In fact, these heavy nuclei are also produced with low kinetic energy, that associated with their high A and Z, makes impossible their full identification with a large-acceptance magnetic spectrometer such a PRISMA [36, 53] or VAMOS [54].

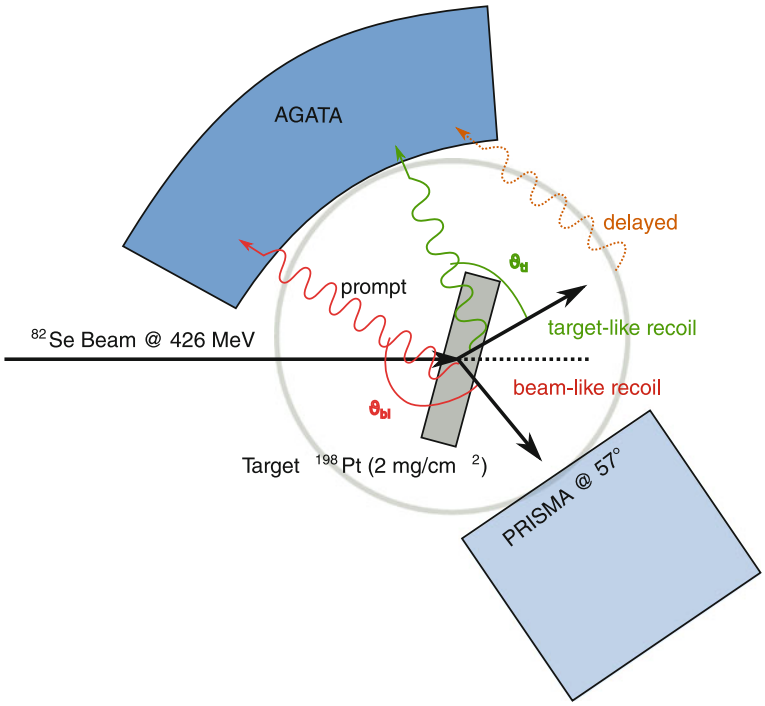

Fig. 10 Sketch showing the binary reaction where the lighter beam-like recoil is identified in the magnetic spectrometer, PRISMA, that has been positioned at the grazing angle of the reaction. The velocity vector for the heavier target-like recoil is also shown. The angles used for the Doppler correction for the target-like (θ_{tl}) and beam-like (θ_{bl}) recoils are also indicated. Adapted from [29]

To explain the binary partner method a specific example will be taken; a beam of ^{82}Se with an energy of 426 MeV impinging on a ^{198}Pt target, where only the lighter beam-like recoil is identified in the magnetic spectrometer. Information about the heavier target-like recoil will be reconstructed under the assumption of a pure binary reaction, i.e. a two-body reaction. This can be done using relativistic kinematics, as described in detail in [55]. The two binary partners, the beam- and target-like, will de-excite emitting γ rays, see Fig. 10. In order to identify the γ-ray transitions belonging to the beam- or target-like recoils one needs to perform the Doppler correction using the angle between the recoil and the γ emitted, i.e. θ_{tl} or θ_{bl}, respectively, see Fig. 10. The velocity vector for the target-like case will be obtained via the kinematics calculations as mentioned above. Figure 11 exemplifies this method for the heavy-partner ^{196}Os and the light partner ^{84}Kr populated in the reaction ^{198}Pt + ^{82}Se. In this case the nucleus ^{196}Os is populated via the two-proton transfer reaction ^{198}Pt(^{82}Se; ^{84}Kr)^{196}Os. Figure 11a shows the Doppler corrected γ spectrum for the ion ^{84}Kr, that has been directly detected by the PRISMA spectrometer. The FWHM of the γ peaks is of around 3.6 ‰ very close to the nominal intrinsic resolution of 2.0 ‰. Instead, the panel b shows the Doppler corrected γ spectrum for ^{196}Os after its kinematical reconstruction. Here the FWHM of the γ peaks is of around 6.7 ‰, three times worse than the intrinsic resolution, and this is expected since the reconstruction of the velocity vector presents an inherent uncertainty due to secondary processes, such as neutron evaporation and the energy loss in the target. It is worth to keep in mind that the average velocity for the beam-like fragments is $\beta \approx 8.5$ %, while for the target-like fragments is of $\beta \approx 3.5$ %. In addition, it can be noticed that in spectrum (b) of Fig. 11 peaks arise from osmium isotopes with lower masses due to the evaporation of neutrons. It is possible to observe osmium isotopes down to ^{190}Os, which corresponds to 6 neutron evaporation. The Doppler corrected γ spectrum (c) of Fig. 11 is obtained from spectrum (b) with an additional gate on the excitation energy, i.e. a gate in the Total Kinetic Energy Loss (TKEL) of the reaction derived from the energy measurement at the magnetic spectrometer focal plane [56]. When applying a gate at low values of TKEL the secondary processes, such as neutron evaporation, are reduced. Therefore, the pure two-proton transfer channel, ^{196}Os, is enhanced. The final level scheme of ^{196}Os derived from this analysis can be found in [57].

Since AGATA has no collimators and no anti-Compton shields, γ rays can be detected with a high efficiency even when they are emitted away from the target position. This is not the case with the traditional arrays with anti-Compton shields since the detectors are collimated to observe ± 1 mm around the center of the γ-ray array, where the reaction target is located. This feature of γ-ray tracking arrays makes then possible the observation of delayed γ rays. After a time of flight of around 10–15 ns, the target-like recoils are deposited in the target chamber. If the implanted ion is produced in a long living excited nuclear level, i.e. isomeric state, it can de-excite via the emission of γ rays. This process is schematically shown in Fig. 10.

Figure 12 shows a matrix of time versus energy of γ rays, gated on ^{80}Se, the binary partner of ^{200}Pt. This channel corresponds to the two-neutron transfer ^{198}Pt(^{82}Se, ^{80}Se)^{200}Pt. Due to the evaporation of neutrons, this spectrum contains also γ rays

from other platinum isotopes with a lower mass. The prompt peak has an arbitrary offset, set to 2200 ns, and has a FWHM of around 15 ns. On the right hand side of the prompt peak, delayed γ rays can be observed. The transitions belonging to ^{200}Pt are highlighted in green. From the time distribution of the delayed γ ray de-exciting an isomer it is possible to calculate the lifetime that, depending on the yield of the isotope, can range from a few tenths of nanoseconds to hundreds of nanoseconds.

It is worth to mention that also the region of the highly deformed ^{170}Dy has been studied using the binary partner method [58].

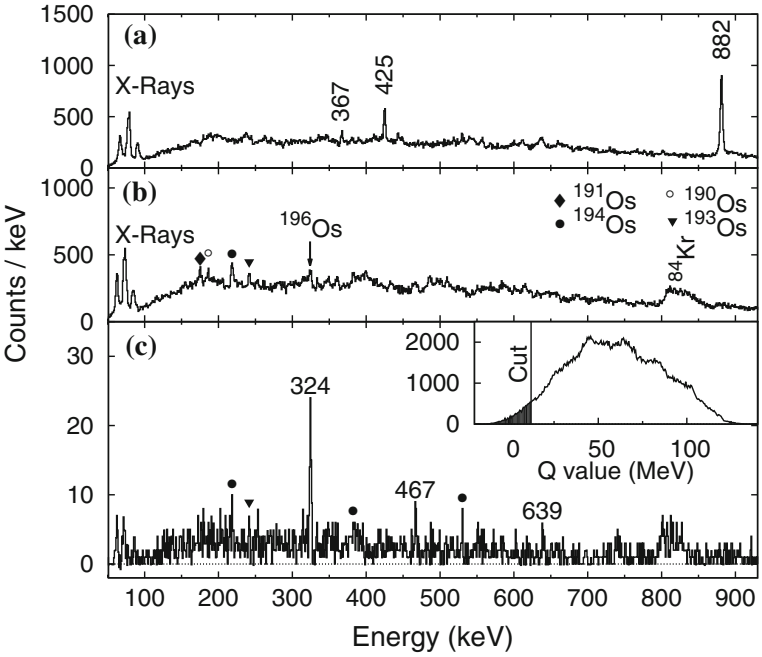

Fig. 11 These γ-ray spectra has been obtained after gating on the beam-like recoils ^{84}Kr identified with PRISMA. **a** The spectrum is Doppler corrected for ^{84}Kr. The strongest γ-ray transitions of ^{84}Kr are labeled. **b** The spectrum is Doppler corrected for ^{196}Os, the binary partner of ^{84}Kr. The wrongly Doppler corrected $2_1^+ \rightarrow 0_{gs}^+$ γ transition of ^{84}Kr and the $(2_1^+) \rightarrow 0_{gs}^+$ of ^{196}Os are indicated. The strongest transitions from other Os isotopes, populated after neutron evaporation, are indicated by *different symbols*. **c** The same as (**b**) with an additional gate on the reconstructed TKEL value $<$12 MeV (see *inset*) and a multiplicity of the γ rays of one. Peaks labeled by the energy are assigned to ^{196}Os. Taken from [57]

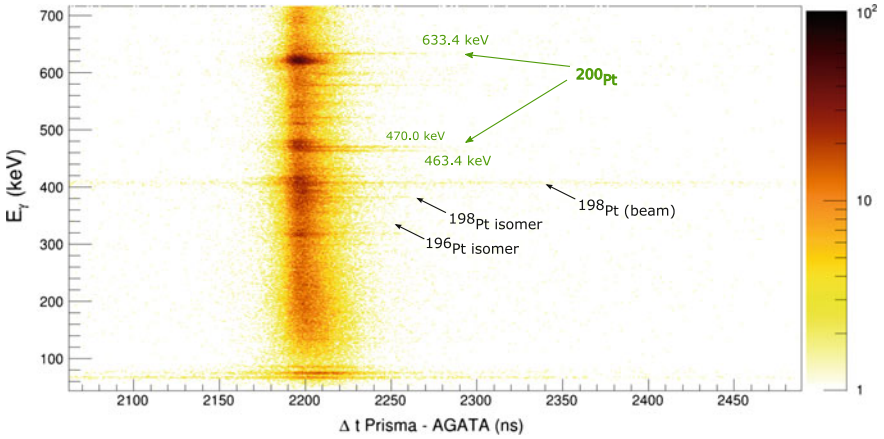

Fig. 12 Matrix of γ-ray time versus γ-ray energy gated on two-neutron transfer to ^{80}Se, where the binary partner is ^{200}Pt. A gate on the TKEL smaller than 60 MeV has been performed. Figure taken from [29]

5 Lifetime Measurements in Neutron-Rich Nuclei Populated in Multinucleon-Transfer Reactions

The electromagnetic transition probabilities can be derived from the lifetimes of the nuclear states, that can be measured using various methods including the Recoil Distance Doppler Shift method (RDDS) which is sensitive to lifetimes ranging from few to hundreds of picoseconds. Equation 6 shows, as an example, the relation between the reduced transition probability of a quadrupole transition $E2$ and the lifetime of the state emitting that transition:

$$B(E2)\uparrow = \frac{40.81 \cdot 10^9}{\tau E_\gamma^5 (1+\alpha)} \tag{6}$$

where the $B(E2)\uparrow$ is given in $e^2 fm^4$, τ in ps, the energy of the γ transition in keV and α is the internal conversion coefficient. All the relations between the reduced transition probabilities and the lifetime of a state can be found in [39]. The RDDS technique has been widely employed in the past by making use of plunger setups in a broad range of nuclear reactions, see [59] and references therein. A plunger device is formed by a thin target where the beam-induced nuclear reaction populates the nuclei of interest and a stopper where the recoils will be stopped. The stopper foil is placed at a well defined distance d from the target foil. In the case of multinucleon-transfer reactions since after the target the recoils have to be identified by a magnetic spectrometer, a non-collinear differential plunger (the stopper is substituted by a degrader), that can be positioned at the grazing angle, was developed for grazing reactions by the IKP University of Cologne group, and was commissioned for the

first time in a CLARA-PRISMA campaign at INFN-LNL [44]. A design and a picture of the non-collinear differential plunger device at the Laboratori Nazionali di Legnaro can be seen in Fig. 13.

The cross sections for the most exotic channels in multinucleon-transfer reactions is low as well as the γ multiplicity. Therefore, only singles γ data can be collected with sufficient statistics. However, since more than one excited level can be populated, for a correct lifetime determination it is important to take into account the feeding of the level. The effective level feeding can be controlled by gating on the Total Kinetic Energy Loss (TKEL). Figure 14 illustrates the population dependence of the 2^+ and 4^+ states as a function of the TKEL for the nucleus ^{64}Ni. A possible TKEL gate is shown as a vertical line. This variable is of utmost importance to determine the lifetime of a state. In [60] it has been shown the importance of gating on the TKEL of the reaction to get correctly the lifetime of the first 2^+ excited state in ^{46}Ca.

As an example of a RDDS measurement for a nucleus populated in a multinucleon-transfer reaction, the experiment described in [61], performed with the γ-ray array CLARA [44] and the magnetic spectrometer PRISMA [53], will be illustrated. The nuclei ^{50}Ca and ^{51}Sc were populated as products of a multinucleon-transfer reaction following the collision of a ^{48}Ca beam onto a ^{208}Pb target. The ^{48}Ca beam, at a bombarding energy of 310 MeV, was delivered by the LNL Tandem-ALPI accelerator complex. The target consisted of 1.0 mg/cm^2 of enriched ^{208}Pb evaporated onto a 1.0 mg/cm^2 Ta support to accomplish the stretching of the target. A thick 4 mg/cm^2 ^{nat}Mg foil used as an energy degrader of the recoiling ejectiles was positioned after the target. Different target-degrader distances, ranging from 30 to 2200 μm were employed during the experiment. Figure 15 shows, for different target-degrader distances, Doppler-corrected γ-ray spectra associated with ^{50}Ca and ^{51}Sc for selected energy regions including their respective $2^+ \rightarrow 0^+$ 1027-keV and $11/2^- \rightarrow 7/2^-$ 1065-keV transitions. The Doppler correction is performed on an event by event basis using the velocity reconstructed by PRISMA, i.e. β_{After}. Depending whether

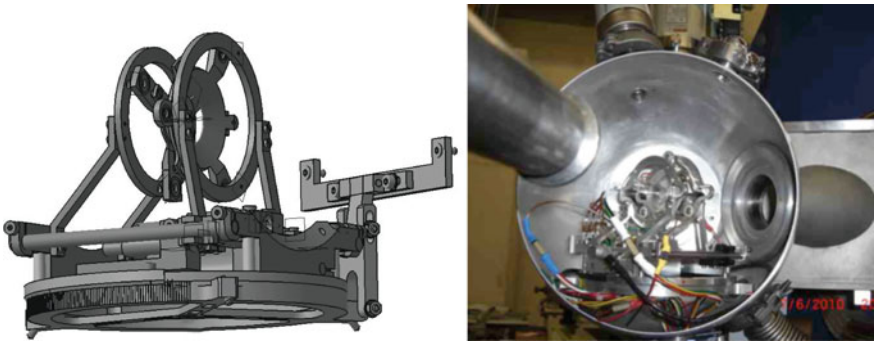

Fig. 13 *Left* Drawing of the plunger device and its supporting structure used for multinucleon-transfer reactions. *Right* Picture of the plunger device mounted at AGATA/PRISMA target chamber at the Laboratori Nazionali di Legnaro

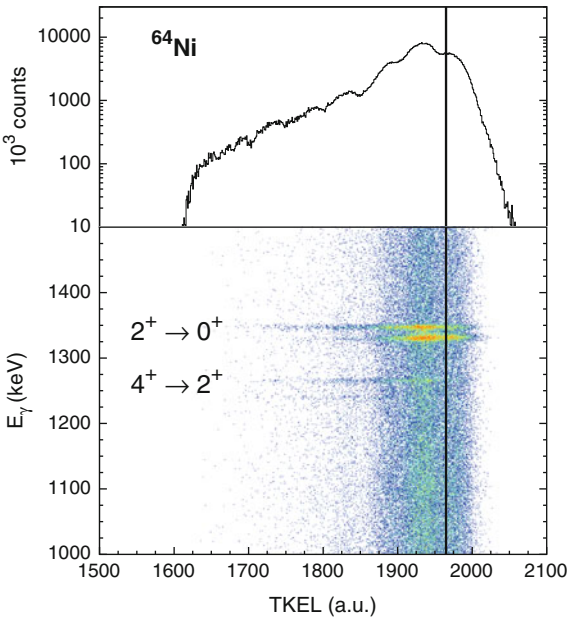

Fig. 14 Doppler-corrected γ-ray spectra corresponding to the $2^+ \rightarrow 0^+$ and $4^+ \rightarrow 2^+$ transitions in ^{64}Ni as a function of TKEL. It can be observed the difference in the population for the 2^+ state with respect to the 4^+ state that appears for higher values of TKEL. A *vertical line* defines the position of a possible gate in TKEL to reduce the feeding to the 2^+

the γ ray was emitted before or after the degrader the γ rays exhibit different Doppler shifts. Therefore, the γ spectrum shows two peaks for the transition of interest, as can be seen in Fig. 15. The higher-energy one, E_{After}, which has an energy resolution of 0.6 %, corresponds to γ rays emitted after passing the degrader, with an average velocity of $\langle\beta_{After}\rangle \approx 8.0\,\%$, while the lower-energy one, E_{Before}, corresponds to γ rays emitted before the degrader, with an average velocity of $\langle\beta_{Before}\rangle \approx 10.0\,\%$. The average velocity before the degrader $\langle\beta_{Before}\rangle$, which is the one that defines the lifetime, could be determined by using the centroid data of the peaks E_{After} and E_{Before}, according to the following relation,

$$\frac{E_{After} - E_{Before}}{E_{After}} = (\beta_{After} - \beta_{Before})\cos(\theta) + \vartheta(2) \tag{7}$$

where θ is the angle between the recoil trajectory and the γ-ray array and $\vartheta(2)$ represents a second order term, which is negligible. The relative intensities of the peak areas as a function of the target-degrader distance allow a determination of the lifetime of the state of interest. Figure 16 shows the negative logarithm of the experimental ratio $R = \frac{I_{After}}{I_{Before}+I_{After}}$, where $I_{After,Before}$ is the peak area of the transitions emitted after and before the degrader, for the different target-degrader distances, as well as the lifetime fit for both the 2^+ and the $11/2^-$ states in ^{50}Ca and ^{51}Sc, respectively. The lifetime obtained for the 2^+ state in ^{50}Ca is $\tau = 96 \pm 3$ ps. Different gates in the TKEL value yielded always a lifetime compatible with this value, indicating that the states feeding the 2^+ level have much shorter lifetimes and hence do not

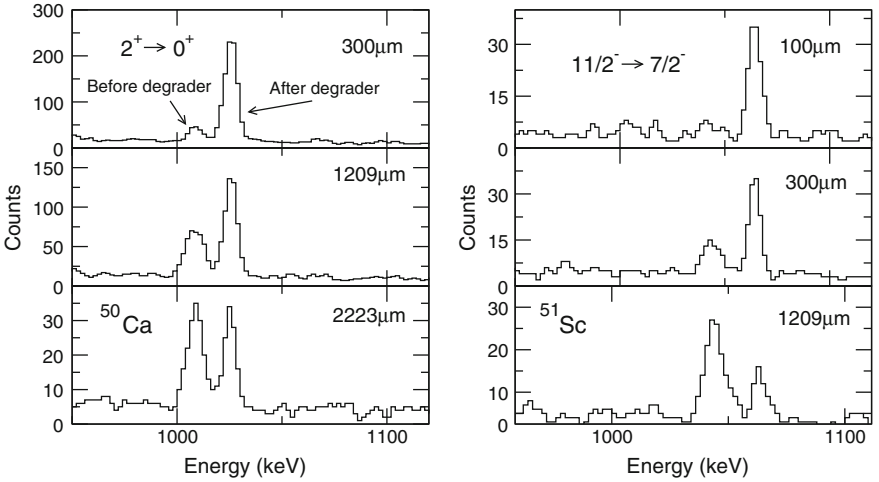

Fig. 15 Doppler-corrected γ-ray spectra showing the $2^+ \rightarrow 0^+$ 1027-keV and the $11/2^- \rightarrow 7/2^-$ 1065-keV transitions in ^{50}Ca and ^{51}Sc for different target-degrader distances. The higher-energy and lower-energy peaks correspond to the decays after and before the degrader, respectively. Taken from [61]

significantly affect the measured lifetime. The lifetime obtained for the $11/2^-$ state in ^{51}Sc is $\tau = 28 \pm 7$ ps. The experimental errors take into account the statistical error and the velocity uncertainty. In the case of ^{51}Sc a low-TKEL gate, which corresponds to low-excitation energies, was set in order to reduce the feeding from upper states that could bias the lifetime. The absence of such a feeding has been confirmed by the fact that after a low-TKEL gating, one does not observe any other γ peak, besides the $11/2^- \rightarrow 7/2^-$ 1065-keV transition in the ^{51}Sc γ spectrum. From the measured lifetimes, the reduced transition probabilities, according to (6), have been extracted, giving $B(E2\downarrow) = 38 \pm 1\ e^2\text{fm}^4$ and $B(E2\downarrow) = 105 \pm 25\ e^2\text{fm}^4$ for the $2^+ \rightarrow 0^+$ and the $11/2^- \rightarrow 7/2^-$ transitions in ^{50}Ca and ^{51}Sc, respectively.

Several other successful measurements were performed with this plunger to determine the lifetime of the low-lying excited states in neutron-rich nuclei at the CLARA-PRISMA setup [44]: ^{44,46}Ar [62], ^{49}K [63], as well as at the AGATA-PRISMA setup [3]: $^{70-74}$Zn [64], $^{63-65}$Co [65] and ^{69,71,73}Cu [66]. The same plunger was also used at the EXOGAM-VAMOS setup [54, 67] to measure the lifetimes of the low-lying excited states in ^{62,64}Fe [68], ^{63,65}Co [69] and ^{69,71}Zn [70]. All these measurements have contributed greatly to improve the knowledge on the nucleon-nucleon interaction in the presence of an excess of neutrons in the nuclear medium.

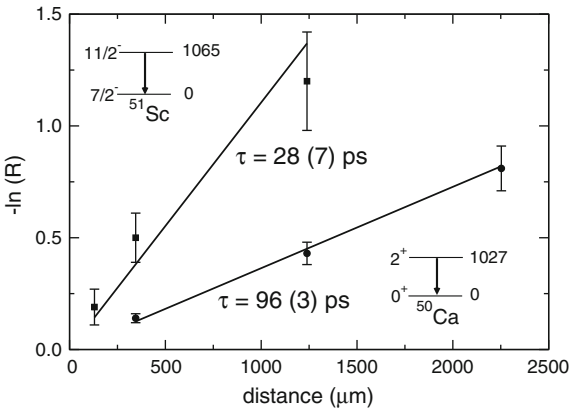

Fig. 16 Negative logarithm of the experimental ratio $R = \frac{I_{After}}{I_{Before} + I_{After}}$, where $I_{After,Before}$ is the peak area of the transitions emitted after and before the degrader, for the different target-degrader distances. It shows as well the fitted lifetime of the 2^+ and the $11/2^-$ states in ^{50}Ca and ^{51}Sc. Taken from [61]

6 Summary

In this paper, the main principles of γ-ray spectroscopy have been discussed followed by a description of the main developments in γ-ray spectroscopy from inorganic scintillators to semiconductor germanium detectors with anti-Compton shields and finally the γ-ray tracking arrays such as AGATA. Later on, thin-target experiments exploiting multinucleon-transfer reactions used to access spectroscopy information of moderately neutron-rich nuclei have been review. The characteristics of multinucleon-transfer reactions have been explained in detail. The advantages of these experiments such as: ion-γ coincidence identification, the possibility to measure angular distributions, polarization of the emitted γ rays and the lifetimes of the states have been discussed. Some results obtained in various regions of the Segré Chart are discussed throughout the text showing the fast progress that has been achieved with this technique in the last decade. In the near future one of the big challenges, ad pleniorem scientiam, will be to perform multinucleon-transfer reactions with radioactive ion beams that will allow to push further our knowledge on neutron-rich nuclei with a large neutron excess.

Acknowledgments I would like to thank all of my colleagues who have assisted with putting together, performing and analyzing the results from the experiments described in this work whose names are listed in the cited publications. Special thanks go to all the colleagues from the CLARA, AGATA and PRISMA groups, whose expertise and involvement in this research was essential.

References

1. H. Morinaga, P.C. Gugelot, Nucl. Phys. **46**, 210 (1963)
2. S. Akkoyun et al., Nucl. Instrum. Methods Phys. Res. A **668**, 26 (2012)
3. A. Gadea et al., Nucl. Instrum. Methods Phys. Res. A **654**, 88 (2011)
4. M.A. Deleplanque et al., Nucl. Instrum. Methods Phys. Res., Sect. A **430**, 292 (1999)

5. S. Paschalis et al., Nucl. Instrum. Methods Phys. Res., Sect. A **709**, 44 (2013)
6. R.D. Evans, *The Atomic Nucleus* (Mc Graw-Hill, New York, 1955)
7. M. Jaskelainen et al., Nucl. Instrum. Methods Phys. Res. **204**, 385 (1983)
8. R.S. Simon, J. Physique **41**, C 10 (1980)
9. D. Guillemaud-Mueller, in *Tours Symposium on Nuclear Physics III, AIP Conference Proceedings*, vol. 425 (1997), p. 290
10. D. Weisshaar et al., Nucl. Instrum. Methods Phys. Res. Sect. A **624**, 615 (2010)
11. S. Takeuchi et al., Nucl. Instrum. Methods Phys. Res., Sect. A **763**, 596 (2014)
12. D. Steppenbeck et al., Nature (London) **502**, 207 (2013)
13. A. Maj et al., Acta Phys. Pol. B **40**, 565 (2009)
14. A. Giaz et al., Nucl. Instrum. Methods Phys. Res. Sect. A **729**, 910 (2013)
15. G.F. Knoll, *Radiation Detection and Measurement*, 4th edn. (Wiley, 2010)
16. P.J. Nolan et al., Nucl. Instrum. Methods Phys. Res. Sect. A **236**, 95 (1985)
17. D. Bazzacco, in *Proceedings of Workshop on Large Gamma-ray Detector Arrays*, Chalk River, Canada, AECL-10613, vol. 376 (1992)
18. J. Simpson, Z. Phys. A **358**, 139 (1997)
19. I.Y. Lee, Nucl. Phys. A **520**, 641c (1990)
20. W. Gelletly, J. Eberth, Gamma-ray arrays: past, present and future. Lect. Notes Phys. **700**, 79 (2006)
21. http://physics.nist.gov/PhysRefData/Xcom/Text/XCOM.html
22. M.A. Deleplanque et al., Nucl. Instrum. Methods Phys. Res. Sect. A **430**, 292 (1999)
23. I.Y. Lee, M.A. Deleplanque, K. Vetter, Rep. Prog. Phys. **66**, 1095 (2003)
24. S. Agostinelli et al., Nucl. Instrum. Methods Phys. Res. Sect. A **506**, 250 (2003)
25. J.J. Valiente-Dobón et al., LNL-Annual Report, vol. 95 (2014)
26. C.H. Dasso et al., Phys. Rev. Lett. **73**, 1907 (1994)
27. R. Broda et al., Phys. Lett. B **251**, 245 (1990)
28. R. Broda, J. Phys. G: Nucl. Part. Phys. **32**, R151 (2006)
29. P.R. John, Study of shape evolution in the neutron-rich osmium isotopes with the advanced gamma-tracking array AGATA. Ph.D. thesis, Universitá di Padova (2014)
30. L. Corradi, G. Pollarolo, S. Szilner, Phys. G: Nucl. Part. Phys. **36**, 113101 (2009)
31. R. Bass, *Nuclear Reactions of Heavy Ions* (Springer-Verlag, New York, 1980)
32. T. Mijatovic, Study of heavy-ion reactions with large solid angle magnetic spectrometers. Ph.D. thesis, University of Zagreb (2015)
33. F. Zardi, Teoria delle collissioni fra ioni pesanti, Laboratori Nazionali di Legnaro (1979)
34. G. Pollarolo (private communication)
35. R. Bock et al., Nukleonika **22**, 1 (1977)
36. S. Szilner et al., Phys. Rev. C **76**, 024604 (2007)
37. S. Szilner et al., Phys. Rev. C **84**, 014325 (2011)
38. S. Bhattacharyya et al., Phys. Rev. C **79**, 014313 (2009)
39. H. Morinaga, T. Yamazaki, *In-Beam Gamma-Ray Spectroscopy* (North-Holland Publishing Company, New York, Oxford, Amsterdam, 1976)
40. P. Aguer et al., Phys. Rev. Lett. **43**, 1778 (1979)
41. D. Montanari et al., Phys. Rev. C **85**, 044301 (2012)
42. P.G. Bizzeti et al., Eur. Phys. J. A **51** (2015)
43. D. Montanari et al., Phys. Lett. B **697**, 288 (2011)
44. A. Gadea et al., Acta. Phys. Pol. B **38**, 1311 (2007)
45. F. Recchia et al., Phys. Rev. C **85**, 064305 (2012)
46. E. Sahin et al., Nucl. Phys. A **893**, 1 (2012)
47. L.M. Garcia-Raffi et al., Nucl. Instrum. Methods Phys. Res. Sect. A **391**, 461 (1997)
48. S. Lunardi et al., Phys. Rev. C **76**, 034303 (2007)
49. J.J. Valiente-Dobón et al., Phys. Rev. C **78**, 024302 (2008)
50. W. Krolas et al., Phys. Rev. C **84**, 064301 (2011)
51. M. Rejmund et al., Phys. Rev. C **76**, 021304R (2007)
52. S. Bhattacharyya et al., Phys. Rev. Lett. **101**, 032501 (2008)

53. A. Stefanini et al., Nucl. Phys. A **701**, 217c (2002)
54. M. Rejmund et al., Nucl. Instrum. Methods Phys. Res., Sect. A **646**, 184 (2011)
55. M.A. Baldin, V.I. Gol'Danskii, I.L. Rozenthal, *Kinematics of Nuclear Reactions*, 1st edn. (Pergamon Press, New York, 1961)
56. A.B. Brown et al., Phys. Rev. **82**, 159 (1951)
57. P.R. John et al., Phys. Rev. C **90**, 021301(R) (2014)
58. P.A. Söderström et al., Phys. Rev. C **81**, 034310 (2010)
59. A. Dewald et al., Prog. Part. Nucl. Phys. **67**, 786 (2012)
60. D. Mengoni et al., Eur. Phys. J. A **42**, 387 (2009)
61. J.J. Valiente-Dobón et al., Phys. Rev. Lett. **102**, 242502 (2009)
62. D. Mengoni et al., Phys. Rev. C **82**, 024308 (2010)
63. R. Broda et al., Phys. Rev. C **82**, 034319 (2010)
64. C. Louchart et al., Phys. Rev. C **87**, 054302 (2013)
65. V. Modamio et al., Phys. Rev. C **88**, 044326 (2013)
66. E. Sahin et al., Phys. Rev. C **91**, 034302 (2015)
67. J. Simpson et al., Acta Phys. Hung., New Ser., Heavy Ion Phys. **11**, 159 (2000)
68. J. Ljungvall et al., Phys. Rev. C **81**, 061301 (2010)
69. A. Dijon et al., Phys. Rev. C **83**, 064321 (2011)
70. I. Celikovic et al., Phys. Rev. C **99**, 044311 (2015)

Nuclear Structure Models Based on Relativistic Energy Density Functionals

Dario Vretenar and Tamara Nikšić

Abstract Relativistic energy density functionals provide an accurate global description of nuclear ground states and collective excitations. Guided by the medium dependence of microscopic nucleon self-energies in nuclear matter, semi-empirical functionals have been adjusted to the nuclear matter equation of state and to bulk properties of finite nuclei, and applied to studies of arbitrarily heavy nuclei, exotic nuclei far from stability, and even systems at the nucleon drip-lines. Based on this framework, structure models have been developed that go beyond the mean-field approximation and include collective correlations related to restoration of broken symmetries and fluctuations of collective variables. These models have become standard tools for nuclear structure calculations, able to describe and explain a wealth of new data from radioactive-beam facilities, the exciting phenomenology of nuclear astrophysics, and provide microscopic predictions for low-energy nuclear phenomena.

1 Nuclear Density Functional Theory

Nuclear density functional theory (DFT) provides a global framework for studies of ground-state properties and collective excitations that is applicable across the entire nuclide chart. Among the microscopic approaches to the nuclear many-body problem no other method achieves comparable global accuracy at the same computational cost, and it is the only one that can describe the evolution of structure phenomena from relatively light systems to superheavy nuclei, and from the valley of β-stability

D. Vretenar (✉) · T. Nikšić
Faculty of Science, Physics Department, University of Zagreb,
Bijenička c. 32, Zagreb, Croatia
e-mail: vretenar@phy.hr

T. Nikšić
e-mail: tniksic@phy.hr

J.-E. García-Ramos et al. (eds.), *Basic Concepts in Nuclear Physics: Theory, Experiments and Applications*, Springer Proceedings in Physics 182,
DOI 10.1007/978-3-319-21191-6_4

to the particle drip-lines [1–5]. In practical implementations nuclear energy density functionals (EDFs) are analogous to Kohn-Sham density functional theory, the most widely used method for electronic structure calculations in condensed matter physics and quantum chemistry. In DFT a quantum many-body system is described in terms of a universal energy density functional that, for a given inter-particle interaction, has the same functional form for all systems.

The unknown exact nuclear EDF is approximated by relatively simple functionals of powers and gradients of ground-state nucleon densities and currents, representing distributions of matter, spins, momentum and kinetic energy. Both relativistic and non-relativistic realizations of EDFs are employed in studies of nuclear matter and finite nuclei. In principle a nuclear EDF can incorporate all short-range correlations related to the repulsive core of the inter-nucleon interaction, and long-range correlations mediated by nuclear resonance modes. An additional functional of the pairing density is included to account for effects of superfluidity in open-shell nuclei. Even though it originates in the effective interaction between nucleons, a generic density functional is not necessarily related to any given nucleon-nucleon potential and, in fact, some of the most successful modern functionals are entirely empirical. The advantages of using EDFs in the description of nuclear structure phenomena are evident already at the basic level of implementation—the self-consistent mean-field (SCMF) method: an intuitive interpretation of mean-field results in terms of intrinsic shapes and single-particle states, calculations performed in the full model space of occupied states, and the universality of EDFs that enables their applications to all nuclei throughout the periodic chart.

When considering spectroscopic applications, an important challenge for the framework of EDF is the systematic treatment of collective correlations related to restoration of broken symmetries and fluctuations in collective coordinates. Collective correlations are sensitive to shell effects, display pronounced variations with particle number and, therefore, cannot be incorporated in a universal EDF. The Kohn-Sham nuclear EDF framework has to be extended to take into account these dynamical effects. Important advances have been reported in recent years, and several accurate and efficient methods, based on energy density functionals, have been developed that perform restoration of symmetries broken by the static nuclear mean field, and take into account fluctuations of collective variables around mean-field minima.

1.1 DFT Basics

Density Functional Theory has become a predominant “ab initio” method for structure calculations in quantum many-body systems (atoms, molecules, solids) [6–11]. The DFT framework enables high-speed accurate modelling of ground-state densities and energies. The basic concept is that ground-state properties of a stationary many-body system are determined by the ground-state density alone. Since the density $\rho(\boldsymbol{r})$ is a function of only three spatial coordinates, rather than the 3N coordinates of the N-body wave function, DFT is computationally feasible even for large systems. The

basis of this theory are the Hohenberg-Kohn theorem and the Kohn-Sham scheme, as well as systematic approximations to the central ingredient of the DFT approach: the exchange-correlation energy functional.

For a system of N interacting particles, the Hohenberg-Kohn theorem states that the nondegenerate ground-state (GS) wave function is a unique functional of the GS density $\rho_{\rm gs}(\boldsymbol{r})$, and it follows that the GS expectation value of any observable $\mathscr{O}$ is also a functional of the density. Further, the GS energy and the density $\rho_{\rm gs}(\boldsymbol{r})$ of a system characterised by an external potential $v_0(\boldsymbol{r})$ can be obtained from a variational principle that involves only the density and, finally, there exists a functional $F[\rho]$ such that the energy functional can be expressed in the form:

$$E_{v_0}[\rho] = F[\rho] + \int d^3r\ v_0(\boldsymbol{r})\rho(\boldsymbol{r}). \tag{1}$$

The functional $F[n]$ is *universal* in the sense that for a given particle-particle interaction it does not depend on the external potential $v_0(\boldsymbol{r})$, that is, it has the same functional form for all systems. The Hohenberg-Kohn theorem establishes the variational character of the energy functional, but it does not specify the construction of the universal functional, and the explicit density dependence of $F[\rho]$ is not known.

Practical applications of DFT use the effective single-particle Kohn-Sham (KS) equations [6], introduced for an auxiliary system of N non-interacting particles. According to the Hohenberg-Kohn theorem, there exists a unique energy functional

$$E_s[\rho] = T_s[\rho] + \int d^3r\ v_s(\mathbf{r})\rho(\mathbf{r}), \tag{2}$$

for which the variational equation yields the exact ground-state density $\rho_s(\mathbf{r})$. $T_s[\rho]$ is the universal kinetic energy functional of the non-interacting system. The KS scheme is based on the following assertion: for any interacting system there exists a unique local single-particle potential $v_s(\mathbf{r})$, such that the exact ground-state density $\rho_{\rm gs}(\mathbf{r})$ of the interacting system equals the ground-state density $\rho_s(\mathbf{r})$ of the auxiliary non-interacting system:

$$\rho_{\rm gs}(\mathbf{r}) = \rho_s(\mathbf{r}) = \sum_i^N |\phi_i(\mathbf{r})|^2, \tag{3}$$

expressed in terms of the N lowest occupied single-particle orbitals—solutions of the Kohn-Sham equations:

$$\left[-\nabla^2/2m + v_s(\mathbf{r})\right]\phi_i(\mathbf{r}) = \varepsilon_i\phi_i(\mathbf{r}). \tag{4}$$

The uniqueness of $v_s(\mathbf{r})$ follows from the Hohenberg-Kohn theorem and the single-particle orbitals are unique functionals of the density: $\phi_i(\mathbf{r}) = \phi_i([\rho]; \mathbf{r})$.

For a self-bound system like the atomic nucleus, the energy functional can be decomposed into three separate terms:

$$F[\rho] = T_s[\rho] + E_H[\rho] + E_{xc}[\rho], \tag{5}$$

where T_s is the kinetic energy of the non-interacting A-nucleon system, E_H is a Hartree energy, and E_{xc} denotes the exchange-correlation energy which, by definition, contains everything else—all the many-body effects. The corresponding local exchange-correlation potential is defined by:

$$v_{xc}[\rho](\mathbf{r}) = \frac{\delta E_{xc}[\rho]}{\delta \rho(\mathbf{r})}, \tag{6}$$

and thus

$$v_s[\rho](\mathbf{r}) = v_H[\rho](\mathbf{r}) + v_{xc}[\rho](\mathbf{r}). \tag{7}$$

Since the effective potential depends on the ground-state density, the system of equations (3), (4), and (7) has to be solved self-consistently. This is the Kohn-Sham scheme of density functional theory. By including correlation effects the KS framework goes beyond the Hartree-Fock approximation but, in addition, it has the advantage of being a *local* scheme. It is clear, however, that the usefulness of the Kohn-Sham scheme crucially depends on our ability to construct accurate approximations to the exact exchange-correlation energy. The true exchange-correlation energy functional is *universal*, and one possible approach is to develop E_{xc} from first principles by incorporating known exact constraints. Another is empirical and a parametric ansatz is optimized by adjusting it to a set of data. Structured approximations for E_{xc} typically combine both approaches.

The basic level is the well known local density approximation (LDA). In LDA the exchange-correlation energy functional reads:

$$E_{xc}^{LDA}[\rho] = \int d^3r \; \rho(\boldsymbol{r}) e_{xc}^{unif}(\rho(\boldsymbol{r})), \tag{8}$$

where $e_{xc}^{unif}(\rho(\boldsymbol{r}))$ is the exchange-correlation energy per particle of a uniform infinite system of density ρ (electron gas, nuclear matter), which can be obtained from an "ab initio" calculation. By construction, the LDA should be valid for spatially slowly varying densities, however, it is surprisingly accurate also for many-body systems with pronounced density variations.

Realistic systems are spatially inhomogeneous and it is clearly useful to incorporate the information on the rate of density variation in E_{xc}. In the generalized-gradient approximation (GGA) the exchange-correlation functional is written as:

$$E_{xc}^{GGA}[\rho] = \int d^3r \; f(\rho(\boldsymbol{r}), \nabla\rho(\boldsymbol{r})). \tag{9}$$

GGA is more accurate then LDA but, unlike the input e_{xc}^{unif} in LDA, the function f is not unique and, depending on the method of constructing $f(\rho(\boldsymbol{r}), \nabla\rho(\boldsymbol{r}))$, very different GGAs can be obtained.

The next rung on the ladder of approximations for E_{xc} are "meta-GGA" functionals which, in addition to the density and its gradient, depend on the kinetic energy density of the occupied Kohn-Sham orbitals

$$\tau(\boldsymbol{r}) = \frac{1}{2}\sum_{i}^{occ} |\nabla\phi_i(\boldsymbol{r})|^2. \tag{10}$$

Unlike LDA and GGA, which are explicit functionals of the density alone, the meta-GGA functional

$$E_{xc}^{MGGA}[\rho] = \int d^3r\ g(\rho(\boldsymbol{r}), \nabla\rho(\boldsymbol{r}), \tau(\boldsymbol{r})) \tag{11}$$

explicitly depends on the Kohn-Sham orbitals. Meta-GGA is the highest level of approximation which does not include full non-locality. Approximations of even higher level of accuracy incorporate increasingly complex ingredients, and include fully non-local functionals of the Kohn-Sham orbitals, occupied as well as unoccupied.

The Hohenberg-Kohn theorem and the self-consistent Kohn-Sham scheme can be extended to the relativistic domain [8, 10]. The relativistic Kohn-Sham equation for the auxiliary non-interacting system is represented by the single-particle Dirac equation with a local four-potential that depends on the ground-state four-current.

1.2 Nuclear Energy Density Functionals

The earliest applications of DFT in nuclear structure modelling used the zero-range density-dependent effective Skyrme interaction [12–14]. The corresponding Skyrme functional can be written as the most general energy-density functional in isoscalar and isovector density, spin density, current, spin-current tensor, kinetic density, and kinetic spin density [2, 4, 5]:

$$\begin{aligned}
\rho_0(\mathbf{r}) &= \textstyle\sum_{\sigma\tau} \rho(\mathbf{r}\sigma\tau;\mathbf{r}\sigma\tau) & \rho_1(\mathbf{r}) &= \sum_{\sigma\tau} \rho(\mathbf{r}\sigma\tau;\mathbf{r}\sigma\tau)\,\tau \\
\mathbf{s}_0(\mathbf{r}) &= \textstyle\sum_{\sigma\sigma'\tau} \rho(\mathbf{r}\sigma\tau;\mathbf{r}\sigma'\tau)\,\boldsymbol{\sigma}_{\sigma'\sigma} & \mathbf{s}_1(\mathbf{r}) &= \sum_{\sigma\sigma'\tau} \rho(\mathbf{r}\sigma\tau;\mathbf{r}\sigma'\tau)\,\boldsymbol{\sigma}_{\sigma'\sigma}\,\tau \\
\mathbf{j}_T(\mathbf{r}) &= \tfrac{i}{2}(\nabla'-\nabla)\,\rho_T(\mathbf{r},\mathbf{r}')\big|_{\mathbf{r}=\mathbf{r}'} & \mathscr{J}_T(\mathbf{r}) &= \frac{i}{2}(\nabla'-\nabla)\otimes\mathbf{s}_T(\mathbf{r},\mathbf{r}')\big|_{\mathbf{r}=\mathbf{r}'} \\
\tau_T(\mathbf{r}) &= \nabla\cdot\nabla'\,\rho_T(\mathbf{r},\mathbf{r}')\big|_{\mathbf{r}=\mathbf{r}'} & \mathbf{T}_T(\mathbf{r}) &= \nabla\cdot\nabla'\,\mathbf{s}_T(\mathbf{r},\mathbf{r}')\big|_{\mathbf{r}=\mathbf{r}'},
\end{aligned} \tag{12}$$

respectively, where σ denotes the spin, and τ the isospin of the nucleon. Isoscalar ($T = 0$) quantities are sums ($\rho_0 = \rho_n + \rho_p$), whereas isovector ($T = 1$) densities correspond to proton-neutron differences ($\rho_1 = \rho_n - \rho_p$). The Skyrme functional contains systematically all possible bilinear terms in the local densities and currents of (12) up to second order in the derivatives, which are invariant with respect to parity, time-reversal, rotational, translational and isospin transformations:

$$E_{\rm Sk} = \sum_{T=0,1} \Big\{ C_T^{\rho}\,\rho_T^2 + C_T^{\Delta\rho}\,\rho_T\,\Delta\rho_T + C_T^{\tau}\,\rho_T\tau_T + C_T^{J}\,\mathscr{J}_T^2 + C_T^{\nabla J}\,\rho_T\,\nabla\cdot\mathbf{J}_T C_T^{s}\,\mathbf{s}_T^2 + C_T^{\Delta s}\,\mathbf{s}_T\cdot\Delta\mathbf{s}_T + C_T^{sT}\,\mathbf{s}_T\cdot\mathbf{T}_T + C_T^{\nabla s}\,(\nabla\cdot\mathbf{s}_T)^2 + C_T^{j}\,\mathbf{j}_T^2 + C_T^{\nabla j}\,\mathbf{s}_T\cdot\nabla\times\mathbf{j}_T \Big\} \tag{13}$$

where the coefficients C_T in the isoscalar and isovector channels can be either constants or explicitly depend on the nucleon density.

Even though the functional can be derived from the ground-state expectation value of a zero-range momentum-dependent inter-nucleon force, in modern applications the Skyrme functional is parameterized directly by fitting the coefficients to nuclear ground-state data, without reference to any nucleon-nucleon interaction. Over the last thirty years a large number of different Skyrme parameterizations have been adjusted and used in various applications [4, 5]. However, it is often difficult to compare results obtained with different models, also because they include different subsets of terms from the general functional (13). Ideally, model dependencies could be removed by including all terms allowed by symmetries but available data on finite nuclei can only constrain a subset of parameters, and additional criteria are necessary for selecting the optimal energy density functional form [15].

A number of successful structure models have been based on the relativistic mean-field (RMF) framework of quantum hadrodynamics (QHD) [16, 17]. There are advantages in using mean-field models with manifest covariance. The most obvious is the natural inclusion of the nucleon spin degree of freedom, and the resulting nuclear spin-orbit potential which automatically reproduces the empirical energy spacings between spin-orbit partner states. The consistent treatment of large, isoscalar, Lorentz scalar and vector self-energies provides a unique parametrization of time-odd components of the nuclear mean-field, that is, nucleon currents, which is absent in the non-relativistic representation of the energy density functional. In conventional QHD a nucleus is described as a system of Dirac nucleons coupled to exchange mesons through an effective Lagrangian. The isoscalar scalar σ meson, the isoscalar vector ω meson, and the isovector vector ρ meson build the minimal set of meson fields that, together with the electromagnetic field, is necessary for a description of bulk and single-particle nuclear properties. In the mean-field approximation the meson-field operators are replaced by their expectation values in the nuclear ground state. In addition, a quantitative treatment of nuclear matter and finite nuclei necessitates a medium dependence of effective mean-field interactions that takes into account

higher-order many-body effects. A medium dependence can either be introduced by including nonlinear meson self-interaction terms in the Lagrangian, or by assuming an explicit density dependence for the meson-nucleon couplings. The former approach has been adopted in the construction of several successful phenomenological RMF interactions, for instance, the very popular NL3 [18], or the more recent PK1, PK1R [19], FSUGold [20] and FSUGold2 [21] parametrizations of the effective Lagrangian. In the latter case, the density dependence of the meson-nucleon vertex functions can be parameterized starting from microscopic Dirac-Brueckner calculations of symmetric and asymmetric nuclear matter [22], or it can be fully phenomenological [23–25], with parameters adjusted to data on finite nuclei and empirical properties of symmetric and asymmetric nuclear matter.

At the energy scale characteristic for nuclear binding and low-lying excited states, meson exchange (σ, ω, ρ, ...) is just a convenient representation of the effective nuclear interaction. The exchange of heavy mesons is associated with short-distance dynamics that cannot be resolved at low energies, and therefore in each channel (scalar-isoscalar, vector-isoscalar, scalar-isovector, and vector-isovector) meson exchange can be replaced by the corresponding local four-point (contact) interactions between nucleons. Of course, also in the case of contact interactions, medium effects can be taken into account by the inclusion of higher-order interaction terms, for instance, six-nucleon vertices $(\bar{\psi}\psi)^3$, and eight-nucleon vertices $(\bar{\psi}\psi)^4$ and $[(\bar{\psi}\gamma_\mu\psi)(\bar{\psi}\gamma^\mu\psi)]^2$ [26, 27], or it can be encoded in the effective couplings, that is, in the density dependence of strength parameters in the isoscalar and isovector channels [28–30].

Self-consistent mean-field methods and structure models based on DFT have been very successful in analyzing a variety of nuclear properties and predicting new phenomena. However, a fully microscopic foundation of nuclear energy density functionals (NEDFs), based on the underlying theory of strong interactions, has yet to be established [31]. Even if this task is accomplished in the near future, still the parameters of a NEDF will have to be adjusted to data on finite nuclei, and this is because of the inherent complexity of effective in-medium inter-nucleon interactions. A number of successful NEDFs are semi-phenomenological and approximate the exact unknown functional by an expansion in powers of ground-state nucleon densities and currents and their gradients, and/or assume a relatively simple ansatz for the density dependence of the effective inter-nucleon interactions, often based on a microscopic nuclear matter equation of state. In the following sections we will explore in more detail one particular relativistic energy density functional (DD-PC1) that has extensively been employed in self-consistent mean-field calculations over the entire nuclear chart, except for light nuclei, and has also been used as a basis for several beyond-mean-field spectroscopic models that explicitly consider dynamical effects related to restoration of symmetries broken at the mean-field level, and fluctuations in collective coordinates.

2 The Relativistic Density Functional DD-PC1

The basic building blocks of a relativistic nuclear energy density functional are the densities and currents bilinear in the Dirac spinor field ψ of the nucleon:

$$\bar{\psi}\mathscr{O}_\tau\Gamma\psi, \quad \mathscr{O}_\tau \in \{1, \tau_i\}, \quad \Gamma \in \{1, \gamma_\mu, \gamma_5, \gamma_5\gamma_\mu, \sigma_{\mu\nu}\}. \tag{14}$$

Here τ_i are the isospin Pauli matrices and Γ generically denotes the Dirac matrices. The nuclear ground-state density and energy are determined by the self-consistent solution of relativistic linear single-nucleon Kohn-Sham equations. To derive those equations it is useful to construct an interaction Lagrangian with four-fermion (contact) interaction terms in the various isospace-space channels:

$$\begin{aligned}
&\text{isoscalar-scalar:} \quad (\bar{\psi}\psi)^2 \\
&\text{isoscalar-vector:} \quad (\bar{\psi}\gamma_\mu\psi)(\bar{\psi}\gamma^\mu\psi) \\
&\text{isovector-scalar:} \quad (\bar{\psi}\ \vec{\tau}\ \psi)\cdot(\bar{\psi}\ \vec{\tau}\ \psi) \\
&\text{isovector-vector:} \quad (\bar{\psi}\ \vec{\tau}\ \gamma_\mu\psi)\cdot(\bar{\psi}\ \vec{\tau}\ \gamma^\mu\psi).
\end{aligned}$$

Vectors in isospin space are denoted by arrows. A general Lagrangian can be written as a power series in the currents $\bar{\psi}\mathscr{O}_\tau\Gamma\psi$ and their derivatives, with higher-order terms representing in-medium many-body correlations. The empirical data set of bulk properties of finite nuclei, however, can only constrain a relatively small set of parameters in the general expansion of an effective Lagrangian. An alternative, that directly leads to linear single-nucleon Kohn-Sham equations, is to construct a Lagrangian with second-order interaction terms only, while many-body correlations are encoded in density-dependent parameters [28, 29]. In analogy to the successful meson-exchange RMF approach, an effective Lagrangian that includes the isoscalar-scalar, isoscalar-vector and isovector-vector four-fermion interactions reads:

$$\begin{aligned}
\mathscr{L} &= \bar{\psi}(i\gamma_\mu\partial^\mu - m)\psi \\
&- \frac{1}{2}\alpha_s(\hat{\rho}_v)(\bar{\psi}\psi)(\bar{\psi}\psi) - \frac{1}{2}\alpha_v(\hat{\rho}_v)(\bar{\psi}\gamma^\mu\psi)(\bar{\psi}\gamma_\mu\psi) \\
&- \frac{1}{2}\alpha_{tv}(\hat{\rho}_v)(\bar{\psi}\ \vec{\tau}\ \gamma^\mu\psi)(\bar{\psi}\ \vec{\tau}\ \gamma_\mu\psi) \\
&- \frac{1}{2}\delta_s(\partial_\nu\bar{\psi}\psi)(\partial^\nu\bar{\psi}\psi) - e\bar{\psi}\gamma\cdot A\frac{(1-\tau_3)}{2}\psi.
\end{aligned} \tag{15}$$

In addition to the free-nucleon Lagrangian and the point-coupling interaction terms, when applied to finite nuclei the model must include the coupling of the protons to the electromagnetic field. The derivative term in (15) accounts for next-order finite-range and correlation effects from a density-matrix expansion [14, 32], and is essential for a quantitative description of density distributions, e.g. nuclear radii. Similar interactions can be included in each space-isospace channel, but in practice available data can only constrain a single derivative term. The inclusion of an adjustable derivative

term only in the isoscalar-scalar channel is consistent with conventional meson-exchange RMF models, in which the mass of the σ meson is adjusted to nuclear matter and ground-state properties of finite nuclei, whereas free values are used for the masses of the ω and ρ mesons.

The strength parameters α_c of the interaction terms in (15) are density-dependent functionals of $\sqrt{j^\mu j_\mu}$, with the nucleon 4-current: $j^\mu = \bar{\psi}\gamma^\mu\psi$. However, at low velocities the parameters α_c depend only on the baryon density $\hat{\rho}_v = \psi^\dagger\psi$. The single-nucleon Dirac equation, that is, the relativistic analogue of the Kohn-Sham equation [8], is obtained from the variation of the Lagrangian:

$$\left[\gamma_\mu(i\partial^\mu - \Sigma^\mu - \Sigma_R^\mu) - (m + \Sigma_S)\right]\psi = 0, \tag{16}$$

with the nucleon self-energies Σ defined by the following relations:

$$\Sigma^\mu = \alpha_V(\rho_v)j^\mu + e\frac{(1-\tau_3)}{2}A^\mu \tag{17}$$

$$\Sigma_R^\mu = \frac{1}{2}\frac{j^\mu}{\rho_v}\left\{\frac{\partial\alpha_s}{\partial\rho}\rho_s^2 + \frac{\partial\alpha_v}{\partial\rho}j_\mu j^\mu + \frac{\partial\alpha_{tv}}{\partial\rho}\vec{j}_\mu\vec{j}^\mu\right\} \tag{18}$$

$$\Sigma_S = \alpha_s(\rho_v)\rho_s - \delta_s\partial^\nu\partial_\nu\rho_s \tag{19}$$

$$\Sigma_{TV}^\mu = \alpha_{tv}(\rho_v)\vec{j}^\mu. \tag{20}$$

In addition to contributions from the isoscalar-vector four-fermion interaction and the electromagnetic interaction, the isoscalar-vector self-energy includes the "rearrangement" terms Σ_R^μ that arise from the variation of the vertex functionals α_s, α_v, and α_{tv} with respect to the nucleon fields in the vector density operator $\hat{\rho}_v$. The importance of self-energies Σ becomes more apparent in the non-relativistic limit [33]. Of particular interest is the interplay between the scalar Σ_S and the vector component Σ^0. The non-relativistic local mean-field potential is determined by the sum $\Sigma_S + \Sigma^0$, which is relatively small because these self-energies have opposite signs. The difference $\Sigma_S - \Sigma^0$, on the other hand, is large and determines the comparatively large energy spacings between spin-orbit partner states.

At the mean-field level the nuclear ground state $|\phi_0\rangle$ is represented by the self-consistent solution of the system of (16)–(20), with the isoscalar and isovector four-currents and scalar density defined as expectation values:

$$j_\mu = \langle\phi_0|\bar{\psi}\gamma_\mu\psi|\phi_0\rangle = \sum_{k=1}^{N} v_k^2\ \bar{\psi}_k\gamma_\mu\psi_k, \tag{21}$$

$$\vec{j}_\mu = \langle\phi_0|\bar{\psi}\gamma_\mu\ \vec{\tau}\ \psi|\phi_0\rangle = \sum_{k=1}^{N} v_k^2\ \bar{\psi}_k\gamma_\mu\ \vec{\tau}\ \psi_k, \tag{22}$$

$$\rho_s = \langle\phi_0|\bar{\psi}\psi|\phi_0\rangle = \sum_{k=1}^{N} v_k^2\ \bar{\psi}_k\psi_k, \tag{23}$$

where ψ_k are the Dirac spinors, and the sum runs over occupied positive-energy single-nucleon orbitals, including the corresponding occupation factors v_k^2. The single-nucleon Dirac equations are solved self-consistently in the "*no-sea*" approximation, that omits explicit contributions of negative-energy solutions of the relativistic equations to densities and currents [16, 33, 34]. Vacuum polarization effects are implicitly included in the adjustable density-dependent parameters of the functional.

To determine the density dependence of the coupling functionals one starts from a microscopic equation of state (EoS) of symmetric and asymmetric nuclear matter, and maps the corresponding nucleon self-energies on the mean-field self-energies (17)–(20) that determine the single-nucleon Dirac equation (16). In general, EDFs determined directly from a microscopic EoS do not provide a very accurate description of data in finite nuclei. This is because a calculation of the nuclear matter EoS involves approximation schemes and includes adjustable parameters that are not really constrained by nuclear structure data and, therefore, cannot determine uniquely the parameters of nuclear EDFs. In a phenomenological construction of a relativistic energy density functional one starts from an assumed ansatz for the medium dependence of the mean-field nucleon self-energies, and adjusts the free parameters directly to ground-state data on finite nuclei. Guided by the microscopic density dependence of the vector and scalar self-energies, the following practical ansatz for the functional form of the couplings was adopted in [30]:

$$\begin{aligned} \alpha_s(\rho) &= a_s + (b_s + c_s x)e^{-d_s x}, \\ \alpha_v(\rho) &= a_v + b_v e^{-d_v x}, \\ \alpha_{tv}(\rho) &= b_{tv} e^{-d_{tv} x}, \end{aligned} \tag{24}$$

with $x = \rho/\rho_{\rm sat}$, where $\rho_{\rm sat}$ denotes the nucleon density at saturation in symmetric nuclear matter. The parameters of a nuclear EDF can be constrained by the choice of the nuclear matter (symmetric and asymmetric) equation of state. The functional DD-PC1 was eventually fine-tuned to experimental binding energies of finite nuclei and, since the calculated nuclear masses are not very sensitive to the nuclear matter saturation density, this quantity, together with the compression modulus and the Dirac mass, were kept fixed. The choice for the saturation density $\rho_{sat} = 0.152$ fm^{-3}, and the Dirac effective nucleon mass $m_D^* = m + \Sigma_S = 0.58m$, are in accordance with values predicted by most modern relativistic functionals. To reproduce experimental excitation energies of isoscalar giant monopole resonances, the value $K_\infty = 230$ MeV was used for the nuclear matter compression modulus. Low-energy data do not constrain the nuclear matter EoS at high nucleon densities and, therefore, two additional points on the $E(\rho)$ curve in symmetric matter were fixed to the microscopic EoS of Akmal, Pandharipande and Ravenhall [35], which has extensively been used in studies of high-density nuclear matter.

The isovector channel of the energy density functional determines the density dependence of the nuclear matter symmetry energy

$$S_2(\rho) = a_4 + \frac{p_0}{\rho_{sat}^2}(\rho - \rho_{sat}) + \frac{\Delta K_0}{18\rho_{sat}^2}(\rho - \rho_{sat})^2 + \cdots . \tag{25}$$

The parameter p_0 characterizes the linear density dependence of the symmetry energy, and ΔK_0 is the isovector correction to the compression modulus. Experimental masses, unfortunately, do not place very strict constraints on the parameters of the expansion of $S_2(\rho)$, but self-consistent mean-field calculations show that binding energies can restrict the values of S_2 at nucleon densities somewhat below saturation density, e.g. at $\rho \approx 0.1$ fm^{-3}. Relativistic effective interactions, in particular, with volume asymmetry a_4 in the range 31 MeV $\leq a_4 \leq$ 35 MeV predict values for neutron skin thickness that are consistent with data, and reproduce experimental excitation energies of isovector giant dipole resonances. Therefore, the volume asymmetry was fixed at $a_4 = 33$ MeV, and the symmetry energy was varied at a density that corresponds to an average nucleon density in finite nuclei: $\langle\rho\rangle = 0.12\,\text{fm}^{-3}$.

With this choice for the empirical properties of symmetric and asymmetric nuclear matter, the set of 10 parameters of the relativistic functional DD-PC1 was fine-tuned in a χ^2 fit to the masses of 64 axially deformed nuclei in the mass regions $A \approx 150$–180 and $A \approx 230$–250. Calculated masses of finite nuclei are primarily sensitive to the three leading terms in the empirical mass formula: volume, surface and symmetry energy

$$B.E. = a_v A + a_s A^{2/3} + a_4 \frac{(N-Z)^2}{4A} + \cdots , \tag{26}$$

where a_v, a_s and a_4 denote the volume binding energy, surface energy, and symmetry energy, respectively, at saturation density in nuclear matter. One can, therefore, generate families of effective interactions that are characterized by different values of a_v, a_s and a_4 (or symmetry energy at a lower density, as explained above), and determine which parametrization minimizes the deviation from empirical binding energies. Of course, if a functional is adjusted by varying the volume, symmetry, and surface energies, the parameters that determine these quantities will generally be correlated because of (26). When only a small number of nuclei is considered, satisfactory results can be obtained with different linearly dependent combinations of parameters.

A careful analysis of differences between calculated and experimental binding energies (residuals) for a set of 64 nuclei in the mass intervals $A \approx 150$–180 and $A \approx$ 230–250, displays a pronounced isospin and mass dependence of the deviations on the nuclear matter volume energy at saturation. To reduce the absolute mass deviations to less than 1 MeV, and to contain their mass and isotopic dependence, strict constraints on the value of a_v must be met. The narrow window of allowed values of the volume energy cannot be determined microscopically already at the nuclear matter level, but rather results from a fine-tuning of the parameters of the energy density functional to experimental masses. Calculated binding energies and charge radii are also sensitive to the choice of the surface coefficient a_s that determines the surface energy and surface thickness of semi-infinite nuclear matter. The optimal density functional

Table 1 Parameters of the relativistic energy density functional DD-PC1 (24)

Parameter	
a_s (fm^2)	−10.0462
b_s (fm^2)	−9.1504
c_s (fm^2)	−6.4273
d_s	1.3724
a_v (fm^2)	5.9195
b_v (fm^2)	8.8637
d_v	0.6584
b_{tv} (fm^2)	1.8360
d_{tv}	0.6403
δ_s (fm^4)	−0.8149

DD-PC1 does not display any visible isotopic or mass dependence of the deviations of calculated masses, and the absolute errors for all 64 axially deformed nuclei are smaller than 1 MeV.

As it will be illustrated in the following sections, DD-PC1 has been further tested in calculations of binding energies, charge radii, deformation parameters, neutron skin thickness, and excitation energies of giant monopole and dipole resonances. The parameters of DD-PC1 are included in Table 1. The nuclear matter equation of state that corresponds to DD-PC1 is characterized by the following properties at the saturation point: nucleon density $\rho_{\rm sat} = 0.152$ fm^{-3}, volume energy $a_v = -16.06$ MeV, surface energy $a_s = 17.5$ MeV, symmetry energy $a_4 = 33$ MeV, and the nuclear matter compression modulus $K_{nm} = 230$ MeV.

3 DD-PC1: Covariance Analysis

As illustrated in the previous section with the example of DD-PC1, a new generation of density functionals is currently being developed that, on the one hand, is more firmly constrained by a microscopic treatment of effective inter-nucleon interactions and, on the other hand, their parameters are adjusted to much larger data sets of ground-state properties, including both spherical and deformed nuclei. Methods of statistical analysis [36, 37] can be used to assess the uniqueness and predictive power of particular functionals, as well as the stability or sensitivity of model parameters. These methods can also be used to determine the type of data that better constrain model parameters.

Let $\mathbf{p} = \{p_1, \ldots, p_F\}$ denote a point in an F-dimensional parameter space and, therefore, each value of $\mathbf{p}$ corresponds to a particular model. A calibration of model parameters starts with defining a quality measure:

$$\chi^2(\mathbf{p}) = \sum_{n=1}^{N} \left(\frac{\mathscr{O}_n^{(th)}(\mathbf{p}) - \mathscr{O}_n^{(exp)}}{\Delta \mathscr{O}_n} \right)^2, \tag{27}$$

where N is the number of observables $\hat{\mathscr{O}}_n$ considered in the analysis; (*th*) and (*exp*) denote theoretical and experimental values, respectively. Every observable is weighted by the inverse of $\Delta \mathscr{O}_n$. When fine-tuning a model one often uses an "adopted error" which is supposed to include all sources of uncertainty and is adjusted in such a way that $\chi^2(\mathbf{p}_0) \approx N - F$. The optimal set $\mathbf{p}_0$, that is, the "best model" corresponds to the minimum of χ^2 on the multidimensional parameter surface, and this implies that all first derivatives of the function χ^2 vanish at $\mathbf{p}_0$:

$$\left. \frac{\partial \chi^2(\mathbf{p})}{\partial p_i} \right|_{\mathbf{p}=\mathbf{p}_0} = 0, \quad \forall\, i = 1, \ldots, F. \tag{28}$$

Moreover, the symmetric $F \times F$ matrix of second derivatives $\partial^2 \chi^2 / (\partial p_i \partial p_j)$ has to be positive-definite at $\mathbf{p}_0$. To analyze deviations of χ^2 from its minimum value, it is convenient to define dimensionless parameters

$$x_i = \frac{(\mathbf{p} - \mathbf{p}_0)_i}{(\mathbf{p}_0)_i}. \tag{29}$$

The minimum is then determined by $\mathbf{x} = 0$. In the vicinity of the minimum χ^2 can be represented by a Taylor series expansion. The lowest-order (quadratic) deviation of χ^2 reads

$$\Delta \chi^2(\mathbf{x}) = \chi^2(\mathbf{p}) - \chi^2(\mathbf{p}_0) = \mathbf{x}^T \hat{\mathscr{M}} \mathbf{x}, \tag{30}$$

$$\mathscr{M}_{ij} = \frac{1}{2} \left. \frac{\partial^2 \chi^2}{\partial x_i \partial x_j} \right|_{\mathbf{x}=0} = \frac{1}{2} \, (\mathbf{p}_0)_i \, (\mathbf{p}_0)_j \, \partial_i \partial_j \chi^2(\mathbf{p}_0). \tag{31}$$

The curvature matrix $\hat{\mathscr{M}}$ is symmetric and can be diagonalized by an orthogonal transformation: $\hat{\mathscr{M}} = \hat{\mathscr{A}} \hat{\mathscr{D}} \hat{\mathscr{A}}^T$, where $\hat{\mathscr{A}}$ denotes the orthogonal matrix with columns corresponding to normalized eigenvectors of $\hat{\mathscr{M}}$, and the diagonal matrix $\hat{\mathscr{D}}$ contains the eigenvalues of $\hat{\mathscr{M}}$. The deviation of χ^2 from its minimum value can therefore be expressed as

$$\Delta \chi^2(\mathbf{x}) = \mathbf{x}^T \left(\mathscr{A} \mathscr{D} \mathscr{A}^T \right) \mathbf{x} = \xi^T \mathscr{D} \xi = \sum_{\alpha=1}^{F} \lambda_\alpha \xi_\alpha^2. \tag{32}$$

The transformed vectors $\xi = \hat{\mathscr{A}}^T \mathbf{x}$ define the principal axes on the F-dimensional surface in parameter space. Soft directions are characterized by small eigenvalues λ_α, that is, there is very little deterioration in the function χ^2 as one moves along a direction defined by the eigenvector that corresponds to a small eigenvalue of $\hat{\mathscr{M}}$.

This implies that the corresponding linear combinations of model parameters are poorly constrained by the observables included in the χ^2 adjustment. On the other hand, stiff directions are characterized by large eigenvalues λ_α, that is, the function χ^2 increases rapidly along these directions and the corresponding linear combinations of parameters are tightly constrained by the observables that determine the χ^2 measure.

Another important concept in statistical analysis is the covariance between two observables A and B:

$$\mathrm{cov}(A, B) = \sum_{i,j=1}^{F} \frac{\partial A}{\partial x_i} (\mathscr{M}^{-1})_{ij} \frac{\partial B}{\partial x_j} = \sum_{\alpha=1}^{F} \frac{\partial A}{\partial \xi_\alpha} \lambda_\alpha^{-1} \frac{\partial B}{\partial \xi_\alpha}, \tag{33}$$

from which one defines the correlation coefficient

$$\rho(A, B) = \frac{\mathrm{cov}(A, B)}{\sqrt{\mathrm{var}(A)\mathrm{var}(B)}}, \tag{34}$$

and where the variance of an observable is simply: $\mathrm{var}(A) = \mathrm{cov}(A, A)$. The observables A and B are fully correlated if $\rho(A, B) = 1$, anti-correlated if $\rho(A, B) = -1$, and independent if $\rho(A, B) = 0$. Methods of statistical error analysis have recently been used in a number of studies that explored sources of uncertainties and correlations in nuclear energy density functionals [38–44].

In the case of the functional DD-PC1, instead of analyzing correlations between the individual parameters: a_i, b_i, c_i and d_i in (24), we will examine correlations between the lowest-order terms in a Taylor expansion of the density-dependent coupling functions around the saturation point: $\alpha_i(\rho_{\mathrm{sat}})$, $\alpha_i'(\rho_{\mathrm{sat}})$ and $\alpha_i''(\rho_{\mathrm{sat}})$, because these are the quantities that directly determine the expressions for the binding energy, pressure and compressibility of nuclear matter at saturation. For the isovector channel, we will use the values of the parameters $\alpha_{tv}(\rho_{\mathrm{sub}})$ and $\alpha_{tv}'(\rho_{\mathrm{sub}})$ at the subsaturation density $\rho_{\mathrm{sub}} = 0.12\ \mathrm{fm}^{-3}$ that corresponds to an average nucleon density in finite nuclei.

The parameters of the functional DD-PC1 given in Table 1, or the corresponding terms in the Taylor expansion of the density-dependent couplings around the saturation point, correspond to the "best model", that is, they determine the point $\mathbf{p}_0$ in the F-dimensional parameter space. To examine the "uniqueness" [40] of DD-PC1, we start with the basic system for which an energy density functional can give definite predictions: infinite nuclear matter. In this system we define a set of N pseudo-observables ($N > F$) that can be used to compute the quality measure $\chi^2(\mathbf{p})$. The model is "unique" if all the eigenvalues of the $F \times F$ matrix of second derivatives $\mathscr{M}$ in (31) are large. In that case all eigenvectors correspond to stiff directions in the parameter space along which the function χ^2 increases rapidly and, therefore, the corresponding linear combinations of parameters are tightly constrained by the selected observables. In addition to the quantities that are evaluated at the saturation point (nucleon density $\rho_{\mathrm{sat}} = 0.152\ \mathrm{fm}^{-3}$, volume energy $a_v = -16.06\,\mathrm{MeV}$, symmetry energy $a_4 = 33\,\mathrm{MeV}$, the Dirac mass $m_D = m + \alpha_s \rho_s = 0.58m$, the non-relativistic

effective mass $m^* = m - \alpha_v \rho_v = 0.66$ m, and the nuclear matter compression modulus $K_{nm} = 230\,\text{MeV}$), we have included four more quantities that characterize the equation of state of symmetric and asymmetric matter at lower and higher densities: the binding energy of symmetric nuclear matter at low density $\rho_{low} = 0.04\,\text{fm}^{-3}$ and high density $\rho_{high} = 0.56\,\text{fm}^{-3}$; and both the symmetry energy S_2 and its slope at the sub-saturation density $\rho_{\text{sub}} = 0.12\,\text{fm}^{-3}$. To analyze the uncertainty and the corresponding correlations for the strength parameter of the derivative term δ_S, we have extended the calculation of the quality measure $\chi^2(\mathbf{p})$ to include the surface energy of semi-infinite nuclear matter with the value $a_s = 17.5\,\text{MeV}$. Since we are considering quantities that cannot be measured directly, to calculate χ^2 and the matrix of second derivatives at the point $\mathbf{p}_0$ (DD-PC1), an arbitrary uncertainty of 2 % is assigned to each observable.

The symmetric 10×10 matrix $\mathscr{M}$ of second derivatives of $\chi^2(\mathbf{p})$ at the point $\mathbf{p}_0$ (DD-PC1) is diagonalized by means of an orthogonal transformation. The diagonal matrix elements in order of decreasing values and the components of the corresponding eigenvectors are displayed in Fig. 1. Stiff directions in the ten-parameter space are characterized by large eigenvalues, that is, the function χ^2 increases rapidly along these directions. This means that the particular linear combinations of parameters corresponding to the stiff eigenvectors are firmly determined by the pseudo-observables in nuclear matter. On the other hand, comparatively small eigenvalues belong to soft directions in the multi-parameter space, along which the quality measure displays little deterioration and the corresponding linear combinations of parameters that define the energy density functional are poorly constrained.

The four stiffest directions in Fig. 1 are dominated by isoscalar parameters, as denoted by the components of the corresponding eigenvectors, whereas modes five to eight contain sizeable admixtures of isovector parameters. The two softest directions are again predominantly isoscalar, although mode nine also contains some contribution from the isovector parameters. The first mode, characterised by the largest eigenvalue, corresponds to out-of-phase contributions of the $\alpha_s(\rho_{\text{sat}})$ and $\alpha_v(\rho_{\text{sat}})$ coupling parameters. An increase of the scalar attraction and a simultaneous decrease of the vector repulsion leads to a pronounced increase of the binding energy and, therefore, to a rapid deterioration of χ^2. Mode two, which corresponds to out-of-phase contributions of the derivatives $\alpha_s'(\rho_{\text{sat}})$ and $\alpha_v'(\rho_{\text{sat}})$, is predominantly constrained by the values of the binding energy at ρ_{low} and ρ_{high}, etc. We note that only modes six and seven contain significant amplitudes that arise from the derivative term. Mode number nine corresponds almost entirely to the parameter d_s in the isoscalar-scalar channel (cf. (24)), which is obviously poorly determined. The softest mode represents the in-phase contributions from the first and second derivatives of the isoscalar couplings at saturation density.

The uncertainties, that is, the variances of model parameters are given by the diagonal elements of the inverse matrix $\mathscr{M}^{-1}$ of second derivatives of χ^2—the covariance matrix (cf. (33)): $\sigma_i^2 = \left(\mathscr{M}^{-1}\right)_{ii} = \left(\mathscr{A}\mathscr{D}^{-1}\mathscr{A}^T\right)_{ii}$. For each parameter $p_i = p_{0i}(1 \pm \sigma_i)$, the uncertainty σ_i in percentage is shown in the upper panel of Fig. 2. As one would have expected, the values of the couplings $\alpha_s(\rho_{\text{sat}})$, $\alpha_v(\rho_{\text{sat}})$ and $\alpha_{tv}(\rho_{\text{sub}})$ have the smallest uncertainties ($\lesssim$5 %), whereas uncertainties increase

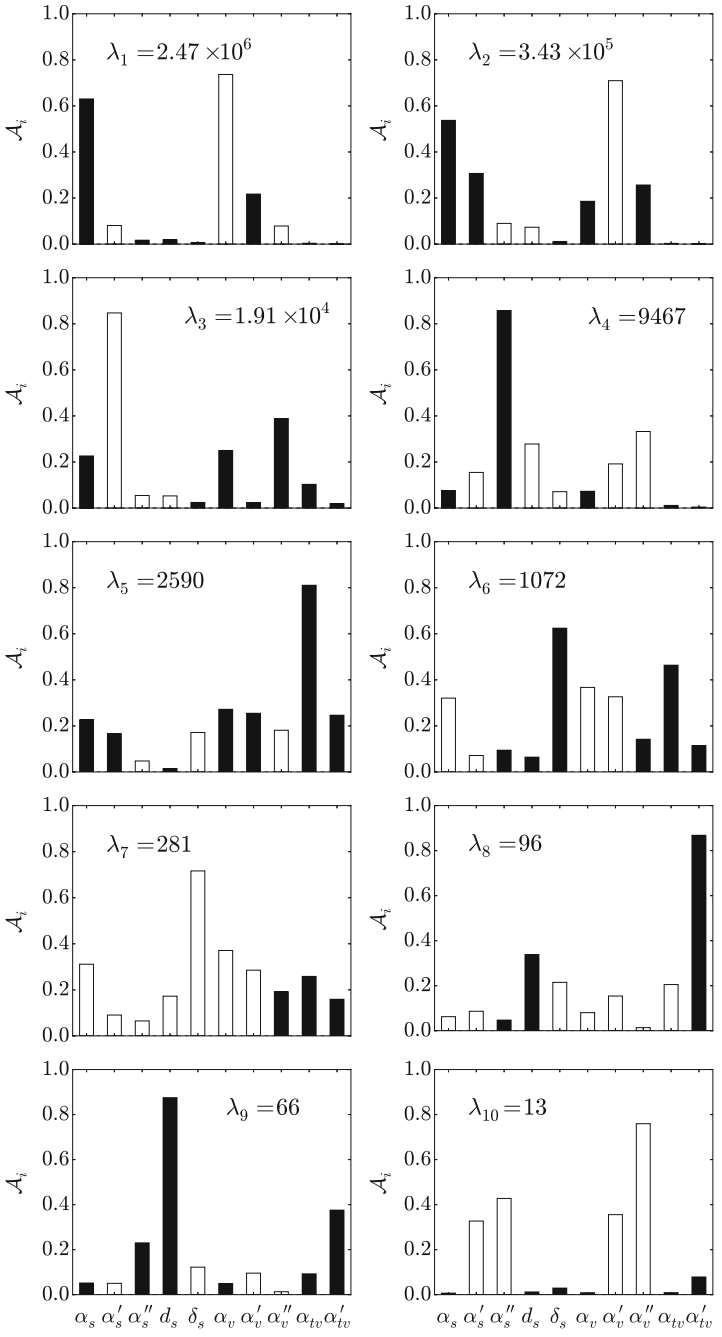

Fig. 1 Eigenvalues and eigenvectors of the matrix of second derivatives $\mathscr{M}$ of $\chi^2(\mathbf{p})$ in symmetric nuclear matter for the functional DD-PC1. The *empty* and *filled bars* indicate that the corresponding amplitudes contribute with opposite signs

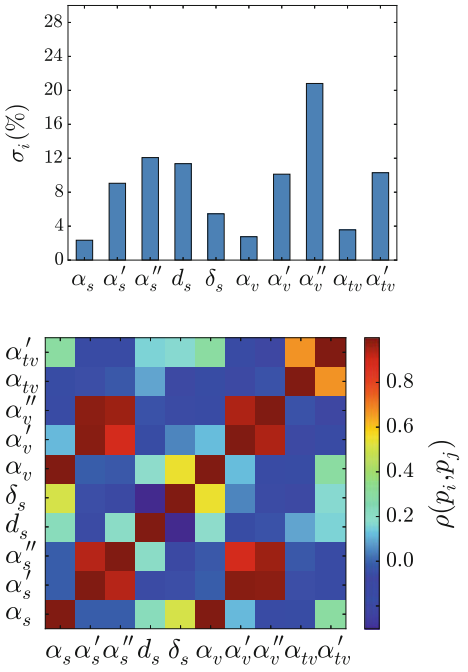

Fig. 2 Uncertainties σ_i in percentage of the model parameters for the functional DD-PC1 (*upper panel*). Correlation coefficients between the model parameters (*lower panel*)

rapidly for their first and second derivatives. As shown in Fig. 1, the parameter d_s completely determines the very soft mode number nine, and the corresponding uncertainty of this parameter is rather large (>10 %). The color coded plot of the 45 independent correlation coefficients for the present calculation of nuclear matter is displayed in the lower panel of Fig. 2. One notices the strong correlations between the isoscalar scalar and isoscalar vector couplings, as well as between their first derivatives and also second derivatives. There is also a significant correlation between $\alpha_{tv}(\rho_{\rm sub})$ and $\alpha'_{tv}(\rho_{\rm sub})$ because the coupling $\alpha_{tv}(\rho_{\rm sub})$ enters the expression for the slope of the symmetry energy. The correlation between the isoscalar and isovector parameters originates from the Dirac mass contribution to the symmetry energy:

$$S_2(\rho_v) = \frac{k_f}{6\sqrt{k_f^2 + m_D^2}} + \frac{1}{2}\alpha_{tv}(\rho_v)\rho_v, \tag{35}$$

where k_f denotes the Fermi momentum. We note that the uncertainty of the parameter δ_s of the derivative term is larger than those of $\alpha_s(\rho_{sat})$ and $\alpha_v(\rho_{sat})$ with which δ_s displays significant correlation.

As an illustration of covariance analysis for finite nuclei, in Fig. 3 we display results for the variances of ground-state observables of tin isotopes: binding energies and charge radii. Note that tin isotopes were not included in the calibration of the parameters of DD-PC1. The top panel of Fig. 3 shows the relative contributions of

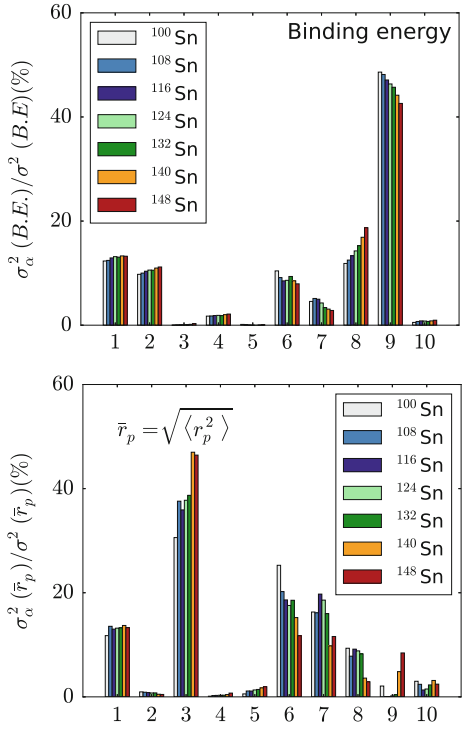

Fig. 3 Relative contributions in percentage of the ten linear combinations of model parameters that correspond to the eigenvectors of the matrix of second derivatives $\mathscr{M}$ (31), to the variances of the binding energies (*upper panel*), and radii of the proton distribution (*lower panel*) of tin isotopes

the eigenmodes of $\mathscr{M}$ to the variance of binding energies of Sn isotopes with mass number $100 \leq A \leq 148$, where

$$\frac{\sigma^2_\alpha(\mathrm{B})}{\sigma^2(\mathrm{B})} = \frac{\left(\frac{\partial \mathrm{B}}{\partial \xi_\alpha}\right)^2 \lambda_\alpha^{-1}}{\sum_{\alpha=1}^{F} \left(\frac{\partial \mathrm{B}}{\partial \xi_\alpha}\right)^2 \lambda_\alpha^{-1}}, \tag{36}$$

for an observable B (e.g. binding energy). The largest contribution to the variances originates from the next-to-softest mode, that is, from a combination of parameters (d_s and the derivative α'_{tv}) poorly constrained by the set of pseudo-data that determine $\chi^2(\mathbf{p})$. We also note the increase of the relative contribution of the predominantly isovector mode eight in tin isotopes with a larger neutron excess. It is interesting to compare the relative contributions to the variance of the binding energy to those of an observable that was not included in the fit of the parameters of DD-PC1. In the lower panel we plot the relative contributions of the eigenmodes of $\mathscr{M}$ to the variance of the radius of the proton distribution of tin isotopes. In this case the variance for all isotopes is dominated by the relatively stiff combination of parameters that corresponds to mode three, and its relative contribution increases with neutron number. The significant contributions from the soft modes six, seven, and eight decrease in

neutron-rich tin isotopes, whereas the out-of-phase contributions of isoscalar couplings in the stiff mode one do not show significant variation with neutron number.

This illustrative study shows how a simple covariance analysis of the quality function χ^2 around its minimum in nuclear matter can be used as a starting point in the selection of the type of data and calibration of the parameters of a nuclear EDF.

4 Ground-State Properties

Models based on relativistic energy density functionals have successfully been used in studies of structure phenomena over the entire nuclide chart, from relatively light systems to superheavy nuclei, and from the valley of β-stability to the particle drip-lines. In the lowest order—the self-consistent mean-field approximation, an EDF is constructed as a functional of one-body nucleon density matrices. The many-body wave function is a single Slater determinant that corresponds to the symmetry-breaking static mean-field. Symmetry breaking (translational, rotational, particle number) incorporates static correlations, such as deformations and pairing, that are crucial for a description of equilibrium (ground-state) properties: binding energies, charge radii, etc. The EDF framework provides an accurate microscopic description of infinite nuclear matter, ground-state properties, low-energy vibrations, rotational spectra, small-amplitude vibrations, and large-amplitude adiabatic collective motion. By employing global functionals, adjusted to reproduce empirical properties of nuclear matter and bulk properties of finite nuclei, the current generation of self-consistent mean-field models has achieved a high level of accuracy in the description of ground states and properties of excited states.

For the examples considered here, self-consistent mean-field calculations have been carried out using the relativistic Hartree-Bogoliubov model (RHB) [3, 34, 45], which represents a relativistic extension of the Hartree-Fock-Bogoliubov framework. The RHB model includes particle-hole (ph) and particle-particle (pp) correlations on a mean-field level by using two average potentials: the self-consistent mean-field that encloses all the long-range ph correlations, and a pairing field $\hat{\Delta}$ which sums up the pp-correlations. The ground state of a nucleus is described by a generalized Slater determinant $|\Phi\rangle$ that represents the vacuum with respect to independent quasiparticles. The quasiparticle operators are defined by the unitary Bogoliubov transformation of the single-nucleon creation and annihilation operators:

$$\alpha_k^+ = \sum_l U_{lk} c_l^+ + V_{lk} c_l, \tag{37}$$

where U and V are the Hartree-Bogoliubov wave functions determined by the solution of the RHB equation. In coordinate representation:

$$\begin{pmatrix} h_D - m - \lambda & \Delta \\ -\Delta^* & -h_D^* + m + \lambda \end{pmatrix} \begin{pmatrix} U_k(\mathbf{r}) \\ V_k(\mathbf{r}) \end{pmatrix} = E_k \begin{pmatrix} U_k(\mathbf{r}) \\ V_k(\mathbf{r}) \end{pmatrix}. \tag{38}$$

In the relativistic case the self-consistent mean-field corresponds to the single-nucleon Dirac Hamiltonian $\hat{h}_D$ of (16). m is the nucleon mass, and the chemical potential λ is determined by the particle number subsidiary condition such that the expectation value of the particle number operator in the ground state equals the number of nucleons. The pairing field Δ reads

$$\Delta_{ab}(\mathbf{r}, \mathbf{r}') = \frac{1}{2} \sum_{c,d} V_{abcd}(\mathbf{r}, \mathbf{r}') \kappa_{cd}(\mathbf{r}, \mathbf{r}'). \tag{39}$$

where $V_{abcd}(\mathbf{r}, \mathbf{r}')$ are the matrix elements of the two-body pairing interaction, and the indices a, b, c and d label quantum numbers that specify the Dirac indices of the spinor. The column vectors denote the quasiparticle wave functions, and E_k are the quasiparticle energies. The dimension of the RHB matrix equation is two times the dimension of the corresponding Dirac equation. For each eigenvector (U_k, V_k) with positive quasiparticle energy $E_k > 0$, there exists an eigenvector (V_k^*, U_k^*) with quasiparticle energy $-E_k$. Since the nucleon quasiparticle operators satisfy fermion commutation relations, the levels E_k and $-E_k$ cannot be occupied simultaneously. For the solution that corresponds to a ground state of a nucleus with even particle number, one usually chooses the eigenvectors with positive eigenvalues E_k.

The single-particle density and the pairing tensor, constructed from the quasiparticle wave functions

$$\rho_{cd}(\mathbf{r}, \mathbf{r}') = \sum_{k>0} V_{ck}^*(\mathbf{r}) V_{dk}(\mathbf{r}'), \tag{40}$$

$$\kappa_{cd}(\mathbf{r}, \mathbf{r}') = \sum_{k>0} U_{ck}^*(\mathbf{r}) V_{dk}(\mathbf{r}'), \tag{41}$$

are calculated in the *no-sea* approximation (denoted by $k > 0$): the summation runs over all quasiparticle states k with positive quasiparticle energies $E_k > 0$, but omits states that originate from the Dirac sea. The latter are characterized by quasiparticle energies larger than the Dirac gap ($\approx$1200 MeV).

Pairing correlations in nuclei are restricted to an energy window of a few MeV around the Fermi level, and their scale is well separated from the scale of binding energies, which are in the range of several 100–1000 MeV and, therefore, a hybrid RHB model with a non-relativistic pairing interaction can be justified. For a general two-body interaction, the matrix elements of the relativistic pairing field read

$$\hat{\Delta}_{a_1 p_1, a_2 p_2} = \frac{1}{2} \sum_{a_3 p_3, a_4 p_4} \langle a_1 p_1, a_2 p_2 | V^{pp} | a_3 p_3, a_4 p_4 \rangle_a \, \kappa_{a_3 p_3, a_4 p_4}, \tag{42}$$

where the indices $(p_1, p_2, p_3, p_4 \equiv f, g)$ refer to the large and small components of the quasiparticle Dirac spinors:

$$U(\mathbf{r}, s, t) = \begin{pmatrix} f_U(\mathbf{r}, s, t) \\ i g_U(\mathbf{r}, s, t) \end{pmatrix} \qquad V(\mathbf{r}, s, t) = \begin{pmatrix} f_V(\mathbf{r}, s, t) \\ i g_V(\mathbf{r}, s, t) \end{pmatrix}. \tag{43}$$

In practical applications of the RHB model only the large components of the spinors $U_k(\mathbf{r})$ and $V_k(\mathbf{r})$ are used to build the non-relativistic pairing tensor $\hat{\kappa}$ in (41). The resulting pairing field reads

$$\hat{\Delta}_{a_1 f, a_2 f} = \frac{1}{2} \sum_{a_3 f, a_4 f} \langle a_1 f, a_2 f | V^{pp} | a_3 f, a_4 f \rangle_a \, \kappa_{a_3 f, a_4 f}. \tag{44}$$

For the pairing interaction we employ a finite-range force [46] that is separable in momentum space, and completely determined by two parameters adjusted to reproduce the nuclear matter bell-shaped curve of the pairing gap of the Gogny force. The gap equation in the $^1S_0$ channel reads

$$\Delta(k) = -\int_0^\infty \frac{k'^2 dk'}{2\pi^2} \langle k | V^{^1S_0} | k' \rangle \frac{\Delta(k')}{2E(k')}, \tag{45}$$

and the pairing force is separable in momentum space:

$$\langle k | V^{^1S_0} | k' \rangle = -G p(k) p(k'). \tag{46}$$

By assuming a simple Gaussian ansatz $p(k) = e^{-a^2 k^2}$, the two parameters G and a were adjusted to reproduce the density dependence of the gap at the Fermi surface in symmetric nuclear matter, as calculated with a Gogny force. For the D1S parameterization [47] of the Gogny force the following values are obtained: $G = -728\,\text{MeV fm}^3$ and $a = 0.644\,\text{fm}$. When the pairing force (46) is transformed from momentum to coordinate space, it takes the form:

$$V(\mathbf{r}_1, \mathbf{r}_2, \mathbf{r}_1', \mathbf{r}_2') = G\delta\left(\mathbf{R} - \mathbf{R}'\right) P(\mathbf{r}) P(\mathbf{r}') \frac{1}{2} \left(1 - P^\sigma\right), \tag{47}$$

where $\mathbf{R} = \frac{1}{2}(\mathbf{r}_1 + \mathbf{r}_2)$ and $\mathbf{r} = \mathbf{r}_1 - \mathbf{r}_2$ denote the center-of-mass and relative coordinates, respectively, and $P(\mathbf{r})$ is the Fourier transform of $p(k)$:

$$P(\mathbf{r}) = \frac{1}{\left(4\pi a^2\right)^{3/2}} e^{-\mathbf{r}^2/4a^2}. \tag{48}$$

The pairing force has finite range and, because of the presence of the factor $\delta\left(\mathbf{R} - \mathbf{R}'\right)$, it preserves translational invariance. Even though $\delta\left(\mathbf{R} - \mathbf{R}'\right)$ implies that this force is not completely separable in coordinate space, the corresponding anti-symmetrized pp matrix elements

$$\left\langle \alpha\bar{\beta} \right| V \left| \gamma\bar{\delta} \right\rangle_a = \left\langle \alpha\bar{\beta} \right| V \left| \gamma\bar{\delta} \right\rangle - \left\langle \alpha\bar{\beta} \right| V \left| \bar{\delta}\gamma \right\rangle, \tag{49}$$

can be represented as a sum of a finite number of separable terms in a harmonic oscillator basis.

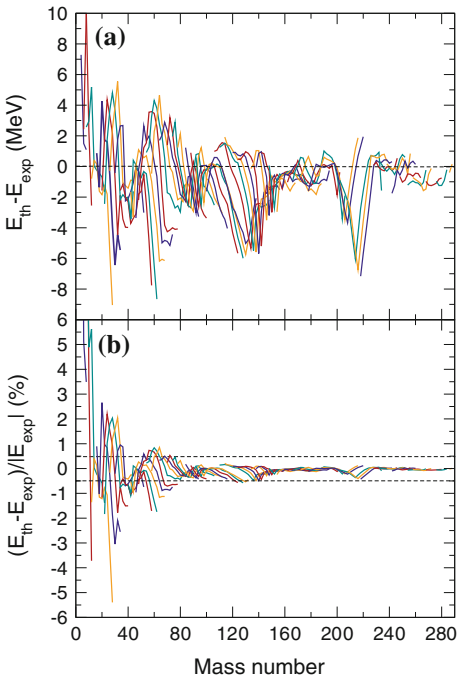

Fig. 4 Absolute differences between calculated and experimental masses of 835 even-even nuclei (*top*), and the relative accuracy of theoretical mass predictions. Isotopic chains are denoted by *lines*. The theoretical values are computed using the RHB model with the energy density functional DD-PC1 and the finite-range separable pairing interaction (46)

In the following examples we will explore the global performance of the relativistic energy density functional DD-PC1 plus the finite-range separable pairing interaction (46), in calculations of ground-state properties of spherical and deformed nuclei. Figure 4 displays the absolute differences between calculated and experimental masses [48] of 835 even-even nuclei (top), and the relative accuracy of theoretical mass predictions. The theoretical values are obtained using the RHB model, and lines connect nuclei that belong to isotopic chains. Even though DD-PC1 was not adjusted to be used as a mass formula, nevertheless the overall agreement with data is very good and, except for light nuclei, the relative accuracy of mass predictions is better than 0.5 %. In the case of spherical nuclei the variance between calculated masses and the corresponding experimental values is somewhat larger. Because it was adjusted to masses of deformed nuclei in the mass regions $A \approx 150$–180 and $A \approx 230$–250, DD-PC1 necessarily overbinds spherical closed-shell nuclei, and the origin of this additional binding is in the corresponding single-nucleon shell structure [30].

In Fig. 5 we plot the equilibrium charge quadrupole deformations β_2 in the (N, Z) plane. The map exhibits regions of spherical (single or double closed-shell) and deformed (away from closed shells) nuclei, and the predicted quadrupole deformations are generally in very good agreement with data obtained from Coulomb excitation or life-time measurements. A notable exception are β and/or γ soft nuclei, and nuclei that exhibit shape coexistence. In those cases a simple SCMF approach, which does not include quantum fluctuation effects, might not be sufficient to identify the

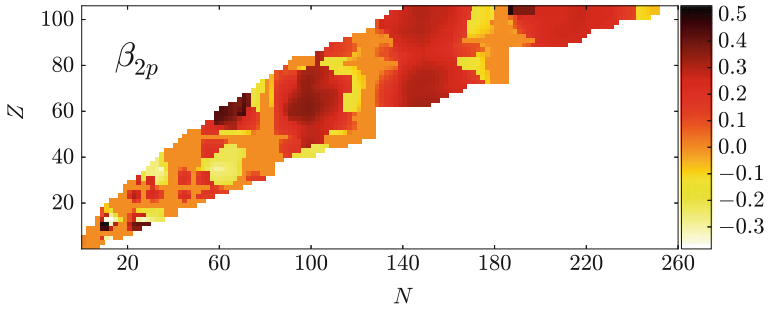

Fig. 5 Equilibrium charge quadrupole deformations β_2 calculated with the RHB model (density functional DD-PC1 plus finite-range separable pairing)

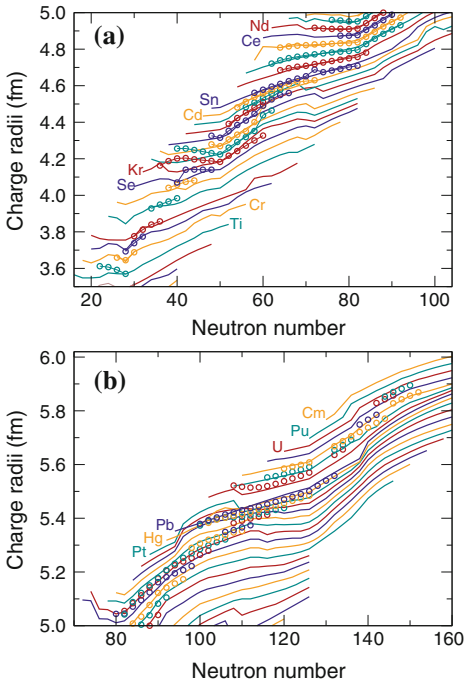

Fig. 6 Experimental (*circles*) [49] and theoretical (*lines*) charge radii calculated with the RHB model (functional DD-PC1 plus finite-range separable pairing)

true minimum and/or beyond mean-field collective correlations could significantly contribute to the degree of ground-state deformations.

The charge density is obtained by folding the theoretical point-proton density with the Gaussian proton-charge distribution. For the latter an *rms* radius of 0.8 fm is used, and the resulting ground-state charge radius reads $r_c = \sqrt{r_p^2 + 0.64}\,\text{fm}$, where r_p is the radius of the point-proton density distribution. In Fig. 6 we compare the theoretical charge radii with experimental values [49] in regions of medium-mass and heavy nuclei. It is remarkable that, even though only experimental binding

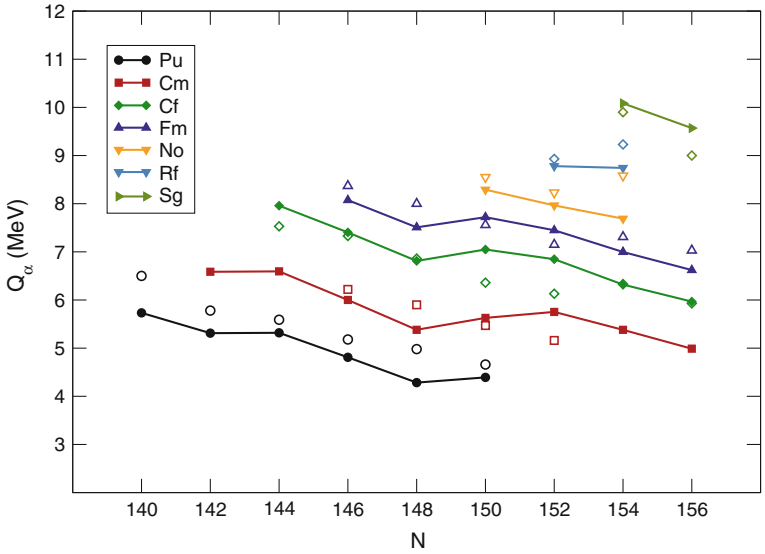

Fig. 7 Q_α values for even-even actinide chains obtained in a self-consistent axially symmetric RHB calculations using the functional DD-PC1 plus the separable pairing interaction. The theoretical values (*filled symbols*) are connected by *lines* and compared to data (*open symbols*) [48]

energies were used to fine-tune the parameters of DD-PC1, this functional predicts nuclear charge radii in excellent agreement with experiment. In fact, for a set of more than 300 even-even nuclei over the entire chart of nuclides, the *rms* deviation between calculated and experimental charge radii is only 0.025 fm [50].

A very interesting mass region for applications of energy density functionals is the one that comprises very heavy and superheavy nuclei [51]. As an illustration of the accuracy with which the functional DD-PC1 predicts ground-state observables of the heaviest nuclear systems, in Fig. 7 results of axially symmetric RHB calculations of Q_α values, that is, energies of α particles emitted by even-even actinide nuclei are shown in comparison to data [48]. Even in this simple calculation in which axial symmetry is assumed, the model based on the functional DD-PC1 reproduces the empirical trend of Q_α values. The few cases for which a somewhat larger deviation from data is found probably indicate a more complex energy surface, possibly including shape coexistence.

The global performance of the functional DD-PC1, as well as several other modern relativistic energy density functionals, has recently been analyzed in a series of studies [50, 52, 53] that have reported extensive calculations of ground-state observables and properties in comparison with available data.

5 Beyond the Self-consistent Mean-Field Approximation

The self-consistent mean-field approach based on nuclear energy density functionals is also referred to as single reference (SR) EDF, because it uses one-body nucleon densities (matrices) that correspond to a single product state. The static nuclear mean-field is characterised by the breaking of symmetries of the underlying Hamiltonian—translational, rotational, particle number and, therefore, includes important static collective correlations, e.g. deformations and pairing. However, as we have shown in the previous section, this framework can only provide an approximate description of bulk ground-state nuclear properties, such as binding energies, charge radii, deformations, etc.

To be able to calculate excitation spectra and electromagnetic transition rates it is necessary to extend the Kohn-Sham EDF framework, that is, the SCMF scheme, to include correlations that arise from symmetry restoration and fluctuations around the mean-field minima [1, 2, 54–56]. Collective correlations are sensitive to shell effects, display pronounced variations with particle number and, therefore, cannot be incorporated in a universal EDF. On the second level of implementation of nuclear EDFs—the multi-reference (MR) EDF approach—that takes into account collective correlations through the restoration of broken symmetries and configuration mixing of symmetry-breaking product states, the many-body energy takes the form of a functional of all transition density matrices that can be constructed from the selected set of product states. This set is chosen to restore symmetries or/and to perform a mixing of configurations that correspond to specific collective modes using, for instance, the (quasiparticle) random-phase approximation (QRPA) or the Generator Coordinate Method (GCM). The latter includes correlations related to finite-size fluctuations in a collective degree of freedom, and can also be used to restore selection rules that are essential for spectroscopic observables.

A quantitative description of low-energy structure phenomena usually starts from a constrained SCMF calculation of the energy surface with mass multipole moments as constrained quantities. When based on microscopic EDFs or effective interactions, such calculations comprise short- and long-range many-body correlations, and result in static symmetry-breaking product many-body states. Spectroscopic calculations necessitate the inclusion of collective correlations. In quadrupole deformed nuclei, for instance, the rotational energy correction, that is, the energy gained by the restoration of rotational symmetry, is proportional to the quadrupole deformation of the symmetry-breaking state and can reach several MeV for a well deformed configuration. Fluctuations of quadrupole deformation also contribute to the correlation energy. Both types of correlations can be included simultaneously by mixing angular-momentum projected states corresponding to different quadrupole moments. The most effective approach for configuration mixing calculations is the generator coordinate method, with multipole moments used as coordinates that generate the intrinsic wave functions.

GCM configuration mixing of angular-momentum and particle-number projected axially symmetric states is routinely used in nuclear structure studies even for the heaviest nuclei with more than two hundred nucleons. The application of this method to triaxial shapes presents a much more involved and technically difficult problem. Only recently structure models have been implemented, based on triaxial symmetry-breaking intrinsic states, that are projected on particle number and angular momentum, and finally mixed by the generator coordinate method. This corresponds to a seven-dimensional GCM calculation, mixing all five degrees of freedom of the quadrupole operator and the gauge angles for protons and neutrons. Multidimensional GCM calculations involve a number of technical and computational issues [55–60], that have so far impeded systematic applications to medium-heavy and heavy nuclei.

In an alternative approach to multidimensional collective dynamics that restores rotational symmetry and allows for fluctuations around mean-field minima, a collective Bohr Hamiltonian can be formulated, with deformation-dependent parameters determined by microscopic self-consistent mean-field calculations. There are two principal approaches to derive the collective Hamiltonian starting from a microscopic framework based on an effective inter-nucleon interaction or energy density functional: (i) the adiabatic approximation to the time-dependent HFB theory (ATDHFB) [61], and (ii) the generator coordinate method with the Gaussian overlap approximation (GOA) [62–64]. With the assumption that the GCM overlap kernels can be approximated by Gaussian functions [65], the local expansion of the kernels up to second order in the non-locality transforms the GCM Hill-Wheeler equation into a second-order differential equation—the Schrödinger equation for the collective Hamiltonian. The kinetic part of this Hamiltonian contains an inertia tensor [66], and the potential energy is determined by the diagonal elements of the Hamiltonian kernel, and also includes zero-point energy (ZPE) corrections [67]. The self-consistent solution of constrained mean-field calculations, that is, the single-quasiparticle energies and wave functions for the entire energy surface as functions of deformation parameters, provide the microscopic input for the calculation of vibrational inertial functions and moments of inertia of the collective Hamiltonian for vibrational and rotational degrees of freedom.

In the following sections we will present an overview of nuclear structure models that are entirely based on the framework of relativistic energy density functionals. All the parameters of these models (QRPA, particle-number and angular momentum projected GCM, five-dimensional quadrupole collective Hamiltonian, quadrupole-octupole collective Hamiltonian) are completely determined by the choice of a particular EDF and pairing functional (effective pairing interaction) and, in this sense, can be considered microscopic. It is interesting to explore how EDFs, adjusted to empirical properties of nuclear matter and ground-state data of finite nuclei, perform when used to construct structure models and compute collective excitation spectra and transition rates.

5.1 Small-Amplitude Oscillations: The Relativistic (Quasiparticle) Random-Phase Approximation

Collective nuclear excitations that correspond to small-amplitude oscillations of the equilibrium nucleonic density can be described as a coherent superposition of two-quasiparticle excitations [65]. The generalized Dirac Hamiltonian $\mathscr{H}$ of the RHB model can be expressed as a functional derivative of the total energy with respect to the generalized density $\mathscr{R}$:

$$\mathscr{R} = \begin{pmatrix} \rho & \kappa \\ -\kappa^* & 1-\rho^* \end{pmatrix}, \tag{50}$$

where ρ and κ are the single-nucleon and pairing densities (40–41), respectively, and $\mathscr{R}$ obeys the equation of motion:

$$i\,\partial_t \mathscr{R} = [\mathscr{H}(\mathscr{R}), \mathscr{R}]\,. \tag{51}$$

The relativistic quasiparticle random-phase approximation (RQRPA) represents the small-amplitude limit of the time-dependent RHB framework [68]. This means that the RQRPA equations can be derived from the response of the generalized density matrix $\mathscr{R}$ to an external field that oscillates with small amplitude. In the linear approximation the generalized density matrix is expanded

$$\mathscr{R} = \mathscr{R}_0 + \delta\mathscr{R}(t), \tag{52}$$

where $\mathscr{R}_0$ is the stationary equilibrium density. Since $\mathscr{R}(t)$ is a projector at all times, in linear order

$$\mathscr{R}_0\delta\mathscr{R} + \delta\mathscr{R}\mathscr{R}_0 = \delta\mathscr{R}. \tag{53}$$

In the quasiparticle basis the matrices $\mathscr{R}_0$ and $\mathscr{H}_0 = \mathscr{H}(\mathscr{R}_0)$ are diagonal

$$\mathscr{R}_0 = \begin{pmatrix} 0 & 0 \\ 0 & 1 \end{pmatrix} \quad \text{and} \quad \mathscr{H}_0 = \begin{pmatrix} E_n & 0 \\ 0 & -E_n \end{pmatrix}. \tag{54}$$

From (53) it follows that the matrix $\delta\mathscr{R}$ has the form

$$\delta\mathscr{R} = \begin{pmatrix} 0 & \delta R \\ -\delta R^* & 0 \end{pmatrix}. \tag{55}$$

The linearized equation of motion (51) reduces to

$$i\,\partial_t \mathscr{R} = [\mathscr{H}_0, \delta\mathscr{R}] + \left[\frac{\delta\mathscr{H}}{\delta\mathscr{R}}\delta\mathscr{R}, \mathscr{R}_0\right]. \tag{56}$$

Assuming an oscillatory solution

$$\delta\mathscr{R}(t) = \sum_{\nu} \delta\mathscr{R}^{(\nu)} e^{i\omega_\nu t} + h.c., \tag{57}$$

the RQRPA equation is obtained

$$\begin{pmatrix} A & B \\ -B^* & -A^* \end{pmatrix} \begin{pmatrix} X^\nu \\ Y^\nu \end{pmatrix} = \omega_\nu \begin{pmatrix} X^\nu \\ Y^\nu \end{pmatrix}, \tag{58}$$

with the matrix elements

$$A_{kk'll'} = (E_k + E_{k'})\delta_{kl}\delta_{k'l'} + \frac{\delta^2 E}{\delta R^*_{kk'}\delta R_{ll'}} \qquad \text{and} \qquad B_{kk'll'} = \frac{\delta^2 E}{\delta R^*_{kk'}\delta R^*_{ll'}}, \tag{59}$$

where E is the total energy, and E_k denotes single-quasiparticle energies.

Instead of evaluating the matrix elements of the Dirac Hamiltonian in the basis of Hartree-Bogoliubov spinors, it is simpler to solve the RQRPA equations in the canonical basis [68], in which the relativistic Hartree-Bogoliubov wave functions can be expressed in the form of BCS-like wave functions. Taking into account the rotational invariance of the nuclear system, the quasiparticle pairs can be coupled to good angular momentum and the matrix equation takes the form

$$\begin{pmatrix} A^J & B^J \\ B^{*J} & A^{*J} \end{pmatrix} \begin{pmatrix} X^{\nu,JM} \\ Y^{\nu,JM} \end{pmatrix} = \omega_\nu \begin{pmatrix} 1 & 0 \\ 0 & -1 \end{pmatrix} \begin{pmatrix} X^{\nu,JM} \\ Y^{\nu,JM} \end{pmatrix}. \tag{60}$$

For each RQRPA energy ω_ν, X^ν and Y^ν denote the corresponding forward- and backward-going two-quasiparticle amplitudes, respectively. The coupled RQRPA matrices in the canonical basis read

$$\begin{aligned} A^J_{\kappa\kappa'\lambda\lambda'} &= H^{11(J)}_{\kappa\lambda}\delta_{\kappa'\lambda'} - H^{11(J)}_{\kappa'\lambda}\delta_{\kappa\lambda'} - H^{11(J)}_{\kappa\lambda'}\delta_{\kappa'\lambda} + H^{11(J)}_{\kappa'\lambda'}\delta_{\kappa\lambda} \\ &\quad + \frac{1}{2}(\xi^+_{\kappa\kappa'}\xi^+_{\lambda\lambda'} + \xi^-_{\kappa\kappa'}\xi^-_{\lambda\lambda'})V^{ppJ}_{\kappa\kappa'\lambda\lambda'} \\ &\quad + \zeta_{\kappa\kappa'\lambda\lambda'}V^{phJ}_{\kappa\lambda'\kappa'\lambda} \qquad (61) \\ B^J_{\kappa\kappa'\lambda\lambda'} &= \frac{1}{2}(\xi^+_{\kappa\kappa'}\xi^+_{\lambda\lambda'} - \xi^-_{\kappa\kappa'}\xi^-_{\lambda\lambda'})V^{ppJ}_{\kappa\kappa'\lambda\lambda'} \\ &\quad + \zeta_{\kappa\kappa'\lambda\lambda'}(-1)^{j_\lambda - j_{\lambda'}+J}V^{phJ}_{\kappa\lambda\kappa'\lambda'}. \qquad (62) \end{aligned}$$

and H^{11} denotes the one-quasiparticle terms

$$H^{11}_{\kappa\lambda} = (u_\kappa u_\lambda - v_\kappa v_\lambda)h_{\kappa\lambda} - (u_\kappa v_\lambda + v_\kappa u_\lambda)\Delta_{\kappa\lambda}, \tag{63}$$

that is, the canonical RHB basis does not diagonalize the Dirac single-nucleon mean-field Hamiltonian $\hat{h}_D$ and the pairing field $\hat{\Delta}$. The occupation amplitudes v_k of the

canonical states are eigenvalues of the density matrix. V^{ph} and V^{pp} are the particle-hole and particle-particle residual interactions, respectively. Their matrix elements are multiplied by the pairing factors $\xi^{\pm}$ and ζ, defined by the occupation amplitudes of canonical states.

The RQRPA configuration space includes the Dirac sea of negative energy states. In addition to configurations built from two-quasiparticle states of positive energy, the RQRPA configuration space must also contain pair configurations formed from fully or partially occupied states of positive energy and empty negative-energy states from the Dirac sea. The inclusion of configurations built from occupied positive-energy states and empty negative-energy states is essential for current conservation and the decoupling of spurious states. The RQRPA model is fully consistent [68]: the same interactions, both in the particle-hole and particle-particle channels, are used in the RHB equation (38) that determines the SCMF solution, and in the RQRPA equation (60). A detailed review of the RQRPA formalism and applications can be found in [69].

As illustrative examples we present RQRPA results for the multipole response of spherical nuclei. For the multipole operator $\hat{Q}_{\lambda\mu}$ the response function $R(E)$ is defined

$$R(E, J) = \sum_{\nu} B(J, \omega_\nu) \frac{1}{\pi} \frac{\Gamma/2}{(E - \omega_\nu)^2 + (\Gamma/2)^2}, \tag{64}$$

where Γ is the width of the Lorentzian distribution, and

$$B(J, \omega_\nu) = \left| \sum_{\kappa\kappa'} \left\{ X^{\nu,J0}_{\kappa\kappa'} \langle \kappa || \hat{Q}_J || \kappa' \rangle + (-1)^{j_\kappa - j_{\kappa'} + J} Y^{\nu,J0}_{\kappa\kappa'} \langle \kappa' || \hat{Q}_J || \kappa \rangle \right\} (u_\kappa v_{\kappa'} + (-1)^J v_\kappa u_{\kappa'}) \right|^2. \tag{65}$$

In the examples considered here, the discrete strength distribution are folded by a Lorentzian of width $\Gamma = 1$ MeV.

Figure 8 displays the isovector dipole strength functions in ^{116,118,120,124}Sn, calculated with the energy density functional DD-PC1 and the finite-range separable pairing interaction (46), in comparison to experimental excitation energies of isovector giant dipole resonances (IVGDR). The isovector dipole response is determined by the nuclear matter symmetry energy and its slope at saturation density [72]. We note that, although the strength distributions exhibit considerable fragmentation in the region of giant resonances, the RQRPA calculation reproduces the isotopic dependence of the IVGDR and the experimental excitation energies. The theoretical peak energies 15.56 MeV (^{116}Sn), 15.35 MeV (^{118}Sn), 15.26 MeV (^{120}Sn), 15.13 MeV (^{124}Sn), are in excellent agreement with the experimental values: 15.68 MeV (^{116}Sn), 15.59 MeV (^{118}Sn), 15.36 MeV (^{120}Sn), 15.19 MeV (^{124}Sn), respectively [70].

In Fig. 9 we show the RQRPA isoscalar monopole strength functions for the chain of even-even Sn isotopes: $^{112-124}$Sn. These results can be compared to data on the isoscalar giant monopole resonances (ISGMR) [71]. The ISGMR in heavy nuclei

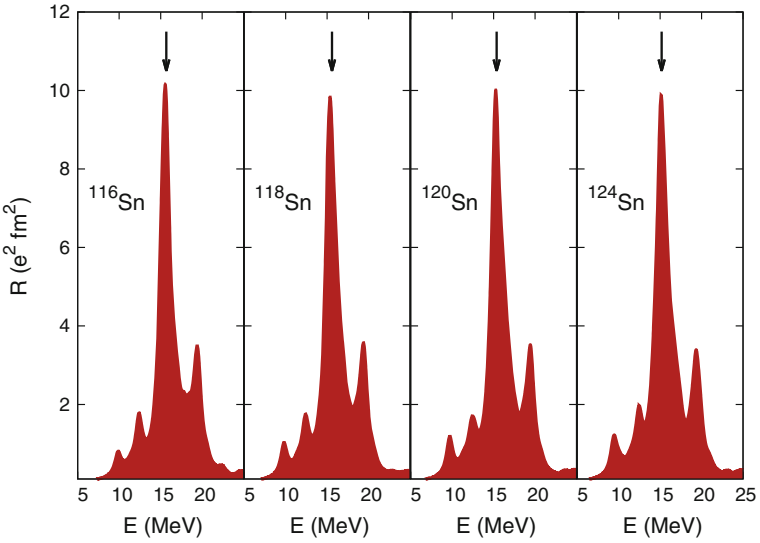

Fig. 8 The RQRPA isovector dipole strength functions in ^{116,118,120,124}Sn, calculated with the energy density functional DD-PC1 plus finite-range separable pairing. The experimental IVGDR excitation energies are denoted by *arrows* [70]

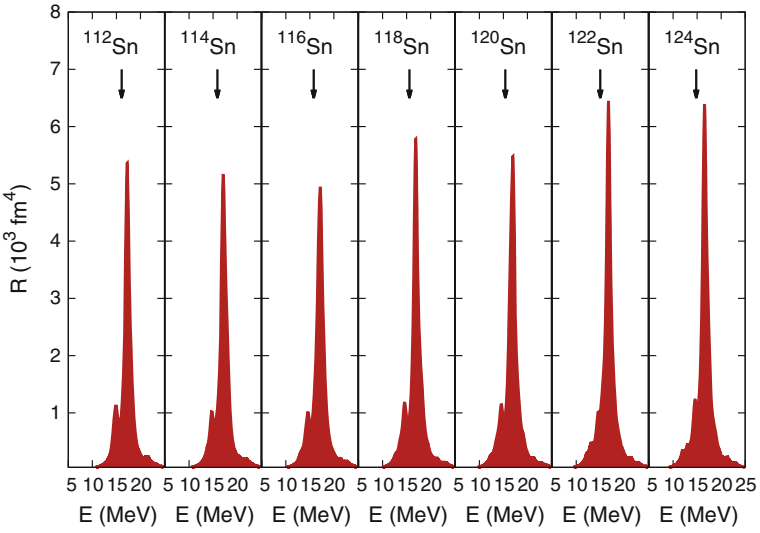

Fig. 9 The RQRPA isoscalar monopole strength distributions in even-even $^{112-124}$Sn nuclei, calculated with the energy density functional DD-PC1 plus finite-range separable pairing. *Arrows* denote the positions of experimental ISGMR excitation energies [71]

provides experimental information on the nuclear matter compression modulus K_∞. This quantity determines basic properties of nuclei, supernovae explosions, neutron stars and heavy-ion collisions. The presently available data set of ISGMR excitation energies, however, does not limit the range of K_∞ to better than 200–240 MeV. The microscopic determination of the nuclear matter compressibility is based on the construction of sets of effective interactions that differ mostly by their prediction of the excitation energies of ISGMR, i.e. by the value of K_∞, but otherwise reproduce reasonably well data on ground-state nuclear properties. In particular, the excitation energies of Sn isotopes calculated using the functional DD-PC1, when compared to the experimental values determined in the energy interval between 10.5 and 20.5 MeV [71], are systematically higher: between 0.8 and 1 MeV. This could indicate that the DD-PC1 nuclear matter compression modulus $K_\infty = 230$ MeV is somewhat too large, even though the calculated ISGMR of Sn isotopes also include the effect of surface compressibility.

5.2 *Configuration Mixing of Angular-Momentum and Particle-Number Projected SCMF States*

In the analysis of low-energy collective structure phenomena related to shell evolution, one can start from constrained SCMF calculations of total energy surfaces. The deformation energy surface is obtained by imposing constraints on the mass multipole moments and, for instance, the method of quadratic constraints uses an unrestricted variation of the function

$$\langle \hat{H} \rangle + \sum_{\lambda\mu} C_{\lambda\mu} \left(\langle \hat{Q}_{\lambda\mu} \rangle - q_{\lambda\mu} \right)^2, \tag{66}$$

where $\langle \hat{H} \rangle$ is the total energy, and $\langle \hat{Q}_{\lambda\mu} \rangle$ denotes the expectation value of the mass multipole operators. For example, in the case of quadrupole deformations

$$\hat{Q}_{20} = 2z^2 - x^2 - y^2 \quad \text{and} \quad \hat{Q}_{22} = x^2 - y^2. \tag{67}$$

$q_{2\mu}$ is the constrained value of the multipole moment, and $C_{2\mu}$ the corresponding stiffness constant. To obtain a constrained self-consistent solution the quadratic constraint adds an extra force $\sum_{\mu=0,2} \lambda_\mu \hat{Q}_{2\mu}$, such that the nucleus is kept at a point different from the stationary point. The result are static symmetry-breaking product many-body states. The mass quadrupole moments can be related to the polar deformation parameters β and γ. The parameter β is simply proportional to the intrinsic quadrupole moment, and the angular variable γ specifies the type and orientation of the shape. The limit $\gamma = 0°$ corresponds to axial prolate shapes, whereas the shape is oblate for $\gamma = 60°$. Triaxial shapes are associated with intermediate values $0° \leq \gamma \leq 60°$. The constrained SCMF method, however, produces semi-classical

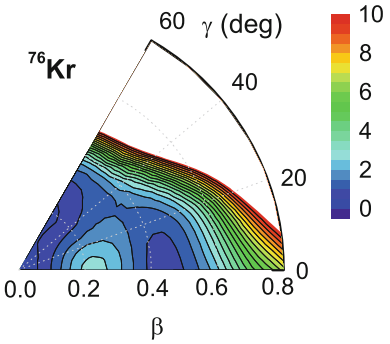

Fig. 10 Self-consistent mean-field triaxial quadrupole energy surface of ^{76}Kr in the $\beta - \gamma$ plane ($0° \leq \gamma \leq 60°$). All energies are normalized with respect to the binding energy of the absolute minimum. The contours join points on the surface with the same energy (in MeV)

deformation energy surfaces, as shown in the example of ^{76}Kr in Fig. 10. To calculate excitation spectra and electromagnetic transition rates it is necessary to extend the SCMF scheme to include collective correlations that arise from symmetry restoration and fluctuations around the mean-field minima. Collective correlations are sensitive to finite-size effects and cannot be incorporated in a universal EDF. This type of correlations requires an explicit treatment for specific nuclei.

The generator coordinate method is based on the assumption that, starting from a set of intrinsic symmetry-breaking states $|\phi(q)\rangle$ that depend on a collective coordinate q, one can build approximate eigenstates of the nuclear Hamiltonian [65]

$$|\Psi_\alpha\rangle = \sum_j f_\alpha(q_j) \left|\phi(q_j)\right\rangle. \tag{68}$$

Here the intrinsic basis states $|\phi(q)\rangle$ are Slater determinants of single-particle or quasi-particle states generated by solving the constrained self-consistent mean-field plus pairing equations with mass quadrupole moments (quadrupole, octupole) as the generating coordinates q. The deformed mean-field breaks rotational symmetry, and the particle number is not conserved because of the approximate treatment of pairing correlations, that is, the basis states $|\phi(q)\rangle$ are not eigenstates of the total angular momentum and particle number operators. Therefore, to be able to compare model predictions to data such as, for instance, transition rates between states with good angular momentum, one must construct states with good angular momentum and particle number by performing projections from the SCMF solutions. In the first step we consider the trial angular-momentum projected GCM collective wave function $|\Psi_\alpha^{JM}\rangle$, an eigenfunction of $\hat{J}^2$ and $\hat{J}_z$, with eigenvalues $J(J+1)\hbar^2$ and $M\hbar$, respectively,

$$|\Psi_\alpha^{JM}\rangle = \int dq \sum_{K\geq 0} f_\alpha^{JK}(q) \frac{1}{(1+\delta_{K0})} |JMK, q\rangle, \tag{69}$$

where $\alpha = 1, 2, \ldots$ labels collective eigenstates for a given angular momentum J. In the illustrative case of a quadrupole deformed even-even nucleus, the projection of the angular momentum J along the intrinsic z-axis (K in (69)) takes only non-negative even values:

$$K = \begin{cases} 0, 2, \ldots, J & \text{for } J \bmod 2 = 0 \\ 2, 4, \ldots, J-1 & \text{for } J \bmod 2 = 1 \end{cases} \tag{70}$$

The basis states $|JMK, q\rangle$ are projected from the intrinsic wave functions $|\Phi(q)\rangle$:

$$|JMK, q\rangle = [\hat{P}^J_{MK} + (-1)^J \hat{P}^J_{M-K}]|\Phi(q)\rangle, \tag{71}$$

where $\hat{P}^J_{MK}$ is the angular-momentum projection operator:

$$\hat{P}^J_{MK} = \frac{2J+1}{8\pi^2} \int d\Omega\, D^{J*}_{MK}(\Omega)\hat{R}(\Omega). \tag{72}$$

Ω denotes the three Euler angles: (ϕ, θ, ψ), and $d\Omega = d\phi \sin\theta d\theta d\psi$. $D^J_{MK}(\Omega)$ is the Wigner D-function, with the rotation operator $\hat{R}(\Omega) = e^{i\phi\hat{J}_z} e^{i\theta\hat{J}_y} e^{i\psi\hat{J}_z}$.

The set of intrinsic wave functions $|\Phi(q)\rangle$, with the generic notation for quadrupole deformation parameters $q \equiv (\beta, \gamma)$, is generated by imposing constraints on the axial and triaxial mass quadrupole moments in a SCMF calculation. The weight functions $f^{JK}_\alpha(q)$ in the collective wave function (69) are determined from the variational equation:

$$\delta E^J = \delta \frac{\langle \Psi^{JM}_\alpha | \hat{H} | \Psi^{JM}_\alpha \rangle}{\langle \Psi^{JM}_\alpha | \Psi^{JM}_\alpha \rangle} = 0, \tag{73}$$

that is, by requiring that the expectation value of the Hamiltonian is stationary with respect to an arbitrary variation δf^{JK}_α. This leads to the Hill-Wheeler-Griffin (HWG) integral equation [65, 73]

$$\int dq' \sum_{K' \geq 0} \left[\mathscr{H}^J_{KK'}(q, q') - E^J_\alpha \mathscr{N}^J_{KK'}(q, q')\right] f^{JK'}_\alpha(q') = 0, \tag{74}$$

where $\mathscr{H}$ and $\mathscr{N}$ are the angular-momentum projected GCM kernel matrices of the Hamiltonian and the norm, respectively. With the generic notation $\mathscr{O} \equiv \mathscr{N}$ or $\mathscr{H}$, the expression for the kernel reads:

$$\begin{aligned} \mathscr{O}^J_{KK'}(q, q') = \Delta_{KK'}[&O^J_{KK'}(q, q') + (-1)^{2J} O^J_{-K-K'}(q, q') \\ &+ (-1)^J O^J_{K-K'}(q, q') + (-1)^J O^J_{-KK'}(q, q')], \end{aligned} \tag{75}$$

where for the operator $\hat{O} \equiv 1$ or $\hat{H}$:

$$O^J_{KK'}(q,q') = \langle \Phi(q)|\hat{O}\,\hat{P}^J_{KK'}|\Phi(q')\rangle, \tag{76}$$

and $\Delta_{KK'} = 1/[(1+\delta_{K0})(1+\delta_{K'0})]$. The overlap can be evaluated in coordinate space, and thus we rewrite the Hamiltonian kernel $H^J_{KK'}(q,q')$ in the following form:

$$H^J_{KK'}(q,q') = \int d\boldsymbol{r}\, H^J_{KK'}(\boldsymbol{r};q,q'), \tag{77}$$

where

$$H^J_{KK'}(\boldsymbol{r};q,q') = \frac{2J+1}{8\pi^2}\int d\Omega\, D^{J*}_{KK'}\mathscr{H}(\boldsymbol{r};q,q';\Omega)n(q,q';\Omega) \tag{78}$$

The norm overlap $n(q,q';\Omega)$ is defined by:

$$n(q,q';\Omega) \equiv \langle \Phi(q)|\hat{R}(\Omega)|\Phi(q')\rangle. \tag{79}$$

$\mathscr{H}(\boldsymbol{r};q,q';\Omega)$ has the same form as the mean-field functional provided the *intrinsic* densities are replaced by *transition* densities.

The weight functions $f^{JK}_\alpha(q)$ in (74) are not orthogonal and cannot be interpreted as collective wave functions for the deformation variables. In practice, the first step in the solution of the HWG matrix eigenvalue equation is the diagonalization of the norm overlap kernel $\mathscr{N}^J(i,j)$

$$\sum_j \mathscr{N}^J(i,j)u^J_k(j) = n^J_k u^J_k(i). \tag{80}$$

The resulting collective Hamiltonian

$$\mathscr{H}^J_{kl} = \frac{1}{\sqrt{n^J_k}\sqrt{n^J_l}}\sum_{i,j} u^J_k(i)\mathscr{H}^J(i,j)u^J_l(j), \tag{81}$$

is subsequently diagonalized

$$\sum_l \mathscr{H}^J_{kl}\, g^{J\alpha}_l = E^J_\alpha\, g^{J\alpha}_k. \tag{82}$$

The solution of (82) determines both the energies and amplitudes $f^{JK}_\alpha(q)$ of collective states

$$f^{JK}_\alpha(q) = \sum_k \frac{g^{J\alpha}_k}{\sqrt{n^J_k}}u^J_k(i). \tag{83}$$

The collective wave functions $g_\alpha^J(i)$ are calculated from the norm overlap eigenstates:

$$g_\alpha^J(i) = \sum_k g_k^{J\alpha} u_k^J(i). \tag{84}$$

$g_\alpha^J(i)$ are orthonormal and, therefore, $|g_\alpha^J(i)|^2$ can be interpreted as a probability amplitude.

The basis states $|\Phi(q)\rangle$ are not eigenstates of the proton and neutron number operator $\hat{Z}$ and $\hat{N}$ and, therefore, the wave functions $\left|\Psi_\alpha^{JM}\right\rangle$ are generally not eigenstates of the nucleon number operator. Moreover, the average value of the nucleon number in these states is not necessarily equal to the number of nucleons in a given nucleus. To restore the correct mean value of the nucleon number, the standard method is to modify the HWG equation by replacing $\mathscr{H}(\boldsymbol{r}; q, q'; \Omega)$ with

$$\begin{aligned}\mathscr{H}'(\boldsymbol{r}; q, q'; \Omega) = \mathscr{H}(\boldsymbol{r}; q, q'; \Omega) - \lambda_p[Z(\boldsymbol{r}; q, q'; \Omega) - Z_0] \\ -\lambda_n[N(\boldsymbol{r}; q, q'; \Omega) - N_0],\end{aligned} \tag{85}$$

where Z_0 and N_0 are the desired proton and neutron numbers, respectively. $Z(\boldsymbol{r}; q, q'; \Omega)$ and $N(\boldsymbol{r}; q, q'; \Omega)$ are the transition densities in $\boldsymbol{r}$-space for protons and neutrons.

An exact treatment of the non-conservation of particle number necessitates the extension of the angular-momentum projected GCM approach to include the full restoration of particle number in the wave functions of GCM states. The nuclear wave function is expressed:

$$\left|\Psi_\alpha^{JM}\right\rangle = \sum_{j,K} f_\alpha^{JK}(q_j) \hat{P}_{MK}^J \hat{P}^Z \hat{P}^N \left|\phi(q_j)\right\rangle, \tag{86}$$

where the particle-number projection operators read

$$\hat{P}^N = \frac{1}{2\pi} \int_0^{2\pi} d\varphi_n e^{i(\hat{N}-N)\varphi_n}, \quad \hat{P}^Z = \frac{1}{2\pi} \int_0^{2\pi} d\varphi_p e^{i(\hat{Z}-Z)\varphi_p}. \tag{87}$$

$\hat{N}(\hat{Z})$ is the number operator for neutrons (protons), and $N(Z)$ denotes the number of neutrons (protons).

The weight functions $f_\alpha^{JK}(q_j)$ are again determined from the requirement that the expectation value of the energy is stationary with respect to an arbitrary variation δf_α^{JK}, and this leads to the HWG equation:

$$\sum_{j,K} f_\alpha^{JK}(q_j) \left(\langle\phi(q_i)| \hat{H} \hat{P}_{MK}^J \hat{P}^N \hat{P}^Z \left|\phi(q_j)\right\rangle - E_\alpha^J \langle\phi(q_i)| \hat{P}_{MK}^J \hat{P}^N \hat{P}^Z \left|\phi(q_j)\right\rangle \right) = 0. \tag{88}$$

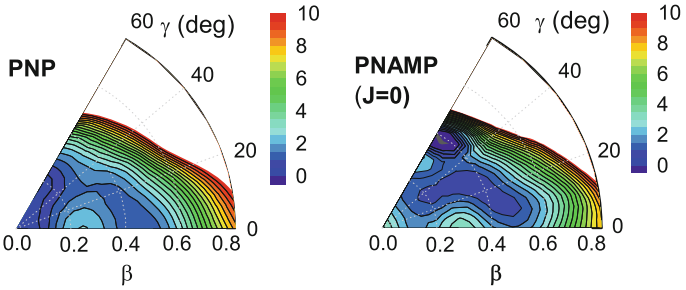

Fig. 11 Constrained energy surfaces in the (β, γ) plane for ^{76}Kr: (*left*) RMF+BCS with particle-number projection (*PNP*), and (*right*) RMF+BCS with both PNP and angular-momentum projection (AMP) on $J = 0$. The energy density functional is PC-PK1 [27], and a density-independent delta force is used in the pairing channel

In the solution of this equation the integrals in (87) are discretized as follows:

$$\hat{P}^N = \frac{1}{L}\sum_{n=1}^{L} e^{i(\hat{N}-N)\phi_n}, \quad \phi_n = \frac{\pi}{L}n. \tag{89}$$

To avoid numerical instabilities that might arise at $\phi = \pi/2$ when the occupation probability of a state is exactly 1/2, an odd number of points is used in the expansion. The HGW equation defines an ordinary eigenvalue problem and, once the amplitudes $f_\alpha^{JK}(q)$ of the nuclear collective wave functions $|\Psi_\alpha^{JM}\rangle$ are obtained, it is straightforward to calculate all physical observables, such as electromagnetic transition probabilities and spectroscopic quadrupole moments.

As an illustration, in Figs. 10 and 11 we display the deformation energy surfaces of ^{76}Kr. Figure 10 shows the energy map calculated with the relativistic energy density functional PC-PK1 [27] and a density-independent delta-interaction in the pairing channel, using the constrained SCMF method with pairing correlations treated in the BCS approximation. We note the spherical minimum which extends along oblate shapes and competes with the prolate deformed minimum. In the left panel of Fig. 11 we plot the corresponding energy surface obtained with the inclusion of particle number projection and, finally, the energy surface shown in the panel on the right includes also angular momentum projection on $J = 0$ mean-field states. Even though particle number projection does not lead to a significant modification of the SCMF energy surface, with the projection on angular momentum one notices considerable differences between the SCMF deformation energy and the energy map of $J = 0$ states in the $\beta - \gamma$ plane. In particular, triaxial deformation develops, soft along the curve that connects the minimum with weak oblate deformation ($|\beta| \approx 0.2$) and the minimum with large prolate deformation ($\beta \approx 0.5$). As a result of angular-momentum projection both these minima become saddle points on the triaxial energy surface. Because of this effect, calculations restricted to axially symmetric configurations obviously cannot provide a quantitative description of the structure of ^{76}Kr. These calculations

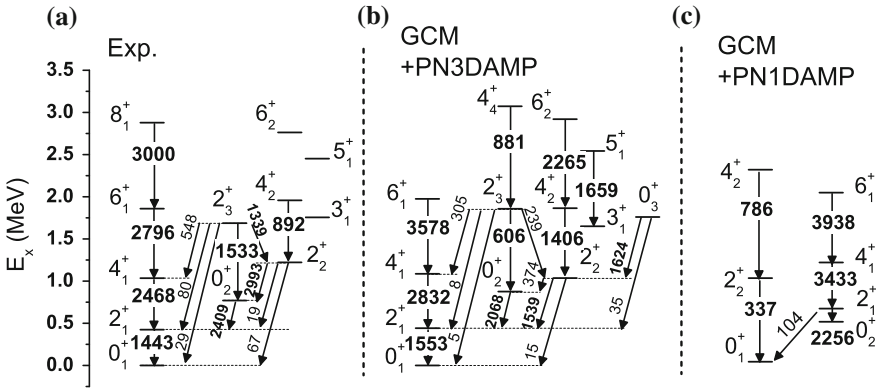

Fig. 12 Low-lying collective states and $B(E2)$ values (in $e^2\text{fm}^4$) of ^{76}Kr. The experimental spectrum [74] (**a**) is compared to the results obtained with the full particle-number and 3D angular-momentum projected GCM (**b**), and to those of the corresponding particle-number and 1D angular-momentum projected GCM restricted to axially symmetric configurations (**c**)

predict the equilibrium minimum at a small oblate deformation and, consequently, fail to reproduce the low-energy excitation spectrum of the isotope ^{76}Kr.

This is shown in Fig. 12 where we compare the low-energy experimental spectrum of ^{76}Kr [74] with results obtained with the full particle-number and 3D angular-momentum projected GCM (b), and to those of the corresponding particle-number and 1D angular-momentum projected GCM restricted to axially symmetric configurations (c). The comparison clearly shows that axially symmetric configurations represent a poor approximation that fails to reproduce the excitation spectrum and transition rates. The axially symmetric 1D GCM predicts the coexistence of the ground-state band built on the oblate deformed minimum and the first excited prolate band. The results, however, are not in agreement with the data. The GCM calculation that includes the triaxial degree of freedom reproduces the experimental spectrum, not only for the ground-state band (yrast states) but also for structures above the yrast. In particular, the strong electric quadrupole transition from the low-lying 0_2^+ state to the 2_1^+ state in the ground-state band observed in the data, and which indicates the degree of mixing between the two lowest oblate and prolate structures, is also reproduced by the 3D model. These results illustrate the importance of the triaxial degree of freedom in the description of collective states of Kr isotopes.

5.3 Quadrupole Collective Hamiltonian

Nuclear excitations determined by quadrupole vibrational and rotational degrees of freedom can be treated simultaneously by considering five collective coordinates α_μ, $\mu = -2, -1, \ldots, 2$ that describe the surface of a quadrupole deformed nucleus:

$R = R_0[1 + \sum_\mu \alpha_\mu Y^*_{2\mu}]$. To separate rotational and vibrational motion, these coordinates are usually parameterized in terms of the two deformation parameters β and γ, and three Euler angles $(\phi,\ \theta,\ \psi) \equiv \Omega$ that define the orientation of the intrinsic principal axes in the laboratory frame

$$\alpha_\mu = D^2_{\mu 0}(\Omega)\beta\cos\gamma + \frac{1}{\sqrt{2}}\left[D^2_{\mu 2}(\Omega) + D^2_{\mu -2}(\Omega)\right]\beta\sin\gamma, \tag{90}$$

where $D^\lambda_{\mu\nu}$ is the Wigner function. The three terms of the classical collective Hamiltonian, expressed in terms of the intrinsic variables β, γ and Euler angles

$$\mathscr{H}_{\rm coll} = \mathscr{T}_{\rm vib}(\beta,\gamma) + \mathscr{T}_{\rm rot}(\beta,\gamma,\Omega) + \mathscr{V}_{\rm coll}(\beta,\gamma), \tag{91}$$

denote the contributions from the vibrational kinetic energy:

$$\mathscr{T}_{\rm vib} = \frac{1}{2}B_{\beta\beta}\dot\beta^2 + \beta B_{\beta\gamma}\dot\beta\dot\gamma + \frac{1}{2}\beta^2 B_{\gamma\gamma}\dot\gamma^2, \tag{92}$$

the rotational kinetic energy:

$$\mathscr{T}_{\rm rot} = \frac{1}{2}\sum_{k=1}^{3}\mathscr{I}_k\omega_k^2, \tag{93}$$

and the collective potential energy $\mathscr{V}_{\rm coll}(\beta,\gamma)$. The mass parameters $B_{\beta\beta}$, $B_{\beta\gamma}$, $B_{\gamma\gamma}$, and the moments of inertia $\mathscr{I}_k$ depend on the quadrupole deformation variables β and γ.

The Hamiltonian (91) is quantized according to the general Pauli prescription [75]: for the classical kinetic energy

$$T = \frac{1}{2}\sum_{ij} B_{ij}(q)\dot q_i\dot q_j, \tag{94}$$

the corresponding quantized form reads:

$$\hat H_{\rm kin} = -\frac{\hbar^2}{2}\frac{1}{\sqrt{{\rm det}B}}\sum_{ij}\frac{\partial}{\partial q_i}\sqrt{{\rm det}B}(B^{-1})_{ij}\frac{\partial}{\partial q_j}. \tag{95}$$

The kinetic energy tensor in (91) takes the block diagonal form:

$$B = \begin{pmatrix} B_{\rm vib} & 0 \\ 0 & B_{\rm rot}\end{pmatrix}, \tag{96}$$

with the vibrational part of the tensor

$$B_{\text{vib}} = \begin{pmatrix} B_{\beta\beta} & \beta B_{\beta\gamma} \\ \beta B_{\beta\gamma} & \beta^2 B_{\gamma\gamma} \end{pmatrix}. \tag{97}$$

In general the rotational part is a complicated function of the Euler angles but, using the quasi-coordinates related to the components of the angular momentum in the body-fixed frame, it takes a simple diagonal form

$$(B_{\text{rot}})_{ik} = \delta_{ik}\mathscr{I}_k, \quad k = 1, 2, 3, \tag{98}$$

with the moments of inertia expressed as

$$\mathscr{I}_k = 4B_k\beta^2 \sin^2(\gamma - 2k\pi/3). \tag{99}$$

The quantized collective Hamiltonian can be expressed in the form:

$$\hat{H} = \hat{T}_{\text{vib}} + \hat{T}_{\text{rot}} + V_{\text{coll}}, \tag{100}$$

with

$$\begin{aligned} \hat{T}_{\text{vib}} = &- \frac{\hbar^2}{2\sqrt{wr}} \left\{ \frac{1}{\beta^4} \left[\frac{\partial}{\partial\beta}\sqrt{\frac{r}{w}}\beta^4 B_{\gamma\gamma}\frac{\partial}{\partial\beta} - \frac{\partial}{\partial\beta}\sqrt{\frac{r}{w}}\beta^3 B_{\beta\gamma}\frac{\partial}{\partial\gamma} \right] \right. \\ &\left. + \frac{1}{\beta\sin 3\gamma} \left[-\frac{\partial}{\partial\gamma}\sqrt{\frac{r}{w}}\sin 3\gamma\, B_{\beta\gamma}\frac{\partial}{\partial\beta} + \frac{1}{\beta}\frac{\partial}{\partial\gamma}\sqrt{\frac{r}{w}}\sin 3\gamma\, B_{\beta\beta}\frac{\partial}{\partial\gamma} \right] \right\}, \end{aligned} \tag{101}$$

where $w = B_{\beta\beta}B_{\gamma\gamma} - B_{\beta\gamma}^2$ and $r = B_1 B_2 B_3$, and

$$\hat{T}_{\text{rot}} = \frac{1}{2}\sum_{k=1}^{3}\frac{\hat{J}_k^2}{\mathscr{I}_k}. \tag{102}$$

$\hat{J}_k$ denotes the components of the angular momentum in the body-fixed frame of a nucleus, and V_{coll} is the collective potential. The Hamiltonian describes quadrupole vibrations, rotations, and the coupling between these collective modes.

The result of the diagonalization of the Hamiltonian (100) is the collective energy spectrum E_α^J and the corresponding eigenfunctions

$$\Psi_\alpha^{JM}(\beta, \gamma, \Omega) = \sum_{K\in\Delta J} \psi_{\alpha K}^J(\beta, \gamma)\Phi_{MK}^J(\Omega), \tag{103}$$

where the angular part corresponds to a linear combination of Wigner functions

$$\Phi_{MK}^J(\Omega) = \sqrt{\frac{2J+1}{16\pi^2(1+\delta_{K0})}}\left[D_{MK}^{J*}(\Omega) + (-1)^J D_{M-K}^{J*}(\Omega)\right], \tag{104}$$

and the summation in (103) is over the allowed set of K values (defined in (70)). Using the collective wave functions (103), various observables can be calculated and compared with experimental results. For instance, the quadrupole E2 reduced transition probability:

$$B(\mathrm{E2};\ \alpha J \rightarrow \alpha' J') = \frac{1}{2J+1}|\langle \alpha' J'||\hat{\mathscr{M}}(E2)||\alpha J\rangle|^2, \tag{105}$$

and the spectroscopic quadrupole moment of the state $|\alpha J\rangle$:

$$Q_{\mathrm{spec},\alpha J} = \frac{1}{\sqrt{2J+1}} C^{JJ}_{JJ20}\langle \alpha J||\hat{\mathscr{M}}(E2)||\alpha J\rangle, \tag{106}$$

where $\hat{\mathscr{M}}(E2)$ denotes the electric quadrupole operator. Detailed expressions for the reduced matrix elements $\langle \alpha' J'||\hat{\mathscr{M}}(E2)||\alpha J\rangle$ can be found in [76].

The entire dynamics of the collective Hamiltonian is governed by the seven functions of the intrinsic deformations β and γ: the collective potential, the three mass parameters: $B_{\beta\beta}$, $B_{\beta\gamma}$, $B_{\gamma\gamma}$, and the three moments of inertia $\mathscr{I}_k$. These functions are determined by the choice of a particular nuclear energy density functional and effective pairing interaction (pairing functional). The quasiparticle wave functions and energies, generated from constrained SCMF solutions at each point on the deformation energy surface, provide the microscopic input for the parameters of the collective Hamiltonian [77].

In the simplest approximation the moments of inertia are calculated from the Inglis-Belyaev formula:

$$\mathscr{I}_k = \sum_{i,j} \frac{|\langle ij|\hat{J}_k|\Phi\rangle|^2}{E_i + E_j} \quad k = 1, 2, 3, \tag{107}$$

where k denotes the axis of rotation, the summation runs over proton and neutron quasiparticle states $|ij\rangle = \beta^\dagger_i \beta^\dagger_j |\Phi\rangle$, and $|\Phi\rangle$ represents the quasiparticle vacuum. The mass parameters associated with the two quadrupole collective coordinates $q_0 = \langle \hat{Q}_{20}\rangle$ and $q_2 = \langle \hat{Q}_{22}\rangle$ are calculated in the cranking approximation:

$$B_{\mu\nu}(q_0, q_2) = \frac{\hbar^2}{2}\left[\mathscr{M}^{-1}_{(1)}\mathscr{M}_{(3)}\mathscr{M}^{-1}_{(1)}\right]_{\mu\nu}, \tag{108}$$

where

$$\mathscr{M}_{(n),\mu\nu}(q_0, q_2) = \sum_{i,j} \frac{\left|\langle\Phi|\hat{Q}_{2\mu}|ij\rangle\langle ij|\hat{Q}_{2\nu}|\Phi\rangle\right|}{(E_i + E_j)^n}. \tag{109}$$

The collective energy surface includes the energy of zero-point motion, and this quantity has to be subtracted. The collective zero-point energy (ZPE) corresponds

to a superposition of zero-point motion of individual nucleons in the single-nucleon potential. In the general case the ZPE corrections on the potential energy depend on deformation. The ZPE includes terms originating from the vibrational and rotational kinetic energy, and a contribution of potential energy

$$\Delta V(q_0, q_2) = \Delta V_{\text{vib}}(q_0, q_2) + \Delta V_{\text{rot}}(q_0, q_2) + \Delta V_{\text{pot}}(q_0, q_2). \tag{110}$$

The latter is much smaller than the contribution of the kinetic energy, and is usually neglected. Simple prescriptions for the calculation of vibrational and rotational ZPE have been derived in [67]. Both corrections are calculated in the cranking approximation, that is, on the same level of approximation as the mass parameters and the moments of inertia. The vibrational ZPE is given by the expression:

$$\Delta V_{\text{vib}}(q_0, q_2) = \frac{1}{4}\text{Tr}\left[\mathscr{M}_{(3)}^{-1}\mathscr{M}_{(2)}\right]. \tag{111}$$

The rotational ZPE is a sum of three terms:

$$\Delta V_{\text{rot}}(q_0, q_2) = \Delta V_{-2-2}(q_0, q_2) + \Delta V_{-1-1}(q_0, q_2) + \Delta V_{11}(q_0, q_2), \tag{112}$$

with

$$\Delta V_{\mu\nu}(q_0, q_2) = \frac{1}{4}\frac{\mathscr{M}_{(2),\mu\nu}(q_0, q_2)}{\mathscr{M}_{(3),\mu\nu}(q_0, q_2)}. \tag{113}$$

The individual terms are calculated from (113) and (109), with the intrinsic components of the quadrupole operator defined by:

$$\hat{Q}_{21} = -2iyz, \quad \hat{Q}_{2-1} = -2xz, \quad \hat{Q}_{2-2} = 2ixy. \tag{114}$$

The potential V_{coll} in the collective Hamiltonian (100) is obtained by subtracting the ZPE corrections from the total mean-field energy:

$$V_{\text{coll}}(q_0, q_2) = E_{\text{tot}}(q_0, q_2) - \Delta V_{\text{vib}}(q_0, q_2) - \Delta V_{\text{rot}}(q_0, q_2). \tag{115}$$

As an example we consider the EDFs-based description of the collective spectrum of ^{152}Sm. Figure 13 displays the self-consistent triaxial quadrupole deformation energy surface of this isotope, calculated with the RHB model based on the energy density functional DD-PC1 and the finite-range separable pairing interaction (46). The filled circle denotes the equilibrium minimum; all energies are normalized with respect to the binding energy of the absolute minimum. The contours join points with the same energy. We note that the equilibrium minimum corresponds to a prolate shape ($\gamma = 0°$), but the potential shows considerable softness in the γ degree of freedom. Starting from the single-quasiparticle nucleon wave functions and energies that correspond to each point on the energy surface, the parameters of the collective Hamiltonian: the mass parameters $B_{\beta\beta}$, $B_{\beta\gamma}$, $B_{\gamma\gamma}$, the three moments of inertia

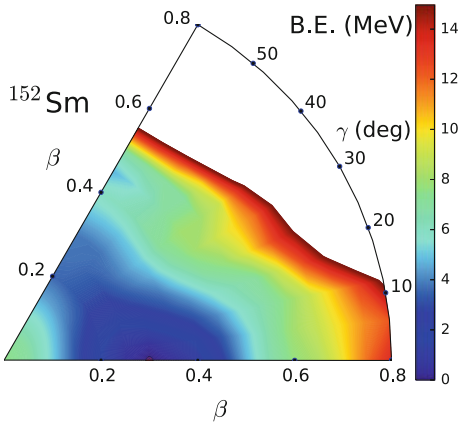

Fig. 13 Self-consistent RHB triaxial quadrupole binding-energy map of ^{152}Sm in the $\beta - \gamma$ plane ($0 \leq \gamma \leq 60°$). Energy points are normalized with respect to the binding energy of the absolute minimum, and the contours join points on the surface with the same energy (in MeV)

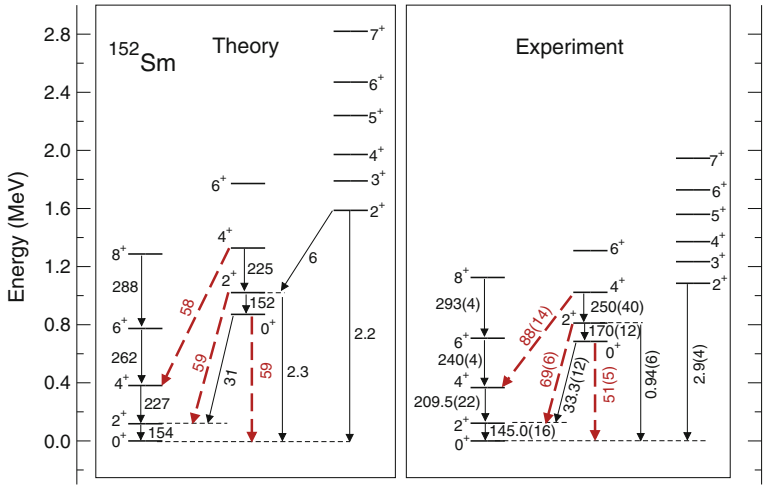

Fig. 14 The theoretical excitation spectrum of ^{152}Sm (*left*), compared to data [78]. The intraband and interband B(E2) values (*thin solid arrows*) are in Weisskopf units, and (*red*) *dashed arrows* denote E0 transitions with the corresponding $\rho^2(E0) \times 10^3$ values

$\mathscr{I}_k$, as well as the zero-point energy corrections, are calculated as functions of the deformations β and γ. The diagonalization of the resulting Hamiltonian gives the excitation energies and the collective wave functions for each value of the total angular momentum and parity J^π. Observables are calculated in the full configuration space and there are no effective charges in the model. In Fig. 14 we plot the the low-energy spectrum of ^{152}Sm in comparison to available data [78] for the excitation energies, reduced electric quadrupole transition probabilities $B(E2)$ (in Weisskopf

units), and the electric monopole transition strengths $\rho^2(E0)$. In addition to the yrast ground-state band, in deformed and transitional nuclei low-energy collective states are usually also ordered in (quasi) β and γ bands. This is done according to the distribution projection K of the angular momentum J on the z axis in the body-fixed frame:

$$N_K = 6 \int_0^{\pi/3} \int_0^{\infty} |\psi^J_{\alpha,K}(\beta,\gamma)|^2 \beta^4 |\sin 3\gamma| d\beta d\gamma, \tag{116}$$

where the components $\psi^J_{\alpha,K}(\beta,\gamma)$ are defined in (103). For large deformations the quantum number K is to a good approximation conserved. Consequently, only one of the integrals (116) will give a value close to 1. A broader distribution of N_K values in the state $|\alpha J\rangle$ provides a measure of the mixing of intrinsic configurations. Excited states with predominant $K = 2$ components in the wave function are assigned to the γ-band, whereas the β-band comprises states above the yrast characterised by dominant $K = 0$ components.

For the ground-state band the theoretical excitation energies and $B(E2)$ values for transitions within the band are in very good agreement with data, except for the fact that the empirical moments of inertia are systematically larger than those calculated with the collective Hamiltonian. This is a well known effect of using the simple Inglis-Belyaev approximation for the moments of inertia, and is also reflected in the excitation energies of the excited $K = 0$ and $K = 2$ bands [79]. The effect is also illustrated in the left panel of Fig. 16, in which we plot the ground-state band excitation energies relative to the energy of the level 2^+_1. The collective wave functions, however, are not affected by this approximation and the model reproduces both the intraband and interband $E2$ transition probabilities. The $K = 2$ γ-band is predicted at somewhat higher excitation energies compared to its experimental counterpart, and this is most probably due to the potential energy surfaces being too stiff in γ. The deformed rare-earth $N = 90$ isotones are characterised by very low $K = 0$ bands based on the 0^+_2 states. In ^{152}Sm, for instance, this state is found at 685 keV excitation energy, considerably below the $K = 2$ γ-band. In ^{152}Sm the excited $K = 0$ band is calculated at moderately higher energy compared to data. The $E0$ transitions strengths reflect the degree of mixing between the two lowest $K = 0$ bands, and we note that the theoretical values that correspond to transitions between the eigenstates of the collective Hamiltonian reproduce the empirical $\rho^2(E0)$ values. The structure of the band-head states 0^+_1, 2^+_3 and 0^+_2 is illustrated in Fig. 15, where we plot the probability density distributions in the (β,γ) plane

$$\rho_{J\alpha}(\beta,\gamma) = \sum_{K\in\Delta J} \left|\psi^J_{\alpha K}(\beta,\gamma)\right|^2 \beta^3, \tag{117}$$

with the summation over the allowed set of values of the projection K of the angular momentum J on the body-fixed symmetry axis, and with the normalization

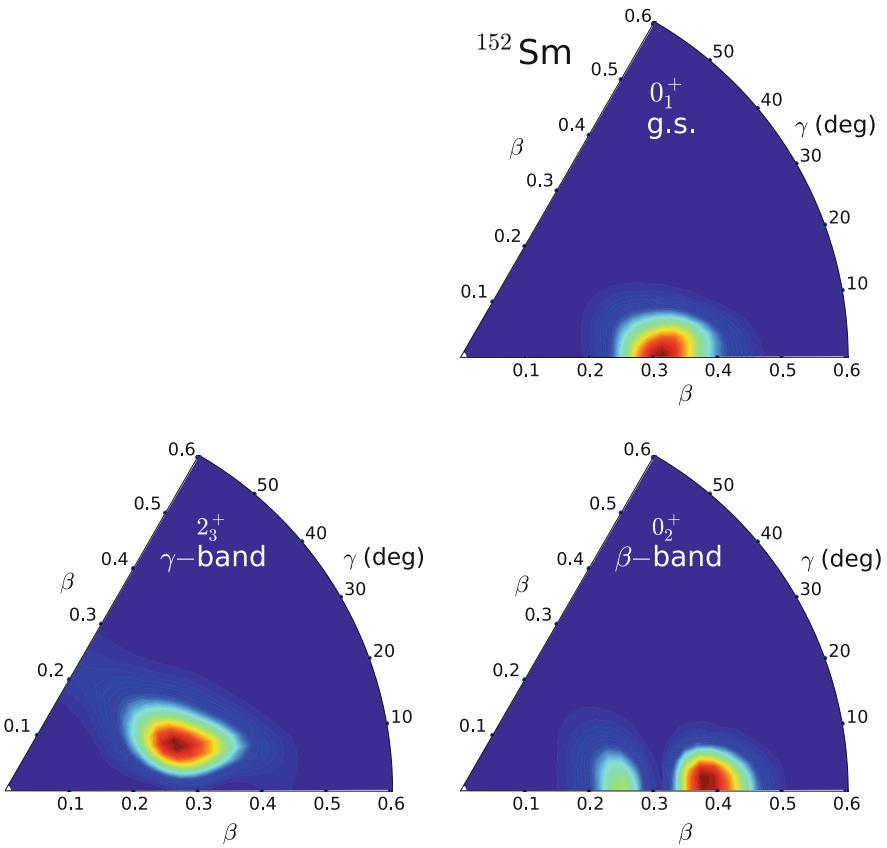

Fig. 15 Probability distributions (117) in the $\beta - \gamma$ plane for the band-head states of the lowest $K = 0$ and $K = 2$ bands in ^{152}Sm

$$\int_0^\infty \beta d\beta \int_0^{2\pi} \rho_{J\alpha}(\beta, \gamma) |\sin 3\gamma| d\gamma = 1. \tag{118}$$

The probability distributions for the 0_1^+ and 0_2^+ states are concentrated on the prolate axis $\gamma = 0°$, in contrast to the band-head of the γ-band, for which the dynamical γ-deformation clearly point to the γ-vibrational nature of the $K = 2$ states. The average value of the deformation parameter β for the collective ground-state wave function of ^{152}Sm is $<\beta> = 0.32$. The state 0_2^+ with the large $B(E2; 0_2^+ \rightarrow 2_1^+) = 31$ W.u. (experimental value 33.3 ± 1.3 W.u.) is considered a candidate for a β-vibration [80]. For a pure harmonic β-vibrational state one expects that the average deformation is the same as for the ground-state and that the probability density distribution displays one node at $<\beta>_{\text{g.s.}}$ and two peaks of the same amplitude. Here the average deformation for the first excited 0^+ states is $<\beta> = 0.33$ but the two peaks of the

probability distribution are not of equal amplitude, thus indicating additional mixing effects.

The level of K-mixing is reflected in the staggering in energy between odd- and even-spin states in the (quasi) γ-bands (cf. Fig. 14). The staggering can be quantified by considering the differential quantity [81]

$$S(J) = \frac{\{E[J_\gamma^+] + E[(J-2)_\gamma^+] - 2E[(J-1)_\gamma^+]}{E[2_1^+]} \tag{119}$$

which quantifies the displacement of the $(J-1)_\gamma^+$ level relative to the average of its neighbors, J_γ^+ and $(J-2)_\gamma^+$, normalized to the energy of the first excited state of the ground-state band 2_1^+. Because of its differential form, $S(J)$ is very sensitive to structural changes. For an axially symmetric rotor $S(J)$ is, of course, constant. In a nucleus with a deformed γ-soft potential, $S(J)$ oscillates between negative values for even-spin states and positive values for odd-spin states, with the magnitude slowly increasing with spin. For a triaxial potential the level clustering in the (quasi) γ-band is opposite, and $S(J)$ oscillates between positive values for even-spin states and negative values for odd-spin states. In this case the magnitude of $S(J)$ increases more rapidly with spin, as compared to the γ-soft potential. In the panel on the right of Fig. 16 we plot the staggering in the γ-band of ^{152}Sm. One notices how the K-mixing leads to the staggering observed in the corresponding γ-band. The calculation reproduces the empirical oscillatory behaviour (negative values for even-spin states

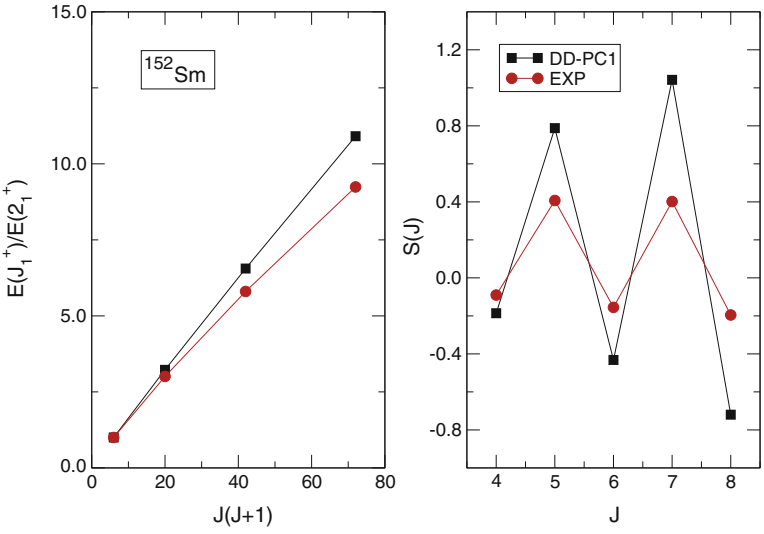

Fig. 16 Relative ground-state band excitation energies in ^{152}Sm. The theoretical energies are scaled by a common factor, adjusted to the experimental energy of the 2_1^+ state (*left panel*). The staggering parameter $S(J)$ (119) in the γ band of ^{152}Sm, compared to experiment (*right panel*)

and positive values for odd-spin states), although with larger amplitudes, and this effect confirms the γ-softness of the quadrupole potential of ^{152}Sm.

5.4 Octupole Degrees of Freedom

Most deformed medium-heavy and heavy nuclei exhibit quadrupole, reflection-symmetric equilibrium shapes, but there are also regions of the mass table in which octupole deformations (reflection-asymmetric, pear-like shapes) occur (see [82] for a review). In particular, nuclei with neutron (proton) number N (Z) $\approx$ 34, 56, 88 and 134. Reflection-asymmetric shapes are characterised by the presence of negative-parity bands, and by pronounced electric dipole and octupole transitions. In the case of static octupole deformation, for instance, the lowest positive-parity even-spin states and negative-parity odd-spin states form an alternating-parity band, with states connected by enhanced E1 transitions. In a simple microscopic picture octupole deformation is expected to develop through a coupling of orbitals in the vicinity of the Fermi surface with quantum numbers (l, j) and an intruder unique-parity orbital with $(l + 3, j + 3)$ [82, 83]. For instance, in the case of heavy ($N \approx 134$ and $Z \approx 88$) nuclei in the region of light actinides, the coupling of the neutron orbitals $g_{9/2}$ and $j_{15/2}$, and that of the proton single-particle states $f_{7/2}$ and $i_{13/2}$, can lead to octupole mean-field deformations.

Reflection-asymmetric nuclear shapes have been explored in numerous experiments [82, 83], and very recently evidence for pronounced octupole deformation in the region $N \approx 134$ and $Z \approx 88$, e.g., ^{220}Rn and ^{224}Ra, has been reported in Coulomb excitation experiments with radioactive ion beams [84]. A number of theoretical methods have been developed to describe pear-like nuclear shapes and the evolution of the corresponding negative-parity collective states, including SCMF methods, algebraic approaches, shell-corrected liquid-drop models, and α-particle cluster models. In particular, several recent systematic SCMF studies of octupole excitations have based on the EDF framework [85–90].

For a nucleus with static or dynamic octupole deformation, the radius $R = R_0\left[1 + \sum_\mu \alpha_{2\mu} Y^*_{2\mu} + \sum_\mu \alpha_{3\mu} Y^*_{3\mu}\right]$ is specified in terms of quadrupole and octupole collective coordinates. The full description of triaxial quadrupole and octupole deformed shapes presents a significant computational challenge and, therefore, one can consider a simplified case in which axial symmetry is imposed and the collective coordinates can be parameterized in terms of two deformation parameters β_2 and β_3, and three Euler angles $\Omega \equiv (\phi, \theta, \psi)$:

$$\alpha_{\lambda\mu} = \beta_\lambda D^\lambda_{0\mu}(\Omega), \quad \lambda = 2, 3. \tag{120}$$

The classical collective Hamiltonian is expressed as the sum of the vibrational kinetic energy, rotational kinetic energy, and the collective potential $\mathcal{V}_{coll}$. The vibrational and rotational kinetic energies read:

$$\mathscr{T}_{\rm vib} = \frac{1}{2}B_{22}\dot{\beta}_2^2 + B_{23}\dot{\beta}_2\dot{\beta}_3 + \frac{1}{2}B_{33}\dot{\beta}_3^2, \tag{121}$$

$$\mathscr{T}_{\rm rot} = \frac{1}{2}\sum_{k=1}^{3}\mathscr{I}_k\omega_k^2, \tag{122}$$

respectively, where the mass parameters B_{22}, B_{23} and B_{33}, and the moments of inertia $\mathscr{I}_k$, are functions of the quadrupole and octupole deformations β_2 and β_3. After quantization the collective Hamiltonian takes the form

$$\begin{aligned}\hat{H}_{\rm coll} = &-\frac{\hbar^2}{2\sqrt{w\mathscr{I}}}\left[\frac{\partial}{\partial\beta_2}\sqrt{\frac{\mathscr{I}}{w}}B_{33}\frac{\partial}{\partial\beta_2} - \frac{\partial}{\partial\beta_2}\sqrt{\frac{\mathscr{I}}{w}}B_{23}\frac{\partial}{\partial\beta_3}\right.\\ &\left.-\frac{\partial}{\partial\beta_3}\sqrt{\frac{\mathscr{I}}{w}}B_{23}\frac{\partial}{\partial\beta_2} + \frac{\partial}{\partial\beta_3}\sqrt{\frac{\mathscr{I}}{w}}B_{22}\frac{\partial}{\partial\beta_3}\right]\\ &+\frac{\hat{J}^2}{2\mathscr{I}} + V(\beta_2,\beta_3),\end{aligned} \tag{123}$$

where $w = B_{22}B_{33} - B_{23}^2$. Since we only consider axially deformed nuclei, the projection of angular momentum on the symmetry axis $K = 0$, and the collective wave function reads

$$\Psi_\alpha^{JM\pi}(\beta_2,\beta_3,\Omega) = \psi_\alpha^{J\pi}(\beta_2,\beta_3)D_{M0}^J(\Omega). \tag{124}$$

Just as in the case of the quadrupole five-dimensional collective Hamiltonian, the moments of inertia are calculated using the Inglis-Belyaev formula:

$$\mathscr{I} = \sum_{i,j}\frac{|\langle ij|\hat{J}|\Phi\rangle|^2}{E_i + E_j}, \tag{125}$$

where $\hat{J}$ is the angular momentum along the axis perpendicular to the symmetric axis, the summation runs over quasiparticle states $|ij\rangle = \beta_i^\dagger\beta_j^\dagger|\Phi\rangle$, and $|\Phi\rangle$ represents the quasiparticle vacuum. The quasiparticle energies E_i and wave functions are determined by a SCMF calculation of the deformation energy surface with constraints on the quadrupole and octupole deformation parameters. The mass parameters associated with the collective coordinates $q_2 = \langle\hat{Q}_2\rangle$ and $q_3 = \langle\hat{Q}_3\rangle$ are calculated in the cranking approximation, as well as the vibrational and rotational zero-point energy corrections to the collective energy surface [67].

It is interesting to consider negative-parity states (octupole vibrations) in ^{152}Sm [80], that is, in the same system for which in the previous subsection we have analyzed low-lying quadrupole collective states. The self-consistent RHB (functional DD-PC1 plus finite-range separable pairing) deformation energy map of ^{152}Sm in the plane of axial quadrupole and octupole deformation parameters (β_2, β_3) is shown in Fig. 17.

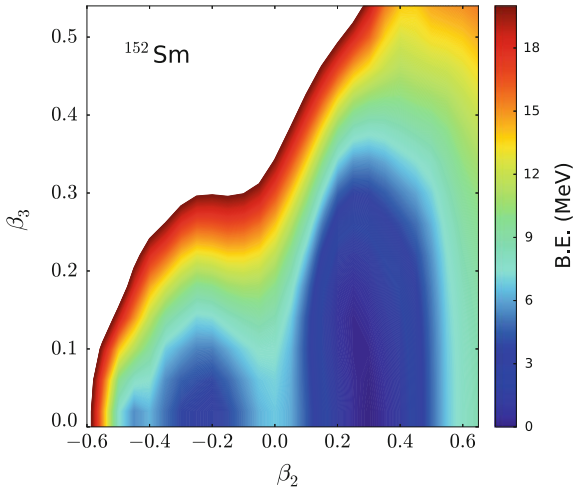

Fig. 17 Self-consistent RHB (functional DD-PC1 plus finite-range separable pairing) axially symmetric deformation energy map of ^{152}Sm in the $\beta_2 - \beta_3$ plane. The contours join points on the surface with the same energy. Positive (negative) values of β_2 correspond to prolate (oblate) configurations. The energy surface is symmetric with respect to the $\beta_3 = 0$ axis

Positive (negative) values of β_2 correspond to prolate (oblate) configurations and the energy surface is symmetric with respect to the $\beta_3 = 0$ axis. We note that the quadrupole deformed prolate minimum at $\beta_2 \approx 0.3$ actually extends in the β_3 direction. This means that the energy surface is soft in the octupole degree of freedom and one can expect the occurrence of octupole vibrations. Ideally one would try to simultaneously describe triaxial quadrupole and octupole degrees of freedom, but this is computationally too demanding. Instead, starting from the axially symmetric SCMF solution shown in Fig. 17, we compute the parameters of the quadrupole-octupole collective Hamiltonian (123). The diagonalization of the Hamiltonian result in the partial level scheme shown in Fig. 18, where the two lowest positive-parity ($K = 0^+$) and negative-parity ($K = 0^-$) bands, and the corresponding B(E2) (in Weisskopf units) and B(E1) (in 10^{-3} Weisskopf units) values, are compared to the experimental excitation spectrum [80]. In the order of increasing excitation energy, octupole bands that arise from the coupling to a quadrupole deformed shape are: $K = 0^-$, 1^-, 2^-, and 3^- but, since in our model axial symmetry is assumed, we can only analyse $K = 0^-$ states. One notices that the calculated excitation energies are in very good agreement with data. In particular, compared to the triaxial quadrupole calculation discussed in the previous subsection, the excited $K = 0^+$ band is much closer to the experimental excitation energy. This is most probably due to the reduced mixing with the ground-state band in the axially symmetric calculation. The lowest $K = 0^-$ band corresponds to an octupole excitation based on the ground state. This is clearly seen in Fig. 19, where we plot the probability distributions in the β_2-β_3 plane for the band-head states of the lowest $K = 0^+$ and $K = 0^-$ bands. The calculated B(E1) values for transitions to the ground-state band are, however, significantly larger than the experimental values. A remarkable feature are the relatively large E1 rates for transitions from the second $K = 0^-$ band to the second $K = 0^+$ band, nicely

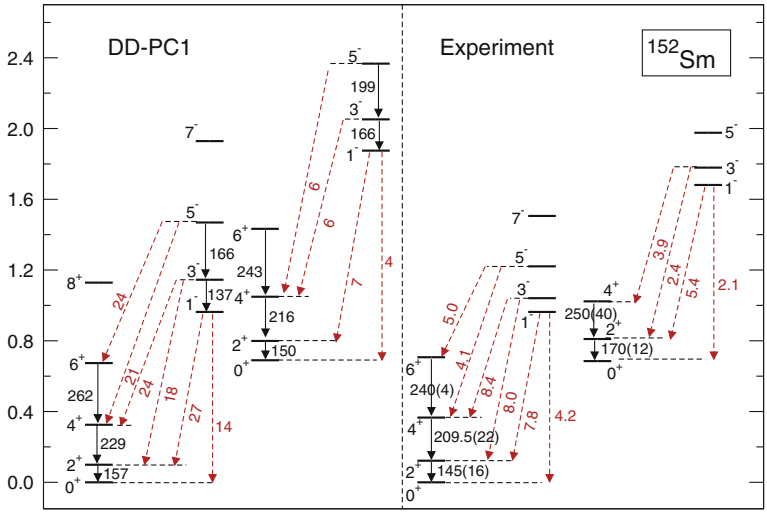

Fig. 18 Partial level scheme of ^{152}Sm, calculated with the axially symmetric quadrupole-octupole collective Hamiltonian (123), based on the relativistic energy density functional DD-PC1. The calculated two lowest $K = 0^+$ and $K = 0^-$ bands and corresponding B(E2) (in Weisskopf units) and B(E1) (in 10^{-3} Weisskopf units) values are compared to data [80]

reproduced by the model calculation based on the axially symmetric quadrupole-octupole Hamiltonian. The assignment of the $K = 0_2^-$ band as an octupole excitation built on the 0_2^+ state (β-vibration) [80] is supported by the comparison of the probability distributions of the states 0_2^+ and 1_2^- (cf. Fig. 19).

6 Outlook

Low-energy theoretical nuclear physics has seen a strong revival in recent years with fully microscopic investigations of nuclei far from stability and nuclear astrophysics applications. Short-lived nuclei far from the valley of beta-stability provide information on the origin of heavy elements, and there are strong connections with mesoscopic systems in atomic and condensed-matter physics. The structure of exotic nuclei is explored, in particular, by radioactive ion beams (RIBs). Future advances and access to new regions of the nuclear chart necessitate the development of new RIB facilities. Experimental programs must be complemented by the development of advanced theoretical methods that will reproduce and explain a large body of data, and also provide microscopic predictions for a variety of nuclear structure phenomena.

Nuclei are complex systems and a complete understanding and description of their structure is not possible within a single theoretical framework. Ab initio methods have

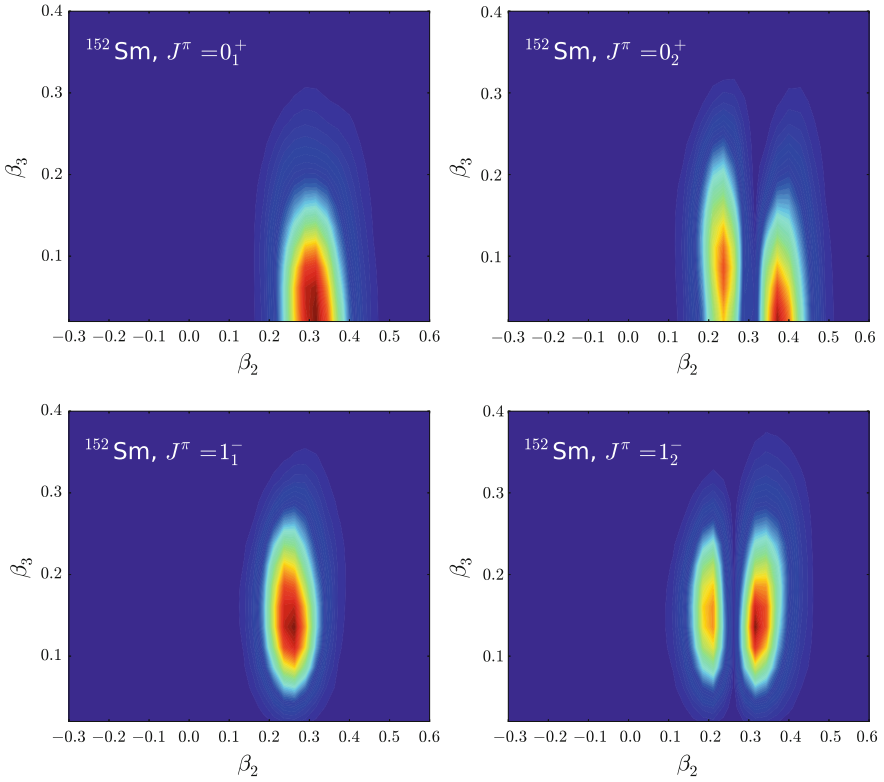

Fig. 19 Probability distributions in the β_2-β_3 plane for the band-head states of the lowest $K = 0^+$ and $K = 0^-$ bands in ^{152}Sm (cf. Fig. 18)

been very successful in the description of lighter nuclei, and large-scale shell-model calculations can be performed for medium-heavy and even some heavy nuclei in the vicinity of closed shells. However, at present the only comprehensive approach to the structure of nuclei is provided by the density functional framework. Based on nuclear energy density functionals (EDFs), adjusted to reproduce empirical properties of symmetric and asymmetric nuclear matter and data on finite nuclei, self-consistent mean-field methods have achieved a high level of accuracy in the description of ground states and properties of excited states in arbitrarily heavy nuclei, exotic nuclei far from β-stability, and in nuclear systems at the nucleon drip-lines.

The goal of nuclear DFT is to build a consistent microscopic framework that will, on the one hand, bridge the gap between the underlying theory of strong interactions and the phenomenology of finite nuclei and, on the other, provide a reliable microscopic description of infinite nuclear and neutron matter, ground-state properties of all bound nuclei, low-energy vibrations, rotational spectra, small-amplitude vibrations, and large-amplitude adiabatic properties. On the self-consistent mean-field level this will be achieved by developing non-empirical EDFs, and reducing

model dependencies through the inclusion of all terms allowed by symmetries, provided their parameters can be completely determined by data. In addition, to describe complex excitation spectra and transition rates, as well as dynamical processes, it will be crucial to formulate and refine models that, based on the microscopic EDF framework, extend the mean-field scheme and include dynamical correlations.

Acknowledgments We would like to thank A.V. Afanasjev, Z.P. Li, J. Meng, K. Nomura, N. Paar, V. Prassa, P. Ring, J.M. Yao and J. Zhao for their contribution to the work reported in these notes. This work was supported in part by the Croatian Science Foundation—project "Structure and Dynamics of Exotic Femtosystems" (IP-2014-09-9159).

References

1. G.A. Lalazissis, P. Ring, D. Vretenar (eds.), *Extended Density Functionals in Nuclear Structure Physics*, vol. 641, Lecture Notes in Physics (Springer, Heidelberg, 2004)
2. M. Bender, P.-H. Heenen, P.-G. Reinhard, Rev. Mod. Phys. **75**, 121 (2003)
3. D. Vretenar, A.V. Afanasjev, G.A. Lalazissis, P. Ring, Phys. Rep. **409**, 101 (2005)
4. J.R. Stone, P.-G. Reinhard, Prog. Part. Nucl. Phys. **58**, 587 (2007)
5. J. Erler, P. Klüpfel, P.-G. Reinhard, J. Phys. G **38**, 033101 (2011)
6. W. Kohn, Rev. Mod. Phys. **71**, 1253 (1999)
7. N. Argaman, G. Makov, Am. J. Phys **68**, 69 (2000)
8. R.M. Dreizler, E.K.U. Gross, *Density Functional Theory* (Springer, Berlin, 1990)
9. C. Fiolhais, F. Nogueira, M. Marques (eds.), *A primer in Density Functional Theory*, vol. 620, Lecture Notes in Physics (Springer, Heidelberg, 2003)
10. E. Engel, R.M. Dreizler, *Density Functional Theory* (Springer-Verlag, Heidelberg, 2011)
11. R.O. Jones, Rev. Mod. Phys. **87**, 897 (2015)
12. J.W. Negele, Phys. Rev. C **1**, 1260 (1970)
13. D. Vautherin, D.M. Brink, Phys. Rev. C **5**, 626 (1972)
14. J.W. Negele, D. Vautherin, Phys. Rev. C **5**, 1472 (1972)
15. J. Dobaczewski, K. Bennaceur, F. Raimondi, J. Phys. G **39**, 125103 (2012)
16. B.D. Serot, J.D. Walecka, Adv. Nucl. Phys. **16**, 1 (1986)
17. B.D. Serot, J.D. Walecka, Int. J. Mod. Phys. E **6**, 515 (1997)
18. G.A. Lalazissis, J. König, P. Ring, Phys. Rev. C **55**, 540 (1997)
19. W. Long, J. Meng, N.V. Giai, S.-G. Zhou, Phys. Rev. C **69**, 034319 (2004)
20. B.G. Todd-Rutel, J. Piekarewicz, Phys. Rev. Lett. **95**, 122501 (2005)
21. W.C. Chen, J. Piekarewicz, Phys. Rev. C **90**, 044305 (2014)
22. F. Hofmann, C.M. Keil, H. Lenske, Phys. Rev. C **64**, 034314 (2001)
23. S. Typel, H.H. Wolter, Nucl. Phys. A **656**, 331 (1999)
24. T. Nikšić, D. Vretenar, P. Finelli, P. Ring, Phys. Rev. C **66**, 024306 (2002)
25. G.A. Lalazissis, T. Nikšić, D. Vretenar, P. Ring, Phys. Rev. C **71**, 024312 (2005)
26. T. Bürvenich, D.G. Madland, J.A. Maruhn, P.-G. Reinhard, Phys. Rev. C **65**, 044308 (2002)
27. P.W. Zhao, Z.P. Li, J.M. Yao, J. Meng Phys. Rev. C **82**, 054319 (2010)
28. P. Finelli, N. Kaiser, D. Vretenar, W. Weise, Nucl. Phys. A **735**, 449 (2004)
29. P. Finelli, N. Kaiser, D. Vretenar, W. Weise, Nucl. Phys. A **770**, 1 (2006)
30. T. Nikšić, D. Vretenar, P. Ring, Phys. Rev. C **78**, 034318 (2008)
31. J.W. Holt, N. Kaiser, W. Weise, Prog. Part. Nucl. Phys. **73**, 35 (2013)
32. P.-G. Reinhard, C. Toepffer, Int. J. Mod. Phys. E **3**, 435 (1994)
33. P.-G. Reinhard, Rep. Prog. Phys. **52**, 439 (1989)
34. P. Ring, Prog. Part. Nucl. Phys. **37**, 193 (1996)

35. A. Akmal, V.R. Pandharipande, D.G. Ravenhall. Phys. Rev. C **58**, 1804 (1998)
36. S. Brandt, *Statistical and Computational Methods in Data Analysis* (Springer, New York, 1997)
37. P.R. Bevington, D.K. Robinson, *Data Reduction and Error Analysis for the Physical Sciences* (McGraw-Hill, 2003)
38. J. Dobaczewski, W. Nazarewicz, P.-G. Reinhard, J. Phys. G **41**, 074001 (2014)
39. P.-G. Reinhard, W. Nazarewicz, Phys. Rev. C **81**, 051303 (2010)
40. F.J. Fattoyev, J. Piekarewicz. Phys. Rev. C **84**, 064302 (2011)
41. Y. Gao, J. Dobaczewski, M. Kortelainen, D. Tarpanov, Phy. Rev. C **87**, 034324 (2013)
42. W.-C. Chen, J. Piekarewicz, Phys. Rev. C **90**, 044305 (2014)
43. T. Nikšić, N. Paar, P.-G. Reinhard, D. Vretenar, J. Phys. G **42**, 034008 (2015)
44. N. Schunck, J.D. McDonnell, J. Sarich, S.M. Wild, D. Higdon, J. Phys. G **42**, 034024 (2015)
45. J. Meng, H. Toki, S.G. Zhou, S.Q. Zhang, W.H. Long, L.S. Geng, Prog. Part. Nucl. Phys. **57**, 470 (2006)
46. Y. Tian, Z.Y. Ma, P. Ring, Phys. Lett. B **676**, 44 (2009)
47. J.F. Berger, M. Girod, D. Gogny, Comp. Phys. Comm. **63**, 365 (1991)
48. M. Wang, G. Audi, A.H. Wapstra, F.G. Kondev, M. MacCormick, X. Xu, B. Pfeiffer, Chin. Phys. C **36** (2012)
49. I. Angeli, K.P. Marinova, At. Data Nucl. Data Tables **99**, 69 (2013)
50. S.E. Agbemava, A.V. Afanasjev, D. Ray, P. Ring, Phys. Rev. C **89**, 054320 (2014)
51. P.-H. Heenen, J. Skalski, A. Staszczak, D. Vretenar, Nucl. Phys. A (2015). doi:10.1016/j.nuclphysa.2015.07.016
52. A.V. Afanasjev, S.E. Agbemava, D. Ray, P. Ring, Phys. Rev. C **91**, 014324 (2015)
53. S.E. Agbemava, A.V. Afanasjev, T. Nakatsukasa, P. Ring, Phys. Rev. C (2015), (in press)
54. T. Nikšić, D. Vretenar, P. Ring, Prog. Part. Nucl. Phys. **66**, 519 (2011)
55. T. Duguet, J. Sadoudi, J. Phys. G **37**, 064009 (2010)
56. T. Duguet, in *Lecture Notes in Physics*, vol. 879 (Springer, Heidelberg, 2014), p. 293
57. M. Bender, P.-H. Heenen, Phys. Rev. C **78**, 024309 (2008)
58. T.R. Rodriguez, J.L. Egido, Phys. Rev. C **81**, 064323 (2010)
59. J.M. Yao, K. Hagino, Z.P. Li, J. Meng, P. Ring, Phys. Rev. C **89**, 054306 (2014)
60. B. Bally, B. Avez, M. Bender, P.-H. Heenen, Phys. Rev. Lett. **113**, 162501 (2014)
61. M. Baranger, M. Veneroni, Ann. Phys. (N.Y.) **114**, 123 (1978)
62. P.-G. Reinhard, K. Goeke, Rep. Prog. Phys. **50**, 1 (1987)
63. P. Bonche, J. Dobaczewski, H. Flocard, P.-H. Heenen, J. Meyer, Nucl. Phys. A **510**, 466 (1990)
64. L. Próchniak, S.G. Rohoziński, J. Phys. G **36**, 123101 (2009)
65. P. Ring, P. Schuck, *The Nuclear Many-Body Problem* (Springer-Verlag, Heidelberg, 1980)
66. B. Giraud, B. Grammaticos, Nucl. Phys. A **255**, 141 (1975)
67. M. Girod, B. Grammaticos, Nucl. Phys. A **330**, 40 (1979)
68. N. Paar, P. Ring, T. Nikšić, D. Vretenar, Phys. Rev. C **67**, 034312 (2003)
69. N. Paar, D. Vretenar, E. Khan, G. Colo, Rep. Prog. Phys. **70**, 691 (2007)
70. B.L. Berman, S.C. Fultz, Rev. Mod. Phys. **47**, 713 (1975)
71. T. Li et al., Phys. Rev. Lett. **99**, 162503 (2007)
72. D. Vretenar, T. Nikšić, P. Ring, Phys. Rev. C **68**, 024310 (2003)
73. J.P. Blaizot, G. Ripka, *Quantum Theory of Finite Systems* (MIT, Cambridge, 1986)
74. E. Clément et al., Phys. Rev. C **75**, 054313 (2007)
75. W. Pauli, in *Handbuch der Physik*, vol. XXIV (Springer Verlag, Berlin, 1933), p. 120
76. K. Kumar, M. Baranger, Nucl. Phys. A **92**, 608 (1967)
77. T. Nikšić, Z.P. Li, D. Vretenar, L. Próchniak, J. Meng, P. Ring, Phys. Rev. C **79**, 034303 (2009)
78. *Brookhaven National Nuclear Data Center*. http://www.nndc.bnl.gov
79. J.-P. Delaroche, M. Girod, J. Libert, H. Goutte, S. Hilaire, S. Péru, N. Pillet, G.F. Bertsch, Phys. Rev. C **81**, 014303 (2010)
80. P.E. Garrett et al., Phys. Rev. Lett. **103**, 062501 (2009)
81. E.A. McCutchan, D. Bonatsos, N.V. Zamfir, R.F. Casten, Phys. Rev. C **76**, 024306 (2007)
82. P.A. Butler, W. Nazarewicz, Rev. Mod. Phys. **68**, 349 (1996)
83. P.A. Butler, L. Willmann, Nucl. Phys. News **25**, 12 (2015)

84. L.P. Gaffney et al., Nature **497**, 199 (2013)
85. L.M. Robledo, G.F. Bertsch, Phys. Rev. C **84**, 054302 (2011)
86. L.M. Robledo, P.A. Butler, Phys. Rev. C **88**, 051302(R) (2013)
87. Z.P. Li, B.Y. Song, J.M. Yao, D. Vretenar, J. Meng, Phys. Lett. B **726**, 866 (2013)
88. K. Nomura, D. Vretenar, T. Nikšić, B.-N. Lu, Phys. Rev. C **89**, 024312 (2014)
89. K. Nomura, R. Rodríguez-Guzmán, L.M. Robledo, Phys. Rev. C **92**, 014312 (2015)
90. J.M. Yao, E.F. Zhou, Z.P. Li, Phys. Rev. C **92**, 041304(R) (2015)

Part II
Student's Seminars

Reactions Induced by ^{9}Be in a Four-Body Continuum-Discretized Coupled-Channels Framework

J. Casal, M. Rodríguez-Gallardo and J.M. Arias

Abstract We investigate the elastic scattering of ^{9}Be on ^{208}Pb at beam energies above (50 MeV) and below (40 MeV) the Coulomb barrier. The reaction is described within a four-body framework using the Continuum-Discretized Coupled-Channels (CDCC) method. The ^{9}Be projectile states are generated using the analytical Transformed Harmonic Oscillator (THO) basis in hyperspherical coordinates. Our calculations confirm the importance of continuum effects at low energies.

1 Introduction

The ^{9}Be nucleus is a stable system but presents a small binding energy below the $\alpha + \alpha + n$ threshold [1], 1.5736 MeV. It shows also a Borromean structure, since none of the binary subsystems $\alpha + \alpha$ or $\alpha + n$ form bound states. Reactions involving ^{9}Be should reflect both its weakly-bound nature and its three-body structure. Previous calculations considering ^{9}Be as a two-body projectile [2] and also as a three-body projectile [3] show that breakup effects are important even at sub-barrier energies.

In this work, we describe the elastic scattering of ^{9}Be on ^{208}Pb within a four-body CDCC method [4, 5], considering a three-body projectile plus a structureless target. We generate the projectile states within an $\alpha + \alpha + n$ three-body model using the analytical THO basis [6, 7] in hyperspherical coordinates. We pay special attention to the position of the relevant states of the system. The $3/2^{-}$ ground state and the ^{9}Be low-energy resonances are fixed to the experimental values. We refer the reader to [5, 8] for details about the theoretical formalism.

J. Casal (✉) · M. Rodríguez-Gallardo · J.M. Arias
Dpto. de Física Atómica, Molecular y Nuclear, Facultad de Física,
Universidad de Sevilla, Apto. 1065, 41080 Seville, Spain
e-mail: jcasal@us.es

J.-E. García-Ramos et al. (eds.), *Basic Concepts in Nuclear Physics: Theory, Experiments and Applications*, Springer Proceedings in Physics 182,
DOI 10.1007/978-3-319-21191-6_5

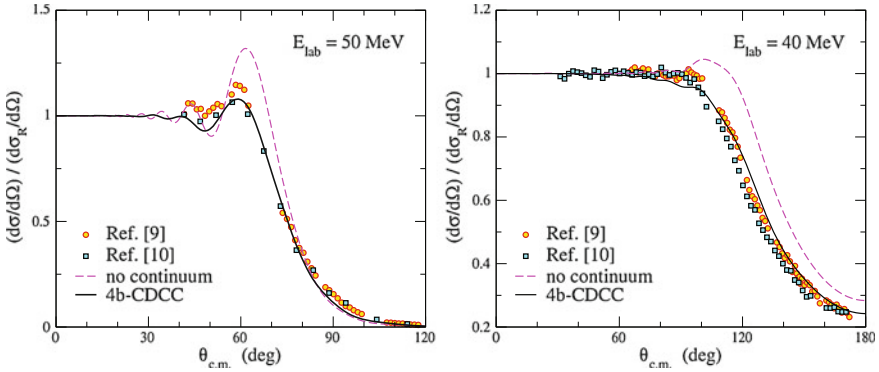

Fig. 1 ^{9}Be + ^{208}Pb elastic cross section at 50 MeV (*left panel*) and 40 MeV (*right panel*)

2 Results

The model space describing the ^{9}Be projectile includes $j^{\pi} = 3/2^{\pm}, 1/2^{\pm}, 5/2^{\pm}$ states. The coupled equations are solved considering the projectile-target interaction multipole couplings to all orders. In Fig. 1 we show the elastic cross section angular distribution in the center of mass frame, relative to the Rutherford cross section, at beam energies above (50 MeV) and below (40 MeV) the Coulomb barrier. Dashed lines correspond to calculations including the ground state only, and solid lines are the full CDCC calculations. The experimental data are from [9] (circles) and [10] (squares). The agreement between our calculations and the data is improved when we include the coupling to breakup channels. We confirm that this effect is important even at energies below the Coulomb barrier.

Acknowledgments This work has been supported by the Spanish Ministerio de Economía y Competitividad under FIS2014-53448-c2-1-P and FIS2014-51941-P, and by Junta de Andalucía under group number FQM-160 and Project P11-FQM-7632. J. Casal acknowledges a FPU grant from the Ministerio de Educación, Cultura y Deporte, AP2010-3124. M. Rodríguez-Gallardo acknowledges a postdoctoral contract by the VPPI of the Universidad de Sevilla.

References

1. D.R. Tilley et al., Nucl. Phys. A **745**, 155 (2004)
2. S.K. Pandit et al., Phys. Rev. C **84**, 031601 (2011)
3. P. Descouvemont et al., Phys. Rev. C **91**, 024606 (2015)
4. T. Matsumoto et al., Phys. Rev. C **73**, 051602(R) (2006)
5. M. Rodríguez-Gallardo et al., Phys. Rev. C **77**, 064609 (2008)
6. J. Casal et al., Phys. Rev. C **88**, 014327 (2013)
7. J. Casal et al., Phys. Rev. C **90**, 044304 (2014)
8. J. Casal et al., Submitted Phys. Rev. C (2015)
9. R.J. Woolliscroft et al., Phys. Rev. C **69**, 044612 (2004)
10. N. Yu et al., J. Phys. G: Nucl. Part. Phys. **37**, 075108 (2010)

Transfer to the Continuum Calculations of Quasifree (p, pn) and $(p, 2p)$ Reactions at Intermediate and High Energies

M. Gómez-Ramos and A.M. Moro

Abstract Nucleon removal (p, pN) reactions at intermediate energies have gained renewed attention in recent years as a tool to extract information from exotic nuclei performing reactions in inverse kinematics with exotic beams incident on proton targets. In this contribution, we present calculations for (p, pN) reactions performed within the so-called *transfer to the continuum* method (TR*), a fully quantum mechanical formalism, focusing on the momentum distributions of the emitted core.

Nucleon removal (p, pN) reactions are reactions in which a high-energy proton beam collides with a target of A nucleons, in such a way that a nucleon is extracted from the target leaving a residual nucleus C with $A - 1$ nucleons, in its ground state or an excited state.

Recently (p, pN) reactions have received a renewed interest due to their extension to the study of unstable nuclei, employing inverse kinematics with radioactive beams impinging on proton targets. Measurements of these reactions are currently under way.

In this contribution we have studied some (p, pN) reactions, employing the *transfer to the continuum* formalism [1]. This formalism is based on the evaluation of the prior form transition amplitude for the process: $p + A \rightarrow p + N + C$:

$$\mathscr{T}^{3b}_{p+A\rightarrow p+N+C} = \left\langle \Psi^{3b(-)}_{p+N+C} | V_{pN} + U_{pC} - U_{pA} | \psi_{N+C} \chi^{(+)}_{p+A} \right\rangle, \tag{1}$$

where U_{pC} and U_{pA} are the optical potentials for $p + C$ and $p + A$, V_{pN} an effective nucleon-nucleon interaction, ψ_{N+C} the initial state of the $N + C$ nucleus and $\Psi^{3b(-)}_{p+N+C}$ the exact 3-body wavefunction. In the TR* formalism, $\Psi^{3b(-)}_{p+N+C}$ is expanded

M. Gómez-Ramos (✉) · A.M. Moro
Departamento de FAMN, Facultad de Física, Universidad de Sevilla,
Apdo. 1065, 41080 Sevilla, Spain
e-mail: mgomez40@us.es

A.M. Moro
e-mail: moro@us.es

J.-E. García-Ramos et al. (eds.), *Basic Concepts in Nuclear Physics: Theory, Experiments and Applications*, Springer Proceedings in Physics 182,
DOI 10.1007/978-3-319-21191-6_6

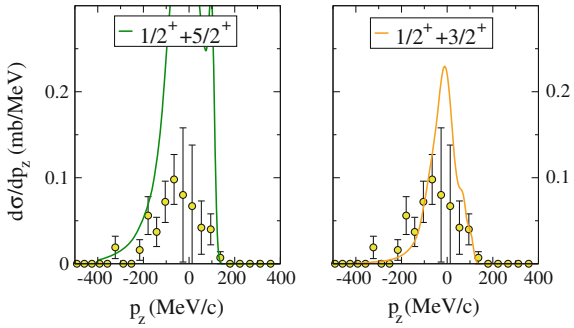

Fig. 1 Longitudinal momentum distribution for the reaction ^{20}C$(p, pn)^{19}$C. The *left panel* includes an excited $5/2^+$ state of ^{19}C, while the *right panel* includes a $3/2^+$ state instead. The calculations consider the states of ^{19}C to be single-particle levels: $2s_{1/2}$, $1d_{5/2}$ and $1d_{3/2}$

on a basis of states of the $p - N$ subsystem with well-defined angular momentum, parity, and energy. Further details on the formalism are given in [1].

As an application of the formalism, we study the reaction ^{20}C$(p, pn)^{19}$C at 40 MeV/A. This reaction is of interest because it populates different states of ^{19}C, a nucleus whose structure is still unclear. Its ground state is known to have an angular momentum $1/2^+$ with neutron separation energy, S_n, of 0.58 MeV, but it has at least one excited state with yet undefined energy and angular momentum. Some structure models indicate it to be a $5/2^+$ state, while others favour a $3/2^+$ state, and some even predict two bound states with both angular momenta. In our contribution, we have performed two calculations, one with a $5/2^+$ bound state and the other with a $3/2^+$ bound state. The corresponding longitudinal momentum distributions, convoluted with the experimental resolution, are compared with the experimental data [2] on Fig. 1.

We find that the calculations agree better with the experimental data [2] when the $5/2^+$ state is unbound, so our calculation seems to favour structure models of ^{19}C with an unbound $5/2^+$ state. This result is consistent with previous studies of this nucleus [3]. Further details on the results and calculations are left for a future publication.

References

1. A.M. Moro, F. Nunes, Nucl. Phys. A **767**, 138 (2006); A.M. Moro, Phys. Rev. C. **92**, 044605 (2015)
2. A. Ozawa et al., Phys. Rev. C **84**, 064315 (2011)
3. N. Kobayashi et al., Phys. Rev. C **86**, 054604 (2012)

First Measurements with the DTAS Detector

V. Guadilla, A. Algora and J.L. Tain

Abstract The DTAS detector will be an important instrument in the DESPEC experiment at FAIR for β-decay studies of exotic nuclei far from stability. The first measurements with this new detector have been performed with low energy radioactive beams at the upgraded IGISOL IV facility. The characterization of the detector was done by comparison of measurements with Monte Carlo (MC) simulations, and the first analysis of the cases of interest are in progress.

1 Introduction

The new segmented Decay Total Absorption γ-ray Spectrometer (DTAS) has been designed and constructed [1] to be employed in the determination of β-decay intensity distributions of exotic nuclei in the Decay SPECtroscopy (DESPEC) experiment at FAIR [2]. The spectrometer is made up of a maximum of 18 rectangular NaI(Tl) crystals of 150 mm $\times$ 150 mm $\times$ 250 mm.

A deconvolution process in needed in order to determine the β-intensity distribution from an experimental DTAS spectrum. The key ingredient in this deconvolution is the response function of the detector, R_{ij} [3, 4], that represents the probability that feeding to the level j gives a count in the experimental channel i of the spectrum. The response function is unique to each detector and each decay scheme, and it has to be calculated with MC codes, using the geometry and the physics involved in the

This study was conducted for the DTAS-IGISOL collaboration.

V. Guadilla (✉) · A. Algora · J.L. Tain
Instituto de Física Corpuscular, CSIC-Universidad de Valencia,
46071 Valencia, Spain
e-mail: guadilla@ific.uv.es

A. Algora
e-mail: algora@ific.uv.es

J.L. Tain
e-mail: tain@ific.uv.es

J.-E. García-Ramos et al. (eds.), *Basic Concepts in Nuclear Physics: Theory, Experiments and Applications*, Springer Proceedings in Physics 182,
DOI 10.1007/978-3-319-21191-6_7

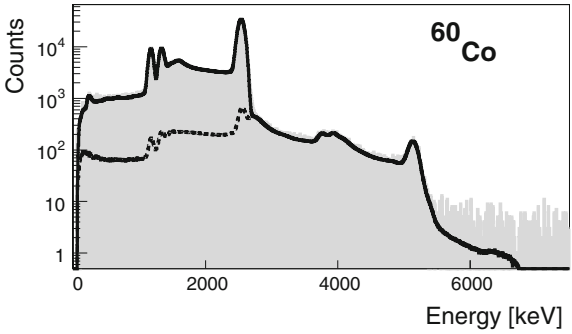

Fig. 1 ^{60}Co background subtracted experimental spectrum (*grey*), MC (*black*), and summing-pileup (*dotted*)

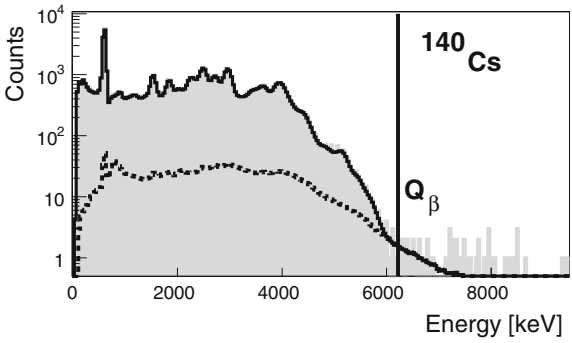

Fig. 2 β-gated spectrum of the ^{140}Cs decay (*grey*), summing-pileup (*dotted*), and reconstructed spectrum after the analysis (*black*)

detection process. To validate this response, it is necessary to simulate the calibration sources to obtain the best agreement with the experimental measurements, as it is shown in Fig. 1. For this purpose the package Geant4 [5] has been used, and the distortion produced by the electronic pileup [6] has been taken into account.

2 First Experiment

The commissioning of the DTAS detector in the 18-crystals configuration at a radioactive facility was carried out in 2014 with beams provided by the mass separator of the upgraded IGISOL IV facility at JYFL [7], further purified by means of the JYFLTRAP Penning trap [8]. Around a dozen Uranium fission products of interest in neutrino physics and reactor technology were measured at IGISOL with DTAS [9]. The nuclei of interest were implanted on a tape placed in vacuum at the centre of DTAS and in front of a plastic scintillator detector devoted to the detection of beta particles. The implantation and measurement times were optimized according to the half life. The software sum of the 18-crystal was reconstructed off-line and β-γ coincidences were required. An example of the preliminary analysis of the ^{140}Cs, important contributor to the antineutrino reactor spectrum, is shown in Fig. 2.

References

1. J.L. Tain et al., Nucl. Instrum. Methods A **803**, 36 (2015)
2. B. Rubio, Int. J. Modern Phys. E **15**, 1979 (2006)
3. J.L. Tain, D. Cano-Ott, Nucl. Instrum. Methods A **571**, 728 (2007)
4. D. Cano-Ott et al., Nucl. Instrum. Methods A **430**, 333 (1999)
5. S. Agostinelli et al., Nucl. Instrum. Methods A **506**, 250 (2003)
6. D. Cano-Ott et al., Nucl. Instrum. Methods A **430**, 488 (1999)
7. V.S. Kolhinen et al., Nucl. Instrum. Methods B **317**
8. T. Eronen et al., Eur. Phys. J. A **48**, 1 (2012)
9. V. Guadilla et al., Nucl. Instr. Meth. B doi:10.1016/j.nimb.2015.12.018

Hospital Neutron Detection Using Diamond Detectors

F. Manchado, L. Acosta, I. Martel, J.A. Dueñas, A.M. Sánchez-Benítez and J. Sánchez

Abstract In this work the preliminary results obtained during a experimental campaign for detecting neutron radiation using a single crystal diamond detector are shown. This investigation was motivated by the need of monitoring neutron radiation in radiotherapy facilities.

1 Introduction

Diamond detectors have many applications in nuclear instrumentation. They can be used in extreme conditions [1], daylight presence and poor vacuum. Moreover, they are sensible to fast neutron [2]. To evaluate its capabilities, three measurements were carried out: first, using a ^{252}Cf neutron source (laboratories at the Huelva University); second a radiotherapy accelerator machine (Juan Ramón Jiménez Hospital); and finally, using a tandem accelerator (National Accelerator Centre, Seville). Some of the characteristics of these measurements are described in the following section.

2 Experimental Setups Description

A single crystal diamond detector of 500 μm thickness was used. The electronic chain and data acquisition system were composed of a charge preamplifier-shaper-amplifier Mesytec model MSI-8, and a VME standard data acquisition system, with an ADC V785 Caen module managed by a CPU and trigger modules adjusted, for

F. Manchado (✉) · J. Sánchez
Hospital Juan Ramón Jiménez, Huelva, Spain
e-mail: franciscomanchadodesola@gmail.com

L. Acosta
Instituto de Física, UNAM, Mexico, Mexico

I. Martel · J.A. Dueñas · A.M. Sánchez-Benítez
Depto. de Física Aplicada, Universidad de Huelva, Huelva, Spain

J.-E. García-Ramos et al. (eds.), *Basic Concepts in Nuclear Physics: Theory, Experiments and Applications*, Springer Proceedings in Physics 182,
DOI 10.1007/978-3-319-21191-6_8

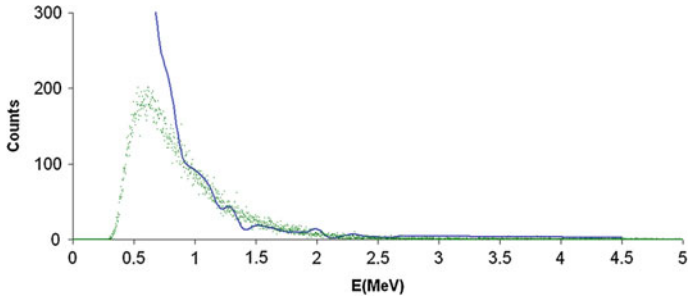

Fig. 1 Energy spectrum produced with neutrons coming from the $^{12}C(^{2}H,n)^{13}N$ reaction (*green*) and the simulation generated to describe the experimental data (*blue*)

visualization propose, to the standard DAQ-MIDAS program. For the first measurement, diamond detector was mounted at 15 cm from a ^{252}Cf source. In order to avoid deposition of heavy products and minimize gamma influence the diamond was shielded with a 3.2 lead plate. The measurement was continued and controlled during 40 days. The second experiment was carried out with a conventional radiotherapy accelerator using the 15 MV photons mode, closing MLC and jaws in order to minimize the photon radiation. A 2 cm lead shield was placed around the diamond in order to reduce as much as possible the gamma incidence. In the last measurement using a 4 MeV deuterium beam, neutrons from $^{12}C(^{2}H,n)^{13}N$ reaction were detected. A carbon-gold target was mounted in vacuum and the diamond detector was placed outside the chamber. A typical spectrum obtained from this three measurements (particularly that obtained in the last one) is shown in the Fig. 1. In all these measurements we could detect neutrons coming form elastic scattering in carbon.

3 Conclusions

From our preliminary results we can conclude that this kind of device is a promising candidate for monitoring neutron yields in hospital environment. Further measurements with this system will be performed, in order to improve our knowledge about this detection system.

References

1. J. Bohon, E. Muller, J. Smedley, Development of diamond-based X-ray detection for high-flux beamline diagnostics. J. Synchrotron Radiat. **169**, 711–718 (2010)
2. M. Pillon, M. Angelone, A.V. Krasilnikov, 14 MeV neutron spectra measurements with 4% energy resolution using a type IIa diamond detector. Nucl. Instr. Meth. Phys. Res. B **169**, 473–483 (1995)

Relativistic Modeling of Inclusive Neutrino-Nucleus Interactions in the SuperScaling Approach

G.D. Megias, J.E. Amaro, M.B. Barbaro, J.A. Caballero and T.W. Donnelly

Abstract We present our recent progresses on the relativistic modeling of neutrino-nucleus reactions (G.D. Megias et al., Phys. Lett. B, 725:170–174, 2003; Phys. Rev. D 89:093002, 2014; M.V. Ivanov et al., Phys. Rev. C 89:014607, 2014; R. González-Jiménez et al., Phys. Rev. C 90:035501, 2014; G.D. Megias et al., Phys. Rev. D 91;073004, 2015; M.V. Ivanov et al., J. Phys. G 43:045101, 2016; A.M. Ankowski et al., Phys. Rev. C 92;025501, 2015) and comparisons with high precision experimental data in a wide energy range (0–100 GeV).

We compare charged-current quasielastic (CCQE) neutrino and antineutrino cross sections obtained within the phenomenological SuperScaling Approach [7] (SuSA model) which is based on the analysis of electron-nucleus scattering data and has been recently improved with the inclusion of Relativistic Mean Field theory effects (SuSAv2 model [3]). This model provides a complete set of reference scaling functions to describe in a consistent way both (e, e′) processes and the neutrino/antineutrino-nucleus reactions in the quasielastic (QE) region. We also evaluate and discuss the impact of meson-exchange currents (2p-2h MEC) on lepton-nucleus interactions (Fig. 1) through the analysis of two-particle two-hole longitudinal (L) and transverse (T) contributions to electroweak response functions in a fully relativistic Fermi gas [4, 8]. This 2p-2h effect includes all the interference terms as

G.D. Megias (✉) · J.A. Caballero
Departamento de Física Atómica, Molecular y Nuclear, Universidad de Sevilla, 41080 Sevilla, Spain
e-mail: megias@us.es

J.E. Amaro
Departamento de Física Atómica, Molecular y Nuclear and Instituto Carlos I de Física Teórica y Computacional, Universidad de Granada, 18071 Granada, Spain

M.B. Barbaro
Dipartimento di Fisica, Università di Torino, Sezione di Torino, Via P. Giuria 1, 10125 Torino, Italy

T.W. Donnelly
Center for Theoretical Physics, Laboratory for Nuclear Science and Department of Physics, Massachusetts Institute of Technology, Cambridge, MA 02139, USA

J.-E. García-Ramos et al. (eds.), *Basic Concepts in Nuclear Physics: Theory, Experiments and Applications*, Springer Proceedings in Physics 182,
DOI 10.1007/978-3-319-21191-6_9

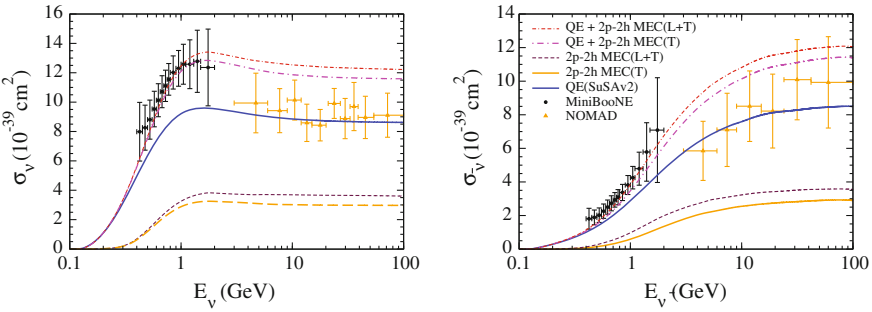

Fig. 1 CCQE $\nu_{\mu}-{}^{12}$C cross section per nucleon displayed versus neutrino energy E_ν and evaluated using the SuSAv2 and the SuSAv2+MEC approaches (*left panel*). CCQE $\bar{\nu}_{\mu}-{}^{12}$C cross section is also shown (*right panel*). Results are compared with the MiniBooNE [9] and NOMAD [10] experimental data. Also presented for reference are the results excluding the longitudinal MEC contributions

well as the vector and axial components arising from the weak current. Finally, our model is extended beyond the QE nuclear regime by including effects such as Δ contributions [5] associated to the pion production region (i.e. nucleonic resonances) and Deep Inelastic Scattering processes (DIS) where quarks and gluons degrees of freedom are relevant for describing the nuclear structure.

This fully relativistic theoretical description of the inelastic spectrum (nucleonic resonances, DIS, etc.) has been succesfully tested against (e, e′) data and work is in progress to include it in the analysis of neutrino-nucleus interactions with the aim of achieving a complete analysis of all present and future neutrino oscillation experiments (MINERνA, ArgoNeuT, SciBooNE, etc.).

Moreover, the possibility of describing the different nuclear regimes, particularly QE and MEC contributions, through a straightforward parametrization might be of interest to Monte Carlo neutrino event simulations used in the analysis of neutrino oscillation experiments.

References

1. G.D. Megias et al., Phys. Lett. B, **725**, 170–174 (2003); Phys. Rev. D **89**, 093002 (2014)
2. M.V. Ivanov et al., Phys. Rev. C **89**, 014607 (2014)
3. R. González-Jiménez et al., Phys. Rev. C **90**, 035501 (2014)
4. G.D. Megias et al., Phys. Rev. D **91**, 073004 (2015)
5. M.V. Ivanov et al., J. Phys. G **43**, 045101 (2016)
6. A.M. Ankowski et al., Phys. Rev. C **92**, 025501 (2015)
7. T.W. Donnelly, I. Sick, Phys. Rev. Lett. **82**, 3212 (1999); Phys. Rev. C **60**, 065502 (1999)
8. I. Ruiz, Simo et al., Phys. Rev. D **90**, 033012 (2014); Phys. Rev. D **90**, 053010 (2014)
9. A.A. Aguilar-Arevalo et al., [MiniBooNE Collaboration], Phys. Rev. D **81**, 092005 (2010); Phys. Rev. D **88**, 032001 (2013)
10. V. Lyubushkin et al., NOMAD Collaboration. Eur. Phys. J. C **63**, 355 (2009)

Direct Reactions: A One Dimensional Toy-Model

Laura Moschini, Andrea Vitturi and Antonio Moro

Abstract A line of research has been developed to describe the structure and the dynamics of weakly-bound systems with one or more valence particles. To simplify the problem we are assuming particles moving in one dimension. Within this model one can describe, for example, direct reactions involving one or two valence neutrons: inelastic scattering, breakup and transfer processes. Exact solutions obtained by directly solving the many-body time-dependent Schrodinger equation can be compared with the results obtained with different approximate schemes (first-order, coupled channels, continuum discretization, etc.). In this contribution we concentrate on inelastic scattering.

Direct nuclear reactions are useful tools to investigate nuclear structure: the collective or single-particle character of a state may be studied with inelastic scattering and one-particle transfer; pairing correlations or clustering could be tested via multi-nucleon transfer; the role of continuum is investigated through breakup channel.

Many models to describe these processes are available and usually compared to experimental data. Since these models are based on approximations, not always the exact solution can be obtained, e.g. for problems related to basis choice, uniqueness or convergence. To investigate such limitations the comparison between approximate models and exact ones would be desirable: but mathematical complexities and high computational power required constitute a huge difficulty. Therefore, we move to one dimension [1] and, despite the drastic assumption, the model encompass many characteristics observed in experiments.

In the test case considered here, the colliding nuclei are described by two Woods-Saxon wells. The target potential has two bound levels with energies -8.56 and -1.96 MeV, and it is assumed to be at rest in a fixed position. The projectile is

L. Moschini (✉) · A. Vitturi
Dipartimento di Fisica "G. Galilei", Universita di Padova and INFN - Padova,
v. Marzolo, 8, 35131 Padua, Italy
e-mail: laura.moschini@pd.infn.it

L. Moschini · A. Moro
Depto. de Física Atómica, Molecular y Nuclear, Universidad de Sevilla,
Apartado 1065, 41080 Seville, Spain

J.-E. García-Ramos et al. (eds.), *Basic Concepts in Nuclear Physics: Theory, Experiments and Applications*, Springer Proceedings in Physics 182,
DOI 10.1007/978-3-319-21191-6_10

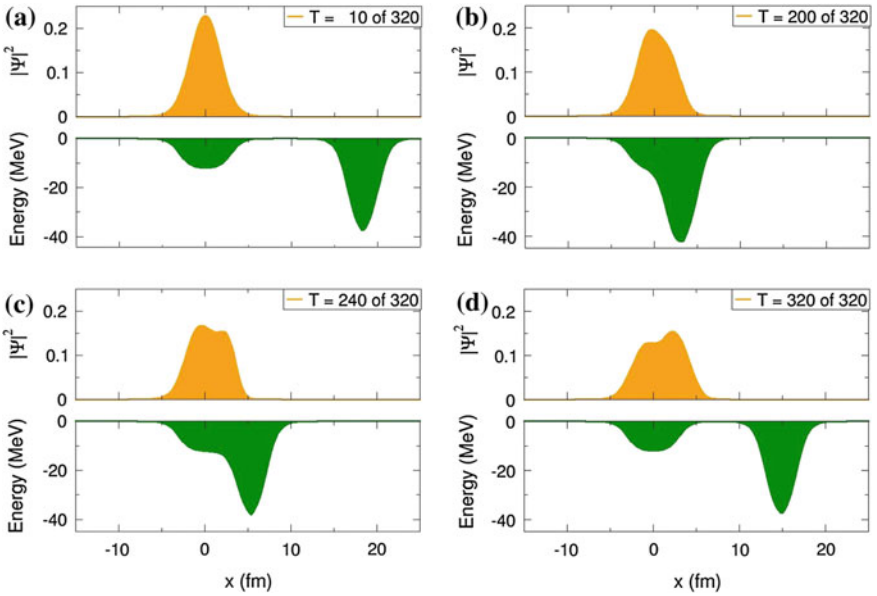

Fig. 1 Time-dependent solution at two different values of t (indicated by the *labels*). In each frame, the upper part gives the square of the one-particle wavefunction (*orange*) while the lower frame gives the actual position of the two potentials at the same time (*green*)

moving following a fixed classical trajectory. Initially, the particle is sitting in the target ground state.

The "exact" results shown in Fig. 1 have been obtained by directly solving the time-dependent one-particle Schroedinger equation

$$i\hbar\frac{\partial}{\partial t}\Psi(x,t) = \mathscr{H}(x,t)\Psi(x,t) \quad \text{where} \quad \mathscr{H}(x,t) = -\frac{\hbar^2}{2\mu}\frac{\partial^2}{\partial x^2} + V_T(x) + V_P(x,t). \quad (1)$$

The probability for populating the different channels after the collision is determined by projecting the asymptotic wavefunction (i.e. the solution for large values of t) onto the corresponding eigenstates of the two wells. This yields 65 % for elastic scattering, 22 % for inelastic scattering and 13 % for breakup.

We solve the same equation within the standard coupled-channels formalism, thus testing the validity of the necessary truncations. In first order approximation, including only target bound states, we find 29 % probability for inelastic scattering. Including also the continuum[1] and solving the full coupled-channels calculation we obtained a probability of 22 %, in perfect agreement with the exact solution.

[1]The discretized continuum is obtained diagonalizing the target potential in an infinite square well basis.

In conclusion, by comparing approximate approaches with exact models, it emerges how fundamental the continuum inclusion is to obtain the proper result expected from the "exact" calculation, even if the system is not weakly-bound.

Reference

1. L. Moschini, (2013). arXiv:1410.7167; L. Moschini, J. Phys.: Conf. Ser. **566**, 012027 (2014); A. Vitturi, L. Moschini, J. Phys.: Conf. Ser. **590**, 012007 (2015)

^{210}Pb-Dating of Pb Deposition in Five Sediment Cores from Ria of Vigo (NW Spain): γ-Spectrometry and CRS Model

M.C. Pedrosa-García

Abstract Sediment samples were obtained during July 2012 in five intertidal muddy, La Coruña, Pontedeume, Cedeira, Betanzos and Ferrol. The cores (L, P, C, B and F) were carefully collected with a hand-driven PVC coring pipe of 60.2 mm inner diameter. Recoveries were 50 cm. Cores were collected in the inner part of the Rias, sliced in situ in 25 layers of 2-cm thickness obtaining 125 samples, stored in pre-cleaned plastic zip bags, and kept at 4 °C. Sediment sub-samples were dried at 45 ± 5 °C to constant weight, and water content was determined. The chronologies and sediment accumulation rates for the five sediment cores have been established by applying three physical-mathematical models, C.F:C.S (Constant Flux: Constant Sedimentation), C.R.S (Constant Rate and Supply) and C.R.S—M.V (Constant Rate and Supply—Minimum Variances) which are based on obtaining in-excess ^{210}Pb ($^{210}Pb_{unsupported}$) (R. García Tenorio, The ^{210}Pb dating method and its application in sediments, 1988). The resulting chronologies were validated using the pollution (L. Eduardo et al., A 700 year record of combustion-derived pollution in northern Spain: Tools to identify the Holocene/Anthropocene transition in coastal environments, 2014; F. Martín Garrido, Evaluación mediante datación con ^{210}Pb del efecto antropogénico en los procesos de sedimentación de las Rías de Vigo y Muros, 2006) instead of using the artificial fallout radionuclides ^{137}Cs and ^{241}Am because for ^{137}Cs migration is observed and ^{241}Am is not observed. Finally, the model that best fits for the pollution data in the study areas has been the CRS model. In the Ferrol sediment core it was necessary to join layers, since the amount of sample collected in each section was insufficient. Therefore, boxes were filled with sediment corresponding to 4 cm layers loosing resolution.

M.C. Pedrosa-García (✉)
Laboratorio de Radiaciones Ionizantes, Universidad de Salamanca USAL,
C/Espejo S/n, 37008 Salamanca, Spain
e-mail: canty@usal.es

J.-E. García-Ramos et al. (eds.), *Basic Concepts in Nuclear Physics: Theory, Experiments and Applications*, Springer Proceedings in Physics 182,
DOI 10.1007/978-3-319-21191-6_11

1 Materials and Methods

^{210}Pb, ^{226}Ra, ^{214}Pb and ^{137}Cs activities in each section of the five cores were simultaneously determined by low-level background gamma-ray spectrometry with a n type hyper-pure germanium detector, by Canberra (HPGe). This is a non-destructive technique that allows the simultaneous detection of several radionuclides of interest. In-excess ^{210}Pb ($^{210}Pb_{xs}$) has to be determined taking into account the total ^{210}Pb activity in the sediment has mainly two contributions: an indirect one coming from the decay of the ^{226}Ra existing in the sediment, which gives rise to the supported ^{210}Pb ($^{210}Pb_{sup}$), and a direct one coming from atmospheric fall-out ($^{210}Pb_{xs}$). To determine the $^{210}Pb_{sup}$ fraction, which is given by the ^{226}Ra activity, secular equilibrium is assumed between ^{226}Ra and $^{210}Pb_{sup}$, an assumption that we have tested by comparing their corresponding specific activities in samples where $^{210}Pb_{xs}$ has become non-detectable. Gamma spectrometry with HPGe detectors can constitute a very useful technique in sediment dating, because it provides, in just one measurement, the full content of the useful gamma emitters in the sediments.

A total of 125 samples were analyzed with Galea [4], one corresponding to each slice measured. Spectra from natural radionuclides are characterized by low-intensity peaks, which are highly overlapped at low energy, where the continuum background is also higher. A precise analysis of these spectra requires a method capable to extract confidently the areas of all emissions in every spectrum. Galea achieved this task in two steps: (1) the whole fit of the spectral continuum and (2) the emission identification with a genetic algorithm and simultaneous area calculation with restrictions based on tabulated intensities, isotopic relations and detector efficiencies. The benefits of using Galea are apparent in ^{210}Pb, ^{226}Ra and ^{238}U results. ^{210}Pb has one emission at 46.54 keV, whose precise quantification requires a reliable baseline determination. ^{226}Ra direct emission at 186.1 keV needs to be deconvoluted from the ^{235}U one at 185.5 keV. For a precise ^{226}Ra determination, emissions from the ^{226}Ra daughters are used for the restriction calculations and to check the secular equilibrium assumption. The ^{238}U activity is also needed to check ^{235}U activity and, therefore, to verify the ^{226}Ra and ^{235}U peak deconvolution. For estimation of ^{238}U activity, peak area restrictions are also needed because of the high overlapping of its emissions at 92.35 and 92.73 keV. It is observed in all cases, secular equilibrium between ^{226}Ra and ^{214}Pb, the latter being estimated with less uncertainty.

^{210}Pb, ^{226}Ra, ^{214}Pb, ^{238}U, ^{325}U and ^{137}Cs activity concentrations are calculated from the activities obtained by the spectrum analysis. All sediment radionuclide concentrations are given in Bq/kg dry weight. Minimum detectable activities (MDA) were typically below 0.60 Bq/kg for ^{210}Pb, 0.56 Bq/kg for ^{214}Pb and 2.26 Bq/kg for ^{226}Ra. From the evaluation of these results, $^{210}Pb_{xs}$ value is calculated by subtracting the activity concentration for the ^{214}Pb at 351.93 keV to the ^{210}Pb one. $^{210}Pb_{xs}$ decreases according to the radioactive decay law ($T_{1/2} = 22.26$ y), its contribution being not measurable below a certain depth. It is worth to mention that $^{210}Pb_{xs}$ activity was estimated by subtraction of the ^{226}Ra (from ^{214}Pb) activity to the total ^{210}Pb

(46.54 keV) one for each sample instead of subtracting the constant ^{210}Pb activity value at depth, to account for any textural differences in core samples [5, 6].

2 Radionucleide Dating Results

The excess of ^{210}Pb with respect to ^{226}Ra and, therefore, to the $^{210}Pb_{sup}$ fraction is observed in the vertical profiles of total ^{210}Pb, ^{214}Pb and ^{226}Ra specific activities as shown in Fig. 1. The specific activity profiles of 137Cs are given in Fig. 2, where migration is appreciated. Dating results versus depth obtained for each model are given in Fig. 3. Then a chronology validation is made with other parameters like metal concentrations.

Several models are available to interpret a $^{210}Pb_{xs}$ activity profile, with the estimated dates depending on the model that better describes the ^{210}Pb geochemistry.

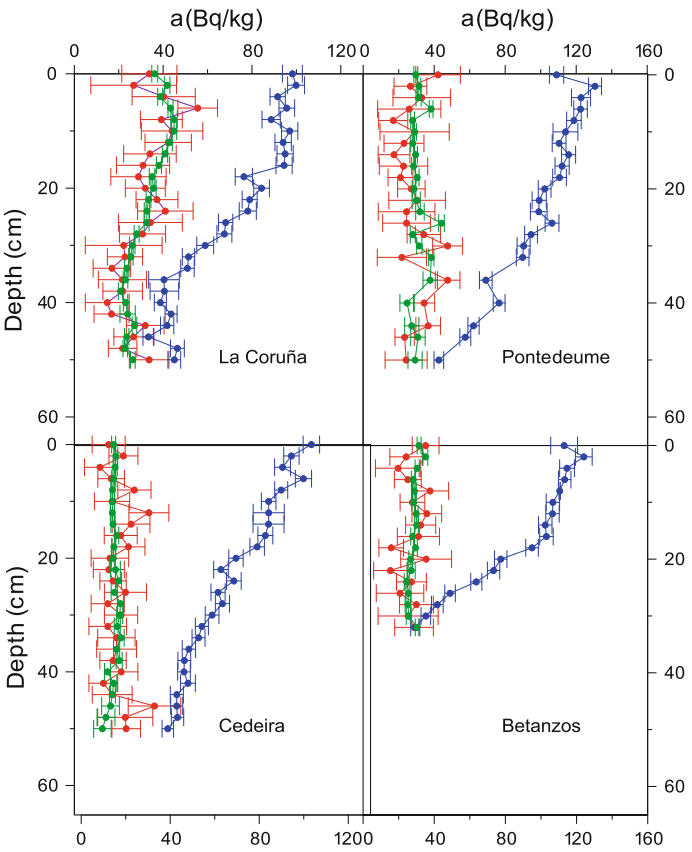

Fig. 1 Depth profiles of ^{210}pb (in *blue*), ^{214}pb (in *green*) and ^{226}Ra (in *red*) activities (Bq/kg)

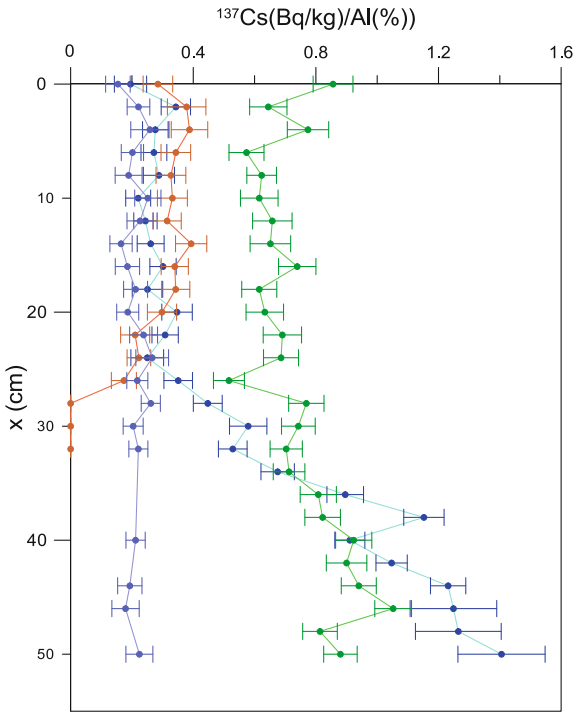

Fig. 2 Depth profiles of ^{137}Cs activities (Bq/kg) in:La Coruña (in *blue*), Pontedeume (in *purple*), Cedeira (in *green*) and Betanzos (in *brown*)

Simple models have been widely applied [7–10]. There are several variations of these simple models, where processes such as vertical mixing are considered [11, 12]. The selection of a particular model depends on the sedimentary characteristics.

The CF:CS (Constant Flux:Constant Sedimentation) model was used t o calculate age depth correlations on a sectional basis. In this model two hypotheses are used: first, the value of the ratio $^{210}Pb_{xs}$ flux contribution to sediments and the sedimentation rate have remained constant during its formation. The sediment accumulation rate is lately estimated from a least-squares fit, considering measured uncertainties, [13]. The CRS—MV (Constant Rate and Supply—Minimum Variances) model and CRS model (Constant Rate and Supply) were also considered [14]. Both models assumes that there was a constant flux of $^{210}Pb_{xs}$ to the sediments over the time of sedimentation and that the specific activity of $^{210}Pb_{xs}$ in the sediment varied exponentially with the cumulative dry mass of the sediment, then keeping track for compaction. The sediment accumulation rate is estimated by a linear least-square fit of the line representing the $^{210}Pb_{xs}$ inventory in the CRS—MV, considering measured uncertainties [15], while obtained directly, without fitting, in the CRS.

Total $^{210}Pb_{xs}$ inventories gave us insight about the uniform sedimentary and ^{210}Pb deposition dynamics in the five areas of study, being 6.83(15) kBq/m^2 in La Coruña, 10.95(16) kBq/m^{2}in Pontedeume, 9.6(15) kBq/m^2 in Cedeira, 6.70(11) kBq/m^2 in Betanzos and 1.78(09) kBq/m^2 in El Ferrol. The corresponding $^{210}Pb_{xs}$ fluxes were 69(02) Bq/m^{2}y, 83(02) Bq/m^{2}y, 96(02) Bq/m^{2}y, 43(04) Bq/m^{2}y and 19(05) Bq/m^{2}y,

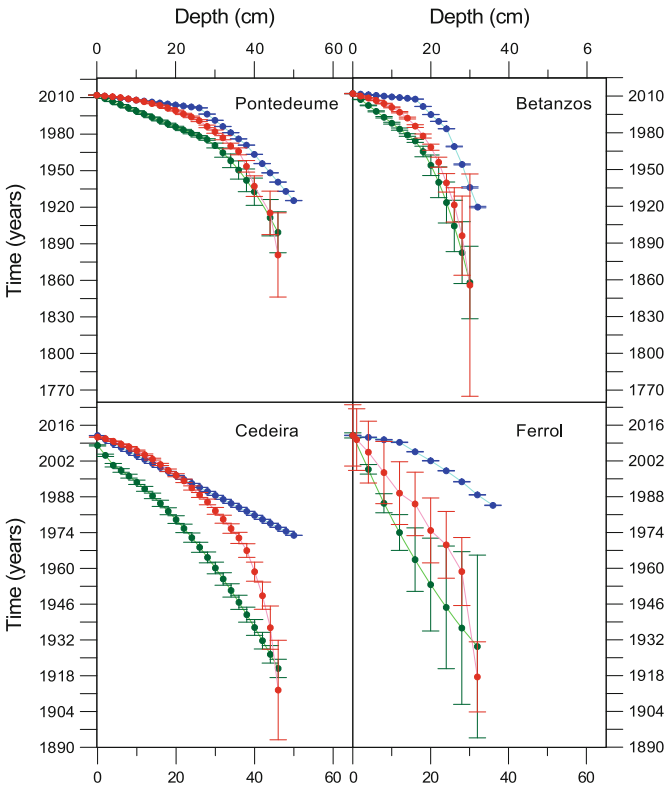

Fig. 3 Results for the three models considered: CF:CS (in *blue*), CRS—MV (in *green*) and CRS (in *red*)

respectively. Atmospheric $^{210}Pb_{xs}$ fluxes have not been reported for the study area, although they have been established for other areas of the Iberian Peninsula, such as the West Mediterranean Sea where the flux is about 80 Bq/m^{2}y, which is of the same order of the ones reported here. The similarity among the inventories obtained allows applying the same model to the five cores [16, 17], La Coruña area being that about which more complementary data to check the dating results are available. Therefore, La Coruña core dating is discussed from now on.

Linear least squares fit in two sections is made when applying CF:CS model to the $^{210}Pb_{xs}$profile: one section going from 0 to 16 cm with a $\chi^2 = 1.3153$ and the second one, from 18 cm to the end with a $\chi^2 = 1.1468$. The setting for the CRS—MV model requires a mixed layer up to 16 cm one, the goodness-of-fit being $\chi^2 = 0.4187$ for the mixing layer and from 16 cm to the end, $\chi^2 = 0.0234$. CRS model does not need any numerical fit as mentioned above. Dating results versus depth obtained for each model are given in Fig. 4. In order to decide the more valid one, some historical data together with the Pb metal pollution profiles shown in Fig. 5 are contrasted with the dating estimations obtained from the three mathematical models.

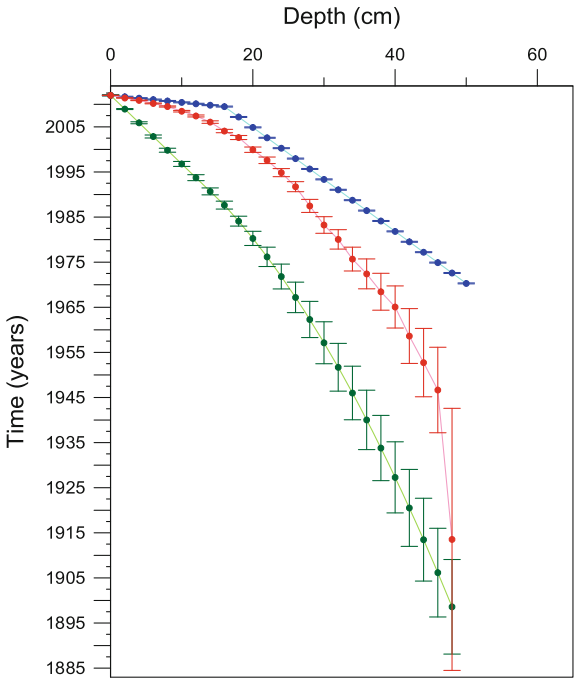

Fig. 4 Results for the three models considered: CF:CS (in *blue*), CRS—MV (in *green*) and CRS (in *red*) in La Coruña core

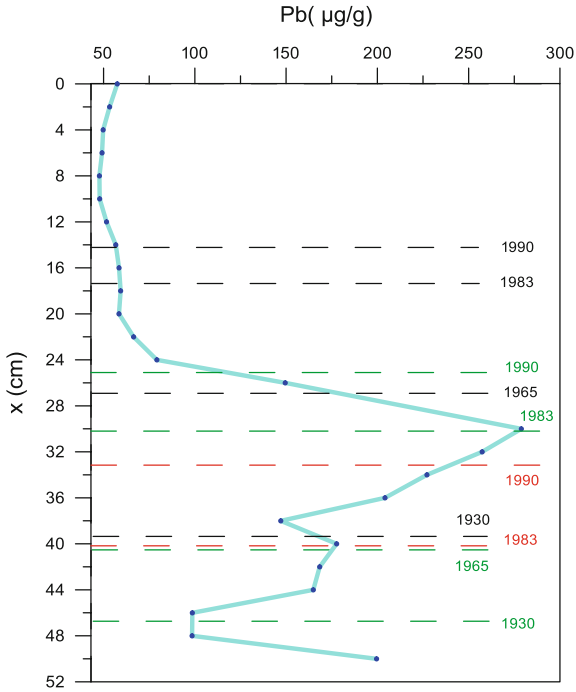

Fig. 5 Pb pollution CF:CS (in *red*), CRS—MV (*black*) and CRS (*green*) in La Coruña core

The historical data are related to the activity of the Cros steel factory in La Coruña. This factory opened in 1930, when a notable change on the Pb content is observed in Fig. 5. The maximum activity of the factory took place between 1965 and 1983, being closed in 1990, which coincides with the lower Pb metal level as estimated for the CRS model. This model assigns the year 1983 to the maximum ^{210}Pb concentration, which is also in agreement with the historical data. The great consistency among historical data and dates as provided for the CRS model tells about the better adaptation of this model for dating at least in the four cores where $^{210}Pb_{xs}$ inventories and flows are similar [16, 17]. The CF:CS, CRS—MV and CRS results for Pontedeume, Betanzos, Cedeira and El Ferrol are given in Fig. 3.

References

1. R. García Tenorio, The ^{210}Pb dating method and its application in sediments. Reist de Geofísica 44, 225–234 (1988)
2. L. Eduardo et al., A 700 year record of combustion-derived pollution in northern Spain: Tools to identify the Holocene/Anthropocene transition in coastal environments. Environ. Pollut. **159**, 889–896 (2014)
3. F. Martín Garrido, Evaluación mediante datación con ^{210}Pb del efecto antropogénico en los procesos de sedimentación de las Rías de Vigo y Muros (2006)
4. B. Quintana, F. Fernandez, Gamma-ray spectral analysis with the COSPAJ continuum fitting-routine. Appl. Radiat. Isot. **49**(9–11), 1235–1240 (1998)
5. J. Pfitzner, G. Brunskill, I. Zgorskis, ^{137}Cs and excess ^{210}Pb deposition patterns in estuarine- and marine sediment in the central region of the Great Barrier Reef Lagoon. North-eastern Australia. J. Environ. Radioact. **76**, 81–102 (2004)
6. E.G. San Miguel, J.P. Bolivar, R. García-Tenorio, Vertical distribution of Th-isotope ratios, ^{210}Pb, ^{226}Ra and ^{137}Cs in sediment cores from an estuary affected by anthropogenic releases. Sci. Total Environ. 318, 143–157 (2004)
7. P.G. Appleby, F. Oldfield, R. Thompson, P. Hottunen, ^{210}Pb dating of annually laminated lake sediments from Finland. Nature **280**, 53–55 (1979)
8. P.G. Appleby, F. Oldfield, The assessment of ^{210}Pb data from sites with varying sediment accumulation rates. Hydrobiologia **103**, 29–35 (1983)
9. P.G. Appleby, F. Oldfield, Application of lead-210 to sedimentation studies (Oxford University Press, 1992) pp. 31–778
10. J.A. Robbins, in *Geochemical and geophysical applications of radioactive lead*, ed. by J.O. Nriagu. The Biogeochemistry of Lead in the Environment (Elservier, Amsterdam, 1978) 285–393
11. F. Oldfield, P.G. Appleby, in *Empirical testing of ^{210}Pb-dating models for lake sediments*. (Leicester University Press, 1984), pp. 93–124
12. J.A. Robbins, Stratigraphic and dynamic effects of sediment reworking by Great Lakes zoobenthos. Hydrobiologia **92**, 611–622 (1982)
13. P. Álvarez-Iglesias et al., Sedimentation rates and trace metal input history in intertidal sediments from San Simón Bay (Ría de Vigo, NW Spain) derived from ^{210}Pb and ^{137}Cs chronology. J. Environ. Radioact. **98**, 229–250 (2007)
14. W.R. Schell, M.J. Tobin, ^{210}Pb dating using the CRS-MV model with historical data to test and evaluate accuracy. in *Proceedings of the Third International Summer School: Low-Level Measurements of Radioactivity in the Environment*, 1994, pp. 355–368
15. H.P. William, A.T. Saul, T.V. William, P.F. Brian, *Numerical Recipes in C*, Second Edition (1992)

16. A.A. Ali, B. Ghaleba, M. Garneaua, H. Asnonga, J. Loisel, Recent peat accumulation rates in minerotrophic peatlands of the Bay ames region, Eastern Canada, inferred by ^{210}Pb and ^{137}Cs radiometric techniques. Appl. Radiat. Isot. **66**, 1350–1358 (2008)
17. O. Carolina et al., Improving the ^{210}Pb-chronology of Pb deposition in peat cores from Chao de Lamoso. Sci. Total Environ. 443, 597–607 (2013), NW, Spain

Magnetic Moment Measurements Using Alpha Transfer Reactions-Challenges and Perspectives

F. Ramírez and D.A. Torres

Abstract The use of α-transfer reactions, in combination with the Transient Field Technique, is an alternative to measure magnetic moments of low-spin states of radioactive nuclei which, otherwise, will be difficult to populate with the present beam facilities. In this contributions a short introduction to the technique and the challenges for future uses are presented.

1 Magnetic Moments Measurements

The study of nuclear magnetic moment, for 2_1^+ states, has been extensively developed during the past decades using the so called Transient Field technique [1, 2]. The use of Coulomb excitation reactions in inverse kinematic has allowed the study of more than 100 isotopes in several mass regions [3]. The natural extension of such works is to study radioactive nuclei in states with $J^\pi \leq 2^+$. An alternative utilized in recent years is the use of α-transfer reactions, to populate low-spin states in radioactive nuclei that are difficult to produce with enough intensity in the present radioactive beam facilities. A complete description of the technique can be consulted in [4].

The use of α-transfer presents an interesting alternative for the use in combination with radioactive beams, to date only stable beams have been utilized. A cluster properties of the carbon nuclei, it can be seen as compound by three $alpha$ particles, made the use of a thin carbon layer the most natural election for the use in the first part of the multi-layered target; a complete theoretical description for the alpha transfer process, from a carbon layer, is important to reduce the errors in the measured

F. Ramírez (✉) · D.A. Torres
Physics Department, Universidad Nacional de Colombia, Bogotá, Colombia
e-mail: framirezmo@unal.edu.co

D.A. Torres
e-mail: datorresg@unal.edu.co

J.-E. García-Ramos et al. (eds.), *Basic Concepts in Nuclear Physics: Theory, Experiments and Applications*, Springer Proceedings in Physics 182,
DOI 10.1007/978-3-319-21191-6_12

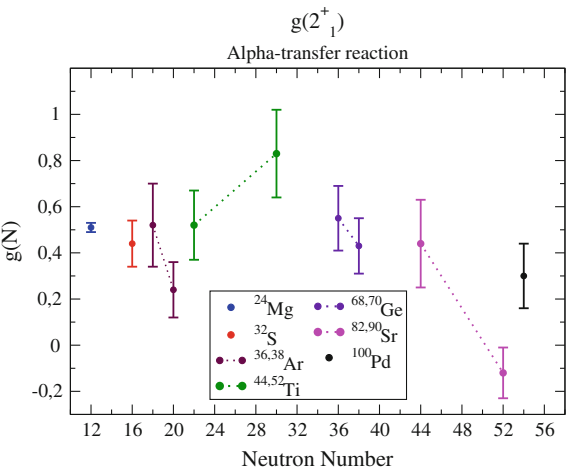

Fig. 1 A partial compilation of $g(2_1^+)$ factor values obtained using the Transient Field technique, the states were populated using α-transfer reactions. Most of the values are consistent with the collective prediction $g = Z/A$. The reduction of the errors is one of the most important goals to improve the comparison with theoretical models

g-factor values, those errors are larger than the ones obtained using Coulomb excitation reactions to populate the states, see Fig. 1. Such studies should focus in the correlation between the different sub-products of the reaction and the γ-ray angular distribution emitted from the states under study.

Acknowledgments This work was supported in part by the Colombian agency for the development of science, COLCIENCIAS, under contract 110165842984, and Universidad Nacional de Colombia.

References

1. G.J. Kumbartzki, Nuclear magnetic moments, a guide to transient field experiments (2015), http://www.physics.rutgers.edu/kum/tfbook.pdf. Accessed 3 Oct 2015
2. N. Benczer-Koller, G.J. Kumbartzki, Magnetic moments of short-lived excited nuclear states: measurements and challenges. J. Phys. G: Nucl. Part. Phys. **34**, R321 (2007), http://stacks.iop.org/0954-3899/34/i=9/a=R01. Accessed 3 Oct 2015
3. D.A. Torres, F. Ramirez, Nuclear structure aspects via g-factor measurements: pushing the frontiers, in *Proceedings of Science Physics Review C* (2014). http://pos.sissa.it/archive/conferences/194/021/X%20LASNPA_021.pdf. Accessed 3 Oct 2015
4. D.A. Torres et al., First g-factor measurements of the 2^+ and the 4^+ states of radioactive ^{100}Pd. Phys. Rev. C **84**, 044327 (2011) doi:10.1103/PhysRevC.84.044327. http://link.aps.org/doi/10.1103/PhysRevC.84.044327. Accessed 3 Oct 2015

Investigation of Fusion Mechanism for Proton-Halo System

J. Rangel, J. Lubian and P.R. Gomes

Abstract Parameter free calculations were performed to predict the near-barrier fusion cross section for the proton-halo ^{8}B + ^{58}Ni system. Standard CC calculations predicted fusion cross section smaller than data, while absorption cross section obtained from CDCC calculation agrees with the data above the barrier. In the whole energy range the transfer cross section is not negligible.

One of the most intriguing questions around weakly bound nuclei concerns the effect of the breakup process and the extended matter density on fusion cross section. The tail of the matter density favors the fusion cross section as long as it hinders Coulomb barrier. The breakup process is responsible for dynamics effects because it is strongly coupled with the elastic channels. This effect can be found to contribute to hinder or enhance the fusion cross section, and the result may be different below and above the Coulomb barrier. In order to avoid ambiguities during the analyzes it is important to re-normalize data. In this work it was used the reduction method, called the Universal fusion function (UFF), reported by Canto et al. [1, 2]. This reduction procedure allows to compare different systems in the same plot. Therefore, systematics can be derived.

In this work, some calculations were done for the ^{8}B + ^{58}Ni system. For the real part of the optical potential, a double folding potential with realistic nuclear density for the p-halo ^{8}B projectile [3] was used. The experimental data for fusion cross section were enhanced when compared to the CC calculations including only target excitations. This enhancement can be attributed to dynamics effects of breakup channels not included in the calculation. This result is not in agreement with the systematic obtained in Ref. [2] where it was shown that the complete fusion cross section is hindered above the barrier and the total fusion coincide with the UFF or

J. Rangel (✉) · J. Lubian · P.R. Gomes
Instituto de Física, Universidade Federal Fluminense, Av. Lintoranea S/n, Gragoatá, Niterói, RJ 24210340, Brazil
e-mail: jeannie@if.uff.br

J. Lubian
e-mail: lubian@if.uff.br

J.-E. García-Ramos et al. (eds.), *Basic Concepts in Nuclear Physics: Theory, Experiments and Applications*, Springer Proceedings in Physics 182,
DOI 10.1007/978-3-319-21191-6_13

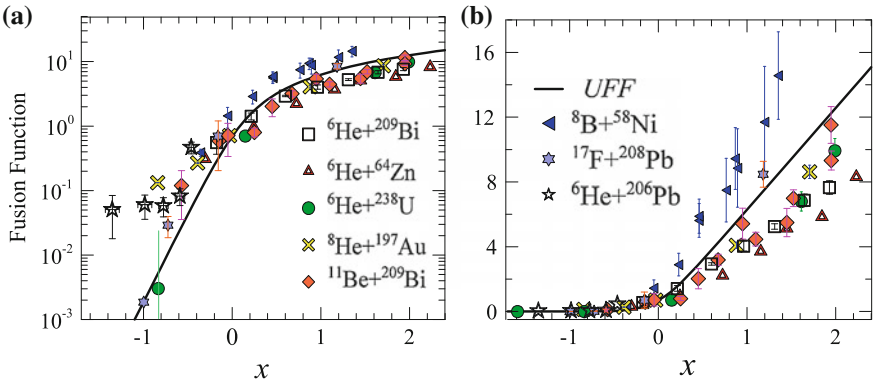

Fig. 1 Experimental renormalised fusion functions for several neutron-halo systems and for the proton-halo systems $^{17}F + ^{208}Pb$ (^{17}F is halo only in its first excited state) and $^{8}B + ^{58}Ni$. The *curve* is the universal fusion function. x is a reduced energy parameter. For details see the text and [1]

it is hindered for neutron halo systems. The results for various proton and neutron halo systems are shown in Fig. 1.

On the other hand, on [4] optical model calculation using the Wong model [5] with three barrier parameter were performed to derive the fusion cross section. The agreement with experimental data was obtained with very large barrier radius, which was attributed to the halo structure of ^{8}B. In order to try to understand this disagreement we performed also CDCC and CRC calculations, this last one for to include the 1p stripping channel. In the CDCC calculation the absorption cross section was derived, that it contained besides fusion also the absorption for other mechanism left out in the coupling scheme, like 1p transfer and inelastic excitations of the target. The absorption cross section was found in agreement with the fusion data for energy above the Coulomb barrier, and enhanced below it. The transfer cross section obtained at energies above the barrier were of the order of 100 mb. Therefore this is not a negligible channel.

In conclusion, it was be found that the fusion data of $^{8}B + ^{58}Ni$ without free parameters does not agree with systematic other weakly bound nuclei and the UFF curve. Independent calculations show the importance of including all channels in the same foot.

Acknowledgments The authors acknowledge the partial support from CNPq, FAPERJ, CAPES and from Pronex.

References

1. Canto et al., Nucl. Phys. A **821**, 51 (2009)
2. Canto et al., J. Phys. G: Nucl. Part. Phys. **36**, 015109 (2009)

3. J. Rangel et al., Eur. Phys. J. A **49**, 57 (2013)
4. E.F. Aguilera et al., Phys. Rev. Lett. **107**, 09271 (2011)
5. C.Y. Wong, Phys. Rev. Lett. **31**, 766 (1973)

Fission Fragment Mass Distribution of ^{256}Fm

Anna Zdeb and Michał Warda

Abstract Fragment mass distribution is one of the major, measurable characteristics of fission. The shape of the observed yield allows to determine type of fission and—indirectly—to investigate structure of the mother nucleus. It has been proven, that basic properties of nascent fragments are preliminary determined by the configuration of pre-scission point. We assume, that the shape of a nucleus obtained in its pre-scission point provides information about the possible fragment mass asymmetry.

1 The Model

Detailed analysis of a nuclear structure in a pre-scission point allows to deduce some information about the fission fragments properties [6]. To obtain fully microscopic description of the pre-scission configuration the self-consistent calculations of Potential Energy Surface (PES) were performed. The Hatree-Fock-Bogolubov (HFB) model with the Gogny type interactions (parametrization D1S) was used. The fission path, leading to the scission point, was found by minimization of the total energy of the system. The HFB equations were solved with constraints on quadrupole and octupole moments. Precise localization of the pre-scission point was determined after application of the Dubray's method [4].

At the end of the fission path nucleus assumes a molecular shape—two preformed fragments are connected by the neck, containing 10–20 nucleons. The final mass division depends mostly on the mechanism of sharing these neck's nucleons between fragments during scission. After Brosa [2, 3], the probability P of the rupture of a neck, leading to fragmentation A_1/A_2 is given by:

$$P(A_1/A_2) = \exp\left[\frac{-2\gamma\sigma(z)}{T}\right], \tag{1}$$

A. Zdeb (✉) · M. Warda
Department of Theoretical Physics, University of Maria Curie-Skłodowska, Lublin, Poland
e-mail: azdeb@kft.umcs.lublin.pl

J.-E. García-Ramos et al. (eds.), *Basic Concepts in Nuclear Physics: Theory, Experiments and Applications*, Springer Proceedings in Physics 182,
DOI 10.1007/978-3-319-21191-6_14

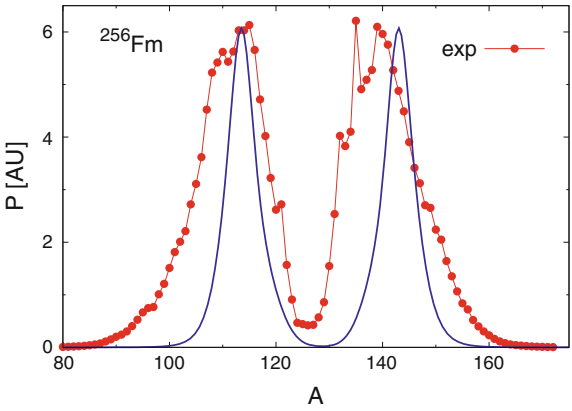

Fig. 1 Fragment mass distribution for the spontaneous fission of ^{256}Fm isotope in comparison to the experimental data, taken from [5]

where $T = \sqrt{12E^{sc}/A}$ is temperature of the pre-scission deformation, which depends on the excitation energy $E^{sc} = E_{g.s.} - E^{sc}_{def}$ and $\gamma = 0.9517[1 - 1.7826(1 - 2Z/A)^2]$ is a surface tension coefficient [1]. The cross section of a neck is equal to $\sigma(z) = 2\pi \int_0^\infty r_\perp \rho(z, r_\perp) dr_\perp$ [7].

2 Results and Conclusions

^{256}Fm represents asymmetric type of fission. The mass yield, obtained using presented method, is shown in Fig. 1.

As one may observe the most probable masses of fragments are quite well reproduced. The peak of the heavier fragment is slightly shifted in comparison with the experimental one. The presented experimental yield was measured after emission of prompt neutrons, what causes the discrepancy. Also the random neck rupture mechanism proposed by Brosa neglects the shell effects, which play an important role during fragmentation. We have shown, that fission mass yields may be partially reproduced by the analysis of the pre-scission shape of a nucleus. The inclusion of dynamic effects should allow to obtain the required broadness of distribution.

Acknowledgments This work was supported by the Polish National Science Centre, grants No. 2013/11/B/ST2/04087 and 2014/13/N/ST2/02551.

References

1. J. Blocki, J. Randrup, W.J. Swiatecki, C.F. Tsang, Ann. Phys. (NY) **68**, 377 (1977)
2. U. Brosa, Phys. Rev. C **38**, 1944 (1988)
3. U. Brosa, S. Grossmann, Z Phys. **A310**, 177 (1983)
4. N. Dubray, D. Regnier, Comput. Phys. Commun. **183**, 2035 (2012)

5. http://ie.lbl.gov/fission/endf349.pdf
6. M. Warda, A. Staszczak, W. Nazarewicz, Phys. Rev. C **86**, 24601 (2012)
7. M. Warda, A. Zdeb, Phys. Scr. **90**, 110301 (2015)

Part III
Student's Posters

Structure and Decay Modes of Superheavy Nuclei

A.I. Budaca, I. Silisteanu and C.I. Anghel

Abstract One calculated the α-decay (Budaca and Silişteanu Phys Rev C 88:044618, 2013 [1]; Silisteanu and Budaca At Data Nucl Data 98:1096, 2012 [2]) and spontaneous fission (SF) (Karpov et al Int J Mod Phys E 21:1250013, 2012 [3]) half-lives of superheavy nuclei with formulas derived from the systematics of experimental data and theoretical results. The parameters of the resulted formula are obtained from the fit of half-lives (Silisteanu and Anghel Rom J Phys 60:444–451, 2015 [4]; Silisteanu and Anghel Rom J Phys 59:724–732, 2014 [5]) in respect with the reaction energies Q_α, the height of the SF barrier B_f and the fissionability Z^2/A. The calculated partial and total half-lives T_α, T_{SF}, T_t are compared with the data (http://www.nndc.bnl.gov/chart [6]).

Many theoretical studies predict ^{270}Hs to be a deformed doubly magic nucleus ($Z = 108$, $N = 162$) and measured [6], as well as calculated [1–5] nuclear decay properties strongly support such a prediction. In this work we give a review of the main nuclear decay properties of nuclei around ^{270}Hs with Z =104–112 and N =158–166. New half-life predictions are made for many unknown nuclei from this region of nuclei by using the methods described in [4]. Figure 1 presents a part of these predictions.

The comparison of calculated partial T_α, T_{SF} and total T_t half-lives with experimental data leads to the conclusions:

- α decay dominates in nuclei over closed shells $Z > 108$, $N > 162$ ($^{274}Ds = {}^{270}Hs + \alpha$). SF dominates in nuclei below the closed shells ($^{266}Ds = {}^{270}Hs - \alpha$).

A.I. Budaca (✉) · I. Silisteanu · C.I. Anghel
Horia Hulubei National Institute of Physics and Nuclear Engineering,
Str. Reactorului no.30, P.O.BOX MG-6, Bucharest-Magurele, Romania
e-mail: abudaca@theory.nipne.ro

I. Silisteanu
e-mail: silist@theory.nipne.ro

C.I. Anghel
e-mail: claudia.anghel@theory.nipne.ro

J.-E. García-Ramos et al. (eds.), *Basic Concepts in Nuclear Physics: Theory, Experiments and Applications*, Springer Proceedings in Physics 182,
DOI 10.1007/978-3-319-21191-6_15

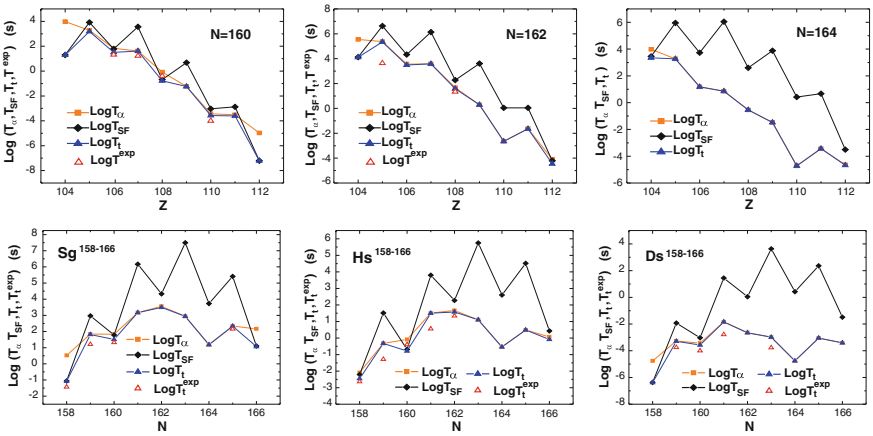

Fig. 1 Calculated [1–5] and experimental [6], partial and total, half-lives for isotonic (*up*) and isotopic (*down*) sequences of nuclei

- T_{SF} increase considerably due to the effect of unpaired nucleons. T_α is much less sensitive to the unpaired nucleons.
- Strong competition α-SF is observed in Z, N = even nuclei.
- Important changes in decay properties are determined by the number of valence particles/holes in the magic nucleus ^{270}Hs.
- The calculated half-lives are in good agreement to existing data.

It is worth to mention that superheavy nuclei in isomeric configurations often prefer the fission over α-decay [7]. The main reason for interest in nuclear decay properties is the insight which the available nuclear decay data afford into the structure of superheavy nuclei. In brief, by studying the decay channels it is possible to interrelate most nuclear species on the energy-time content basis and to determine the regions of greater stability. We show that the decay rates can be predicted with a fair degree of confidence and this may help in the preparation and identification of new superheavy nuclei.

References

1. A.I. Budaca, I. Silişteanu, Phys. Rev. C **88**, 044618 (2013)
2. I. Silisteanu, A.I. Budaca, At. Data Nucl. Data **98**, 1096 (2012)
3. I.V. Karpov et al., Int. J. Mod. Phys. E **21**, 1250013 (2012)
4. I. Silisteanu, C.I. Anghel, Rom. J. Phys. **60**, 444–451 (2015)
5. I. Silisteanu, C.I. Anghel, Rom. J. Phys. **59**, 724–732 (2014)
6. http://www.nndc.bnl.gov/chart
7. R. Budaca, M. Mirea, A. Sandulescu, Mod. Phys. Lett A **30**, 1550129 (2015)

Evaluation of Inclusive Breakup in Reactions Induced by Deuteron within a Three-Body Model

Jin Lei and Antonio M. Moro

Abstract In 1980s Ichimura, Austern and Vincent [Phys. Rev. C 32 431 (1985)] proposed a theory to calculate the inclusive breakup cross sections. Using the finite range DWBA version of this theory, we have performed calculations for the ^{118}Sn(d, pX) inclusive breakup reaction, and compared with available data in order to assess the applicability of the theory.

1 Introduction

An important mechanism that takes place in nuclear collisions is the dissociation of the projectile into two or more fragments. In many experiments, with the stable and radioactive nuclei, only one of the fragments is detected giving rise to so-called inclusive breakup. In the two-body dissociation, the process can be represented as $a(= b + x) + A \rightarrow b + B^*$, in which B^* is any possible state of the $x - A$ system. The theoretical interpretation of these reactions is complicated due to the fact that many processes (compound nuclei, transfer, elastic breakup...) can contribute to the production of the b fragment. The inclusive breakup can be separated into two contributions, namely, the elastic breakup and nonelastic breakup. The former corresponds to the process in which the fragments b and x survive after the collision and the target remains in its ground state. On the other hand, the nonelastic breakup corresponds to those processes of absorption of the unobserved fragment or target excitation.

J. Lei (✉) · A.M. Moro
Departamento de FAMN, Universidad de Sevilla, Apartado 1065,
41080 Seville, Spain
e-mail: jinlei@us.es

A.M. Moro
e-mail: moro@us.es

J.-E. García-Ramos et al. (eds.), *Basic Concepts in Nuclear Physics: Theory, Experiments and Applications*, Springer Proceedings in Physics 182,
DOI 10.1007/978-3-319-21191-6_16

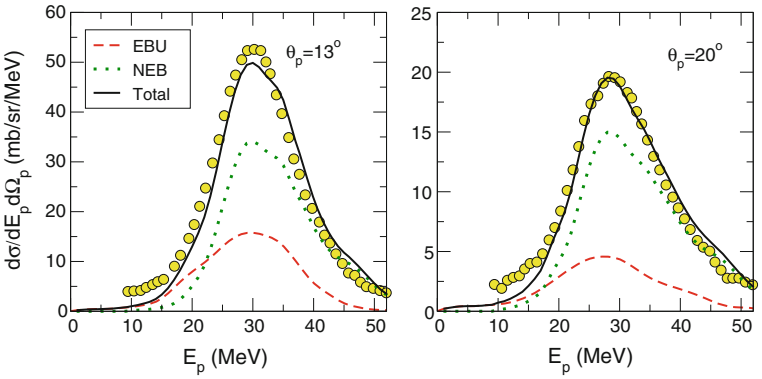

Fig. 1 Experimental and calculated double differential cross section, as a function of the outgoing proton energy, for the protons emitted in the ^{118}Sn(d, pX) reaction with laboratory angles of 13° (*left panel*) and 20° (*right panel*) at an incident energy of 56 MeV

2 Numerical Calculations and Results

In this section, we present calculations for the deuteron induced reaction ^{118}Sn(d, pX), and compare with the available data. Here, we compute separately the contribution of elastic breakup (EBU) and nonelastic breakup (NEB). For the EBU, we use the CDCC formalism, using the coupled-channel code FRESCO [1], whereas for the NEB, we use the formalism of IAV [2, 3] in its DWBA form.

In Fig. 1, we show the double differential cross section $d\sigma/dEd\Omega$ as a function of outgoing proton energy in the laboratory frame for the ^{118}Sn(d, pX) reaction at incident energy of 56 MeV. The experimental data are taken from [4]. The dashed line is the EBU calculation, whereas the dotted line is the calculation of NEB. The solid line is their incoherent sum, which reproduces well the shape and magnitude of the data. We note that, at both angles, the inclusive breakup cross section is dominated by the NEB process.

References

1. I.J. Thompson, Comp. Phys. Rep. **7**, 167 (1988)
2. M. Ichimura, N. Austern, C.M. Vincent, Phys. Rev. C **32**, 431 (1985)
3. J. Lei, A. Moro, Phys. Rev. C (Submitted, 2015)
4. N. Matsuoka et al., Nucl. Phys. A **345**, 1 (1980)

Geant4 Simulations for the Analysis of (n, γ) Measurements at n_TOF

J. Lerendegui-Marco, C. Guerrero, M.A. Cortés-Giraldo and J.M. Quesada

Abstract At the n_TOF facility at CERN, the (n, γ) experiments are usually carriedout with a set of C_6D_6 scintillators, a simple setup characterized by a low neutron sensitivity. The drawback of this simple detection setup is an elaborated analysis procedure, the so called Pulse Height Weighting Technique, that requires a manipulation of the experimental detector response. The modeling of the detector response can just be done with help of Monte Carlo (MC) simulations. The goal of this work is to provide an overview of the analysis technique focusing on the detailed simulations performed with the Geant4 toolkit.

1 Pulse Height Weighting Technique and Geant4 Simulations

Radiative capture measurements with improved accuracy are an important part of the experimental programme of the n_TOF facility at CERN [1]. The radiative capture (n, γ) measurements are carried out either with a 40 BaF_2 crystal Total Absorption Calorimeter [2] or with a set of C_6D_6 scintillators [3], following the Total Energy Detection Principle [4]. This method is based on two principles. First, only one γ-ray per cascade is detected due to the low efficiency of the detection system. Second, the efficiency of detection is proportional to the energy of the γ-ray. Under these conditions the efficiency for detecting a cascade will be proportional to the known cascade energy and independent of the actual cascade path. However, the second condition is not true in general and needs from mathematical manipulation of the detector response. The measured counts for each deposited energy must be weighted with an energy (pulse height) dependent weighting function (WF); this is known as the Pulse Height Weighting Technique (PHWT). To calculate the WF, the response distribution of the detector must be well known. Since its experimental determination is impossible due to the lack of monoenergetic γ-ray sources in the whole energy

J. Lerendegui-Marco (✉) · C. Guerrero · M.A. Cortés-Giraldo · J.M. Quesada
Dpto. de Física Atómica, Molecular y Nuclear, Universidad de Sevilla, 41012 Sevilla, Spain
e-mail: jlerendegui@us.es

J.-E. García-Ramos et al. (eds.), *Basic Concepts in Nuclear Physics: Theory, Experiments and Applications*, Springer Proceedings in Physics 182,
DOI 10.1007/978-3-319-21191-6_17

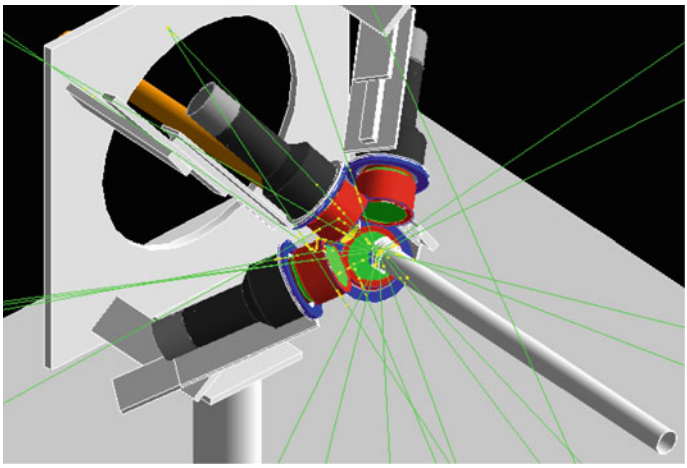

Fig. 1 Geant4 implementation of the capture setup with C_6D_6 detectors in n_TOF experimental area 1(EAR1). The *green tracks* represent the γ-rays isotropically emitted from the sample as it would be the case after a neutron capture

range of interest (0–12 MeV), MC simulations, performed in this work using the Geant4 toolkit [5], are the best solution.

In order to obtain the response distribution of the C_6D_6 detectors we have developed a Geant4 tool that implements in detail the setup. First, the detector geometry has been implemented as detailed as possible. Besides the detectors themselves, the dimensions and compositions of the materials, both of the sample and the experimental setup, can have a non-negligible influence in the response. In addition, an accurate positioning of the detectors in the simulated setup is another key factor to determine the actual response of the detectors in our experimental setup. The geometry of the detection setup as implemented in Geant4 is shown in Fig. 1.

This Geant4 tool is currently being used for the planning and analysis of the (n, γ) measurements of ^{171}Tm, ^{204}Tl, ^{147}Pm and ^{242}Pu at n_TOF, and will help to reduce the systematic uncertainties associated to the PHWT in the final results.

References

1. C. Guerrero et al., Eur. Phys. J. A **49**, 27 (2013)
2. C. Guerrero et al., Nucl. Instrum. Methods A **608**, 424 (2009)
3. R. Plag et al., Nucl. Instrum. Methods A **496**, 425 (2003)
4. R.L. Macklin, J.H. Gibbons, Phys. Rev. **159**, 1007 (1967)
5. S. Agostinelli et al., Nucl. Instrum. Methods A **506**, 250 (2003)

Computer Simulation and Experimental Results of ^{7}Be Photoproduction on ^{12}C and ^{14}N Nuclei

T.V. Malykhina, O.V. Torhovkin, A.N. Dovbnua, A.S. Deiev, V.S. Malyshevsky, V.V. Mitrochenko, G.V. Fomin and B.I. Shramenko

Abstract The yields of A(γ,X)^{7}Be reactions induced by bremsstrahlung photons were measured at the endpoint electron energies of 40, 50, 60, 70, 80, and 90 MeV. Computer simulation of bremsstrahlung converter parameters was carried out with using the Geant4 toolkit. The cross sections for the A(γ,X)^{7}Be reactions on ^{12}C and ^{14}N nuclei were evaluated on the basis of the measured reaction yields and the calculated bremsstrahlung spectra. The agreement of the experimental and evaluated results was demonstrated for ^{12}C nuclei and partly for ^{14}N nuclei.

1 Computer Simulation of Bremsstrahlung Converter Parameters

The radioactivity of air receives a significant contribution from the short-lived isotope ^{7}Be of cosmogenic origin [1]. Dominant reactions leading to the production of beryllium isotopes in the Earth's atmosphere are induced by the interaction of cosmic protons and neutrons with nitrogen and oxygen nuclei [2]. The results obtained in [1] shows that photonuclear reactions may be yet another possible mechanism of the production of the isotope ^{7}Be in the upper atmosphere. However, there are no data on the reactions $^{14}N_7(\gamma,X)^{7}Be_4$ and $^{16}O_8(\gamma,X)^{7}Be_4$ in the literature. Therefore these reactions are of particular interest for an analysis of the photonuclear mechanism of ^{7}Be production in the atmosphere. In order to evaluate the cross section for the photoproduction of the isotope ^{7}Be it is necessary to know the bremsstrahlung flux density at the target position. Initially it was necessary to choose the bremsstrahlung converter material and it thickness. A computer simulation of the passage of primary electrons through various materials was carried out using Geant4 toolkit. The efficiency of the converter model was investigated for the following materials:

T.V. Malykhina (✉)
Kharkiv National University, Kharkiv 61022, Ukraine
e-mail: malykhina@karazin.ua

O.V. Torhovkin · A.N. Dovbnua · A.S. Deiev · V.V. Mitrochenko · B.I. Shramenko
Kharkiv Institute of Physics and Technology, Kharkiv 61108, Ukraine

V.S. Malyshevsky · G.V. Fomin
Southern Federal University, Rostov-on-Don, Russia

J.-E. García-Ramos et al. (eds.), *Basic Concepts in Nuclear Physics: Theory, Experiments and Applications*, Springer Proceedings in Physics 182,
DOI 10.1007/978-3-319-21191-6_18

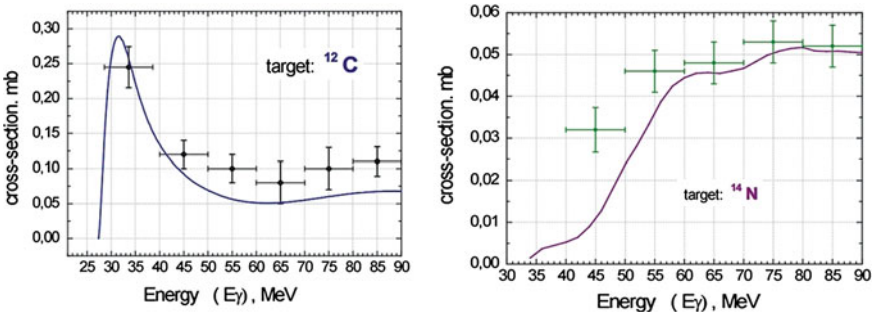

Fig. 1 Cross-section for ^{7}Be production by ^{12}C and ^{14}N nuclei (*points*-experimental data, *curves*-Talys 1.4 calculation)

Au, Pt, Ir, Ta, W, Pb. It was found that tantalum is the most suitable material for the bremsstrahlung converter.

2 Description of the Experiment

In order to determine the cross section for ^{7}Be photoproduction in A(γ,X)^{7}Be$_4$ reactions, the experiment at the linear electron accelerator was carried out. A set of targets containing O, N, and C was irradiated with bremsstrahlung photons. The energy of accelerated electrons was changed from 40 to 90 MeV with a step of 10 MeV at a current of about 4.2 μA. A thin foil made of ^{99}Mo was used as a reference target. In order to ensure thermal stability in series of irradiation, corundum (Al_2O_3), high-purity graphite (C), and aluminum-nitride powder (AlN) were used as targets. The activity of each target after irradiation was measured with the aid of a CANBERRA InSpector 2000 spectrometer with energy resolution 1.74 keV for the 1332 keV line and with relative error in determining activities not greater than 6 %. The averaged cross-sections (Fig. 1) for the ^{7}Be isotope production from different targets were calculated by the following formula:

$$\sigma = \frac{A_0 \cdot A_m}{\Phi_0 \cdot m \cdot N_{Av} \cdot (1 - e^{-\lambda \cdot t}) \cdot 10^{-24}}$$

where σ is the cross-section (b); Φ_0 is the γ-quantum flux density (1/cm^2·s); A_0 is the target activity (Bq); A_m is the atomic weight of the target isotope; N_{Av} is the Avogadro number; m is the mass in the target (g); λ is the decay constant of ^{7}Be.

The Fig. 1 shows partial agreement of the experimental and evaluated results.

References

1. M.V. Bezuglov, V.S. Malyshevsky, G.V. Fomin, A.V. Torgovkin, B.I. Shramenko, T.V. Malykhina, Phys. Rev. C **86**, 024609 (2012)
2. M. Yoshimori, Adv. Space Res. **36**, 922 (2005)

A Compact Detector for Studying Heavy Ion Reactions: GLORIA

G. Marquínez-Durán, L. Acosta, R. Berjillos, J.A. Dueñas, J.A. Labrador, K. Rusek, A.M. Sánchez-Benítez and I. Martel

Abstract In this work we present the GLObal ReactIon Array (GLORIA), a compact silicon array which has been build in order to study heavy ion reactions involving radioactive beams. It has been used for the first time at the SPIRAL-GANIL facility in Caen (France), for studying the scattering of the system ^{8}He + ^{208}Pb at energies around the Coulomb barrier.

1 Introduction and Design of the Detector Array

Silicon detectors have become widespread devices for the construction of charged particles detector arrays, due to their good energy resolution and high detection efficiency at moderate counting rates, as is the case of radioactive beam facilities. GLORIA [1] consists of six DSSSD particle-telescopes with two stages of 40 μm and 1 mm thickness. These telescopes are arranged in such a way that they are tangent to a sphere of 60 mm radius, covering a continuous angular range from 15° to 165° (lab) and a 26.1 % of 4π. In particular, two telescopes cover the forward angles while two others cover the backward angles, and other two are located above and below the target. The target is rotated 30° with respect to the vertical axis avoiding shadows in the detectors. The detectors, delivered by Micron Semiconductors [2] have a total surface of 50×50 mm^2, 16 junction elements and 16 ohmic elements, resulting in

G. Marquínez-Durán (✉) · R. Berjillos · J.A. Dueñas · A.M. Sánchez-Benítez · K. Rusek
Departamento de Física Aplicada, Universidad de Huelva, 21071 Huelva, Spain
e-mail: gloriamarquinez@dfa.uhu.es

L. Acosta
Instituto de Física, Universidad Nacional Autónoma de México, Mexico, Mexico

J.A. Labrador
Centro Nacional de Aceleradores, 41092 Sevilla, Spain

K. Rusek
Heavy Ion Laboratory, University of Warsaw, Pasteura 5a, 02-093 Warsaw, Poland

J.-E. García-Ramos et al. (eds.), *Basic Concepts in Nuclear Physics: Theory, Experiments and Applications*, Springer Proceedings in Physics 182,
DOI 10.1007/978-3-319-21191-6_19

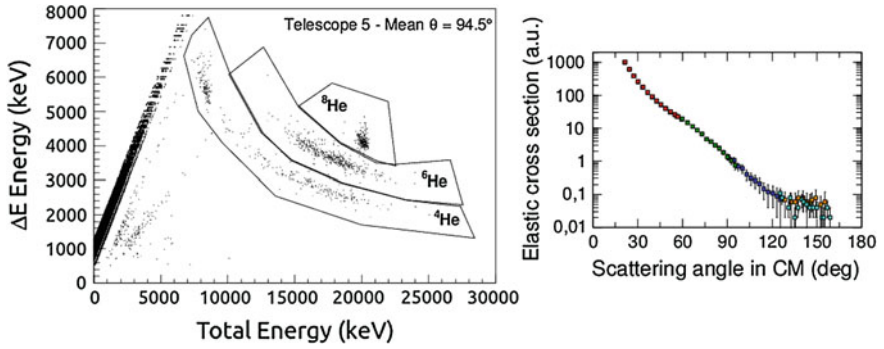

Fig. 1 Identification spectrum obtained with GLORIA, at the observation angle of 94.5° (lab) (*left*) and preliminary angular distribution of the elastic cross section (*right*) for the reaction ^{8}He+^{208}Pb at 22 MeV

256 pixels. All telescopes are attached to a supporting structure manufactured in stainless steel in such a way that their relative position is fixed. The GLORIA array is mounted together with a beam diagnostics system which help operators in the process of focusing and driving the beam through the chamber.

2 First Experimental Results

The GLORIA detection system was used for the first time in the study of the dynamics of the system ^{8}He + ^{208}Pb at 16 and 22 MeV. A typical identification spectrum obtained in one of telescopes is shown in Fig. 1 (left). As it can be observed, the detection system allows for the identification of the different isotopes produced. A preliminary angular distribution of the elastic cross section can be found in Fig. 1 (right) where it is shown how a good matching is achieved between all the telescopes in GLORIA, providing a continuous angular distribution from 20° to 160° (CM).

As a conclusion, this detection system has demonstrated a good isotope separation capability at least up to helium isotopes and it has provided continuous angular distributions of elastic and reaction cross sections in a wide angular range, in the study of the ^{8}He+^{208}Pb system.

References

1. G. Marquínez-Durán et al., GLORIA: A compact detector system for studying heavy ion reactions using radioactive beams. Nucl. Instr. Meth. Phys. Res. **A755**, 69–77 (2014)
2. http://www.microsemiconductor.co.uk/products-strip.asp?productsubcatID=1

A Proposal for a 72.75 MHz RFQ for ECOS-LINCE Project

A.K. Ordúz, C. Bontoiu, J. Dueñas, I. Martel, A. Garbayo, A.C.C. Villari and P.N. Ostroumov

Abstract ECOS-LINCE (Martel I et al., Proceedings IPAC'14, 2014) is a proposal for a new European First Class high intensity heavy-ions accelerator for stable ions, with energies at and above the coulomb barrier. The low energy section will be achieved using a 72.75 MHz normal conducting four vanes RFQ designed to give a 460 keV/u boost for A/Q = 7 ions in about 5 m (Orduz AK et al., IPAC'14, 2014). The geometry vanes are modeled to accommodate windows in order to obtain a clear separation of the RFQ modes (Ostroumov P et al., Rev ST Accel Beams 15:110101, 2012). This article presents the experimental results of the RF test carried out on a aluminum prototype.

1 Introduction

The proposed CW multi-ion superconducting linac ECOS-LINCE should be able to accelerate a wide range of ions and energies, from protons up to Uranium [1–3]. The principal design requirements imposed in present work are [4]: energy range from protons (45 MeV) up to Uranium (8.5 MeV), high intensity beam of 1 mA for light ions and 10 pμ A for heavy ions, transverse emittance rms $<1\,\pi$ mm mrad, longitudinal emittance rms <4 ns keV/u and bunch length <1 ns. The RF analysis has been carried with Comsol Multiphysics [5] and the resistive power losses obtained are coupled with the Heat-transfer module in order to obtain a temperature map. On the other hand, the cooling system is simulated in Fluid-flow module using water

A.K. Ordúz (✉) · C. Bontoiu · J. Dueñas · I. Martel
Department of Applied Physics, University of Huelva, 21071 Huelva, Spain
e-mail: angie.orduz@dfa.uhu.es

A. Garbayo
AVS, ELgobiar, Gipuzkoa, Spain

A.C.C. Villari
FRIB, East Lansing, Michigan, USA

P.N. Ostroumov
ANL, 9700 S. Cass Av. Argonne, Lemont, IL, USA

J.-E. García-Ramos et al. (eds.), *Basic Concepts in Nuclear Physics: Theory, Experiments and Applications*, Springer Proceedings in Physics 182,
DOI 10.1007/978-3-319-21191-6_20

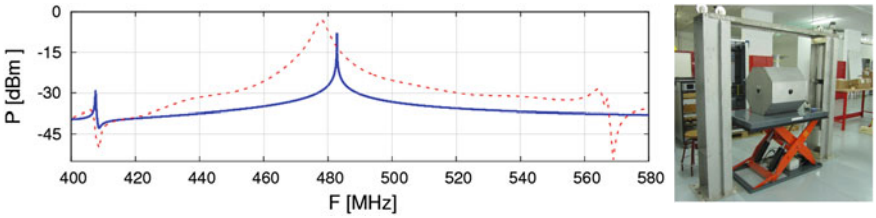

Fig. 1 Experimental and simulated RFQ frequency mode (*left*) and Aluminum RFQ section prototype (*right*)

pipes inside the vanes and walls. The heat flux remained is coupled to a mechanical deformation module, which provides estimates for the displacement due to thermal expansion. Finally, an evaluation of the RF frequency shift is obtained through RF-analysis module, using the deformed structure.

2 RFQ Prototype

A model in aluminium for one RFQ section has been built in Huelva together with Spanish companies an tested in the RF Laboratory at the University of Huelva as shown in Fig. 1. The test was performed with a Agilent N90000A CXA spectrum analyzer to measure the frequency response of the cavity. The cavity without vanes resonates at 485 MHz in agreement with COMSOL simulations as it can be seen from the spectra shown in Fig. 1. Introducing the four vanes in the resonator leads to the appearance of a quadrupole mode TE_{211}, resonating around 183 MHz, very close to a doubly degenerated dipole mode. Future developments will include suitable input matcher and trapezoidal cells to shorten the length and improve the performance of the cavity.

References

1. A.K. Orduz et al., in *Development of a 72.75 MHz RFQ for the LINCE Accelerator Complex*. IPAC'14, Dresden, Germany, June 2014. http://accelconf.web.cern.ch/AccelConf/IPAC2014/. Cited 22 Sept 2015
2. P. Ostroumov et al., Rev. ST Accel. Beams **15**, 110101 (2012)
3. European Collaboration on Stable Ion Beams. http://www.ensarfp7.eu/projects/ecos. Cited 25 Sept 2015
4. I. Martel et al., in *LINCE: a high intensity multi-ion superconducting Linac for nuclear structure and reactions*. Proceedings IPAC'14, Dresden, Germany, June 2014. http://accelconf.web.cern.ch/AccelConf/IPAC2014/. Cited 22 Sept 2015
5. Comsol Website, http://www.comsol.com. Cited 22 Sept 2015

First Approach to the Noise Analysis of a Dual Silicon Strip Detector in a System to Verify Radiotherapy Treatments

M.C. Ovejero, A. Pérez Vega-Leal, A. Selva, M.I. Gallardo, J.M. Espino-Navas, M.A. Cortes-Giraldo, R. Nunez, R. Arrans and M.C. Battaglia

Abstract This work presents the first approach for the noise analysis of a Dual Single Sided Silicon Strip Detector (DSSSSD) in a system specifically designed for radiotherapy treatment verification. In order to obtain the absorbed dose, the system has been designed to measure the charge generated in the detector by the incident radiation from a medical linear accelerator (linac); but, even when there is no irradiation signal from the linac, the system measures the electronic noise and the leakage current of the detector. The amount of charge generated in the detector whose origin is not the irradiation from the linac should be known in order to correct it, if required, from the total amount of accumulated charge. The model below describes and characterizes this effect in the device.

1 Charge Collection and Noise Study in the Detector

In the DSSSSD detector of the radiotherapy treatment verification system [1–3], the behaviour of every strip can be approximated by a single reverse-bias photodiode, whose output signal is a current. The equivalent model for every strip can be approximated by the circuit shown in Fig. 1: the parallel of a photodiode (I_d), with a current source (I_{dark}), a parasitic capacitor (C_j), and a load (R_t). The total amount of current

M.C. Ovejero (✉) · J.M. Espino-Navas · M.I. Gallardo · M.A. Cortes-Giraldo
Departamento de Física Atómica, Molecular y Nuclear (FAMN) de la, Universidad de Sevilla, 41013 Seville, Spain
e-mail: movejero@us.es

A. Pérez Vega-Leal · R. Nunez
Escuela Superior de Ingenieros de la Universidad de Sevilla, 41092 Seville, Spain

A. Selva
Dipartimento di Fisica E Astronomia 'Galileo Galilei', 35131 Padova, Italy

R. Arrans
Hospital Universitario Virgen Macarena, 41071 Seville, Spain

M.C. Battaglia
National Acelerator Centre (CNA), 41092 Seville, Spain

J.-E. García-Ramos et al. (eds.), *Basic Concepts in Nuclear Physics: Theory, Experiments and Applications*, Springer Proceedings in Physics 182,
DOI 10.1007/978-3-319-21191-6_21

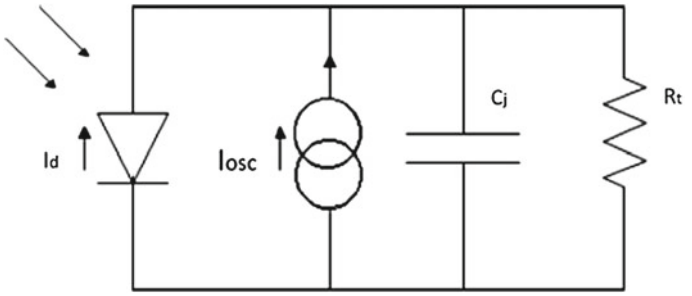

Fig. 1 Behavioural model of every strip

obtained for every photodiode is the addition of the dark current (I_{dark}) plus the current produced by irradiation (I_d).

In a reverse-bias polarized photodiode, there is a current even if there is no incident radiation, that current is called dark current (I_{dark}). It is important to keep into account this concept: the aim of the system is to measure the charge generated by the irradiation current (I_d), but even when there is no irradiation signal in the input, the output is charged with the dark and the electronic noise current. The amount of charge whose origin is in the dark current should be known in order to be able to correct its effect in the total amount of measured charge.

The value of each parameter from the equivalent circuit for the photodiode of every strip is established. It allows to perform a noise analysis and to compare it with the corresponding measures.

References

1. A. Bocci, M.C. Giraldo, M.I. Gallardo, J.M. Espino, Silicon strip detector for a novel 2d dosimetric method for radiotherapy treatment verification. Nucl. Inst. Meth. Phys. Res. A **673**, 98 (2012)
2. M.A.G. Alvarez, Z. Abou-Haid, R. Arrans, M.C. Battaglia, M.A.C. Giraldo, J.M.E. Navas, M.I. Gallardo, M. Ovejero, A.P. Vega-Leal, A. Selva, S. Walsh, Novel dual single sided silicon strip detector chip for radiotherapy verification. Proc. Sci. X LASNPA (2013)
3. I.C. on Translational Research in Radiation Oncology. J. Eur. Soc. Radiother. Oncol. ESTRO (2014)

SM Higgs Exclusion and Anomalous Spin Zero HVV Couplings of the Higgs Boson in Proton Collisions at 7 TeV and 8 TeV

Rashmi Ramesh

Abstract A study of the basic spin parity, interaction and decay of the Higgs Boson is performed. The techniques used in the analysis of Higgs to illustrate the Standard model Higgs Exclusion is depicted. Under the hypothesis that the resonance is a spin zero boson, the tensor structure of the interactions of the Higgs with two vector bosons ZZ, Zγ, $\gamma\gamma$ and WW is investigated and limits on eleven anomalous contributions are set. A dataset recorded by the CMS experiment during LHC Run1, on HVV spin zero coupling is brought into the picture [1]. Finally a few of the mysteries and adventures yet to be undertaken in our current particle quest is highlighted.

The observation of a new boson with a mass around 125 GeV and properties consistent with the standard model (SM) Higgs boson was reported by the ATLAS and CMS Collaborations in 2012 [2]. The discovery was followed by a comprehensive set of measurements of its properties to determine if the new boson follows the SM predictions or if there are indications for physics beyond the SM (BSM). The CMS experiment analyzed the full dataset collected during the CERN LHC Run 1 and [3] measured the properties of the Higgs-like boson, H, using its decay modes to two electroweak gauge bosons $H \rightarrow ZZ \rightarrow 4l$, $H \rightarrow WW \rightarrow l\nu\, l\nu$, and $H \rightarrow \gamma\gamma$, where l denotes $e^{\pm}$ or $m^{\pm}$, and WW denotes $W^{+}W^{-}$. The results showed that the spin-parity properties of the new boson are consistent with the expectations for the scalar SM Higgs boson. In particular, the hypotheses of a pseudoscalar, vector, and pseudovector boson were excluded at a 99.95 % confidence level (CL) or higher, and several spin-two boson hypotheses were excluded at a 98 % CL or higher. The investigated spin-two models included two bosons with graviton like interactions and two bosons with higher-dimension operators and opposite parity. The spin-zero results included the first constraint of the fa3 parameter, which probes the tensor structure of the HZZ interactions and is defined as the fractional pseudoscalar cross section, with $fa3 = 1$ corresponding to the pure pseudoscalar hypothesis. The ATLAS experiment has also excluded at a 98 % CL or higher the hypotheses of a pseudoscalar,

R. Ramesh (✉)
SSN College of Engineering, Chennai, India
e-mail: johnsonrashmi@gmail.com

J.-E. García-Ramos et al. (eds.), *Basic Concepts in Nuclear Physics: Theory, Experiments and Applications*, Springer Proceedings in Physics 182,
DOI 10.1007/978-3-319-21191-6_22

vector, pseudovector, and graviton-inspired spin-two boson with minimal couplings and several assumptions on the boson production mechanisms.

In this poster, a study of the spin-parity properties of the Higgs boson and of the tensor structure of its interactions with electroweak gauge bosons is presented using the $H \to ZZ$, $Z\gamma^*$, $\gamma^*\gamma^* \to 4l$, where the interference between the three intermediate states is included, and $H \to WW \to l\nu\, l\nu$ decay modes at the CMS experiment. The study focuses on testing for the presence of anomalous effects in HZZ and HWW interactions under spin-zero, -one, and -two hypotheses. The $HZ\gamma$ and $H\gamma\gamma$ interactions are probed for the first time using the $4l$ final state. Constraints are set on eleven anomalous coupling contributions to the HVV interactions, where V is a gauge vector boson, under the spin-zero assumption of the Higgs boson, extending the original measurement of the f_{a3} parameter. The exotic-spin study is extended to the analysis of mixed spin-one states, beyond the pure parity states studied earlier, and ten spin-two hypotheses of the boson under the assumption of production either via gluon fusion or quark-antiquark annihilation, or without such an assumption. This corresponds to thirty spin-two models, beyond the six production and decay models. The $H \to \gamma\gamma$ decay channel is also studied in the context of exotic spin-two scenarios, and the results are combined with those obtained in the $H \to ZZ$ and $H \to WW$ channels.

The experimental approaches used here are similar to those used by CMS to study the spinparity and other properties of the new resonance, and use the techniques developed for such measurements. The analysis is based on theoretical and phenomenological studies that describe the couplings of a Higgs-like boson to two gauge bosons. They provide techniques and ideas for measuring the spin and CP properties of a particle interacting with vector bosons. Historically, such techniques have been applied to the analysis of meson decays to four-body final states.

A comprehensive study of the spin-parity properties of the recently discovered H boson and of the tensor structure of its interactions with electroweak gauge bosons is presented using the $H \to ZZ$, $Z\gamma^*$, $\gamma^*\gamma^* \to 4l$, $H \to WW \to l\nu\, l\nu$, and $H \to \gamma\gamma$ decay modes. The results are based on the 2011 and 2012 data from pp collisions recorded with the CMS detector at the LHC, and correspond to an integrated luminosity of up to 5.1 fb^{-1} at a center-of-mass energy of 7 TeV and up to 19.7 fb^{-1} at 8 TeV. The phenomenological formulation for the interactions of a spin-zero, -one, or -two boson with the SM particles is based on a scattering amplitude or, equivalently, an effective field theory Lagrangian, with operators up to dimension five. The dedicated simulation and matrix element likelihood approach for the analysis of the kinematics of H boson production and decay in different topologies are based on this formulation. A maximum likelihood fit of the signal and background distributions provides constraints on the anomalous couplings of the H boson.

The study focuses on testing for the presence of anomalous effects in HZZ and HWW interactions under spin-zero, -one, and -two hypotheses. The combination of the $H \to ZZ$ and $H \to WW$ measurements leads to tighter constraints on the H boson spin-parity and anomalous HVV interactions. The combination with the $H \to \gamma\gamma$ measurements also allows tighter constraints in the spin-two case. The $HZ\gamma$ and $H\gamma\gamma$ interactions are probed for the first time using the $4l$ final state.

The exotic-spin study covers the analysis of mixed-parity spin-one states and ten spin-two hypotheses under the assumption of production either via gluon fusion or quark-antiquark annihilation, or without such an assumption. The spin-one hypotheses are excluded at a greater than 99.999 % CL in the ZZ and WW modes, while in the $\gamma\gamma$ mode they are excluded by the Landau-Yang theorem. The spin-two boson with gravity-like minimal couplings is excluded at a 99.87 % CL, and the other spin-two hypotheses tested are excluded at a 99 % CL or higher.

Given the exclusion of the spin-one and spin-two scenarios, constraints are set on the contribution of eleven anomalous couplings to the HZZ, HZγ, H$\gamma\gamma$, and HWW interactions of a spin-zero H boson, as summarized in the Table. Among these is the measurement of the f_{a3} parameter, which is defined as the fractional pseudoscalar cross section in the H $\rightarrow$ ZZ channel. The constraint is $f_{a3} < 0.43$ (0.40) at a 95 % CL for the positive (negative) phase of the pseudoscalar coupling with respect to the dominant SM-like coupling and $f_{a3} = 1$ exclusion of a pure pseudoscalar hypothesis at a 99.98 % CL.

All observations are consistent with the expectations for a scalar SM-like Higgs boson. It is not presently established that the interactions of the observed state conserve C-parity or CP-parity. However, under the assumption that both quantities are conserved, our measurements require the quantum numbers of the new state to be JPC = 0++. The positive P-parity follows from the f_{VVa3} measurements in the H $\rightarrow$ ZZ, Zγ*, γ*γ* $\rightarrow 4l$, and H $\rightarrow$ WW $\rightarrow$ $lv\,lv$ decays and the positive C-parity follows from observation of the H $\rightarrow$ $\gamma\gamma$ decay. Further measurements probing the tensor structure of the HVV and H*ff* interactions can test the assumption of CP invariance.

References

1. The CMS Collaboration, Constraints on the spin-parity and anomalous HVV couplings of the Higgs boson in proton collisions at 7 and 8 TeV (2014)
2. J. Incandela, Status of CMS SM Higgs search (2012)
3. http://home.web.cern.ch/about/updates/2015/01/cms-pins-down-higgs-first-run-data

A Monte Carlo Study of Clinical PET ECAT EXACT HR+ Using GATE

Rahal Saaidi, Yassine Toufique, Asad Merouani, Othman Elbouhali and Rajaa Cherkaoui El Moursli

Abstract Monte Carlo simulation is an effective tool for the design and development of new systems in nuclear medicine such as Positron emission tomography (PET) in particular. In this work, we used GATE platform (Geant4 Application for Tomographic Emission), based on GEANT4 Monte Carlo simulation, to study the Count rate performance and noise equivalent count rate (NECR) values in different activity concentrations corresponding the different coincidence timing windows of 6, 8 and 12 ns of the ECAT EXAT HR+. The ECAT EXACT HR+ validated using NEMA NU 2-2001, the scatter fraction (SF), sensitivity and NECR show a good agreement with experimental value. The obtained results show that the minimizing time coincidence windows increase the NECR by 38 % and True count rate performance by 15 %.

1 Introduction

PET is a medical imaging modality, which becomes indispensable in clinical oncology, for cancers diagnostics. PET allows estimating the 3-D distribution of radiotracer in the target organ [1–3]. The physics of PET systems based on the detection of the pair photons in coincidence with an energy of 511 keV and an angle of 180°. These photons produced by an electron-positron annihilation [4]. In accordance with the specifications of the manufacturers we applied a coincidence windows time, in this work we used GATE platform [5] to study count rate performance and NECR. The purpose of this simulation is to study the effect of changing the coincidence windows time on Noise Equivalent Count Rate.

R. Saaidi (✉) · A. Merouani · R. Cherkaoui El Moursli
Laboratory of Nuclear Physics, Faculty of Sciences, Mohammed V University, Rabat, Morocco
e-mail: saaidirahal@gmail.com

Y. Toufique · O. Elbouhali
Texas AM University at Qatar, Doha, Qatar

J.-E. García-Ramos et al. (eds.), *Basic Concepts in Nuclear Physics: Theory, Experiments and Applications*, Springer Proceedings in Physics 182,
DOI 10.1007/978-3-319-21191-6_23

2 Methods and Materials

The simulation of a GATE-modeled ECAT EXACT HR+ scanner performed using the geometrical parameters of the scanner and validated through the simulation of standard performance parameters proposed by the National Electrical Manufacturers Association (NEMA) [4], these parameters are the (SF), the Sensitivity (S), and the (NECR).

3 Results and Discussion

The SF, Sensitivity, and NECR performance parameters, as well as the count rates, obtained from the above-described simulations presented in this section. These parameters are compared with experimental data extracted from published works [1–3] for this type of scanner.

Table 1 show respectively a comparison of the obtained Sensitivity with the experimental data extracted, the comparison of the simulated Sensitivities with the experimental data [2, 3], shows an agreement within 2.9 % at R = 0 and 0.15 % at R = 10. This difference of 2.9 % may be explained by inherent limitations of the resolution of the PMTs and not tacking in account of the light shielding modeling within GATE between the detector blocks.

The SF parameter obtained is 42.3 present an agreement of 9.7 % with the experiment data [1, 2]. This difference mainly due to the difficulties to model an accurate geometry of the scanner, in addition to the fact that the scanning bed not taken into account in the simulation.

The obtained results show that the true coincidence rate at lower activity concentrations, not affected by varying the coincidence window times Fig. 1a. However, at higher activity concentrations, the true rates increase slightly for shorter coincidence windows and random decrease. Figure 1b shows a significant improvement of NECR by using the smaller coincidence window time. The peak NECR increased by 38 %. The maximum of the NECR simulated for the scanner is 35162 cps at 6.5 Kbq/ml A deviation of 5 % observed between the simulations and the experimental values of the NECR (37000 cps at 10 kbq/ml) [2].

Table 1 Sensitivity parameter for the ECATEXACT HR+PET scanner, calculated using the NEMA NU2-2001 protocols

Sensitivity	Experimental results cps/MBq	R = 0 cm	6650
		R = 10 cm	7180
		Ratio (R = 0/R = 10 cm)	0.926
	Simulated results cps/MBq	R = 0 cm	6853
		R = 10 cm	7169
		Ratio (R = 0/R = 10 cm)	0.955

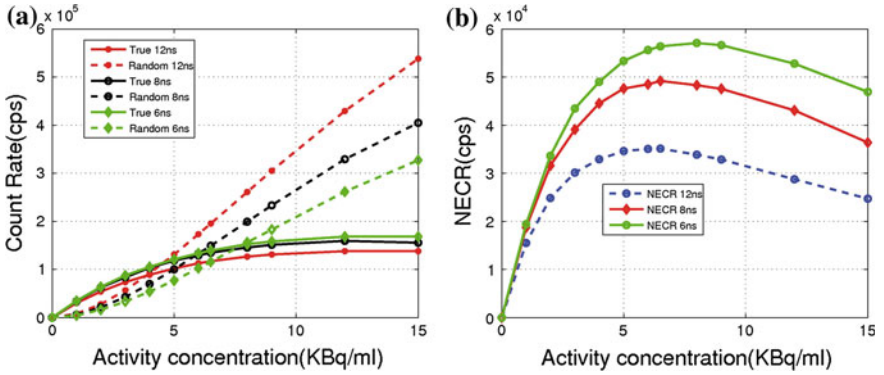

Fig. 1 True rates and random (**a**), NECR (**b**) versus activity concentration for varying coincidence window time

4 Conclusion

The determination of the performance parameters, Scatter Fraction, Sensitivity, NEC, and count rates from the simulations performed with the designed model of the clinical ECAT EXACT HR+ scanner, using GATE, show a good agreements with the published experimental data for this type of scanner. The obtained results show that the true coincidences increase and reduce the number of random, when we minimizing coincidence windows timing. This change increase the NECR factor. This factor is one of those, which improve the image quality in the clinical PET scanner ECAT EXACT HR+.

References

1. N. Karakatsanis, N. Sakellios, N.X. Tsantilas, N. Dikaios, C. Tsoumpas, D. Lazaro, G. Loudos, C.R. Schmidtlein, K. Louizi, J. Valais, D. Nikolopoulos, J. Malamitsi, J. Kandarakis, K. Nikita, Comparative evaluation of two commercial PET scanners, ECAT EXACT HR+ and Biograph 2, using GATE. Nucl. Instrum. Methods Phys. Res. Sect. Accel. Spectrometers Detect. Assoc. Equip. **569**(2), 368–372 (2006)
2. Y. Toufique et al., Applied to simulation of positron emission tomography (PET) systems using gate, 6th Iberian grid infrastructure conference, pp. 123–134 (2012)
3. H. Herzog, L. Tellmann, C. Hocke, U. Pietrzyk, M.E. Casey, T. Kuwert, NEMA NU2-2001 guided performance evaluation of four Siemens ECAT PET scanners. IEEE Trans. Nucl. Sci. **51**(5), 2662–2669 (2004)
4. NEMA standards publication, NU 2-2001: Performance measure-mensts of positron emission tomographs, (Technical Report, National Electrical Manufacturers Association, Washington, DC, 2001)
5. S. Jan et al., GATE: a simulation toolkit for PET and SPECT. Phys. Med. Biol. **49**, 4543 (2004)

Validation of the Monte Carlo Simulation of a Siemens Biograph mCT PET

L. Vázquez Canelas, B. Quintana Arnés, C. Montes Fuentes, M.J. Gutiérrez Palmero, P. Tamayo Alonso and J.M. Blasco

Abstract Geant4 Application for Tomography Emission (GATE) is a simulation platform based on GEANT4. It is designed to perform numerical simulations in medical imaging and radiotherapy. It is also used to simulate Emission Tomography (Positron Emission Tomography, PET and Single Photon Emission Computed Tomography, SPECT), Computed Tomography (CT) and Radiotherapy experiments. The purpose of this study is to validate a GATE model of the commercial PET/CT Siemens Biograph, the latest acquisition of the Clinical Hospital of Salamanca. The geometry of the system has been implemented in GATE, including the detector ring, the crystal blocks, the PMTs etc. Radionuclides for all measurements shall be ^{18}F and a cylindrical source type *twogamma* (which has no attenuation). The GATE simulated results are directly compared to experimental data obtained using a number of NEMA NU-2-2007 performance protocols, including sensitivity and scatter fraction. The PET data generated using GATE can be reconstructed using STIR (Software for Tomographic Imagen Reconstruction). STIR is an open source software, written in C++, consisting of classes, functions and utilities for 3D PET image reconstruction, although it is general enough to accommodate other imaging modalities. Finally we will compare our simulated model with experimental values of the scanner they have at the hospital in Salamanca.

L. Vázquez Canelas (✉) · B. Quintana Arnés
Universidad de Salamanca, Laboratorio de Radiaciones Ionizantes, Salamanca, Spain
e-mail: lorena.vazquez@usal.es

C. Montes Fuentes · M.J. Gutiérrez Palmero · P. Tamayo Alonso
Hospital Universitario de Salamanca, Servicio de Radiología y Protección Radiológica, Salamanca, Spain

J.M. Blasco
Universidad de Valencia, Valencia, Spain

J.-E. García-Ramos et al. (eds.), *Basic Concepts in Nuclear Physics: Theory, Experiments and Applications*, Springer Proceedings in Physics 182,
DOI 10.1007/978-3-319-21191-6_24

1 Objectives

The main objectives are to emulate a Biograph mCT PET and its *twogamma* and ^{18}F sources using the GATE [1] simulation code for diagnostic purposes and to validate of the model with experimental measurements and specifications equipment for different experimental conditions.

2 Materials

2.1 Physical Basis of Positron Emission Tomography (PET)

PET is a technique that allows, for both a functional and an anatomical study, to study the metabolic activity of a human body, through the administration of a radiopharmaceutical positron emitter (^{18}F).

Two photons of 511 keV are produced by annihilation between a positron, emitted by the radiotracer, and an electron of the patient's body. This pair determines a line of response (LOR), along which the annihilation takes place. With the information gathered from all the interactions that occurred in all the crystals, sinograms are constructed and thus the final image is obtained through analytical or iterative algorithms.

2.2 Scanner's Geometry

It comprises four rings of the detectors scintillation crystals, with a total diameter of 842 mm. It is made by 48 blocks, with a total of 624 elements per ring. Each individual block, formed by a matrix 13×13 crystal, has 169 detectors with 4 photomultiplier tubes per block [2]. The detector material is LSO, lutetium orthosilicate. This material is widely used in diagnostic imaging with PET. One drawback of LSO is that 2.6 % of lutetium in the crystal comes from the radioactive isotope ^{176}Lu, which decays by β^-emission followed by a gamma ray cascade of energies 307 and 202 keV. The intrinsic activity of ^{176}Lu is low (276 Bq/cm^3) and it is not noticeable during routine scanning with activity levels o the order of several MBq. But it can become a problem in studies with animals.

3 Methods

3.1 Sensitivity

An important design's factor of PET system is to maximize the sensitivity (S) of system, because it is a determining factor in the quality of the final image. The

sensitivity indicates the ability to detect a type of radiation and energy, quantify the ability of the scanner to detect coincidence photons within the field of view (FOV). The sensitivity is defined as the number of coincidence events per unit of time divided by the activity present in a source. It depends mainly of the geometry of the scanner, geometric and intrinsic efficiency, energy window; dead time… It is usually measured in cps/Ci or cps/kBq. Total events are determined by the amount of radioactivity injected to the patient. The practical limits are determined by amount of radiation administered to the patient and the acquisition time of the study. To measure the sensitivity, we have used a phantom of concentric aluminium cylinders of 70 cm length and a wall thickness of 1.25 mm filled with a solution of ^{18}F.

3.2 Scatter Fraction (SF). The Noise Equivalent Count Rate (NEC) Curve

The scattering is part of attenuation phenomena, where the photons deviate from their original directions and contribute to inappropriate LORs (Lines Of Response). This results in false counts. The purpose of SF is to remove false counts. The scattering contribution increases with density and depth of body tissue, density of detector material and activity in the patient. The NEC curve represents the effective yield counting system, taking into account when calculating the percentages of random events (R) and events that have suffered dispersion (S). In this case, the phantom consists of a solid polyethylene cylinder of 20 cm in diameter and 70 cm in length. At r = 4.5 cm a capillary is introduced with ^{18}F a specified amount.

4 Results

4.1 Sensitivity

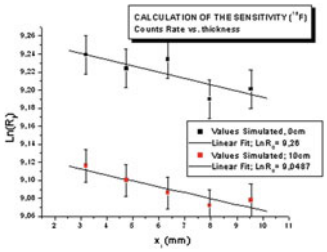

From the different linear fits, we were measured at 0 cm (at the centre of FOV), a value of sensitivity of tomograph of 10.9 kcps/MBq (1.09 %) for the ^{18}F source and

11.2 kcps/MBq (1.12 %) for the *twogamma* source. When we move our source to 10 cm, we get 8.85 kcps/MBq for the ^{18}F source.

$$S = \frac{n^o coincidents\ events}{A_{cal}} \left(\frac{cps}{kBq}, \frac{cps}{\mu Ci} \right)$$

4.2 Scatter Fraction. NEC Curve

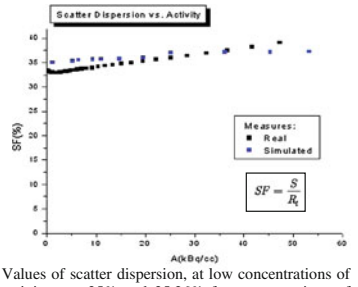

Values of scatter dispersion, at low concentrations of activity, are 35% and 35.26% for concentrations of 1.28 and 5.32 kBq/cc respectively. The value provided by specification's equipment is 38%.

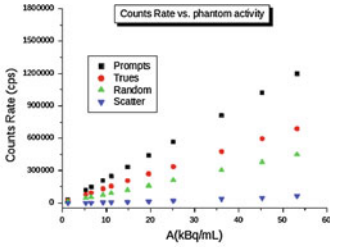

We show the variation of the total events, including true, random and scatter, depending on the radioactivity concentration inner the phantom. The peak of true events occurs at a similar rate within the statistical error, to those presented by the manufacturer, 500 kcps and 36 kBq/cc.

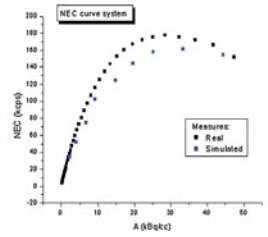

The NEC curve is plotted as a function of activity concentrations. The peak NEC depends on the geometry, scanner materials, energy window and also on acquisition electronics, mainly dead time and coincidence window. It is defined empirically as follows:

$$NEC = \frac{T^2}{T+R+S} \begin{cases} T \equiv \text{number of true coincidences} \\ \text{R} \equiv \text{number of random coincidences} \\ \text{S} \equiv \text{number of scatter coincidences} \end{cases}$$

In our simulation, the coincidence window is 4.1 ns, the energy resolution is 12%, the energy window is (435-650) keV and dead time 3 μs. The NEC peak corresponds to 161 kcps with a value of the activity of 34.5 kBq/cc.

5 Conclusions

We have characterized the scanner Biograph mCT through Geant4 simulations. The sensitivity and scatter fraction were measured using *twogamma* and ^{18}F sources, according to the NEMA NU 2-2007 protocol and compared with real measurements and with those provided by the manufacturer.

References

1. NEMA Standards Publication NU 2-2007 and user's guides of GATE and STIR
2. J.M. Martí-Climent, E. Prieto, Aportación del tiempo de vuelo y de la modelización de la respuesta a una fuente puntual a las características de funcionamiento del tomógrafo PET/TAC Biograph mCT. Rev. Esp. Med. Nucl. Imagen. Mol. **32**(1), 13–21 (2013)

Index

J.-E. García-Ramos et al. (eds.), *Basic Concepts in Nuclear Physics: Theory, Experiments and Applications*, Springer Proceedings in Physics 182,
DOI 10.1007/978-3-319-21191-6